MODELING AND ANALYSIS OF TEMPERATURE MODULATED DIFFERENTIAL SCANNING CALORIMETRY (TMDSC)

XU SHENXI
(*B. Eng., M. Eng., HUAZHONG UNIV. OF SCI. AND TECHNO., CHINA*)

A THESIS SUBMITTED

FOR THE DEGREE OF DOCTOR OF PHILOSOPHY

DEPARTMENT OF MATERIALS SCIENCE

NATIONAL UNIVERSITY OF SINGAPORE

2007

Acknowledgements

First of all, I sincerely thank my research project supervisors. Prof. Li Yi's knowledge and patience were very important throughout my research in the Department of Materials Science, National University of Singapore (NUS). Many thanks are given to Prof. Feng Yuanping for his reviews and careful inspection of my work. I am grateful to Lu Zhaoping, Hu Xiang, Tan Hao, Xu Wei, Irene Lee, Annie Tan, Mitchell Ong, and all other team members, as well as to those who helped me during the long course of the Ph.D. program. I have enjoyed myself at NUS during the last few years and believe that it has been an important part of my life, not only because of the generous offering of a full scholarship by NUS that helped me to complete the research project, but also because of the hospitality and beauty of Singapore, factors that make this country so lovely and energetic.

I am grateful to Prof. Li Z. Y., who was my mentor at Huazhong University of Science and Technology (Wuhan, China) and encouraged me to take the Ph.D. program back in early 1997, when I was still working in southern China. I would also like to extend my gratitude to the teachers and other staff members of my hometown-schools who helped me throughout the 20-year-long learning career. Although I cannot possibly list every one of them here, I thank them all for the help they gave in various forms. In addition, I would like to thank my parents for their never dwindling love and care. Last, but by no means least, I wish to thank my wife and daughter. They have consistently provided me with warmth and sweet distractions, and were able to forgive me for my long absences from time to time.

Xu Shenxi, Oct. 2006 at the National University of Singapore

Modeling and Analysis of Temperature Modulated Differential Scanning Calorimetry

Table of Contents Page

Summary

In this thesis, different aspects of TMDSC are studied and the main results are given below.

(1) Effects of the contact thermal resistance on the observed specific heat

- The relationship among the measured heat capacity, the actual heat capacity and temperature modulation frequency of heat flux type TMDSC is similar to that of a low-pass filter.
- Careful sample preparation is important because too large or too small a sample mass (relative to the mass of the calibration reference) will lead to increased errors in the measured specific heat.
- When TMDSC device works in the conventional differential scanning calorimetry (DSC) mode, the measured specific heat of the sample is not affected by the contact resistance.

(2) Effects of the internal thermal resistance of the sample with a low heat diffusivity

- A model that takes into account the thermal diffusivity of the sample is used and an analytical solution is derived.
- To improve the accuracy of measured specific heat, we may use a longer temperature modulation period, or reduce the sample thickness and mass.

(3) Effects of the non-reversing heat flow on the separability of the reversing heat flow and non-reversing heat flow

The separability of non-reversing heat flow (*NHF*) and reversing heat flow (*RHF*) by TMDSC depends on the *NHF* and temperature modulation conditions. Two

different types of *NHF* are considered: time dependent *NHF* and temperature dependent *NHF*.

- Time dependent *NHF*: The measurement of specific heat (c_p), is applicable for the steady state where there is no *NHF*. While inside the *NHF* temperature range, if the modulation frequency is high enough, it still allows deconvolution of c_p, *HF*, *RHF*, and *NHF* by Fourier transform.
- Temperature dependent *NHF*: The *NHF* will be modulated by the temperature modulation and the *NHF* will contribute to the modulated part of the total heat flow (*HF*). This in turn can affect the linearity of the entire TMDSC system.

(4) Study of the general situation and comparison with experimental results

- A general case that takes into account a kinetic reaction that is both time and temperature dependent is studied.
- Several kinetic models are used to demonstrate the importance of the selection of the experimental parameters as well as their effects on the system linearity.
- TMDSC experiments with several melt spun Al-based amorphous alloys are carried out to demonstrate the unique capabilities of TMDSC. These include the ability to measure the differences between the specific heats of a sample in a fully amorphous, partially crystallized, or fully crystallized state.
- The imaginary part of the complex heat capacity can be defined as $C'' \cong -f_T'/\omega$, where f_T' is the temperature derivative of the kinetic heat flow and ω is the angular frequency of temperature modulation. It should be pointed out that this definition only holds true when the TMDSC system linearity satisfies $(f_T'/ C_s\omega) << 1$.

List of Tables

List of Figures

List of Symbols

Symbols	Description
A	Amplitude of modulated temperature (in K)
A_{HF}	Amplitude of modulated heat flow
$A_{\Delta T}$	Amplitude of the temperature difference between the sample and reference
$A_{T\,b}$	Amplitude of heating block temperature
A_{Ts}	Amplitude of sample temperature
A_{Tr}	Amplitude of reference temperature
B	Reaction constant (in s^{-1})
C_i	Heat capacity (upper case, in J/K) of the heat transfer path or observed heat capacities at different temperature sensing positions. It may have different subscripts, i.e. i=1,2,3…
C_p	Heat capacity (upper case, in J/K)
c_p	Specific heat capacity or specific heat for short (lower case, in J/g·K)
c_{p_r}	Reference specific heat (capacity) (in J/g·K)
c_{p_s}	Sample specific heat (capacity) (in J/g·K)
C_r or C_{pan}	Heat capacity of the reference or pan (in J/K)
C_s	Sample heat capacity (in J/K)
C_{s0}	Heat capacity of sample plus the reference (or pan)
$C_{s\_calibration}$	Heat capacity of the calibration sample
C_{s_m}'	Apparent heat capacity (in J/K)
C_{unit}	Heat capacity of the small sample unit
C^*	Complex heat capacity, $C^*=C'-iC''$
C'	The real part of complex heat capacity, C^*
C''	The imaginary part of complex heat capacity, C^*
d	Sample thickness
E	Non-reversing heat flow (NHF) energy (in J/g)
E_a	Activation energy (in J/mol)

$f(t,T)$	kinetic heat flow that is dependent on both time and temperature
f_T'	The temperature derivative (or sensitivity) of $f(t,T)$
$f(x)$ and $F(x)$	Arbitrary functions
ΔH	Reaction heat per unit mass(in J/g)
HF	Total heat flow or heat flow
$i(t)$	Current
K	System thermal constant (in W/K)
K_{Cp}	Calibration factor
K_{op} and K_{ps}	Thermal conductance as defined in Fig. 1.13
K'	Contact thermal conductance as defined in Fig. 1.8
L	Sample length
m_r	Reference mass (in mg)
m_s or m_{sample}	Sample mass (in mg)
NHF	Non-reversing heat flow
p	Temperature modulation period (in s)
q	Linear or underlying heating (or scanning) rate (in K/min)
dQ/dt	Heat flow
R	Gas constant(in J/mol·K)
RHF	Reversing heat flow
R_i	Thermal resistance of heat conducting path (in K/W), i.e. i=1,2,3…
R_{unit}	Thermal resistance of the small unit
S	Cross section area
S_1 and S_2	Two TMDSC device related factors independent of the sample (Eq. 1.28)
S_r	Boundary conditions for the reference as defined in Fig. 1.6
S_s	Boundary conditions for the sample as defined in Fig. 1.6
t	Time
Δt	Time step used in finite difference calculation
T_0	Initial temperature (in K)
T_b	Heating block temperature (in K)

T_g	Glass transition temperature
T_i	Temperature of a certain sample unit, i=1,2,3…
T_r	Sample temperature (in K)
T_s	Reference temperature (in K)
ΔT	The difference between the sample and reference temperature $\Delta T = T_r - T_s$
ΔT_{cyclic}	The cyclic part of ΔT
$V(t)$	Voltage
$V_{3\omega}(t)$	The third harmonic component of $V(t)$
W	Weight
Y	Heat intensity adjusting factor
α	Concentration of reaction agent
α_c	A complex number as defined in Eq. (1.36)
α_R	temperature coefficient of resistivity
α_T	Thermal diffusivity
α_0	Initial concentration of the decomposition agent
α_1 and α_2	Constants determined by the calorimetry device
β	An intermediate variable, $\beta = (1+i)\sqrt{\frac{\omega}{2\alpha_T}}$
ω	(Modulation) angular frequency
λ	Thermal conductivity of the sample
φ	Phase angle
τ_0 and τ_s	Two intermediate variables, $\tau_s = C_s/K'$, $\tau_0 = C_0/K$, see Eq. (1.27)
ρ	Density

List of Publications

Xu SX, Li Y, Feng YP

Numerical modeling and analysis of temperature modulated differential scanning calorimetry: On the separability of reversing heat flow from non-reversing heat flow

THERMOCHIMICA ACTA **343**: (1-2) 81-88 JAN 14 2000

Xu SX, Li Y, Feng YP

Study of temperature profile and specific heat capacity in temperature modulated DSC with a low sample heat diffusivity

THERMOCHIMICA ACTA **360**: (2) 131-140 SEP 28 2000

Xu SX, Li Y, Feng YP

Temperature modulated differential scanning calorimetry: on system linearity and the effect of kinetic events on the observed sample specific heat

THERMOCHIMICA ACTA **359**: (1) 43-54 AUG 21 2000

Xu SX, Li Y, Feng YP

Some elements in specific heat capacity measurement and numerical simulation of temperature modulated DSC (TMDSC) with R/C network

THERMOCHIMICA ACTA **360**: (2) 157-168 SEP 28 2000

Chapter 1 Literature Review

1.1 Review on dynamic thermal calorimetry

The use of dynamic or temperature modulated calorimetry can be traced back to the early twentieth century [1]. Corbino [1] was the first to develop the temperature modulation method and to describe how to use the electrical resistance of conductive materials to determine the temperature oscillations. By feeding an alternate electrical current (AC) into a sample, the oscillation in resistance can be deduced by recording the third harmonic of the voltage signal over the sample. This in turn allows the determination of the specific heat. This work laid the foundation for the 3-ω method (ω is the angular frequency of the alternate current applied) that has a wide range of applications today [2]. Part of the reason for the increasing use of dynamic calorimetry is the rise of interest in the dynamic heat capacity of materials, which cannot be observed by the conventional differential scanning calorimetry (DSC) [3]. The major developments in dynamic calorimetry since the beginning of the 20th century are listed in Table 1.1 [4—18].

Table 1.1 Historical events in dynamic calorimetry

Year	Event	Researcher(s)	**Ref.**
1910	Theory and application of third harmonic principle	Corbino	[1]
1922	Thermionic current oscillation	Smith, Bigler	[4]
1960	Development of 3-ω method	Rothenthal	[2]
1962	AC method with bridge circuit	Kraftmakher	[5]
1963	Photo detector application	Loewenthal	[6]
1965	Electron bombardment heating	Fillipov& Yuchak	[7]
1966	Resistive heating & low temperature experiment	Sullivan, Seidel	[8]
1967	Modulated light heating	Handler et al.	[9]
1974	High pressure calorimetry	Bonilla,Garland	[10]
1979	Improvement of light modulation method	Hatta et al.	[11,12]
1981	High frequency relaxation study (>10^5Hz)	Kraftmakher	[13]
1986	Specific heat spectrometer	Birge, Dixon	[14-16]
1989	Small sample measurement (<100ug)	Graebner et al.	[17,18]
1993	TMDSC	Reading et al.	[3]

In the early 1960s, significant progresses in dynamic calorimetry were made by Rodenthal [2] and Filoppov [19] in the high-temperature range (>1000^{o}C), where the temperature of metallic or refractory samples was detected by measuring the change in resistance or thermal radiation. In 1962, Kraftmakher developed the AC calorimetry that could measure the heat capacity of metals up to 1200^{o}C [5]. In 1981, Kraftmakher applied very high frequency (10^5 Hz) to AC calorimetry [20]. In 1966, Sullivan and Seidel [8] introduced a new AC calorimetry that used an external light or resistive heating to heat the sample on a supporting platform. This method allowed the determination of the heat capacity of almost any solid or liquid material if certain conditions concerning thermal relaxation times are satisfied [8]. Numerous experiments were carried out in the years that followed. Among them were those that can measure heat capacities near phase transitions with high energy and high temperature resolutions (<10^{-5}K) [11, 21—32], measurements carried out at high temperatures [10, 22, 25, 33—37] or in magnetic fields [17, 21, 30, 37, 38]. There were also experiments conducted with extremely small sample mass (25 μg) [17, 28, 29, 39, 40—42], thermal diffusivity measurement of thin films by periodic heating [11, 43—45], experiments in noisy environment [30] and with slow scanning rates (<0.1 K/h) [29, 32, 46]. The method based on the pioneer work on the modulation frequency dependent heat capacity by Birge, Nagel [14, 15], and Dixon [16] using the 3-ω approach has been further developed [47—51]. The advances in temperature modulated calorimetry in the 1970s and 1980s finally saw the integration of the modulation technique with the widely used conventional DSC instrument, which is now known as “temperature modulated differential scanning calorimetry” (TMDSC) [3]. Some references on dynamic calorimetry are listed in Table 1.2 according to their topics [1—161].

Table 1.2 Some references on dynamic calorimetry classified into different research topics

Subjects	Ref.
Basic theory	
(1)AC calorimetry	[13,20,22, 24,29,32,52-65]
(2)Dynamic specific heat	[8,10,13,14,16,26,33,35,43,44,45, 54,66-85]
Calorimetric heating methods	
(1)Electrical	[5,12,15,34,38,40,86-97]
(2)Light	[9,10,21,36,39,63,76,98-104]
(3)Electron	[19,61,105]
(4)Induction	[106,107]
Detection of temperature oscillations	
(1)Resistance thermometer	[22,23,25,28,30,32,41,108-114]
(2)Thermocouple	[35,42,64,70,93,98,102,115]
(3)Photoelectric detector	[6,56,116]
Different temperature test range	
(1)Low	[40,47,57,60,89,106,117-133]
(2)Normal	[4,9,26,27,29,45,51,85,94,95, 107,134-143]
External conditions for samples	
(1)High magnetic field	[17,21,30,37,102,109,144-146]
(2)High pressure	[10,25,29,33-37,137]
Measured physical parameters	
(1)Thermal conductivity	[43,110,111,147-149]
(2)Thermal diffusion	[63,64,76,77,100-102,109,147,150-152]
(3)Heat capacity and phase	[78,153-155]
(4)Heat capacity and frequency	[130,156]
(5)Heat capacity and time	[89,118-120]
Special implementations	
(1)multi-frequency TMDSC	[157-159]
(2)High precision calorimetry	[18,23-32,39,143,160]
(3)Specific heat spectrometry	[39,71,87,99,153]
(4)Very small samples	[41-43,50,96,102, 161]
(5)High frequency methods	[61,106]
(6)3-ω method	[1,48-51,54,83,91]

Today many different kinds of dynamic calorimetric devices are commercially available, although they may have used different terminologies, different temperature

modulation programs, or slightly different mathematical algorithms. These devices include MDSC (modulated DSC), or TMDSC (temperature modulated DSC), DDSC (dynamic DSC) and SSADSC (steady-state alternating DSC) [162]. The same modulation techniques can be used in other thermal analysis technologies (for example, DTA and TGA) as well [163].

1.2 The 3-ω method: A milestone in dynamic thermal calorimetry

Special attention is given to the 3-ω method here because of its importance in the history of dynamic calorimetry. Many of the later dynamic calorimetric approaches were based on similar principles or are its derivatives. Furthermore, modern improvements to the 3-ω method have greatly extended its capabilities and thus it is applied more frequently in many research fields due to its wide dynamic frequency range. The basic principles of the 3-ω method are discussed below.

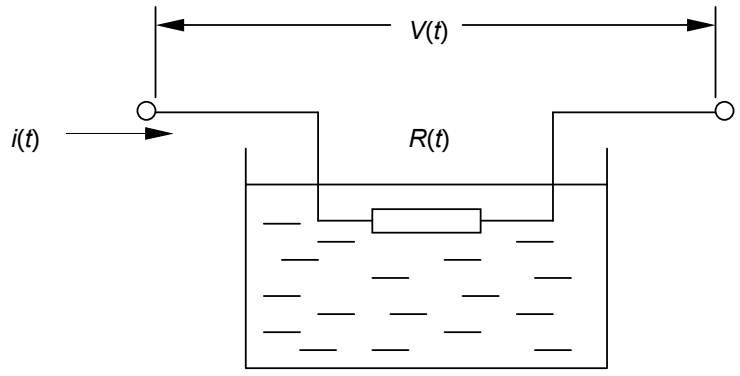

Fig. 1.1 Schematic diagram of the 3-ω method (For solid materials, the heater or thermo-couple is coated on the sample surface; while for liquid samples, it is deposited onto a substrate that is immersed in the liquid).

As shown in Fig. 1.1, a thin film heater with resistance $R(t)$ is coated onto a substrate and submerged in a liquid medium that needs to be tested [54]. This heater is also used as a thermo-couple. When an alternate current $i(t)$ of amplitude I and angular frequency ω passes through the heater, where

$$i(t) = I \cdot \sin(\omega t), \tag{1.1}$$

and t is time, then the heat flow (HF), generated by the alternate current is

$$HF = i^2(t)R = \frac{1}{2}RI^2[1 - \cos(2\omega t)], \tag{1.2}$$

which consists of a DC (direct current) and an AC part. The DC part can produce a constant thermal gradient in the liquid medium, while the AC part with a frequency of 2ω generates a temperature oscillation with an identical frequency. Solving the relevant heat transfer equations associated with the heater-liquid system, one obtains the change in the temperature of the heater [54]

$$\Delta T(t) = \frac{K_1 \cos(2\omega t - 45^o)}{\sqrt{2\omega c_p \lambda}}, \tag{1.3}$$

where K_1 is a system constant that can be obtained by a calibration process, c_p and λ are the specific heat and thermal conductivity of the liquid surrounding the heater, respectively.

Since the resistance of the heater is a linear function of the temperature if the temperature change is small, the temperature change given in Eq. (1.3) in turn can generate an oscillation in the electrical resistance $R(t)$ that satisfies [54]

$$R(t) = R_0 \cdot [1 + \alpha_R \cdot \Delta T(t)], \tag{1.4}$$

where R_0 is a known resistance value at a certain temperature and α_R is the temperature coefficient of resistivity of the heater. Therefore, the voltage drop across the heater is [54]

$$V(t) = R(t)i(t) = IR_0\left\{\sin(\omega t) + \frac{\alpha_R \cdot K_1}{2\sqrt{2\omega c_p \lambda}}\left[\sin(3\omega - 45^0) + \sin(-\omega t + 45^0)\right]\right\} \tag{1.5}$$

On the right hand side of Eq. (1.5), $\sin(\omega t)$ and $\sin(-\omega t+45)$ are the basic oscillation terms, which has the same angular frequency as $i(t)$. Besides, there is a third harmonic term $V_{3\omega}(t)$, which is related to the sample properties α_R, c_p, and λ and given by

$$V_{3\omega}(t) = IR_0 \frac{\alpha_R \cdot K_1}{2\sqrt{2\omega c_p \lambda}} \sin(3\omega t - 45^0) = A_{3\omega} \sin(3\omega t - 45^0), \tag{1.6}$$

where $A_{3\omega}$ is the amplitude of the third harmonic.

For most materials that can be used as the heater as well as thermo-couple, the temperature coefficient of their resistivity α_R generally is small (α_R<<1), hence $\alpha_R \cdot K_1 / 2\sqrt{2\omega c_p \lambda}$ <<1 [54]. Accordingly, the oscillation term that is related to the thermal properties of the sample is easily dominated by the much larger term $IR_o\sin(\omega t)$. However, if the third harmonic component $V_{3\omega}(t)$ in Eq. (1.5) can be obtained from $V(t)$, then one has [54]

$$c_p \lambda = \frac{1}{2\omega}\left(\frac{IR_0 \alpha_R \cdot K_1}{2A_{3\omega}}\right)^2. \tag{1.7}$$

When the 3-ω method was first introduced, the measured result was only a product of c_p and λ, as can be seen in Eq. (1.7). However, it had been observed that λ changed very little as a function of temperature, thus the change in the product of c_p and λ was mostly determined by the change in c_p. Later, by utilizing the phase angle information and a slightly different procedure, c_p and λ could be effectively separated [164].

In 1986, Birge and Nagel [153, 164] introduced this method as a new specific-heat spectroscopy and used it to study glass transitions. The heater or thermo-couple was a metallic thin film deposited on a special substrate with a low $c_p \lambda$ product. The third harmonic signal was obtained with a delicate Wheatstone bridge circuit [54]. This apparatus is schematically shown in Fig. 1.2. Here R_1 is a resistor with high-accuracy but low temperature coefficient of resistivity. The sample and the heater or thermal couple fixture is connected at the lower left side of the bridge (see Fig. 1.2). The values of R_2 and R_v are a couple of orders of magnitude larger than those on the left arm of the bridge. The three-probe method is used to remove the lead effects in balancing the bridge. An electrical sine wave is injected into the circuit, and the third harmonic is monitored at the output side of Fig. 1.2 by a signal scanner. A lock-in amplifier is used to provide the required stability and synchronization.

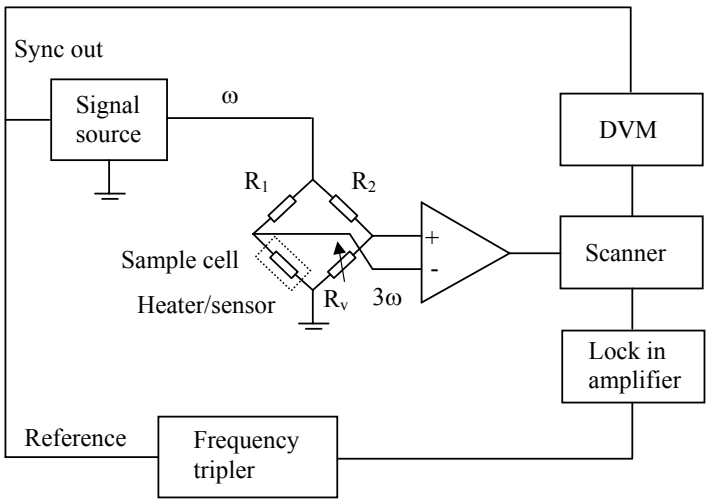

Fig. 1.2 Schematic diagram of the 3-ω dynamic calorimetry with a bridge circuit. Adapted from [54].

Fig. 1.3 shows a typical dynamic specific heat curve which was obtained from a super-cooled liquid polymer in the glass transition process [54]. Due to the relatively large relaxation time of the glass transition, which is comparable to the

modulation period, it can be seen that the specific heat of the sample is not constant at each temperature point. Instead, the specific heat depends on the modulation frequency and is larger at a lower frequency (1/256 Hz) than that at a higher one (1/8 Hz) during the glass transition, while it is frequency independent outside the glass transition. The difference in specific heat before and after the glass transition is quite significant.

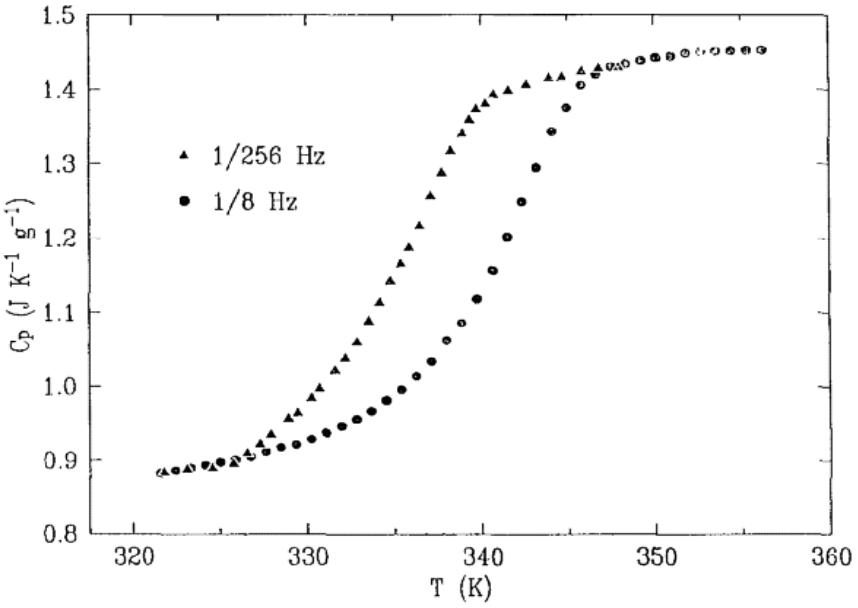

Fig. 1.3 Dynamic heat capacity of a super-cooled liquid at different modulation frequencies. Adapted from [54].

1.3 Comparison between the conventional DSC and TMDSC

1.3.1 Principles and advantages of TMDSC

The AC calorimetry invented by Kraftmakher [5] in 1962 was based on the temperature modulation through a direct heat path to the sample that is confined in a semi-adiabatic heat shield. The thermal relaxation time of the calorimetric cell is in

the order of a few minutes or longer. The basic modulation idea was similar to its modern TMDSC derivatives but did not incorporate a linear temperature ramp [7].

In 1993, Reading [3] proposed using a sinusoidal oscillation temperature that is super-imposed on a linear temperature scan in the conventional DSC device. This idea became the basis of what is known today as the temperature modulated DSC. Fig. 1.4 shows the structural diagram of a heat flux type TMDSC proposed by Reading [3]. TMDSC shares many similarities with a conventional DSC in structure, thus a TMDSC device can switch from TMDSC mode to DSC mode or vice versa conveniently.

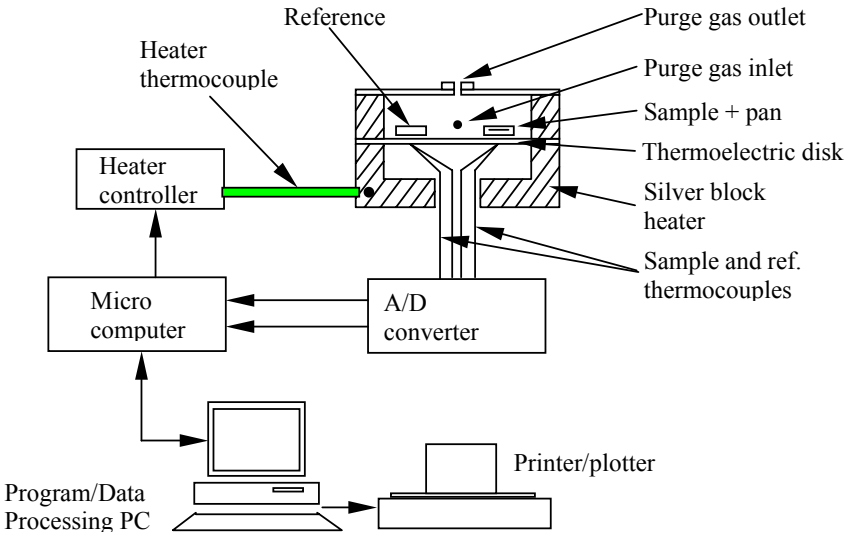

Fig. 1.4 A heat flux type TMDSC device. Adapted from [3].

The main difference between TMDSC and the conventional DSC is in the control of the sample temperature and data treatment method. In addition to the underlying heating rate, TMDSC has incorporated a temperature modulation technique so that the sample temperature follows a periodic wave pattern (such as a sinusoidal wave, see Fig. 1.5). Fourier transform is used in the calculation of specific

heat, heat flows and so on. The temperature modulation may also be in other forms such as a square wave, saw-tooth wave, triangular wave and pulse wave [3]. A fast heating rate (e.g., 200 K/min) can be easily reached with a high-power heater, but the cooling speed is limited by the thermal inertia of the silver block (see Fig. 1.4) itself, especially when the heater reaches the ambient temperature. To overcome this problem, a rapid cooling system can be used to dissipate heat from the TMDSC cell directly if necessary, either through compressed air or liquid nitrogen. Thus a wider dynamic programmable temperature range can be realized. Because of these design features, TMDSC has the following advantages over conventional DSC.

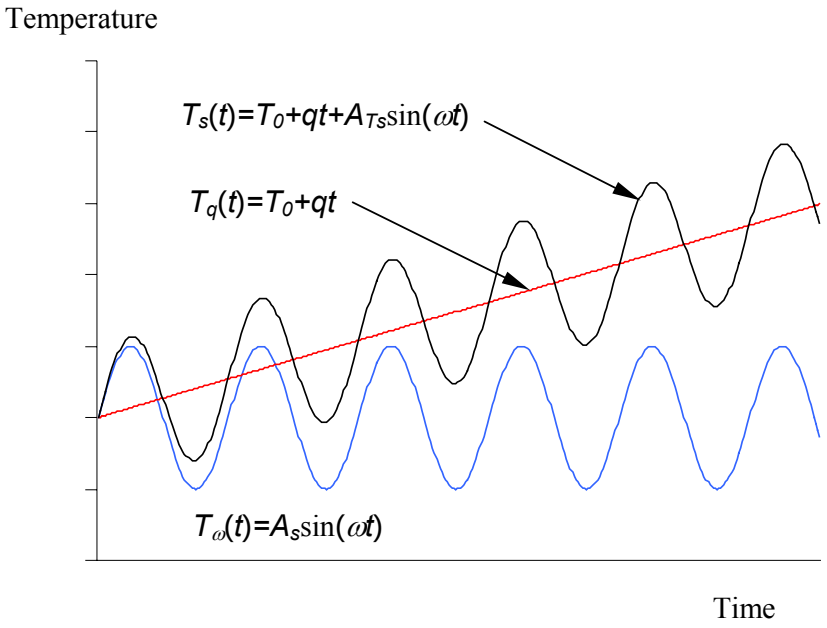

Fig. 1.5 Sinusoidal modulation wave superimposed on a linear heating rate, q. $T_s(t)$ is the sample temperature, $T_q(t)$ is the underlying temperature, $T_\omega(t)$ is the modulated temperature, T_0 is the initial temperature, and A_{Ts} is the modulation amplitude.

1.3.1.1 Better temperature resolution and ability to measure specific heat in a single run

Specific heats of various solid or liquid materials were normally determined by the conventional DSC method before TMDSC became available. In the conventional DSC, the relationship among the heat flow, HF, and the specific heat of the sample, c_p, satisfies the following equation:

$$HF = m_s c_p \cdot \left(\frac{dT_s}{dt} \right) = m_s c_p q = K(T_r - T_s), \tag{1.8}$$

where m_s is the sample mass, K is the system thermal constant, T_s is the sample temperature, T_r is the reference temperature, and q is the linear heating rate. To compensate for the device bias, two different runs are normally carried out, either with two samples of different masses, m_1 and m_2, or a single sample with two different heating rates. For the two-sample method, we have

$$c_p = \frac{HF_1 - HF_2}{q(m_1 - m_2)}, \tag{1.9}$$

while for the single-sample method conducted with two different heating rates, we have

$$c_p = \frac{HF_1 - HF_2}{m(q_1 - q_2)}. \tag{1.10}$$

To obtain a better signal sensitivity, especially for small samples, it is necessary to increase the scanning rate so that the heat flow, HF, can be easily detected and quantified. However, this will sacrifice the temperature resolution.

However, if a modulated temperature is added to the underlying heating rate, the above problem can be largely solved. With proper modulation conditions, both high-temperature resolution and signal sensitivity can be obtained [3, 166]. This is explained below.

If the heater is so modulated that a sinusoidal wave is superimposed on a relatively small linear underlying heating rate q, then the sample temperature T_s is $T_s=T_0+qt+A_{Ts}\sin(\omega t)$ (see Fig. 1.5), where A_{Ts} is the amplitude of sample temperature. We obtain the heat flow

$$HF = C_s\left(\frac{dT_s}{dt}\right) = m_s c_p \cdot \left[q + A_{Ts}\omega\cos(\omega t)\right], \tag{1.11}$$

where C_s or $c_p m_s$ is the heat capacity of the sample.

In this case, both the heat flow and the sample temperature are composed of two parts: one related to the underlying linear scanning; the other to the temperature modulation. The modulated part of the sample temperature is

$$T_s(t)_{cyclic} = A_{Ts}\sin(\omega t), \tag{1.12}$$

and the modulated part of the heat flow is

$$HF_{cyclic} = m_s c_p A_{Ts}\omega\cos(\omega t) = A_{HF}\cos(\omega t). \tag{1.13}$$

Comparing Eq. (1.12) with Eq. (1.13), we notice that if the amplitude of the sample temperature, A_{Ts}, and the amplitude of modulated heat flow, A_{HF}, are obtained simultaneously, we can find the specific heat of the sample

$$c_p = \frac{A_{HF}}{m_s A_{Ts}\omega}. \tag{1.14}$$

The underlying heating rate q does not appear in the above equation, which means that the calculated specific heat is not affected by the underlying heating rate. Thus, even with a small or zero underlying heating rate, the specific heat can still be determined. Hence, a better temperature resolution can be achieved compared to conventional DSC. Furthermore, from Eq. (1.13), it can be seen that by increasing the modulation frequency, ω, a larger heat flow amplitude, A_{HF}, can be obtained, which

means a better signal sensitivity (or better signal to noise ratio) without changing the underlying heating rate.

According to the above analysis, the specific heat of the sample can be determined over a temperature range with a single run even under a low heating rate. This is also an important advantage of TMDSC over conventional DSC in cases where the thermal history of the sample has a significant influence on its properties.

Given that the TMDSC instrument is properly calibrated, we can obtain the specific heat $c_p(T)$ over the temperature range where an experiment is carried out

$$c_p(T) = \frac{A_{HF}(T)}{m_s A_{Ts}(T)\omega}. \tag{1.15}$$

Lacey et al. [165] described a more general case for a three-dimensional differential calorimetry. Their model is shown in Fig. 1.6. Applying the boundary conditions of heat transfer, they obtained the following equations for the heat capacities of the sample and reference (see Fig. 1.6)

$$C_r\left(\frac{dT_r}{dt}\right) = -K\oint_{S_r}\left(\frac{\partial T}{\partial n}\right)dS, \tag{1.16}$$

$$C_s\left(\frac{dT_s}{dt}\right) = -K\oint_{Ss}\left(\frac{\partial T}{\partial n}\right)dS, \tag{1.17}$$

respectively, where $\partial T/\partial n$ is the temperature gradient in the calorimetry, C_s and C_r are the heat capacities of the sample and reference respectively, K is a system thermal constant, S_r and S_s are the boundary conditions for the reference and sample, respectively.

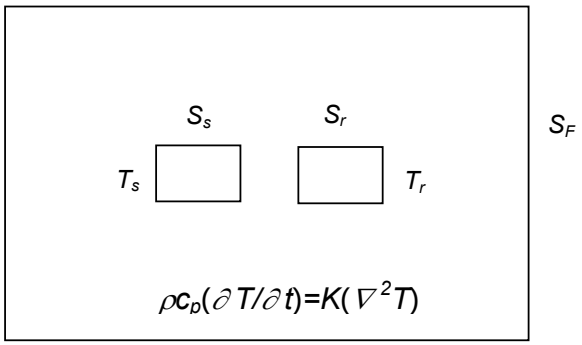

Fig. 1.6 A three-dimensional claorimetry model. S_s, S_r, and S_F are the outside surfaces of the sample, reference, and furnace respectively. The temperature in the enclosed region satisfies $\rho c_p(\partial T/\partial t)=K(\nabla^2 T)$. Adapted from [165].

When the furnace temperature is modulated to follow $Ae^{i\omega t}$ (the complex form of temperature is used here), the cyclic part of the temperature difference between the sample and reference can be derived [165]

$$(T_r - T_s)_{cyclic} = A\omega C_s \,\mathrm{Re}\left[\frac{e^{i\omega t}}{(\alpha_1+\alpha_2)k + i\omega C_r}\right], \tag{1.18}$$

where α_1 and α_2 are two constants determined by the structure of the calorimetry device that can either be calculated via numerical methods or more easily obtained from a calibration run. Thus, the heat capacity of the sample can be determined by [165]

$$C_s = \left|(T_r - T_s)_{cyclic}\right| \cdot \frac{\left|(\alpha_1+\alpha_2)k + i\omega C_r\right|}{A\omega}. \tag{1.19}$$

The phase angle φ between the sample and reference temperature is

$$\varphi = \arg\left[(\alpha_1+\alpha_2)k + i\omega C_r\right]. \tag{1.20}$$

1.3.1.2 Ability to separate the reversing and non-reversing heat flows

In many cases, when heated from room temperature to several hundred degrees or even higher, samples may experience some thermal reactions that can

change their physical and the chemical properties. These reactions include glass transition, crystallization, re-crystallization, chemical reaction, curing, or evaporation and so on. These reactions may occur at the same time or in the same temperature range as that of a reversible heat flow caused by the reversible change in the heat capacity of the sample. Thus, the heat flow signals from these reactions and from the reversible changes of the sample overlap and can hardly be distinguished from each other in a conventional DSC device.

Considering the possible heat released by these reactions, we have the thermal equation in the conventional DSC, [74, 75, 3, 166]

$$HF = C_s q + f(t,T). \tag{1.21}$$

In Eq. (1.21), HF is the total heat flow obtained by the calorimeter, $f(t,T)$ is the kinetic or non-reversing heat flow (NHF) that is related to the kinetic heat generated in the reactions. $C_s q$ is the reversing heat flow (RHF) that is related to the heat capacity. q is the underlying heating or cooling rate.

In TMDSC, the reversing heat flow is a thermodynamic event as it is due to vibrational and translational motions of molecules or lattices. These motions are very fast and can instantaneously follow any modulation of the sample temperature. With a modulated sample temperature, if the kinetic or non-reversing heat flow cannot follow the modulation and does not contribute to the modulated part of the heat flow, the HF in Eq. (1.21) thus is

$$HF = [C_s q + f(t,T)] + C_s A_{Ts}\omega\cos(\omega t). \tag{1.22}$$

By extracting the modulated parts of the total heat flow and sample temperature, and inserting them into Eq. (1.15), we can find the heat capacity of the sample, $C_s(T)$. Multiplying the heat capacity by the underlying heating rate, we can obtain the reversing heat flow

$$RHF = \frac{A_{HF}(t)}{A_{Ts}(t)\omega} q = C_s q \,. \tag{1.23}$$

Hence

$$C_s = \frac{A_{HF}(t)}{A_{Ts}(t)\omega} \,. \tag{1.24}$$

If the modulated part in Eq. (1.22) is averaged over a sliding Fourier transform window, then the total heat flow in TMDSC can be obtained [3]. It is therefore possible to separate the non-reversing heat flow, NHF or $f(t,T)$, from the reversing heat flow, RHF, in a single run, i.e.,

$$NHF = HF - RHF \,. \tag{1.25}$$

The separation of reversing and non-reversing heat flow is also the most important advantage of TMDSC over conventional DSC. It should be noted that the "non-reversing" processes might be reversible with large temperature changes. It is just that at the magnitude of the temperature modulations, they are not reversing. Block diagrams of the NHF and RHF separation or deconvolution process are given in Figs. 1.7 and 1.8, respectively [166]. In Fig. 1.7, the heat capacity is the ratio between the modulated heat flow and the modulated temperature. The total heat flow is an average of the modulated heat flow over a sliding transform window [3]. The reversing heat flow is the product of the heat capacity and the heating rate, and the non-reversing heat flow is the difference between the total heat flow and the reversing heat flow [166]. The difference between Figs. 1.7 and 1.8 is that Fig. 1.8 shows a complete deconvolution algorithm that takes into account the phase angle. This is the additional phase angle between the modulated heat flow and the time derivative of the sample temperature introduced by the non-reversing heat flow. If this additional phase angle is negligible, then these two algorithms produce the same results [166].

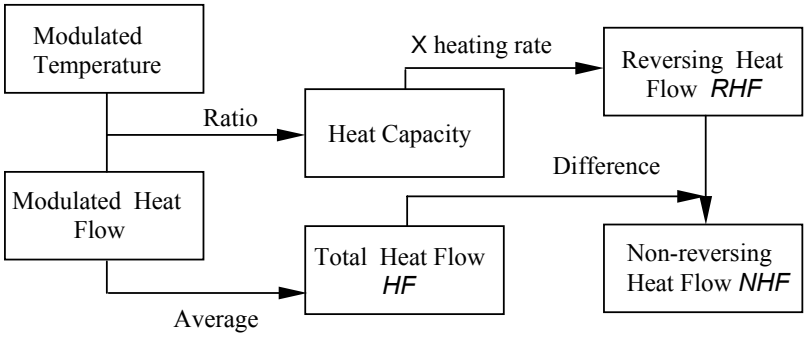

Fig. 1.7 An algorithm used in the deconvolution of *NHF* and *RHF* of a typical heat flux TMDSC, no phase correction applied. Adapted from [166].

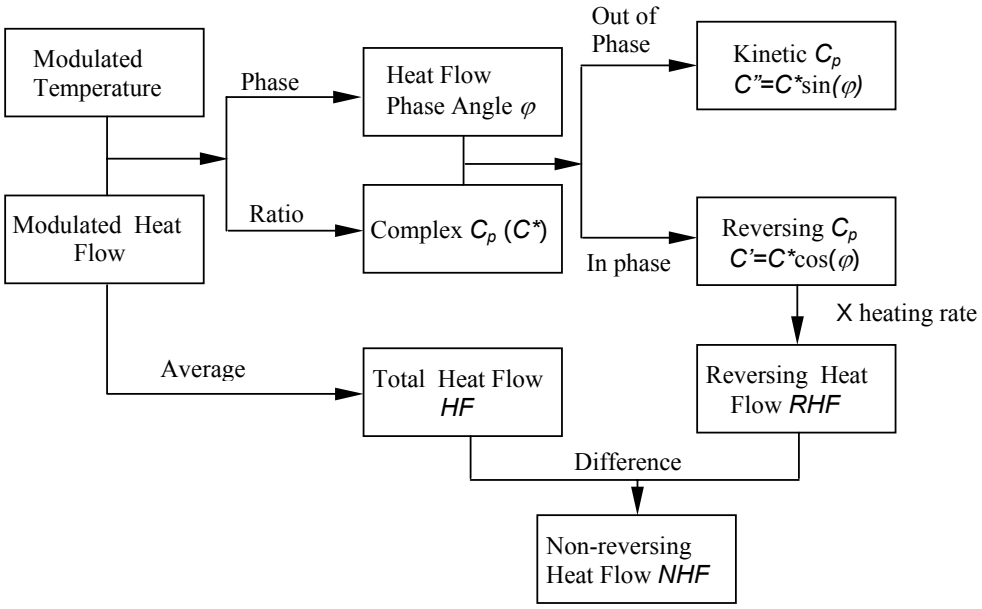

Fig. 1.8 An algorithm used in the deconvolution of *NHF* and *RHF* of a typical heat flux TMDSC with phase correction. Adapted from [166].

An example of the separation of *NHF* and *RHF* is given in Fig. 1.9 [3]. The sample studied is polyethylene terephthalate (PET). The total heat flow is separated into a reversing and non-reversing heat flow. The glass transition, which is hidden in the total heat flow, can be clearly seen in the reversing heat flow at about 350 K.

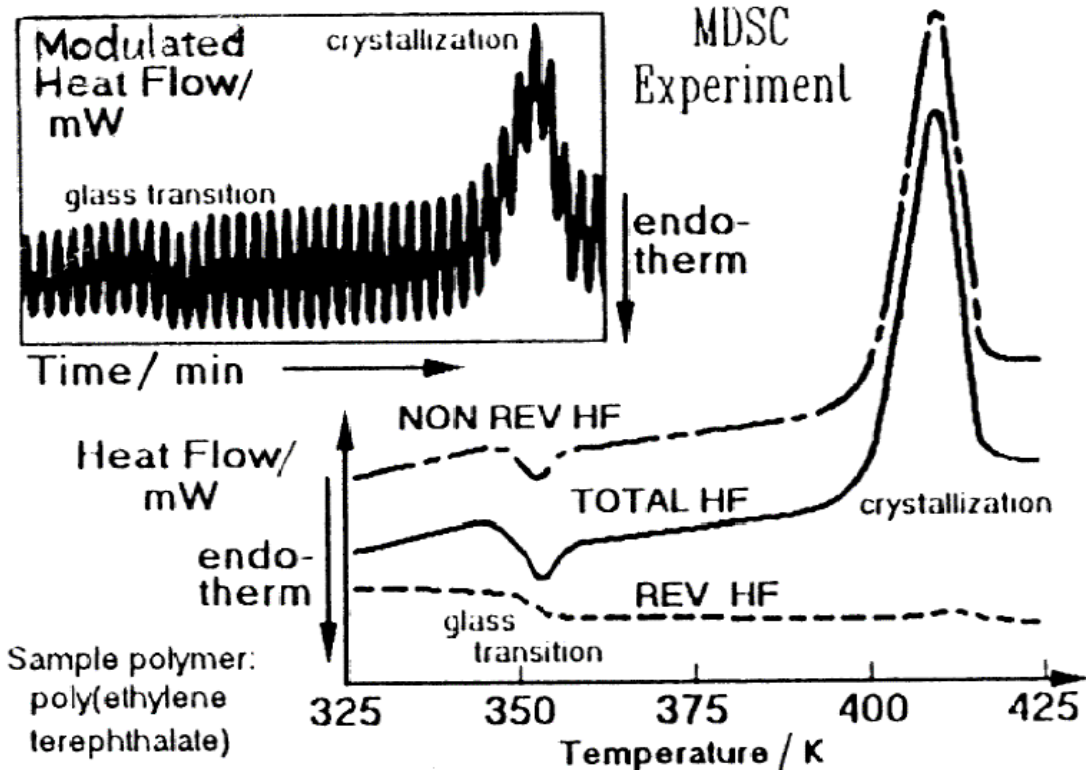

Fig. 1.9 An example of deconvolution of reversing heat flow and non-reversing heat flow. The polymer sample has a glass transition at about 350K and a crystallization peak at 410K. In the reversing heat flow curve, the glass transition can be clearly seen. Adapted from [3].

1.3.2 Current status and limitations of TMDSC

Although the biggest advantage of TMDSC is the separation of reversing heat flow from non-reversing heat flow, there are some issues that can affect the interpretation of results obtained from TMDSC measurement. These are listed below.

a. TMDSC requires system linearity, which is essential for the Fourier transform that is used in the calculation of *NHF* and *RHF* [3, 162].

b. TMDSC has limited accuracy in the measurement of specific heat. Error in measured specific heat can be 1 to 10%, depending on the exact experimental conditions. This is because accurate calibration of TMDSC device for the measurement of specific heat is still an issue [167—169].

c. Experimental results are sensitive to thermal properties of materials. Any type of relaxation phenomenon, whether intrinsic to the sample or it is characteristic of the calorimetric instrument itself, influences the measured specific heat. Stringent boundary conditions are therefore needed [162, 170, 171].

d. There are still applicability issues related to certain kinetic reactions. For example, it is very difficult or even impossible to determine the latent heat of a first-order phase transition [172, 173] due to lack of linearity in the thermal responses.

The above factors in TMDSC set more stringent requirements than conventional DSC with regard to the interpretation of data obtained. The current status and limitations of TMDSC are discussed in more detail below.

1.3.2.1 Accurate calibration for heat capacity measurement

For a TMDSC model described by a single system thermal constant K, elements such as a biased heat transfer path, imperfect thermal contact, and poor thermal conductivity of the sample are ignored. In this case, it can be derived that a strict calibration of TMDSC is possible [75] with a standard reference, for example, a sapphire reference sample. However, a slightly more complicated model shows a different picture. Ozawa et al. [167] used an R-C network model to study TMDSC and found that the measured specific heat was a complicated function of many variables, including the heat capacity of the sample to be determined. They proved that strict calibration was impossible for TMDSC, and that TMDSC was not more accurate than the conventional DSC.

To alleviate the problem in the measurement accuracy, Hatta and Katayama [168] proposed a different calibration method that used the phase angle between the modulated heat flow and the time derivative of the sample temperature. The TMDSC model they used is illustrated in Fig. 1.10. In this model, no reference is used so that the contact thermal conductance, K', only exists on the sample side as shown in Fig. 1.10. T_{s0} is the temperature of the thermal couple on the sample side, and T_{r0} is the temperature on the reference side. It can be shown [168] that

$$\frac{1}{K_{Cp}} = \frac{KA_{\Delta T}}{A_{Ts}\omega C_s} = \frac{1}{\sqrt{\left(1+\omega^2\tau_s{}^2\right)\left(1+\omega^2\tau_0{}^2\right)}}, \tag{1.26}$$

where K_{Cp} is the calibration factor, $A_{\Delta T}$ is the amplitude of the temperature difference between T_{s0} and T_{r0}, C_s is the heat capacity of the sample, and A_{Ts} is the amplitude of the sample temperature. The phase angle between the modulated heat flow and the time derivative of sample temperature satisfies

$$\sin(\varphi) = \frac{1+\omega^2\tau_s\tau_0}{\sqrt{\left(1+\omega^2\tau_s{}^2\right)\left(1+\omega^2\tau_0{}^2\right)}}, \tag{1.27}$$

where $\tau_s = C_s/K'$, $\tau_0 = C_0/K$, C_0 is the heat capacity of the support plate.

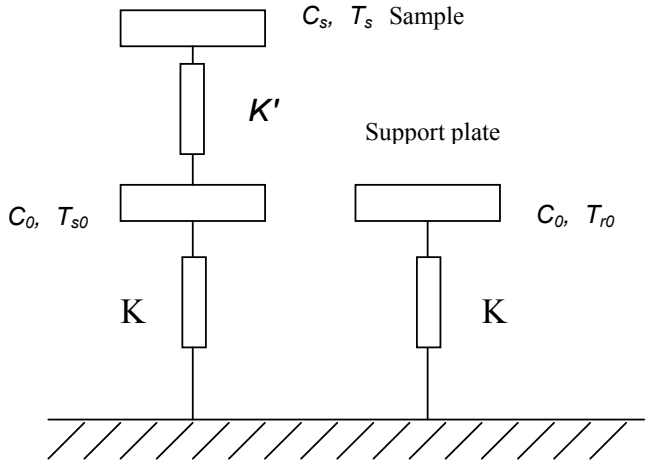

Fig. 1.10 A model that takes into account the contact resistance. Adapted from [168].

In Eqs. (1.26) and (1.27), both $\sin(\varphi)$ and $KA_{\Delta T}/A_{Ts}\omega$ can be directly measured in an actual calorimetric device. The only unknown variables are C_s and τ_s. The rest of the variables are completely determined by the model for a given temperature modulation frequency, ω. Using a number of standard samples with known heat capacities, for instance, $C_{s1}, C_{s2}...C_{sn}$, in the calibrations and plot $\sin(\varphi)$ against K_{Cp}, one can obtain a calibration curve as shown in Fig. 1.11. Each temperature modulation frequency requires such a calibration curve.

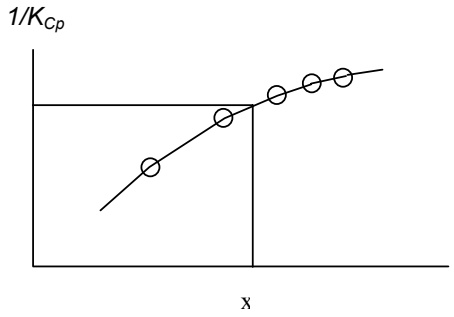

Fig. 1.11 Calibration curve that uses phase angle information

Now, for a sample with unknown C_s and K', if a TMDSC run at a given modulation frequency is carried out, because there are two governing equations, Eqs. (1.26) and (1.27), the data point $(K_{Cp}, \sin(\varphi))$ must fall onto the calibration curve. If $\sin(\varphi)$ which contains the phase angle information is known, one can obtain the corresponding calibration factor K_{Cp}, hence the heat capacity of the sample can be determined by $C_s = K_{Cp}KA_{\Delta T}/(A_{Ts}\omega)$. The accuracy of this method depends on the accuracy of the calibration curves. Therefore, a number of standard reference samples (5 to 8, for example) are required for the calibration and data interpolation purposes at each temperature and temperature modulation frequency of interest. Capitalizing on the same idea that uses the phase angle information in the calibration, Ozawa and

Kanari [169] modified their previous model (see Fig. 1.12 for a diagram of the revised model) and derived the following heat capacity calibration equations:

$$\frac{A_{\Delta T}}{A_{Tps}\omega C_s} = \frac{1}{\sqrt{\left(1+\omega^2\tau_s{}^2\right)\left(S_1{}^2+S_2{}^2\right)}}, \tag{1.28}$$

$$\sin(\varphi) = \frac{S_2 - \omega\ \tau_s S_1}{\sqrt{\left(1+\omega^2\tau_s{}^2\right)\left(S_1{}^2+S_2{}^2\right)}}, \tag{1.29}$$

$$\tau_s = C_s / K', \tag{1.30}$$

where S_1 and S_2 are two TMDSC device-related constants independent of the sample properties, A_{Tps} is the amplitude of T_{ps}, and K' is the contact thermal conductance as indicated in Fig. 1.12.

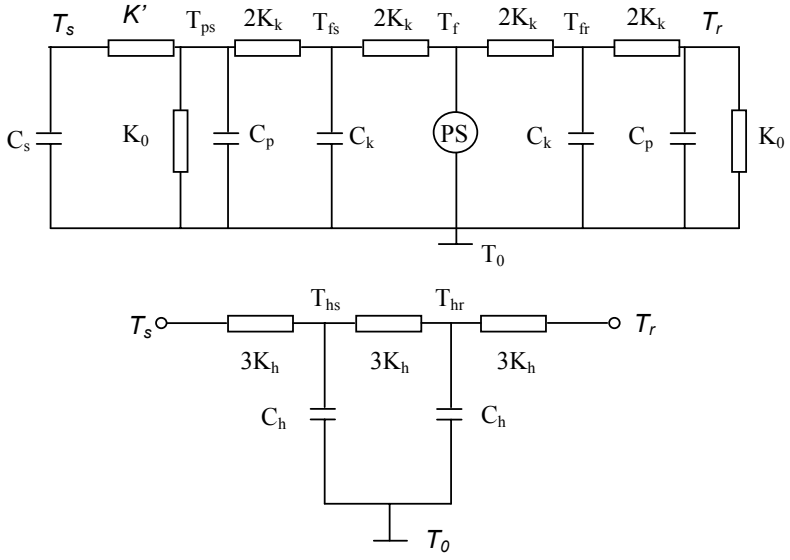

Fig. 1.12 Diagram of the modified TMDSC model by Ozawa. The upper half shows the main circuit, the lower half shows the heat exchange path between T_r and T_s. Adapted from [169].

Comparing Eqs. (1.28) & (1.29) with Eqs. (1.26) & (1.27), it can be found that they are quite similar in structure. In both cases, the two unknown variables, the calibration factor and phase angle, are controlled by two equations, thus the same

calibration procedure used by Hatta [168] can also be used in the model of Ozawa and Kanari.

1.3.2.2 Influence of low sample thermal conductivity

For most metallic materials, the thermal conductivity is not a major concern in TMDSC experiments, and the sample can be treated as a single point if the temperature gradient in the sample is negligible. However, this may not always be the case for poor heat conductors such as polymer, wood, and many other organic or inorganic materials. Their thermal conductivities typically are two to three orders of magnitude lower than those of metallic materials. In these cases, a small sample mass as low as 20 mg can produce considerable temperature variation and phase lag in the sample, and thus significantly affect the measured specific heat [162].

Hatta [170] studied the conditions for high-accuracy heat capacity measurement when the thermal conductivity of the sample was taken into account. He analyzed the case of a cylindrical sample (Fig. 1.13) with a modulated heat input from the bottom surface to find the maximum limit on sample mass in TMDSC.

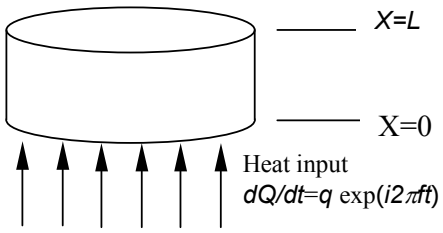

Fig. 1.13 A cylindrical sample of length L with temperature modulation from the bottom, adapted from [170].

The bottom surface temperature of the sample satisfies the following equation [170]

$$T(0) \le \left[1 + \frac{14}{45}(\lambda L)^2\right] \cdot \exp\left[\frac{2}{3}(\lambda L)^2 i\right] \cdot \left(\frac{1}{2fc_p L\rho\pi}\right), \qquad (1.31)$$

where λ is the thermal conductivity of the sample, ρ is the density, L is the sample length, and $f=\omega/2\pi$, with ω being the temperature modulation frequency.

According to the analysis of Hatta [170], in order to reach an accuracy better than 1% for c_p, it is required that $14(\lambda L)^2/45<0.01$ or $\lambda L<0.42$. For a sapphire sample with a bottom area of 0.2 cm^2, the sample mass should not exceed 800 mg. However, according to Boller's experimental results [75], the observed c_p of sapphire begins to drop drastically at 100 mg. Hatta attributed this to the limited thermal contact between the sample and the sealing pan or support plate.

Schenker and Stager [162] studied the effect of thermal conductivity in a variety of temperature modulated calorimetric devices, such as dynamic DSC (DDSC), steady-state alternating DSC (SSADSC), and modulated DSC (MDSC). The main differences among these three dynamic calorimetric devices are in the modulation methods and the deconvolution algorithms used: DDSC and SSADSC use saw tooth temperature modulation while MDSC uses a sinusoidal one. Both DDSC and MDSC use Fourier transform but DDSC uses only the real part of the complex amplitude. In DDSC, a calibration run is carried out to obtain the phase angle of the device, then this phase angle is taken into account in the calculation by rotating the amplitude vectors [162] so that the imaginary part of the modulated heat flow vanishes. SSADSC does not use Fourier transform to find c_p; instead, it simply compares the different temperature excursions [162]. The algorithms used in the three methods are given below,

$$c_p(MDSC) = \left(|A_{sample}|/m_{sample}\right)\left(mc_{p\,calibration}/|A_{calibration}|\right), \quad (1.32)$$

$$c_p(DDSC) = \left[\mathrm{Re}(A_{sample})/m_{sample}\right]\cdot\left[mc_{p\,calibration}/\mathrm{Re}(A_{calibration})\right], \quad (1.33)$$

$$c_p(SSADSC) = \frac{(T_r - T_s)_{max} - (T_r - T_s)_{min}}{m_{sample}}\Big|_{sample} \frac{mc_{p\,calibration}}{(T_r - T_s)_{max} - (T_r - T_s)_{min}}\Big|_{calibration}, \quad (1.34)$$

where m_{sample} and m are the masses of the sample and calibration reference, respectively, and $A_{calibration}$ and A_{sample} are the temperature amplitude of the sample and calibration reference respectively. The simulation model is shown in Fig. 1.14.

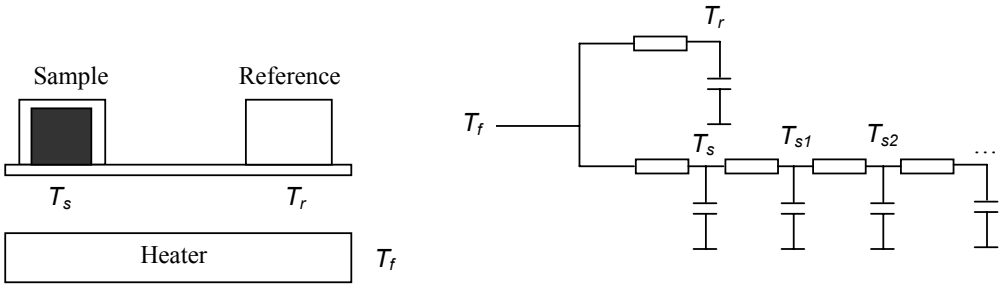

Fig. 1.14 Diagram of a network model for a heat flux TMDSC, adapted from [162].

Despite these differences in algorithm, it was found that even with relatively long modulation periods (120 s, for example), the observed c_p is still much lower than the value reported in literature for polymeric materials [162]. Observed specific heats of the three methods (MDSC, DDSC and SSADSC) showed similar trends although they had varied accuracies. In these cases, measures that can help improve the contact between the sample and the instrument, such as using He as the purge gas, cannot help obtain a more uniform temperature distribution in the sample. Using crimped pans allows slightly larger samples or shorter modulation periods to be used due to better heat transfer conditions. Other factors such as background noise, non-linear

response of instrument and disturbance in the controller, which may be encountered in the actual experiment, can make the situation even more complicated [162].

Merzlyakov and Schick [171] analyzed the combined effect of thermal contact and thermal conductivity in a power compensation type TMDSC using the model shown in Fig. 1.15.

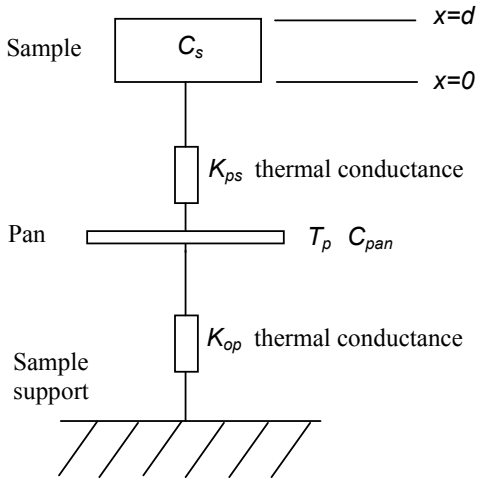

Fig. 1.15 Diagram of a more complicated model for power compensation TMDSC, adapted from [171].

If a thermal couple is placed at different places to measure the sample temperature, different values of measured heat capacity can be obtained. However, there is a general trend: the measured heat capacity drops as the distance between the thermal couple and the sample increases [171], which obeys

$$C_s > |C_\alpha| > |C_\beta| > |C_\delta|, \tag{1.35}$$

where C_s is the heat capacity of the sample, C_α is the heat capacity measured at the bottom of the sample, C_β is the heat capacity obtained at the sample pan and C_δ is the heat capacity measured at the sample support. Moduli are used here since heat capacities C_α, C_β and C_δ are in complex form, which are given below

$$C_\alpha = \frac{-\lambda \cdot S \cdot \alpha_c \cdot \tanh(\alpha_c \cdot d)}{i\omega}, \tag{1.36}$$

where λ is the thermal conductivity, d is the sample thickness. S is the cross-section area of the sample. The complex variable α_c is defined as $(\omega/|\alpha_T|)^{1/2}\exp[(i/2)\arg(-i\omega/\alpha_T)]$, where α_T is the thermal diffusivity,

$$C_\beta = \frac{C_\alpha}{1-(i\omega/K_{ps})C_\alpha}, \tag{1.37}$$

and

$$C_\delta = \frac{C_\beta}{\left[1-(i\omega/K_{ps})(C_{pan}+C_\beta)\right]\cdot\left[1-(i\omega/K_{op})C_{pan}\right]}, \tag{1.38}$$

where K_{op} is the thermal conductance between the pan and sample support, C_{pan} is the heat capacity of the pan, K_{ps} is the thermal conductance between the pan and sample, as shown in Fig. 1.15.

In reality, the sample temperature is obtained at the support plate. Thus only C_δ can be obtained directly by the TMDSC experiments. The heat capacity of the sample, C_p, has to be derived from C_δ. For this purpose, Merzlyakov and Schick [171] proposed a method that involves multi-runs and multi-samples plus a thin layer of grease to improve thermal contact wherever possible. At least two separate runs are required to estimate each of the four parameters: K_{op}, K_{ps}, heat flow asymmetry of the cell, and the thermal conductivity of the sample, λ. For example, after C_α is determined for two samples with different thicknesses, Eq. (1.36) is used to calculate the thermal conductivity of the sample after finding out the complex number α_c in

$$\frac{C_{\alpha 1}}{C_{\alpha 2}} = \frac{\tanh(\alpha_c \cdot d_1)}{\tanh(\alpha_c \cdot d_2)}. \tag{1.39}$$

As a result, at least eight runs are required before the heat capacity of the sample C_s can be finally calculated. When influences from other factors are taken into

account, such as variations from sample to sample in geometry, surface condition and possible sample softening, contraction or expansion during reactions or melting, the accurate calibration of TMDSC is extremely difficult, if not impossible [171].

1.3.2.3 The applicability of TMDSC

Taking kinetic events or reactions into account, Scherrenberg et al. [172, 173] analyzed the applicability of TMDSC to more realistic situations and identified several important aspects that affect its ability in separating heat flows.

1. The variation of material composition on the time scale of temperature modulation.
2. Linearity of the actual process. For a linear process, input ax_1+bx_2 to function $y(x)$ yields an output of ay_1+by_2, which means $y(ax_1+bx_2)= ay_1+by_2$, where $y_1 = y(x_1)$ and $y_2 = y(x_2)$. a and b are two constants.
3. The time scale of a process and its susceptibility to the temperature modulation.
4. TMDSC device performance. Such as linearity and steady state of TMDSC.

According to the analysis of Scherrenberg et al. [172, 173], the general situation of thermal responses in TMDSC was classified into three distinct categories based on the susceptibility of the kinetic or non-reversing events to the temperature modulation.

Category I. Region with baseline heat flow

Taking the glass transition as an example where no entropy relaxation is involved, when the sample temperature satisfies $T<<T_g$, where T_g is the glass transition temperature (see Fig. 1.16(a)), the atomic motion has a relaxation time in the order of 10^{-13} s. This is called a non-cooperative motion. As a result this motion can immediately follow the temperature modulation. In comparison, the relaxation

time of the glass transition or cooperative-motion is far greater than the available temperature modulation period, which is typically between 10 and 100 s. Hence, the glass transition does not contribute to the modulated heat flow.

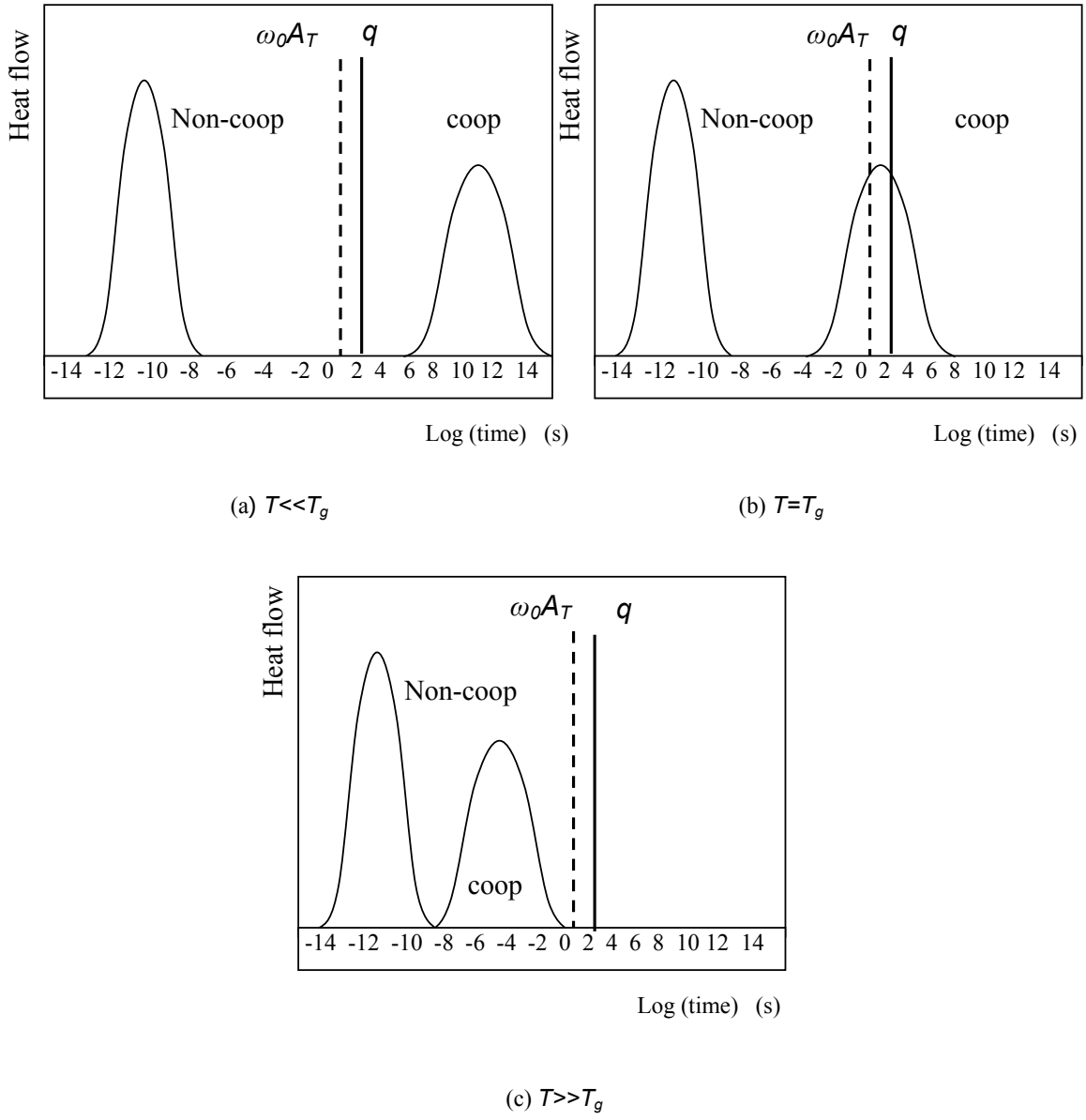

Fig. 1.16 Thermal responses in TMDSC for Category I, which is a baseline heat flow region with no extra heat. The "Non-coop" refers to the heat flow due to atomic motion that can immediately follow the temperature modulation. "coop" refers to the heat flow from the kinetic event. Adapted from [172].

If $T>>T_g$, as shown in Fig. 1.16(c), relaxation times of both the atomic and glass transition are much shorter than the temperature modulation period. Thus, all molecular changes can occur instantaneously with regard to the time scale of the modulation period. In the above two cases, the heat flow is completely determined by the heat capacity of the sample.

However, during the glass transition, as shown in Fig. 1.16(b), the time scale of the heat flow corresponding to the cooperative motion overlaps with that of the temperature modulation. Then a time dependent component is involved in the heat flow. When the underlying heating rate q is much smaller than the maximum instantaneous heating rate caused by the modulation, the total heat flow can be separated into an underlying heat flow and a modulated heat flow.

Category II. Region with excess heat flow

This region has excess kinetic heat flow, such as enthalpy recovery, crystallization, and some chemical reactions, but the material composition is maintained during a modulation cycle, $\partial W_i/\partial T=0$, which is the variation of the mass fraction with temperature of any reaction agent concerned. In this case, there is no contribution to the modulated heat flow from the excess heat as a result of temperature modulation, for example, a curing process.

Figs. 1.17(a) and 1.17(b) show the heat flows for this category when there is excess heat flow. In Fig. 1.17(a), the underlying heating rate is zero. The time scale of the cooperative motion or the kinetics of the curing shifts towards a longer time scale with the extent of the mass fraction conversion, W_i, as a result of the reduced molecular mobility. With further decrease in molecular mobility, the time scale of the cooperative motion may reach the same magnitude of the modulation period.

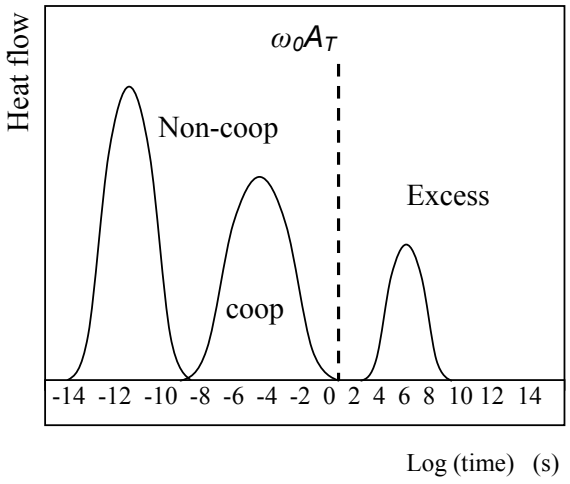

(a)

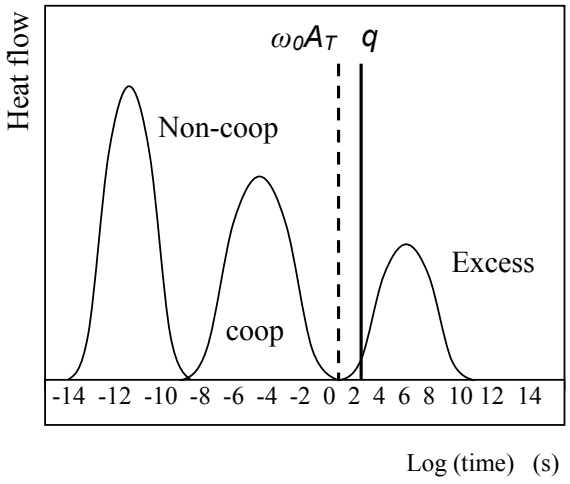

(b)

Fig. 1.17 Thermal responses in TMDSC for Category II, with extra heat "Excess". Adapted from [172]. (a) underlying heating rate q=0, (b) underlying heating rate $q \neq 0$.

In Fig. 1.17(b), because the underlying temperature increases with a positive heating rate, the situation becomes more complicated than that in Fig. 1.17(a): increasing the temperature increases the molecular mobility and the conversion rate of the mass fraction, but an increased conversion rate can result in a lower molecular mobility. Thus, the combined effect of these two factors on the time scale is

determined by both the temperature and the actual physical process involved. Yet, the total heat flow is composed of an underlying and a modulated heat flows.

In both Figs. 1.17(a) and (b), the kinetic heat flow is not susceptible to the temperature modulation. Hence, the modulated part of the heat flow is uniquely determined by the heat capacity of the sample at baseline level, which is a very important feature that allows the separation between the reversing heat flow and the excess or non-reversing heat flow. The separation is possible only under the condition of TMDSC linearity and stability of the material properties, which requires that $\partial W_i/\partial T$ and $\partial W_i/\partial t$ are negligible during a modulation period. Consequently, the selection of the underlying heating rate and the modulation amplitude is critical. In this case, the heat capacity can be derived from the ratio between the amplitudes of the modulated heat flow and the modulated temperature of the sample.

Category III. Region with excess heat flow and material invariance roughly maintained

Fig. 1.18 shows a quasi-isothermal TMDSC run with a susceptibility of the excess kinetic process to the temperature modulation and $dWi/dT \neq 0$. The molecular mobility decreases as a function of time. This is a typical situation for an isothermal crystallization process with reversible melting and crystallization phenomena. In contrast to those shown for Figs. 1.16(a) to (c), the modulated heat flow is no longer uniquely determined by the heat capacity. There is also a contribution from the extra kinetic process due to the modulation. The relevance of linear response theory under quasi-isothermal conditions is disputable, because apart from the question of linearity of the melting and crystallization process, the requirement of material invariance during each modulation cycle cannot be satisfied. As a result, this can lead to complete failure of the TMDSC method. Only when the susceptibility of the extra

kinetic process to temperature modulation is negligibly small can the linear response theory be successfully applied.

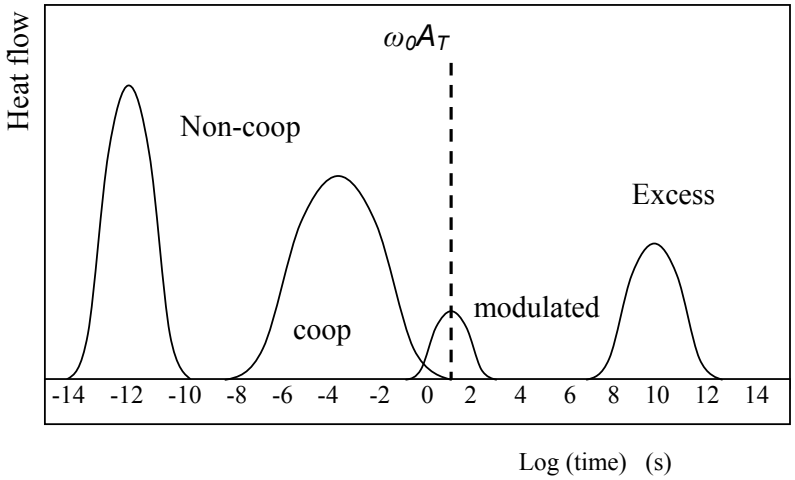

Fig. 1.18 Thermal responses in TMDSC for Category III, with excess heat "Excess". q=0. The modulated heat flow is no longer uniquely determined by the heat capacity. Adapted from [172].

1.3.2.4 Heat capacity and complex heat capacity

1.3.2.4.1 Heat capacity, Debye and Einstein theories

As heat capacity is the one of the major targets that is going to be measured with dynamic thermal calorimetry, we may briefly review what heat capacity is at a fundamental level. In short, heat capacity is the measure of the heat energy required to increase the temperature of a substance by a certain temperature interval [174].

Heat capacity depends on the degrees of freedom of molecules or lattices in a substance. The heat energy stored in the substance may comprise the translational, rotational and vibrational motions of the molecules or lattices. The various degrees of freedom cannot generally be considered to obey classical mechanics, in which the energy residing in each degree of freedom is assumed to be continuous — it can take on any positive value, depending on the temperature. In fact, the amount of energy

that may reside in a particular degree of freedom is quantized: It may only be increased and decreased in finite amounts.

If the temperature of the substance is so low that the equipartition energy of $(1/2)kT$ (here k is Boltsmann's constant, in $J \cdot K^{-1} \cdot molecule^{-1}$, and T is the absolute temperature, in K) is much smaller than the excitation energy, then there will be little or no energy in this degree of freedom. This particular degree of freedom is then said to be "frozen out".

For each degree of freedom there is a critical temperature at which the degree of freedom "unfreezes" and begins to accept energy in a classical way. In the case of translational degrees of freedom, this temperature is the temperature at which the thermal wavelength of the molecules is roughly equal to the size of the container. For a container of macroscopic size (e.g. 10 cm) this temperature is extremely small and has no significance, since the gas will certainly liquify or freeze before this low temperature is reached. For any real gas we may consider translational degrees of freedom to always be classical and contain an average energy of $(3/2)kT$ per molecule.

The rotational degrees of freedom are the next to "unfreeze". In a diatomic gas, for example, the critical temperature for this transition is usually a few tens of kelvins. Finally, the vibrational degrees of freedom are generally the last to unfreeze. As an example, for diatomic gases, the critical temperature for the vibrational motion is usually a few thousands of kelvins. It should be noted that sometimes it is assumed that atoms have no rotational or internal degrees of freedom. Strictly speaking, this is incorrect. For example, atomic electrons can exist in excited states and even the atomic nucleus can have excited states as well. Each of these internal degrees of freedom is assumed to be frozen out due to their relatively high excitation energy.

Nevertheless, for sufficiently high temperatures, these degrees of freedom cannot be ignored.

Einstein model

Einstein solid is a model of a solid based on three assumptions:

a. Each atom in the lattice is a 3D quantum harmonic oscillator

b. Atoms do not interact with each another

c. Atoms vibrate with the same frequency

While the first assumption is quite accurate, the second is not, this is because if atoms did not interact with one another, sound waves would not propagate through solids. Based on the above assumptions, the heat capacity in Einstein's model is derived as

$$C_v = 3Nk\left(\frac{\varepsilon}{kT}\right)^2 \frac{e^{-\varepsilon/kT}}{\left(e^{-\varepsilon/kT}-1\right)^2} \tag{1.40}$$

where N is the number of atoms in a solid.

Einstein temperature T_E is defined as

$$T_E = \frac{\varepsilon}{k} = \frac{h\upsilon}{k}, \tag{1.41}$$

where h is Planck's constant, and υ is the single frequency of quantum harmonic oscillators in Einstein model. Then one has,

$$C_v = 3Nk\left(\frac{T_E}{T}\right)^2 \frac{e^{-T_E/T}}{\left(e^{-T_E/T}-1\right)^2} \tag{1.42}$$

(1) Low temperature limit

When $T<<T_E$,

$$C_v \propto \left(\frac{1}{T}\right)^2 e^{-T_E/T}, \tag{1.43}$$

which is too small if compared with experimental results.

(2) High temperature limit

When $T>>T_E$,

$$C_v = 3Nk . \tag{1.44}$$

Although Einstein model of the solid predicts the heat capacity accurately at high temperatures, it noticeably deviates from experimental values at low temperatures. The following sections discuss the Debye model for an accurate low-temperature heat capacity calculation.

Debye model

This model is applicable to a crystalline solid phase. It treats the vibrations of the atomic lattice (heat) as phonons in a box, in contrast to Einstein model, which treats the solid as many individual, non-interacting quantum harmonic oscillators that has the same frequency. The Debye model correctly predicts the low temperature dependence of the heat capacity, which is proportional to T^3. Just like the Einstein model, it also recovers the Dulong-Petit law at high temperatures. In Debye's model, the dimensionless heat capacity is derived as

$$\frac{C_v}{Nk} = 9\left(\frac{T}{T_D}\right)^3 \int_0^{T_D/T} \frac{x^4 e^x}{\left(e^x - 1\right)^2} dx , \tag{1.45}$$

where N is the number of atoms in a solid, and T_D is the Debye temperature.

The above formula gives the Debye model at all temperatures. The more elementary formulae given further down give the asymptotic behavior in the limit of low and high temperatures.

(1) Low temperature limit

The temperature of a Debye solid is said to be low if

$$T << T_D , \tag{1.46}$$

where Debye temperature T_D is a shorthand for some constants and material-dependent variables, leading to

$$\frac{C_v}{Nk} = 9\left(\frac{T}{T_D}\right)^3 \int_0^{\infty} \frac{x^4 e^x}{\left(e^x - 1\right)^2} dx . \tag{1.47}$$

This definite integral can be evaluated exactly:

$$\frac{C_v}{Nk} = \frac{12\pi^4}{5}\left(\frac{T}{T_D}\right)^3 . \tag{1.48}$$

In the low temperature limit, the limitations of the Debye model mentioned above do not apply, and it gives a correct relationship between heat capacity, temperature, the elastic coefficients, and the volume per atom (the latter quantities being contained in the Debye temperature).

(2) High temperature limit

The temperature of a Debye solid is said to be high if $T >> T_D$. If $| x | << 1$,

$$e^x - 1 \approx x , \tag{1.49}$$

and

$$e^x \approx 1 . \tag{1.50}$$

This leads to

$$\frac{C_v}{Nk} = 9\left(\frac{T}{T_D}\right)^3 \int_0^{T_D/T} \frac{x^4}{x^2} dx , \tag{1.51}$$

and

$$\frac{C_v}{Nk} = 3 . \tag{1.52}$$

This is the Dulong-Petit law, and is fairly accurate although it does not take into account anharmonicity, which causes the heat capacity to rise further. The Dulong-Petit law, which was discovered empirically, states that the dimensionless

specific heat capacity assumes the value 3R. Indeed, for solid metallic chemical elements at room temperature, heat capacities range from about 2.8 to 3.4 (beryllium being a notable exception at 2.0) [175]. The total heat capacity of the solid, if it is a conductor or semiconductor, may also contain a non-negligible contribution from the electrons.

Debye model vs. Einstein model

Debye and Einstein models correspond to experiment fairly close, but Debye is correct at low temperatures whereas Einstein is not (actually too low). Both Debye temperature T_D and Einstein temperature T_E are usually found by fitting the models to the experimental data, and T_D can be calculated from the speed of sound and crystal dimensions. Even though the Debye model is not completely correct, it gives a good approximation for the low temperature heat capacity of insulating, crystalline solids where other contributions (such as highly mobile conduction electrons) are negligible. For metals, the electron contribution to the heat capacity goes as T, which at low temperatures, dominates the Debye T^3 result for lattice vibrations. In this case, the Debye model can only be said to approximate the lattice contribution to the specific heat.

Einstein or Debye's theories are important in understanding the fundamentals of heat capacity. In TMDSC, regardless of whether the heat energy is stored in translational, rotational or vibrational motions, these motions at atomic or molecular level are so fast that they are considered instantaneously and fully reversible with any external temperature change. In other words, heat energy absorbed due to the heat capacity with a temperature increase can be immediately and completely released with the same amount of temperature decrease, or vice versa. While a kinetic event normally requires much longer to complete and the response time to temperature

changes may even be comparable to the external temperature modulation period itself. Even a reversing chemical reaction can't match the speed of response of the lattice vibrations to external heat or energy. Due to the difference in the response time to external temperature changes between the heat flow that is related to heat capacity and the heat flow that is related to a kinetic event, the purpose of the temperature modulation technique is to find out the contributions from each source, either thermal-dynamically or kinetically originated, provided that the thermal response of TMDSC is linear or close to linear.

1.3.2.4.2 Complex heat capacity and phase angle: definition and calculation

The physical implication of complex heat capacity has confused scientists for a long time [176, 177]. The complex form of heat capacity was first reported in 1985 by Birge and Nagel [153] using 3-ω dynamic calorimetry in the study of the glass transition, where heat capacity was represented by $C^*=C'-iC''$ where C' and C'' are the real and imaginary part respectively. Many authors followed on with the same concept of complex heat capacity in the field of TMDSC, and several different explanations were proposed [54, 72, 73, 178—183]. Aubuchon and Gill [178], and Gill et al. [179] attributed the existence of the imaginary part of the heat capacity to either certain kinetic events within the sample or to dissipation processes that are related to entropy production. Schawe [72, 73] associated C'' with dissipation and time dependent thermal events. Later, Schawe modified this by connecting C'' to changes in molecular mobility as well as entropy production in the sample [180, 181]. Jeong [54] drew an analogy between C' and dielectric susceptibility, and concluded that C'' had an entropic origin and was representative of the entropy increase of the heat reservoir during one modulation cycle. Alig [182] proposed to compare sound

absorption due to thermal relaxation in ultrasonic experiment with the complex heat capacity as measured in TMDSC. The conclusion was that C'' arises from the transfer of energy between the external and internal degrees of freedom. Hohne [183] offered yet another explanation which stated that C'' should be related to the dissipated energy of the time dependent process.

The issue of complex heat capacity is still quite controversial [176,177,184,186]. There is an essential difference between the imaginary part, C'', of heat capacity and the imaginary part of some other physical properties, e.g., impedance, dielectric constant, and susceptibility, which are typically related to dissipative processes. Baur and Wunderlich [184] doubted the physical meaning of C''. They thought that the concept of complex heat capacity was of limited significance because solids and liquids had no dissipative or imaginary contributions. In the glass transitions, the thermal response is non-linear. Hence, they believed a detailed kinetic model in real notation was more advantageous in describing the heat capacity. The crystallization is often so far from equilibrium that it is not modulated. During melting and chemical reactions, the extra heat flow is typically so large that the steady state is easily lost. Thus, the observed complex heat capacity is of questionable value, even if the temperature modulation is accomplished [184].

Seferis in publication with Martin [176] and Buehler [177] denied the existence of the imaginary part altogether. They argued that the imaginary part of the heat capacity did not exist at all but was purely a mathematical artifact caused by the heat diffusion difficulty and the algorithms used in TMDSC. According to them, heat capacity is a bulk property of materials, and it should be isotropic. Moreover, heat capacity is a thermodynamic and not a kinetic property. If the heating of an object is not instantaneous, it is not due to the value of the heat capacity but due to the fact that

heat must diffuse into the object. Heat diffusion is a process governed by other thermo-physical property of the material, e.g., the thermal diffusivity. Thermal diffusivity can be anisotropic in some substances such as fibers. Hence, thermal diffusivity can then be expressed as a tensor, and it may be responsible for the existence of the phase lag observed in TMDSC experiments [176, 177].

To support their conclusions, Martin and Seferis [176], Buehler and Seferis [177] analyzed the case of a cylindrical sample, where both the radial and axial temperature distributions in the sample were taken into account. They obtained a rather complicated relationship between the thermal properties of the sample and the phase lag, which is the angle between the heat flow and the time derivative of temperature. This angle and therefore the temperature gradient are quite large for low-heat conductive materials but were typically ignored in a TMDSC model where no thermal gradient is considered. A temperature difference as much as a third of the amplitude of the modulated temperature can exist along the radial and axial dimensions for the samples studied [176, 177].

However, although the difficulty in heat transfer in the sample could account for part of the observed phase lag, Martin and Seferis [176], and Buehler and Seferis [177] only studied a case where no kinetic events are involved. Kinetic events do contribute an extra phase lag and thus can affect the observed specific heat [3]. To evaluate the effect of the kinetic events, it is required that this extra phase lag be properly extracted from the total phase angle. To achieve this goal, Reading and Luyt [3, 185] proposed a baseline correction method, which is schematically shown in Fig. 1.19.

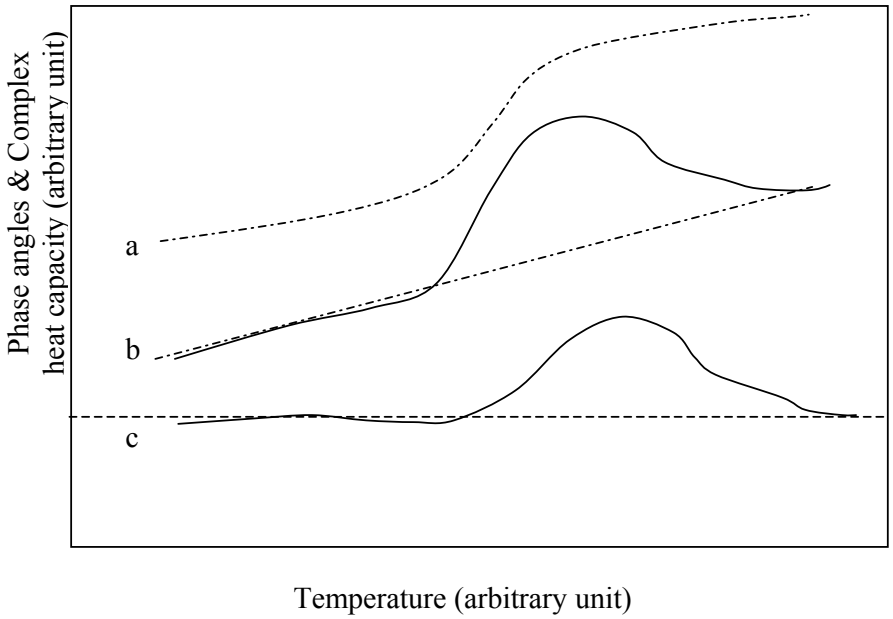

Fig. 1.19 Baseline method by Reading and Luyt. (a) Complex heat capacity $|C_P^*|$, (b) Uncorrected phase angle, (c) Corrected phase angle. Adapted from [165].

According to this method, two data points are selected — one at the beginning and one at the end of the hypothetical transition. A baseline is then drawn between these two data points. This procedure is based on the assumption that no transition occurs at the two selected points. Reasonably accurate phase angles from the out-of-phase or kinetic events were obtained for several polystyrene samples under the protection of nitrogen and helium. They also noticed that for relatively large enthalpy loss, the system linearity was compromised to a certain extent; yet the result remains a useful comparative measure for many applications.

However, Weyer et al. [186] were of the opinion that with the non-optimal measuring conditions, such a correction yielded an unrealistically broad and non-symmetric peak for the phase angle and therefore for the imaginary part of the complex heat capacity. They proposed an alternative method that took into account the change in heat flow due to the change in the heat capacity. Fig. 1.20 shows a

typical glass transition in polymer samples, the transition is accompanied by a step change (see the dotted line in Fig. 1.20) in the complex heat capacity, C^*.

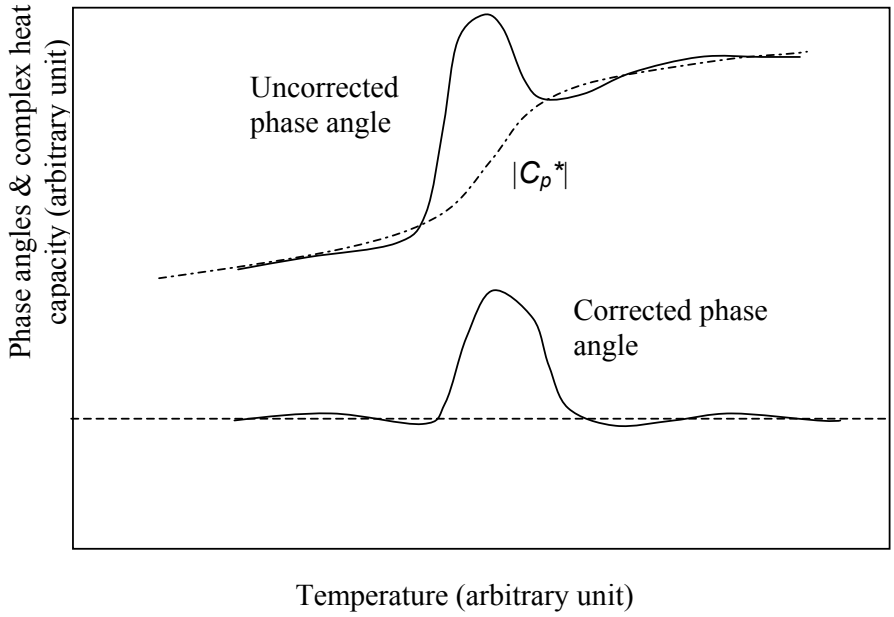

Fig. 1.20 Phase angle correction using fitting baseline that takes into account the change in complex heat capacity $|C_p^*|$. Adapted from [186].

When the phase angle is small, it can be proven that the phase angle change is proportional to the change in heat capacity; that is, $\Delta\varphi=\omega\Delta C_p/K$, where ΔC_p is the change of the heat capacity. Therefore, it is possible to draw a curve proportional to the complex heat capacity so that it fits into the phase angle curve before and after the transition region. This fitted curve takes the form $\varphi=a+b|C^*|$, where a and b are fitting parameters. Then one may treat any difference between this fitting curve and the phase angle curve as the additional phase angle due to the kinetic event. The solid line in the lower half of Fig. 1.20 shows the difference.

Even with this method, Weyer et al. [186] found that complications could occur. For example, when there is a change in the thermal conductivity of the sample, or a change in the effective system thermal constant due to materials softening, or

variations in other thermal properties, the obtained results could be quite difficult to quantify. As shown in Fig. 1.21, the decrease in the phase angle after the transition is an artifact caused by the increase in thermal conductivity and has nothing to do with change in heat capacity. No practical approach is available yet to handle this problem. As a result, care must be taken when interpreting the phase angle behavior observed by TMDSC.

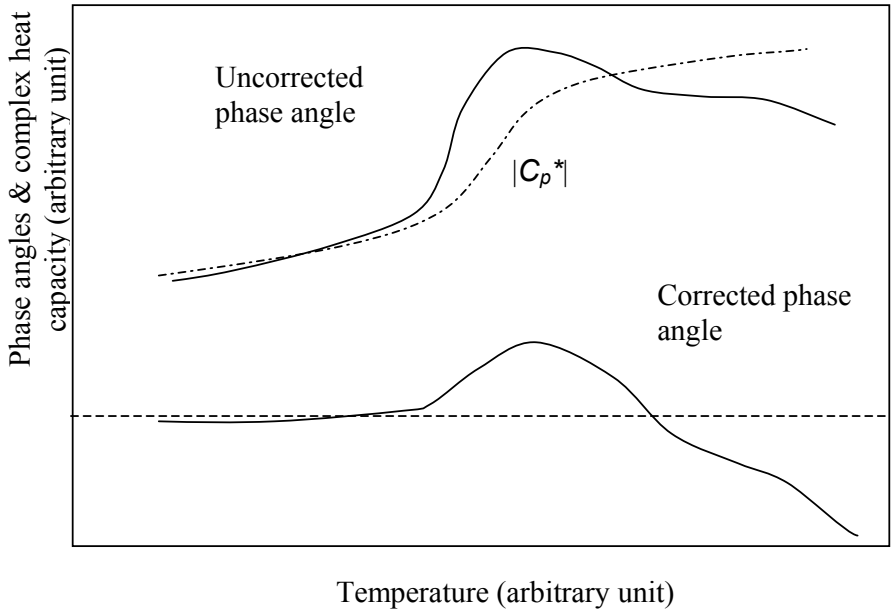

Fig. 1.21 Deformed phase angle data due to complications in the transition such as a change in sample thermal conductivity. Adapted from [186].

1.3.2.5 Calibration and system linearity of TMDSC

Since it is not possible to measure the sample temperature and heat flow directly because the thermal couple is not placed inside the sample, calibration is required. The calibration procedures for heat flow and sample temperature for conventional DSC are well developed. In DSC, temperature calibration takes into account the thermal lag between the thermo-couple and the sample due to heat transfer. To correct this thermal lag, the observed temperature has to be extrapolated

to zero heating rate. Thus, only the dependence of the measured temperature on the heating rate needs to be considered.

Compared with conventional DSC, several additional experimental parameters should be taken into consideration in TMDSC, such as the underlying heating rate, temperature modulation amplitude and frequency, phase angle, and possible errors from the numerical algorithms used in TMDSC data treatment. The heat capacity and heat flows obtained from Fourier transform are valid only if the thermal response of the TMDSC device is linear [176, 177, 187].

The non-linear behavior in the temperature region of a certain transition depends on both the magnitude of heat flow and the properties of the transition itself. Even in the conventional DSC, the thermal response is not always linear. For example, the heat flow from the melting of a 0.48 mg indium sample is not equal to four times that of a 0.12 mg sample [187] (see Fig. 1.22). This is because during the melting, the sample temperature remains constant, despite the designed temperature program. Thus, the measured heat flow is completely determined by the heat transfer path, which is dependent on the physical implementation of the DSC system.

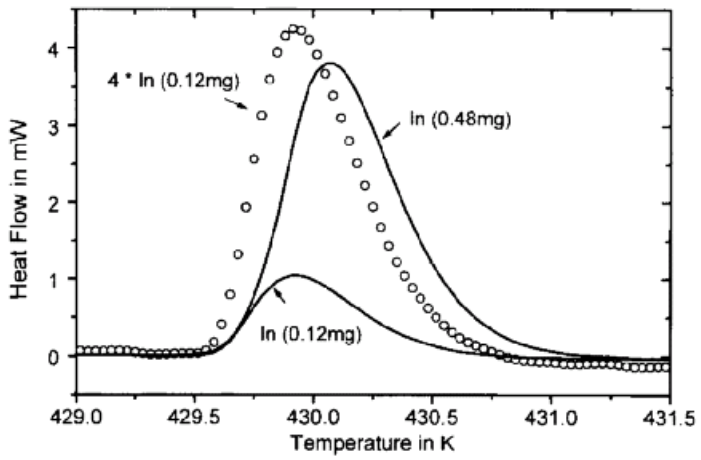

Fig. 1.22 Indium melting process in DSC. Adapted from [187].

For TMDSC, the heat transfer path produces an additional phase angle. Hence, transitions such as the melting of indium are not suitable for the temperature calibration in TMDSC. To evaluate the system linearity of a TMDSC system, Hensel and Schick [187] used a liquid crystal, 8OCB (octyloxy cyanobyphenyl), which was found to have an 0.5 K half-peak transition width. Moreover, it shows no super-cooling and has a weak smectic-nematic (SN) transition (see the DSC curve in Fig. 1.23). The TMDSC experimental results of transition temperatures are shown in Figs. 1.24 to 1.26 [187].

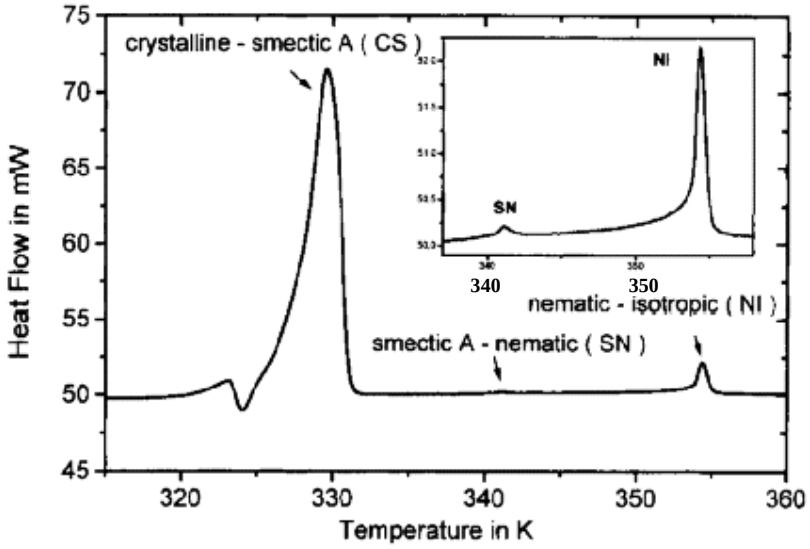

Fig. 1.23 DSC curve of a liquid crystal (8OCB), heating rate=10 K/min. Adapted from [187].

Fig. 1.24 shows the relationship between the modulation amplitude and the measured temperature and height of the transition peak, where the temperature modulation amplitude is changed from 0.07 to 3.4 K. The peak temperature remains quite stable when the amplitude is lower than 2 K, but there is a considerable broadening of the peak due to the decreasing height as the modulation amplitude

increases. The peak becomes significantly wider when the amplitude of the temperature modulation is close to the height of the transition during a heating or cooling cycle. In other words, the temperature resolution of TMDSC is basically determined by the selected modulation amplitude.

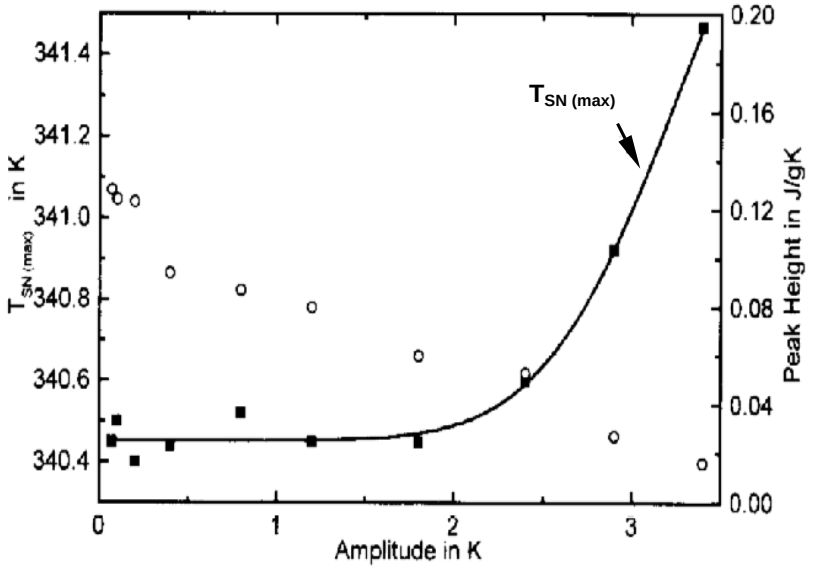

Fig. 1.24 TMDSC curve of 8OCB. Solid square: peak temperature. Circle: peak height. Temperature modulation period=50 s. Underlying heating rate=0.4 K/min. Adapted from [187].

Fig. 1.25 shows the effect of the modulation period on the temperature and height of the transition peak. The peak temperature changes very little for modulation periods shorter than 20 s. However, when the period exceeds 60 s, the peak becomes broader and lower. For an even longer temperature modulation period, which is preferred for a more accurate measurement of specific heat, the requirement to accommodate a number of modulation cycles (at least four, for example) during the transition for effective deconvolution of the heat flows is not satisfied. This can result in a loss of information in the measurement.

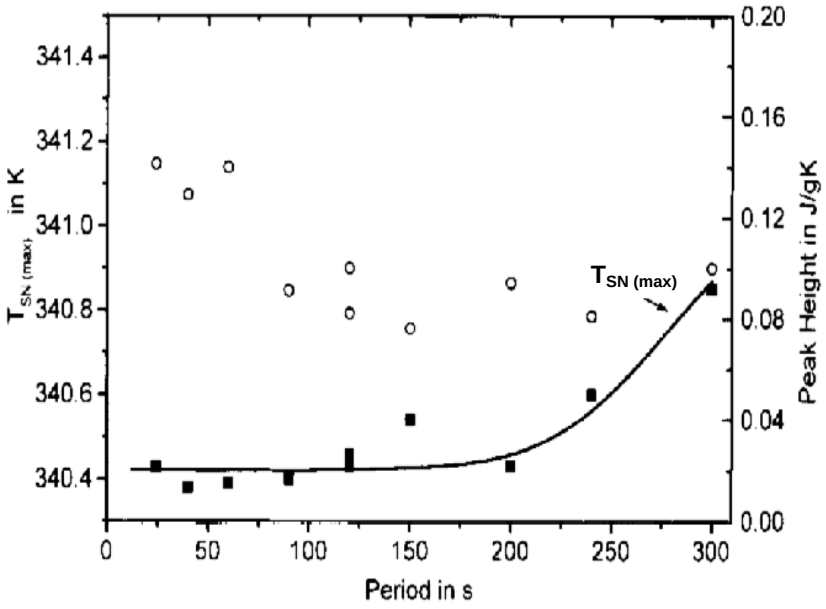

Fig. 1.25 TMDSC curve of 8OCB. Solid square: peak temperature. Circle: peak height. Temperature modulation period=12 to 300 s. Underlying heating rate=0.4 K/min. Adapted from [187].

The influence of the underlying heating rate on peak temperature of the transition is shown in Fig. 1.26 for both DSC and TMDSC. The TMDSC device has been calibrated using the usual method with indium and lead at a heating rate of 10 K/min. It can be seen that the onset temperature of indium in DSC is almost unaffected by the heating rate due to the automatic thermal lag compensation by the instrument. For the smectic-nematic (SN) transition of the liquid crystal in DSC mode, the curve shows a small gradient when compared with that of indium. This can be explained by the fact that indium is in the solid state while 8OCB is in the smectic state before their corresponding transitions, thus their thermal contact conditions between the sample and pan are different. The TMDSC device itself cannot automatically correct this difference in thermal conductivity. However, the onset temperature curve shows a much larger gradient, which agrees well with the typical

thermal lag characteristics of the TMDSC system as determined without any compensation. This demonstrates the rather narrow linear response range of TMDSC and stringent requirements on the selection of TMDSC experimental parameters, indicating the importance of maintaining the steady state if meaningful conclusions are to be obtained [185].

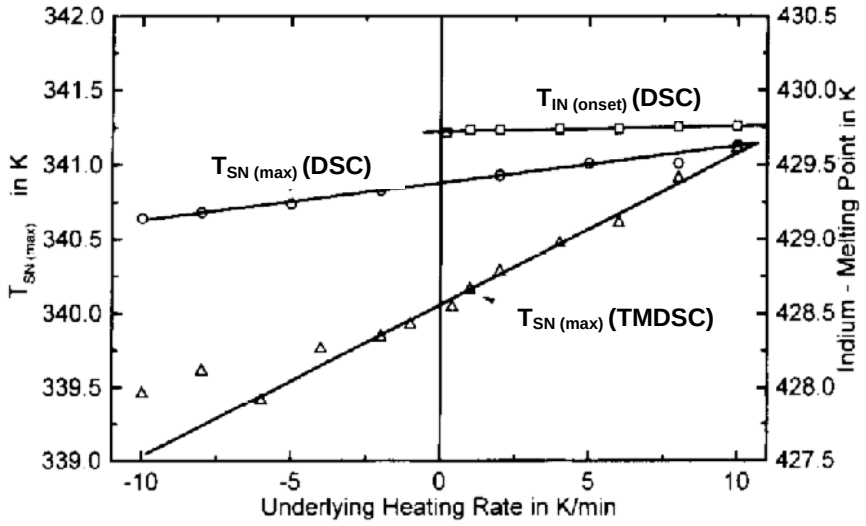

Fig. 1.26 The top line: DSC onset temperature of indium melting. The middle line: DSC onset temperature of the SN transition. The bottom line: TMDSC onset temperature of the SN transition. Temperature modulation period=50 s. Adapted from [187].

1.3.2.6 System linearity inspection

The overall TMDSC system linearity can be visually inspected with the help of the Lissajous figure [3, 166], which uses the relationship between the instantaneous heating rate of the sample and heat flow. For an ideal linear system described by Eqs. (1.12) and (1.13), a diagram similar to that shown in Fig. 1.27 can be obtained. Depending on the experimental parameters, the curve in the diagram can be either an ellipse or a circle. However, if there are higher harmonics which indicate a non-linear response, the ellipse or circle will be deformed accordingly (examples are given in

Chapter 5). Hence, this method is only used for qualitative rather than quantitative comparison of the linearity.

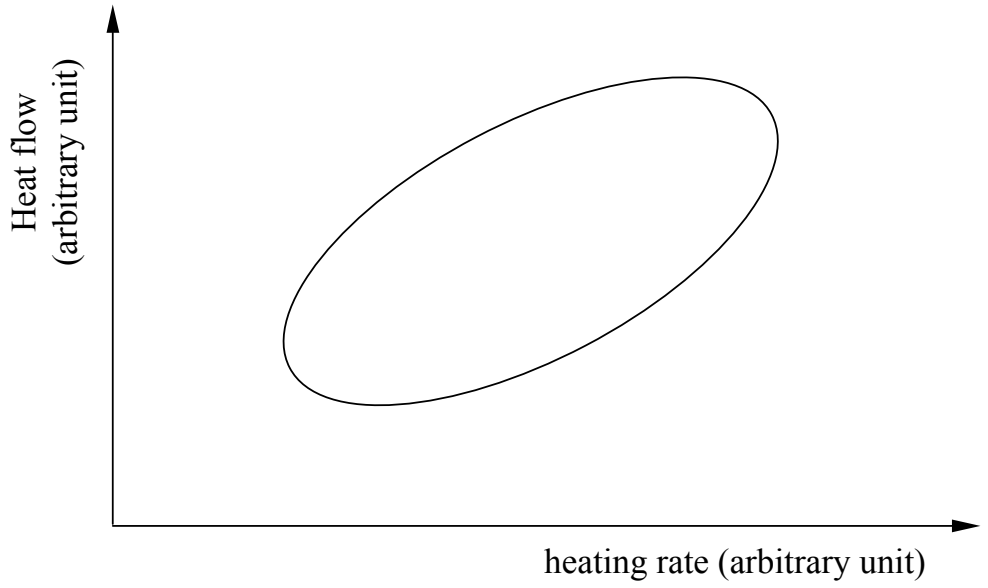

Fig. 1.27 Lissajous figure of a linear response system

1.3.3 Progress in light modulation technique

TMDSC devices that use electric power to heat the sample have a relatively long system thermal latency that restricts the achievable temperature modulation frequency. Using modulated light as the heating source in TMDSC design has become an alternative to overcome this latency issue. Below are some advances in this area.

Fig. 1.28(a) shows the diagram of a light modulated dynamic calorimetry device designed by Nishikawa and Saruyama [188], while a similar design by Ozawa and Kanari [189] is illustrated in Fig. 1.28(b). In Fig. 1.28(a), a beam of light passes through the intensity modulator. Only the sample is radiated with the modulated light, while the intensity of light on the reference side is constant to provide temperature balance. In Fig. 1.28(b), different from that as shown in Fig. 1.28(a), both light sources on the sample and reference sides are modulated. Furthermore, the light

source may come from either the top to heat the sample directly or from the bottom to heat the support plate depending on the actual implementations. Their analysis shows that configuration with the light from the bottom is better than that from the top in terms of accuracy and stability [189].

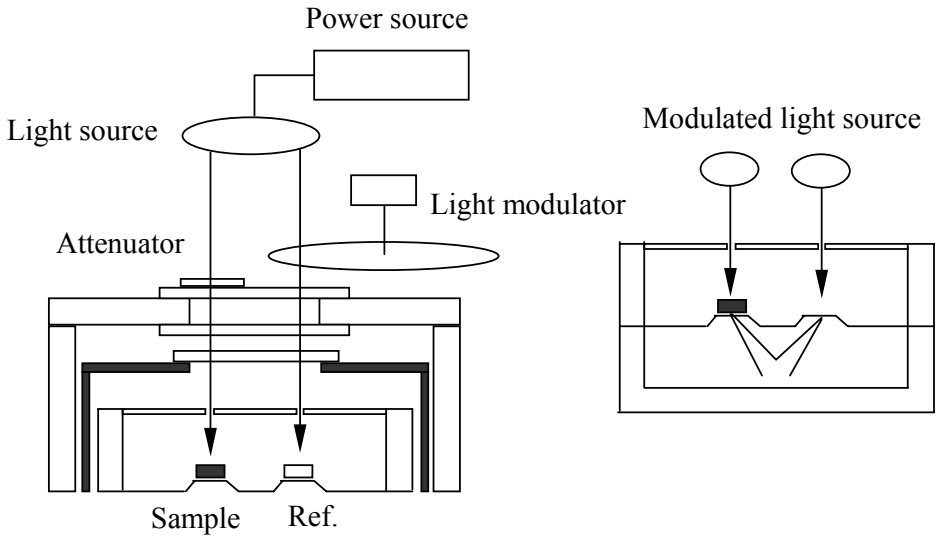

Fig. 1.28 TMDSC with light as the heating source. Adapted from [188, 189]. (a) System schematic diagram. (b) The cell structure diagram. Light may come from the bottom and heat the support plate.

Fig. 1.29 shows the laser-flash device by Pouchon et al. [190]. A ruby laser impulse with energy of 6 J is applied to the front surface of the sample, which produces an increase of about 10 K in local temperature. The photon energy was converted into a heat pulse that penetrates the sample. The temperature change of the sample is detected by an InSb infrared sensor on the rear side. The thermal diffusivity is then deduced from the thermal transient of the rear surface, called the thermo-gram. To obtain consistent experimental results, a gold or carbon coating is required on both sides of the sample in order to effectively transform the laser energy into a heat pulse. Experiments on thermal conductivity have been conducted for some semi-transparent

zirconium-based materials with TMDSC for comparison. While it was found that measurements carried out with TMDSC devices were affected by the position of the sample on the support plate, the laser flash method was believed to have good reproducibility [190]. This could be the reason that the method of measuring thermal conductivity with TMDSC proposed by Aubuchon, Blain and Marcus [191, 192] was not accepted by American Society of Testing & Materials (ASTM).

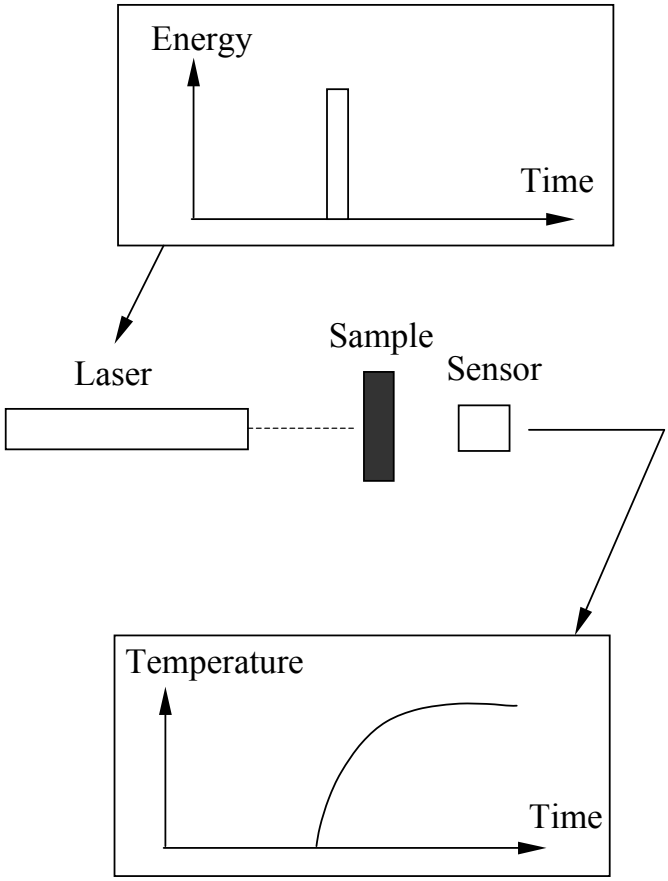

Fig. 1.29 The laser flash method to measure sample thermal conductivity. A laser flash induces an energy pulse into the front surface of the sample. The heat wave is transferred to the back surface and picked up by an IR (infrared) detector. Adapted from [190].

Generally speaking, compared with the heat flux or power compensation type TMDSC, temperature modulation with a light source has the following advantages [188—190]:

1. A laser or light flash has good reproducibility.

2. Much greater flexibility in the design of the apparatus since the control method of the furnace temperature is different. It is kept at a constant temperature or heated at a constant rate by light only. Thus, temperature modulation by electrical power is not required.

3. The temperature modulation is not decided by the heat transfer path as a conventional TMDSC cell is, but implemented directly through the light source. The maximum frequency of temperature modulation is only limited by the thermal conductivity of the sample itself. This can be improved by using small samples at 10^{-6} gram level. Hence, the dynamic test range can be enhanced by several orders of magnitude higher than other TMDSC devices.

1.4 Summary

Dynamic calorimetry has come a long way since its inception in the early twentieth century. As TMDSC is a late derivative of dynamic calorimetry, many different configurations and theories have been proposed. TMDSC has already been shown to be a useful extension of conventional DSC and can provide additional information that may otherwise be hidden or ignored. Nevertheless, a more detailed understanding of its applicability and limitations is needed so that the data obtained from TMDSC can be correctly interpreted.

As has been conveyed in the previous sections, the determination of the heat capacity in a single run by TMDSC is a potential advantage due to its intrinsic higher

temperature sensitivity [3, 166]. This is important when thermal history plays an important role in determining the thermal properties of the sample. A remaining issue is that a strict calibration of TMDSC is difficult because there is no simple relationship between the actual heat capacity of the sample and the measured one, although at a longer modulation period, the error of measurement can be reduced [167, 168].

When there is an extra heat contribution from a kinetic event, the ability to separate the reversing heat flow from the non-reversing heat flow is a valuable property of TMDSC. In this case, one has to be sure that the kinetic event is not sensitive to temperature modulation [172, 173].

When the kinetic event or non-reversing heat flow is sensitive to the temperature modulation, the heat capacity cannot be determined uniquely from the measured complex heat capacity (C^*). Nevertheless, C^* may still provide valuable information with respect to the kinetic event. The requirement of linearity in thermal response indicates that the modulation conditions applied are critical to the reliable measurement of a complex heat capacity.

Due to its unique features, temperature modulation can be applied in other conventional thermal analytical methods. These include differential thermal analysis (DTA), thermal dilatometry [193, 194] pressure differential thermal analysis (PDTA), differential photo-calorimetry (DPA), differential thermo-gravimetry (DTG), or a combination of them, as had been pointed out by Reading [3]. This may open new ground and extend our vision into unknown areas with regard to reaction kinetics of materials in the near future.

1.5 Objectives of the research

Measuring the heat capacity is one of the basic functions of TMDSC, which also is the key to successful separation of the reversing heat flow (related to heat capacity) and non-reversing heat flow (related to kinetic events).

To really understand how TMDSC works and its limitations, we will need to study those factors that can affect the accuracy of the heat capacity measurement, such as the thermal conductivity of the sample material, the thermal inertia of the measuring device itself, and finally, if a kinetic event is introduced into the sample at a certain temperature, what will happen and how much difference it will generate in the measurement of the heat capacity. Apart from Chapter 1, the rest of the thesis essentially comprises four chapters in which different aspects of TMDSC are discussed.

In Chapter 2, measurements that take into account of imperfect thermal transfer path are discussed, this include the contact thermal resistance between the sample and the supporting plate, the thermal conducting properties of the TMSDC device, etc. Besides, we will look at how the external temperature modulation conditions can affect the observed heat capacity. Comparisons are made for the specific heat measurement and the calibration between TMDSC and the conventional DSC.

In Chapter 3, we will analyze the effect of thermal conductivity of the sample on the observed heat capacity; other factors such as sample thickness and temperature modulation frequency are also discussed. Both analytical and numerical approaches will be explored.

In Chapter 4, the separability of reversing heat flow and non-reversing flow is discussed by using several different arbitrary types of non-reversing heat flows (i.e. time or temperature dependent heat flows).

And finally, in Chapter 5, a more general situation based on small perturbations is studied on the relationship between the kinetic event and the complex heat capacity (or rather the observed heat capacity). A concise analytical solution and numerical simulations of several kinetic models will be provided to show the effect of the TMDSC experimental parameters on the observed heat capacity.

References

[1] O. M. Corbino, Phys. Z. **11** (1910) 413.

[2] L. A. Rosenthal, Rew. Sci. Instrum. **32** (1961) 1033.

[3] M. Reading, USA. Patent 5,224,775. 1993.

[4] K. K. Smith, P. W. Bigler, Phys. Rev. **19** (1922) 268.

[5] Y. A. Kraftmakher, Zh. Prikl. Mekh. Tekh. **5** (1962) 176.

[6] G. C. Loewenthal, Australia J. Phys. **16** (1963) 47.

[7] E. Gmelin, Thermochim. Acta **305**(1997)1.

[8] P. F. Sullivan, G. Seidel, Phys. Rev. **173** (1968) 679.

[9] P. Handler, D. E. Mapother, M. Rayl, Phys. Rev. Lett. **19** (1967) 356.

[10] A. Bonilla, C. W. Garland, J. Phys. Chem. Solids **35** (1974) 871.

[11] I. Hatta, A. Ikushima, J. Phys. Chem. Solids **34** (1973) 57.

[12] S. Ikeda, Y. Ishikawa, Jpn. J. Appl. Phys. **18** (1979) 1367.

[13] Y. A. Kraftmakher, High Temp. High Pressure **24** (1992) 145.

[14] N. O. Birge, S. R. Nagel, Rev. Sci. Instrum. **58** (1987) 1964.

[15] N. O. Birge, Phys. Rev. B **34** (1986) 1631.

[16] P. K. Dixon, Phys. Rev. B **42** (1990) 8179.

[17] J. E. Graebner, Rev. Sci. Instrum. **60** (1989) 1123.

[18] D. M. Ginsberg, S. E. Inderhees, M. B. Salamon, N. Goldfeld, J. P. Rice, B. G. Pazol, Physica. C **153/155** (1988) 1082.

[19] L. P. Filippov, Inzh. Fiz. Zh. **3** (1960) 121.

[20] Y. A. Kraftmakher, High Temp. High Pressure **5** (1973) 645.

[21] L. J. Schowalter, M. B. Salomon, C. C. Tsuei, R. A. Craven, Solid State Commun. **24** (1977) 525.

[22] G. B. Kasting, Phys. Rev. B **22** (1980) 321.

[23] R. D. Hemstead, J. M. Mochel, Phys. Rev. **7** (1973) 287.

[24] I. Hatta, A. J. Ikushima, Jpn. J. Appl. Phys. **20** (1981) 1995.

[25] C. W. Garland, G. B. Kasting, K. J. Lushington, Phys. Rev. Lett. **43** (1979) 1420.

[26] G. Bednarz, B. Millier, M. A. White, Rev. Sci. Instrum. **63** (1992) 3944.

[27] G. Bednarz, D. J. W. Geldart, M. A. White, Phys. Rev. B **47** (1993) 14247.

[28] T. W. Kenny, P. L. Richards, Rev. Sci. Instrum. **61** (1990) 822.

[29] C. W. Garland, Thermochim. Acta **88** (1985) 127.

[30] G. M. Schmiedshoff, N. A. Fortune, J. S. Brooks, G. R. Stewart, Rev. Sci. Instrum. **58** (1987) 1783.

[31] J. M. Viner, D. Lamey, C. C. Huang, R. Pindak, J. W. Goodbye, Phys. Rev. A **28** (1983) 2433.

[32] M. Castro, J. A. Puertolas, J. Therm. Anal. **41** (1994) 1245.

[33] A. Eichler, W. Gey, Rev. Sci. Instrum. **50** (1979) 1445.

[34] X. C. Jin, P. H. Hor, M. K. Wu, C. W. Chu, Rev. Sci. Instrum. **55** (1984) 993.

[35] J. D. Baloga, C. W. Garland, Rev. Sci. Instrum. **48** (1977) 105.

[36] S. Stokka, V. Samulionis, Phys. Stat. Sol. (A) **67** (1981) K89.

[37] X. Chen, A. S. Perel, J. S. Brooks, R. P. Guertin, D. G. Hinks, J. Appl. Phys. **73** (1993) 1886.

[38] P. F. Sullivan, G. Sedel, Phys. Lett. A **25A** (1967) 229.

[39] R. Geer, S. Stoebe, T. Ptitchford, C. C. Huang, Rev. Sci. Instrum. **62** (1991) 415.

[40] T. Suzuki, T. Tsuboi, H. Takaki, Jpn. J. Appl. Phys., PT 1 **21** (1982) 368.

[41] G. Kampf, H. Selisky, W. Buckel, Physica. **108B** (1981) 1263.

[42] H. Yao, I. Hatta, Jpn. J. Appl. Phys. 2 **27** (1988) L121.

[43] I. Hatta, H. Yao, R. Kato, A. Maesono, Jpn. J. Appl. Phys. 1 **29** (1990) 2851.

[44] T. Gast, H. Jakobs, Thermochim. Acta **72** (1984) 71.

[45] I. Hatta, Y. Sasuya, R. Kato, A. Maesono, Rev. Sci. Instrum. **56** (1985) 1643.

[46] M. Meichle, Phys. Rev. A **27** (1983) 2624.

[47] D. H. Jung, T. W. Kwon, D. J. Bae, I. K. Moon, Y. H. Yeong, Meas. Sci. Technol. **3** (1992) 475.

[48] A. A. Kurichenko, A. D. Ivliev, V. E. Zinovev, Teplofiz Vys. Temp. **24** (1986) 493.

[49] K. Nahm, C. K. Kim, M. Mittag, Y. H. Jeong, J. Appl. Phys. **78** (1995) 3980.

[50] D. G. Cahill, Rev. Sci. Instrum. **61** (1990) 802.

[51] I. K. Moon, Y. H.Yeong, S. I. Kwun, Rev. Sci. Instrum. **67** (1996) 29.

[52] W. Hemminger, G. Honhe, *Grundlagen Kalorimettrie*, Verlag Chemie, Weinheim, 1979, p.107.

[53] G. W. H. Hohne, W. Hemminger, H. J. Flammersheim, *Differential Scanning Calorimetry*, Springer, Berlin, 1996, p.213.

[54] Y. H. Jeong, Thermochim. Acta **304/305** (1997) 67.

[55] E. S. R. Gopal, *Specific Heat at Low Temperatures*, Heywood, London, 1966, p.187.

[56] C. Y. Ho, *Specific Heat of Solids*, Hemisphere, New York, 1988, p.106.

[57] E. Gmelin, Thermochim. Acta **29** (1979) 1.

[58] A. Junod, *Physical Properties of High Temperature Superconductors*, World Scientific Publication, Singapore, 1990, p.262.

[59] E. F. Westrum, G. T. Furukawa, J. P. McCullough, *Experimental thermodynamics*, Buttterworth, London, 1968, p.133.

[60] E. Gmelin, Thermochim. Acta **110** (1987) 183.

[61] Y. A. Kraftmakher, *Compendium thermophysical property measurement methods*, Plenum Press, New York, 1984, p.591.

[62] B. Wunderlich, *Thermal Analysis*, Academic Press, San Diego, 1990, p.55.

[63] W. Brill, E. Gmelin, J. Therm. Anal. **33** (1988) 365.

[64] I. Hatta, Pure Appl. Chem. **64** (1992) 79.

[65] H. Yao, I. Hatta, Solid State Phys. **24** (1989) 769.

[66] U. Rahm, E. Gemelin, J. Therm. Anal. **38** (1992) 335.

[67] I. V. Velichkov, Cryogenics **32** (1992) 285.

[68] Y. A. Kraftmakher, V. L. Tonaevskii, Phys. Stat. Sol. A **9** (1972) 573.

[69] P. Manuel, H. Niedoba, J. J. Veyssie, Rev. Phys. Appl. **7** (1972) 8.

[70] I. Hatta, A. Ikushima, Phys. Lett. **37A** (1971) 207.

[71] Y. Saruyama, J. Therm. Anal. **38** (1992) 1827.

[72] J. E. K. Schawe, Thermochim. Acta **261** (1995) 1.

[73] J. E. K. Schawe, Thermochim. Acta **271** (1996) 127.

[74] B. Wunderlich, A. Boller, I. Okazaki, K. Ishikiriyama, Thermochim. Acta **304/305** (1997) 125.

[75] A. Boller, Y. Jin, B. Wunderlich, J. Therm. Anal. **42** (1994) 307.

[76] Y. Q. Gu, I. Hatta, Jpn. J. Appl. Phys. 1 **30** (1991) 1295.

[77] P. R. Garnier, M. B. Salamon, Phys. Rev. Lett. **27** (1971) 1523.

[78] M. Barrio, J. Font, J. Muntasell, J. Tamarit, J. Therm. Anal. **37** (1991) 39.

[79] C. A. Schantz, D. L. Johnson, Phys. Rev. A **17** (1978) 1504.

[80] D. L. Connelly, J. L. Loomis, D. E. Mapother, Phys. Rev. B **3** (1971) 924.

[81] M. Fixman, J. Chen, J. Chem. Phys. **36** (1962) 1961.

[82] K. F. Herzfeld, F. O. Rice, Phys. Rev. **31** (1928) 691.

[83] E. Donth, J. Korus, E. Hempel, M. Beiner, Thermochim. Acta **304/305** (1997) 239.

[84] J. E. K. Schawe, E. Bergmann, Thermochim. Acta **304/305** (1997) 179.

[85] V. Calzona, M. Putti, A. S. Siri, Thermochim. Acta **162** (1990) 127.

[86] P. Sullivan, G. Seidel, Ann. Acad. Sci. Fennicae. **210** (1966) 58.

[87] H. Yao, H. Nagano, Y. Kawase, K. Ema, Biochimica et Biophysica Acta **1212** (1994) 73.

[88] R. B. Phelps, J. T. Birmingham, P. L. Richards, J. Low Temp. Phys. **92** (1993) 107.

[89] H. Tietje, M. V. Schickfus, E. Gmelin, Z. Phys. B. Con. Mat. **64** (1986) 95.

[90] F. L. A. Machado, W. G. Clark, Rev. Sci. Instrum. **59** (1988) 1176.

[91] S. M. Lee, S. I. Kwun, Rev. Sci. Instrum. **65** (1994) 966.

[92] A. A. Minakov, O. V. Ershov, Cryogenics **34** (1994) 461.

[93] M. Inoue, Y. Muneta, H. Negishi, M. Sasaki, J. Low Temp. Phys. **63** (1986) 374.

[94] G. H. J. Wantenaar, S. J. Campbell, D. H. Chaplin, G. V. H. Wilson, J. Phys. E: Sci. Instrum. **10** (1977) 825.

[95] R. Viswanathan, D. C. Johnston, J. Low Temp. Phys. **25** (1976) 1.

[96] J. Dutzi, W. Buckel, Z. Phys. B. Con. Mat. **55** (1984) 99.

[97] R. L. Greene, C. L. King, R. B. Zubeck, J. J. Hauser, Phys. Rev. B **6** (1972) 3297.

[98] A. Kishi, R. Kato, T. Azumi, H. Okamoto, Thermochim. Acta **133** (1988) 39.

[99] S. Imaizumi, K. Suzuki, I. Hatta, Rev. Sci. Instrum. **54** (1983) 1180.

[100] M. B. Salamon, R. P. Garnier, E. Buechler, J. Phys. Chem. Solids **35** (1974) 851.

[101] I. Hatta, R. Kato, A. Maesono, Jpn. J. Appl. Phys. **25** (1986) L493.

[102] I. Hatta, K. Sakakibara, J. Suzuki, H. Yao, Jpn. J. Appl. Phys. 1 **27** (1988) 2156.

[103] M. Yoshizawa, T. Fujirnura, T. Goto, K. I. Kamiyoshi, J. Phys. C. Solid State **16** (1983) 131.

[104] Y. Q. Gu, X. Tang, Y. Xu, I. Hatta, Jpn. J. Appl. Phys. 2 **32** (1993) L1365.

[105] A. A. Varchenko, Y. A. Kraftmakher, T. Y. Pinegina, Telpofiz. Vys. Temp. **16** (1978) 844.

[106] Y. A. Kraftmakher, High Temp. High Pressure **24** (1992) 433.

[107] R. K. Wunderlich, H. J. Fetch, R. Willnecker, Appl. Phys. Lett. **62** (1993) 3111.

[108] K. Ema, G. Nounesis, C. W. Garland, R. Shashidher, Phys. Rev. A **39** (1989) 2599.

[109] I. Hatta, Jpn. J. Appl. Phys. 2 **33** (1994) L686.

[110] R. H. Bruce, D. S. Cannell, Rev. Sci. Instrum. **47** (1976) 1323.

[111] M. Mertig, G. Pompe, E. Hegenbarth, Solid State Commun. **49** (1984) 369.

[112] G. S. Iannacchione, D. Finotello, Phys. Rev. Lett. **69** (1992) 2094.

[113] G. Nounesis, K. I. Blum, M. J. Young, C. W. Garland, R. Birgeneau, Phys. Rev. E **47** (1993) 1910.

[114] R. Vargas, A. J. Sanchez, Rev. Mex. Fis., **31** (1985) 663.

[115] C. C. Huang, J. M Viner, R. Pindak, J. W. Goodby, Phys. Rev. Lett. **46** (1981) 1289.

[116] P. Geraghty, M. Wixon, A. H. Francis, J. Appl. Phys. **55** (1984) 2780.

[117] W. Schnelle, E. Gmelin, Thermochim. Acta, **269/270** (1995) 27.

[118] J. Zimmermann, Cryogenics, **24** (1984) 27.

[119] M. T. Loponen, R. C. Dynes, V. Narayanamurti, J. Garno, Phys. Rev. B **25** (1982) 1161.

[120] M. Meissner, K. Spitzmann, Phys. Rev. Lett. **46** (1981) 265.

[121] R. E. Schwall, R. E. Howard, G. R. Stewart, Rev. Sci. Instrum. **46** (1975) 1043.

[122] I. Hatta, W. Rehwald, J. Phys. C. Solid State **10** (1977) 2075.

[123] K. Ema, K. Hamano, K. Kurihara, I. Hatta, J. Phys. Soc. Jpn. **43** (1977) 1954.

[124] P. R. Garnier, Phys. Lett. A **35** (1971) 413.

[125] D. N. Bittner, M. Bretz, Phys. Rev. B **31** (1985) 1060.

[126] W. Statius, J. R. Dillinger, D. L. Huber, AIP Conf. Proc. **10** (1973) 1029.

[127] J. Vanderdeelen, L. Baert, Meded Fac Landbouwwet, Rijksuniv., Gent **40** (1975) 1427.

[128] K. Tashiro, N. Ozawa, K. Sugihara, T. Tsuzuku, J. Phys. Soc. Jpn. **59** (1990) 4022.

[129] O. S. Tanasijczuk, T. Oja, Rev. Sci. Instrum. **49** (1978) 1545.

[130] A. Hensel, J. Dobbertin, J. E. K. Schawe, A. Boller, C. Schick, J. Therm. Anal. **46** (1996) 935.

[131] O. L. Mayorga, A. N. Rascon, E. Freire, Thermochim. Acta **238** (1994) 309.

[132] A. Schilling, O. Jeandupeux, Phys. Rev. B **52** (1995) 9714.

[133] R. W. Willekers, H. C. Meijer, F. Mathu, H. Postman, Cryogenics **31** (1991) 168.

[134] M. Maszkiewicz, Phys. Status Solid. A **47** (1978) K77.

[135] G. Sanchez, M. Meichle, C. W. Garland, Phys. Rev. A **28** (1983) 1647.

[136] H. T. Shang, C. C. Huang, M. B. Salamon, J. Appl. Phys. **49** (1978) 3.

[137] N. Polandou, V. A. Chernenko, K. Novik, High Temp. High Pressure **13** (1981) 399.

[138] E. D. Yakushkin, V. N. Anisimova, Instruments and Experimental Techniques **36** (1993) 492.

[139] G. Tannacchione, A. Strigazzi, D. Finotello, Liquid Crystals **14** (1993) 1153.

[140] G. Yang, A. D. Migone, K. W. Johnson, Rev. Sci. Instrum. **62** (1991) 1836.

[141] A. A. Varchenko, Y. A. Kraftmakher, Phys. Status Solid. A **20** (1973) 387.

[142] N. Ohsawa, N. Tatan, S. Uchiyama, Jpn. J. Appl. Phys. **17** (1979) 1059.

[143] J. E Smaardyk, Rev. Sci. Instrum. **49** (1978) 988.

[144] H. T. Shang, M. B. Salamon, Phys. Rev. B **22** (1980) 4401.

[145] J. D. Legrange, J. M. Mochel, Phys. Rev. A **23** (1981) 3215.

[146] P. Garoche, W. L. Johnson, Solid State Commun. **39** (1981) 403.

[147] K. Ema, Ferroelectrics **168** (1995) 147.

[148] M. Ivanda, D. Djurek, J. Phys. E. Sci. Instrum. **22** (1989) 988.

[149] C. C. Huang, J. M. Viner, J. C. Novac, Rev. Sci. Instrum. **56** (1985) 1390.

[150] D. H. Howling, E. Mendoza, J. E. Zimmermann, Proc. Roy. Soc. London Ser. A **229** (1955) 86.

[151] T. Tamane, S. I. Katayama, M. Todoki, Rev. Sci. Instrum. **66** (1995) 5305.

[152] A. Maesono, R. Kato, I. Hatta, R. P. Tye, Therm. Conduct. **22** (1994) 473.

[153] N. O. Birge, S. R. Nagel, Phys. Rev. Lett. **54** (1985) 2674.

[154] J. K. Wang, J. H. Campbell, D. C. Tsui, A. Y. Cho, Phys. Rev. B **38** (1988) 6174.

[155] S. Imaizumi, K. Tsuchida, T. Matsuda, I. Hatta, Suzuka, Kogyo Koto Semmon Gahho Kiyo **13** (1980) 197.

[156] Hui Xu, Peggy Cebe, Thermochim. Acta **442** (2006) 42-47.

[157] M. Pyda, E. Nowak-Pyda, B. Wunderlich, Thermochim. Acta **442** (2006)35-41.

[158] M. Pyda, Y.K. Kwon, B. Wunderlich, Thermochim. Acta **367-368** (2001)217.

[159] Y.K. Kwon, R. Androsch, M. Pyda, B. Wunderlich, Thermochim. Acta **367/**

368 (2001)203.

[160] C. C. Huang, A. M. Goldman, L. E. Toth, Solid State Commun. **33** (1980) 581.

[161] B. C. Gibson, D. C. Ginsberg, C. P. L. Tai, Phys. Rev. B **19** (1979) 1409.

[162] B. Schenker, F. Stager, Thermochim. Acta **304/305** (1997) 219.

[163] B. Wunderlich, Thermochim. Acta **355**(2000) 43.

[164] N. O. Birge, P. K. Dixon, N. Menon, Thermochim. Acta **304/305** (1997) 51.

[165] A. A. Lacey, C. Nikolopoulos, M. Reading, J. Therm. Anal. **50** (1997) 279.

[166] TA Inc. *TA2920 Temperature Modulated DSC manual*, 1996, p.C-21.

[167] T. Ozawa, K. Kanari, Thermochim. Acta **288** (1996) 39.

[168] I. Hatta, N. Katayama, J. Therm. Anal. **54** (1998) 577.

[169] T. Ozawa, K. Kanari, J. Therm. Anal. **54** (1998) 521.

[170] I. Hatta, Thermochim. Acta **330** (1999) 39.

[171] M. Merzlyakov, C. Scick, Thermochim. Acta **330** (1999) 65.

[172] R. Scherrenberg, V. Mathot, P. Steeman, J. Therm. Anal. **54** (1998) 477.

[173] R. Scherrenberg, V. Mathot, A. V. Hemelrijk, Thermochim. Acta **330** (1999)3.

[174] Laider, Keith, J. *The World of Physical Chemistry*. Oxford University Press, New York, 1993.

[175] *CRC Handbook of Chemistry and Physics*, 58th Edition, CRC Press, Cleveland, Ohio, 1977.

[176] C. J. Martin, J. C. Seferis, J. Therm. Anal. **54** (1998) 501.

[177] F. U. Buehler, J. C. Seferis, Thermochim. Acta **334** (1999) 49.

[178] S. R. Aubuchon, P. S. Gill, J. Therm. Anal. **49** (1997) 1039.

[179] P. S. Gill, W. R. Sauerbrum, M. Reading, J. Therm. Anal. **40** (1993) 931.

[180] J. E. K. Schawe, G. W. H. Hohne, Thermochim. Acta **287** (1996) 312.

[181] J. E. K. Schawe, G. W. H. Hohne, J. Therm. Anal. **46** (1996) 893.

[182] I. Alig, Thermochim. Acta **304/305** (1997) 35.

[183] G. W. H. Hohne, Thermochim. Acta **304/305** (1997) 121.

[184] H. Baur, B. Wunderlich, J. Therm. Anal. **54** (1998) 437.

[185] M. Reading, R. Luyt, J. Therm. Anal. **54** (1998) 535.

[186] S. Weyer, A. Hensel, C. Schick, Thermochim. Acta **304/305** (1997) 267.

[187] A. Hensel, C. Schick, Thermochim. Acta **304/305** (1997) 229.

[188] M. Nishikawa, Y. Saruyama, Thermochim. Acta **267** (1995) 75.

[189] T. Ozawa, K. Kanari, Thermochim. Acta **338** (1999) 7.

[190] M. A. Pouchon, C. Degueldre, P. Tissot, Thermochim. Acta **323** (1998) 109.

[191] S. R. Aubuchon, R. L. Blaine, Therm. Conduct. **23** (1996) 66.

[192] S. M. Marcus, R. L. Blaine, Therm. Conduct. **22** (1994) 826.

[193] P. Kamasa, P. Myslinski, M. Pyda, Thermochim. Acta **442** (2006)48-51.

[194] P. Kamasa, P. Myslinski, M. Pyda, Thermochim. Acta **433** (2005)99.

Chapter 2 Sample Mass, Modulation Parameters vs. Observed Specific Heat, and Numerical Simulation of TMDSC with an R-C Network

2.1 Introduction

Shortly after its introduction in the late twentieth century, TMDSC device became commercially available. Today, TMDSC is widely used in many fields of materials research, which covered polymer, food, pharmaceutical, and metallic materials [1—3]. Although both the conventional DSC and TMDSC can be applied to the measurement of specific heat, their experimental procedure and data processing algorithms are quite different.

Normally, the thermal inertia of the heat transfer path, the heat exchanges between the heating block and the sample by purge gas convection, and thermal radiation of the sample are ignored in a TMDSC device. If there is no kinetic event and the temperature gradient in the sample is negligible, it can be shown that the heat capacity of the sample C_s is [3]

$$C_s = \frac{A_{\Delta T} K}{A_{Ts}\omega}\sqrt{1+\left(\frac{\omega C_r}{K}\right)^2}\,, \tag{2.1}$$

where $A_{\Delta T}$ is the amplitude of the temperature difference between the sample and reference, A_{Ts} is the amplitude of the sample temperature, C_r is the heat capacity of the reference, and ω is the angular frequency of temperature modulation. The apparent heat capacity of the sample, C_{s_m}', on the other hand, is given by [3]

$$C_{s\_m}' = \frac{K A_{\Delta T}}{A_{Ts}\omega}\,. \tag{2.2}$$

In Eq. (2.2), $KA_{\Delta T}$ is the amplitude of modulated heat flow. The difference between Eq. (2.1) and Eq. (2.2) is that in Eq. (2.1), there is a TMDSC device-related factor, $\sqrt{1+(\omega C_r / K)^2}$, which is defined as K_{Cp}. K_{Cp} can be obtained by a calibration process using a standard reference with a well known and stable heat capacity, such as sapphire. This calibration factor can then be used to correct the apparent heat capacity of the sample, C_{s_m}'. That is, C_s should be equal to $K_{Cp}C_{s\_m}'$. Dividing this value by the sample mass, m_s, the specific heat is obtained as $c_p = K_{Cp}C_{s\_m}'/m_s$.

According to Eqs. (2.1) and (2.2), the measured specific heat should be independent of the sample mass. As long as K, C_r, ω, $A_{\Delta T}$, and A_{Ts} are known, the heat capacity and hence the specific heat of the sample can be accurately calculated. However, early experiments suggested that the measured specific heat is not only dependent on the sample mass but also on the modulation frequency [2—6]. This is still the case even if the measured value has been corrected with the calibration factor K_{Cp}, which is obtained from a standard reference under exactly the same modulation conditions. These deviations can partly be attributed to the existence of thermal gradient in the sample [2, 4—6]. Merzlyakov and Schick [7] investigated power compensation TMDSC and found that the measured heat capacity varied when the temperature sensor was placed at different positions, and that the calibration factor was a very complicated function of the thermal properties of the sample.

In this chapter, a thermal resistance-capacitance (R-C) network model is used to study the effect of heat transfer of the TMDSC device and experimental parameters on the c_p measurement. In section 2.2, I will study the thermal resistance of contact between the sample and support through the observation of the melting of indium samples. An R-C network model of TMDSC with contact resistance in consideration is discussed. The thermal conducting equations are derived and experimental

conditions are given. The effects of sample mass, temperature modulation period and modulation amplitude on the measurement of sample specific heat are illustrated in section 2.3. The differences in the measurement of specific heat between conventional DSC and TMDSC are compared in section 2.4.

2.2 Modeling and experiments of TMDSC

To explain the effects of sample mass and modulation period on the measurement of specific heat, factors such as the heat transfer of the measuring cell need to be taken into account in the modeling of TMDSC. A TA Instruments DSC&TMDSC2920 device was used in the following experiments. This device can work in either DSC or TMDSC mode, depending on the different temperature control programs, and has a temperature modulation period ranging from 10 to 100 s. Pure argon was used as the cell purge gas. The melting process of an indium sample in the conventional DSC was used to evaluate the properties of the heat transfer path, and it was assumed that the thermal gradient in the sample is negligible.

2.2.1 Indium melting experiment in the conventional DSC

Fig. 2.1 shows the heat flow and the sample temperature as a function of time for a pure indium sample with a mass of 15.50 mg at a heating rate of 10 K/min in the DSC mode. Since the melting starts at a single temperature, melting temperature should remain constant when it begins, which should generate a plateau in the temperature curve.

However, if we take any two points on the straight portion on the temperature curve during the melting: A (161^{o}C) and B (163^{o}C), for example, we may notice that between A and B, the measured temperature is still rising although the real sample temperature remains constant (see Fig. 2.1).

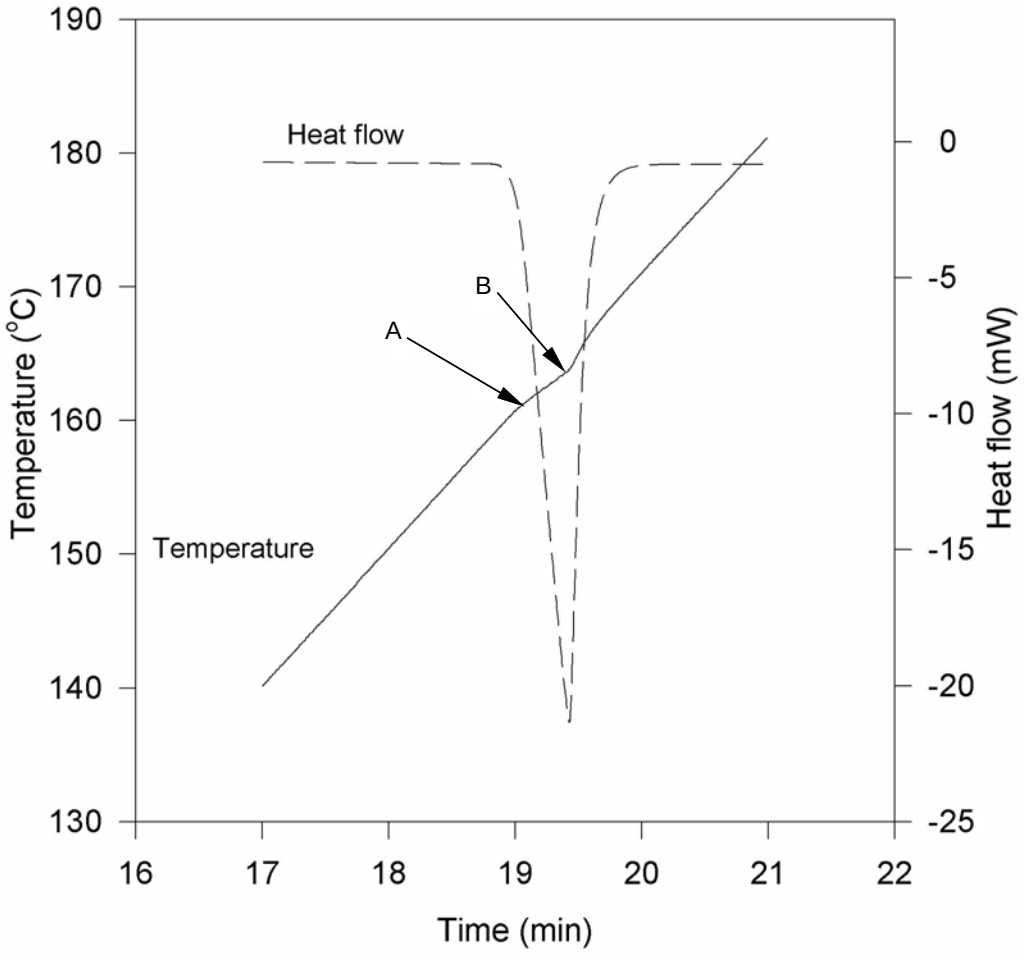

Fig. 2.1 An indium melting curve in conventional DSC. Sample mass: 15.50 mg.

The reason is, in a heat flux type DSC&TMDSC cell (see Fig. 2.2), the thermal couples are located beneath the sample and reference supporting plate which is made of a (constantan) disk. The indicated temperature by the thermal couple is therefore not the real temperature of the sample but the temperature at the point where the thermal couple is located. As the heating block temperature is still rising, between A and B the measured temperature keeps increasing as well. After point B, the rate of temperature increase quickly resumes the programmed value, 10 K/min.

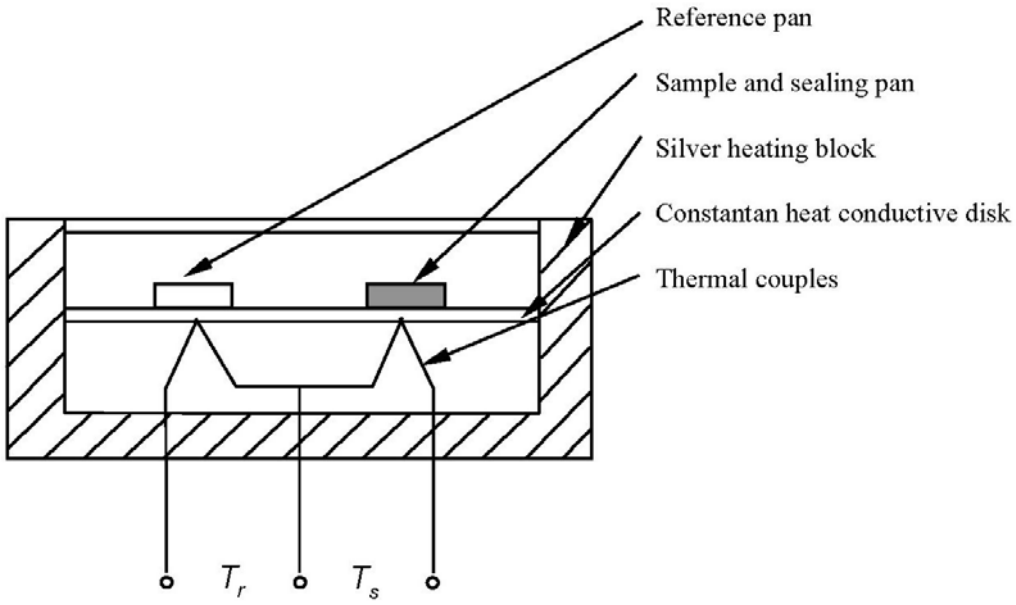

Fig. 2.2 A simplified TMDSC and DSC cell structure

Fig. 2.3 plots the measured rate of temperature increase between A and B as a function of the programmed heating rate. It shows that the rate of temperature increase between A and B is significant under various programmed heating rates ranging from 1 to 40 K/min. There is a good linear relationship between them: The measured rate of temperature increase between A and B is about 70% of the programmed heating rate. Considering the fact that the real sample temperature is constant, this temperature rise is not trivial. As a result, it is reasonable to conclude that considerable contact resistance exists between the thermal couple and the sample itself.

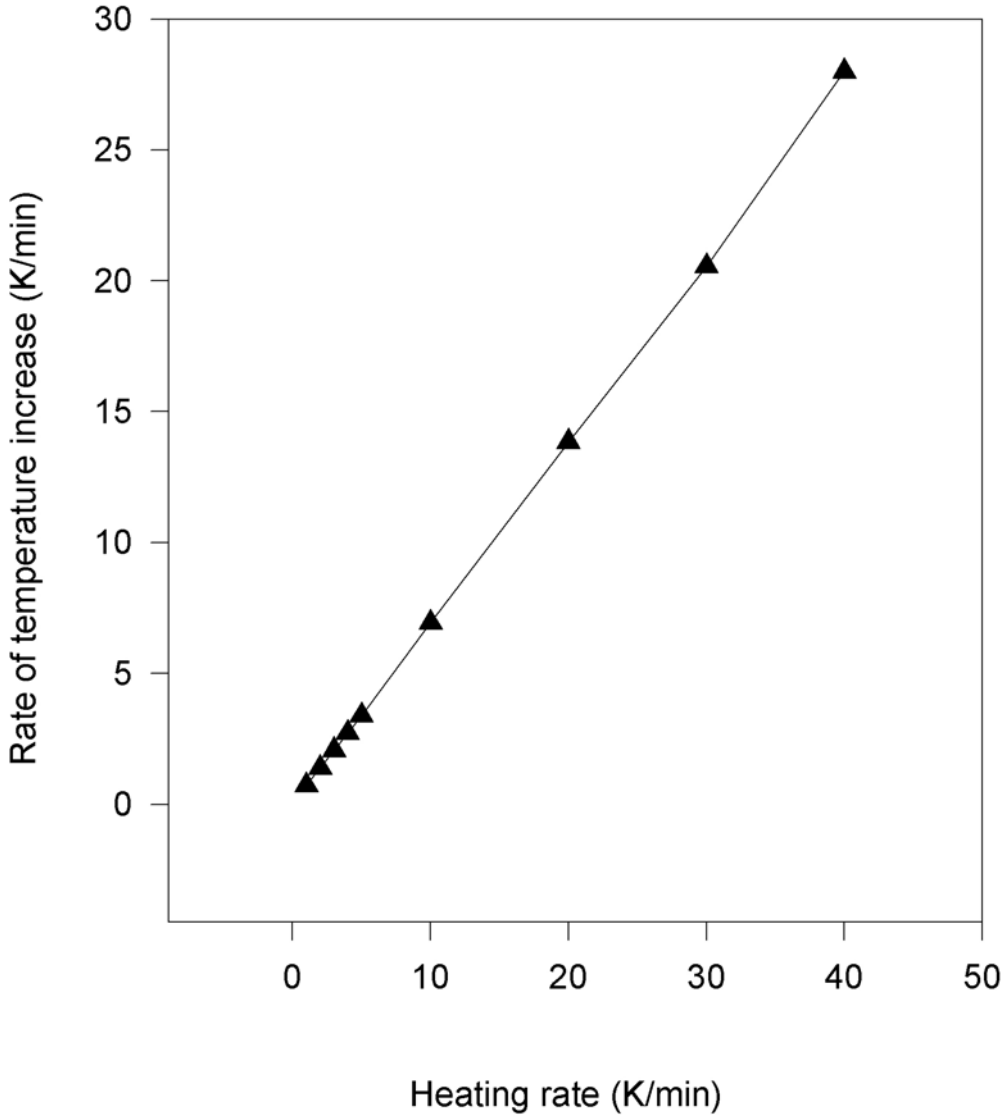

Fig. 2.3 Rate of temperature increase on the sample side between points A and B (see Fig.2.1) as a function of DSC heating rate, exhibiting a good linear relationship between them

2.2.2 A resistance-capacitance network model that takes into account the contact resistance

As has been discussed earlier, heat transfer problems in TMDSC can be analyzed with an equivalent resistance-capacitance (R-C) network (see Fig. 1.12). Similarly, Fig. 2.4 shows an R-C network model with the contact resistance between the sample and the thermal couple in consideration. The thermal resistance and heat

capacity of the heat transfer path of the TMDSC cell are taken into account as well.

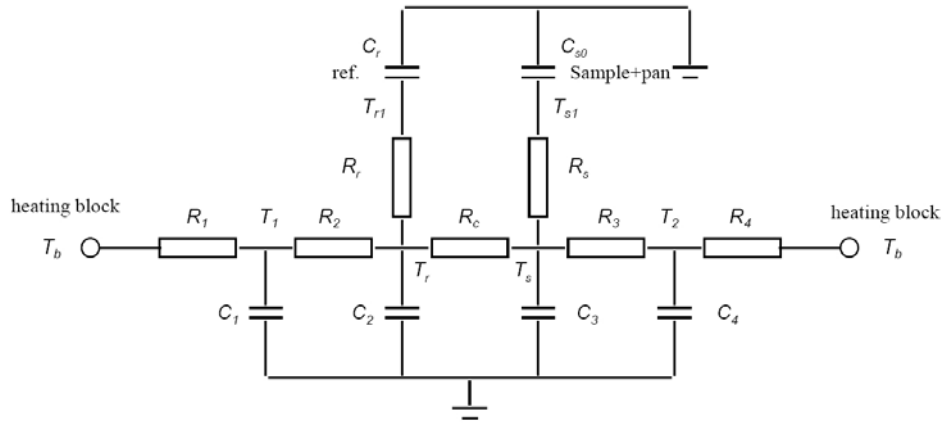

Fig. 2.4 A TMDSC (also a DSC) model represented with thermal resister and capacitor (R-C) network

We can obtain the following thermal conducting equations according to Newton's law of cooling for the nodes in the model:

$$\frac{T_b - T_1}{R_1} = \frac{T_1 - T_r}{R_2} + C_1\left(\frac{dT_1}{dt}\right), \tag{2.3}$$

$$\frac{T_b - T_2}{R_4} = \frac{T_2 - T_s}{R_3} + C_4\left(\frac{dT_2}{dt}\right), \tag{2.4}$$

$$\frac{T_1 - T_r}{R_2} = \frac{T_r - T_s}{R_c} + \frac{T_r - T_{r1}}{R_r} + C_2\left(\frac{dT_r}{dt}\right), \tag{2.5}$$

$$\frac{T_2 - T_s}{R_3} = \frac{T_s - T_r}{R_c} + \frac{T_s - T_{s1}}{R_s} + C_3\left(\frac{dT_s}{dt}\right), \tag{2.6}$$

$$\frac{T_r - T_{r1}}{R_r} = C_r\left(\frac{dT_{r1}}{dt}\right), \tag{2.7}$$

$$\frac{T_s - T_{s1}}{R_s} = C_{s0}\left(\frac{dT_{s1}}{dt}\right), \tag{2.8}$$

where R_1 to R_4 are the thermal resistances of the heat conducting path which is the constantan disk; R_r and R_s are the thermal resistances between the thermal couples

and the reference or sample, respectively; C_1 to C_4 are the heat capacities of the heat conducting path of the TMDSC cell; C_{s0} is the total heat capacity of the sample and the sealing pan; T_b is the temperature of the heating block; T_r is the temperature of the thermal couple on the reference side; T_{r1} is the real temperature of the reference; T_s is the temperature of the thermal couple on the sample side, and T_{s1} is real temperature of the sample.

Finite difference method (FDM) is applied to solve Eqs. (2.3) to (2.8) with a time step of 0.0001 s. The values of physical properties used are given in Table 2.1. A TMDSC cell that has no biased heat flow was assumed. Because it is difficult to obtain the actual heat transfer parameters of the cell, for simplicity, it is assumed that $R_1=R_2=R_3=R_4$, $R_r=R_s$, and $C_1=C_2=C_3=C_4$.

Table 2.1 Parameters of TMDSC simulation

Parameters	Description	**Value**
R_1, R_2, R_3 and R_4	Thermal resistance of heat conducting path(in K/W)	40
R_s , R_r	Thermal resistance between thermal couple and pan (in K/W)	70
C_1, C_2, C_3 and C_4	Heat capacities of the heat conducting path (in J/K)	0.01
T_0	Initial temperature (in K)	400
A	Modulation amplitude (in K)	1
Δt	Time step for Finite difference calculations (in s)	0.0001
Period	Temperature modulation period (in s)	30 to 100
C_r	Heat capacity of aluminum reference (in J/K)	0.0228

2.2.3 TMDSC experimental conditions for the measurement of specific heat

A sapphire disk with a diameter of 5 mm and a mass of 18.25 mg was used as the TMDSC calibration reference sample. The reference sample was sealed in an

aluminum pan. Five copper samples (purity>99.99%) with masses between 4.45 mg and 65.61 mg were used in the measurement of specific heat. Each of the copper samples was also sealed in an aluminum pan and flattened to ensure good thermal contact with the supporting plate. Copper was selected as the test material because of its high thermal conductivity so as to reduce the effect of temperature gradient, its thermal stability in the temperature range studied and the well-defined specific heat. The measurements were conducted at a constant temperature of 400 K with a modulation amplitude of 1 K and modulation periods of 30 to 100 s. Each aluminum sample pan was carefully selected so that its weight matched that of the aluminum reference pan within a difference of 0.1 mg. For comparison, measurements of specific heat of pure aluminum samples with masses between 5.68 mg and 51.10 mg were also carried out under the same conditions as those of the copper samples.

2.3 Results and discussion

In this section, we discuss the effects of experiment conditions such as sample mass, modulation amplitude and period on the measured specific heat and approaches to improving the accuracy of the measurement. Fig. 2.5 shows results from the simulation of the "real" sample temperature and reference temperature T_{s1}, T_{r1}, as well as the "measured" sample temperature and reference temperature T_s, T_r from simulation respectively. It is noted that there exist differences both in the temperature amplitude and phase angle between the "measured" and "real" temperatures. Since only the "measured" temperatures rather than the real temperatures are used to derive the specific heat, errors can develop in the measurement as a result.

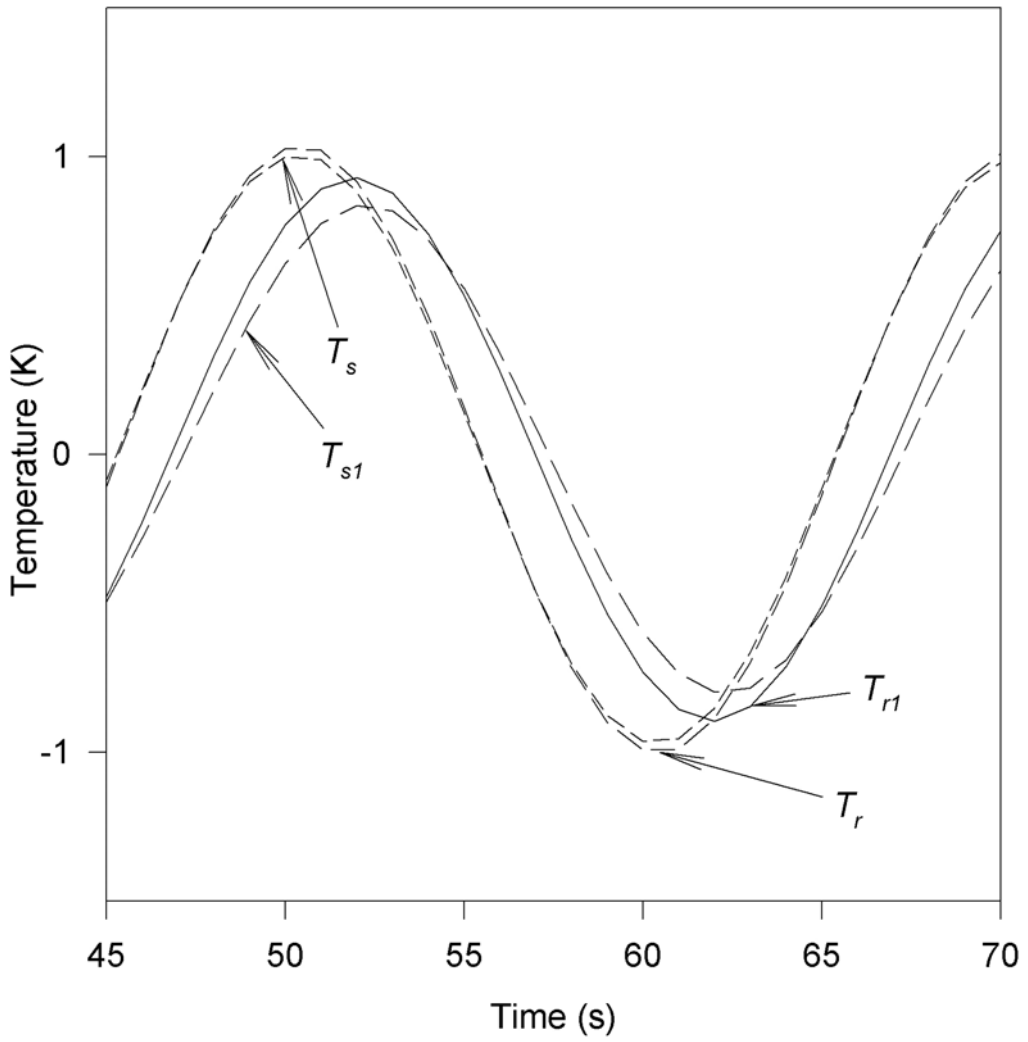

Fig. 2.5 The "real" sample and reference temperatures T_{s1}, T_{r1} vs. the "measured" sample and reference temperatures, T_s, T_r . Simulation conditions: M_s=20 mg, temperature modulation period=20 s

2.3.1 The effect of the sample mass

The results of specific heat obtained for the copper samples under various modulation periods both by the simulations and by the experiments are shown in Figs. 2.6 and 2.7, respectively. For each modulation period, a calibration factor was obtained with a sapphire sample of 18.25 mg. In the computer simulations, the "calibration factor" was determined by a "virtual" run of the sapphire sample in the TMDSC model; while in the experiments, it was obtained from the experimental data

directly. The ratio between the specific heat given in the literature and the measured specific heat is the calibration factor.

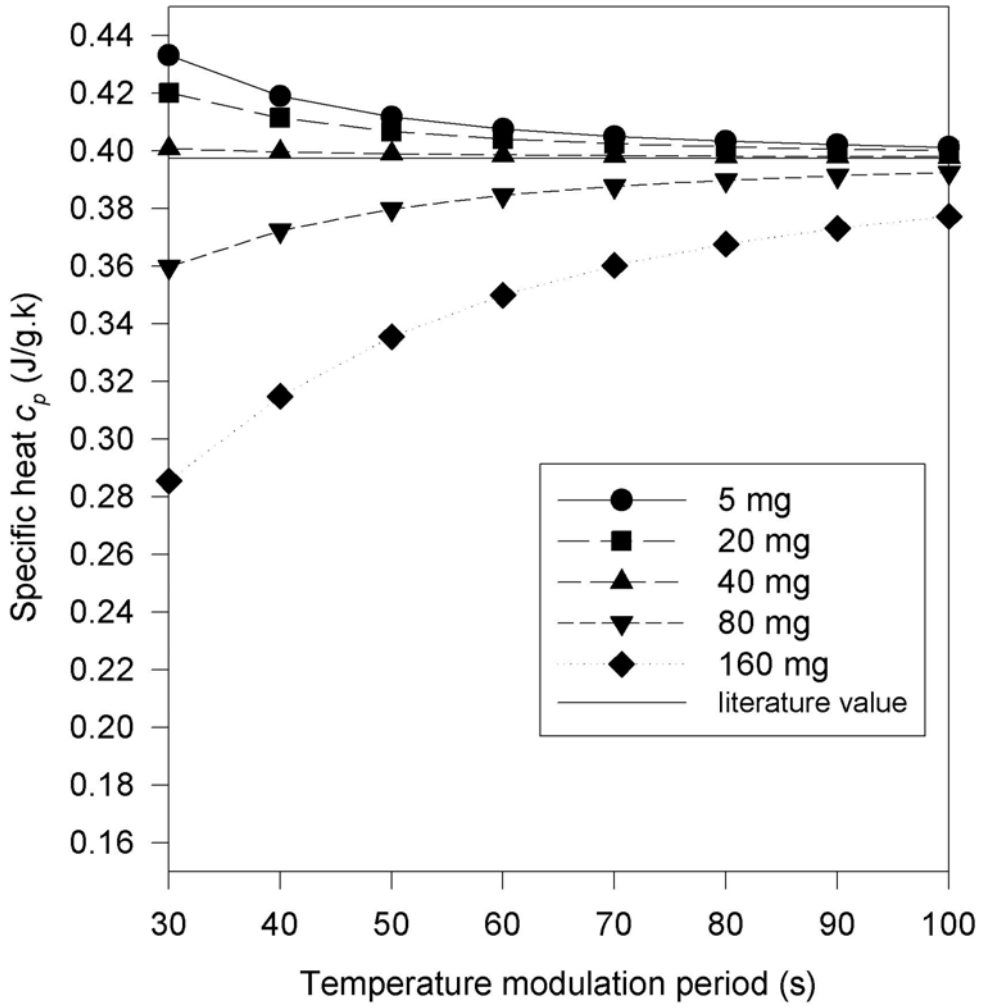

Fig. 2.6 Effect of sample mass and temperature modulation period on the measured specific heat of copper (calibration factor Kc_p has been taken into account) by computer simulation

Fig. 2.6 indicates that a small sample mass does not necessarily produce accurate measurement results. If the mass is too small, as in the cases with the samples of 5 mg and 20 mg, the specific heat (c_p) by simulation is larger than that from the literature: 0.3975 J/g·K at 400 K for copper [8]. The specific heat of the sample of 40 mg shows the most stable results over the entire range of modulation

period in this study: its c_p exhibits only a slightly decreasing trend as the modulation period increases from 30 to 100 s. If the sample mass is too large, the c_p obtained is always smaller than 0.3975 J/g·K, as demonstrated by the c_p of the samples of 80 mg and 160 mg, respectively.

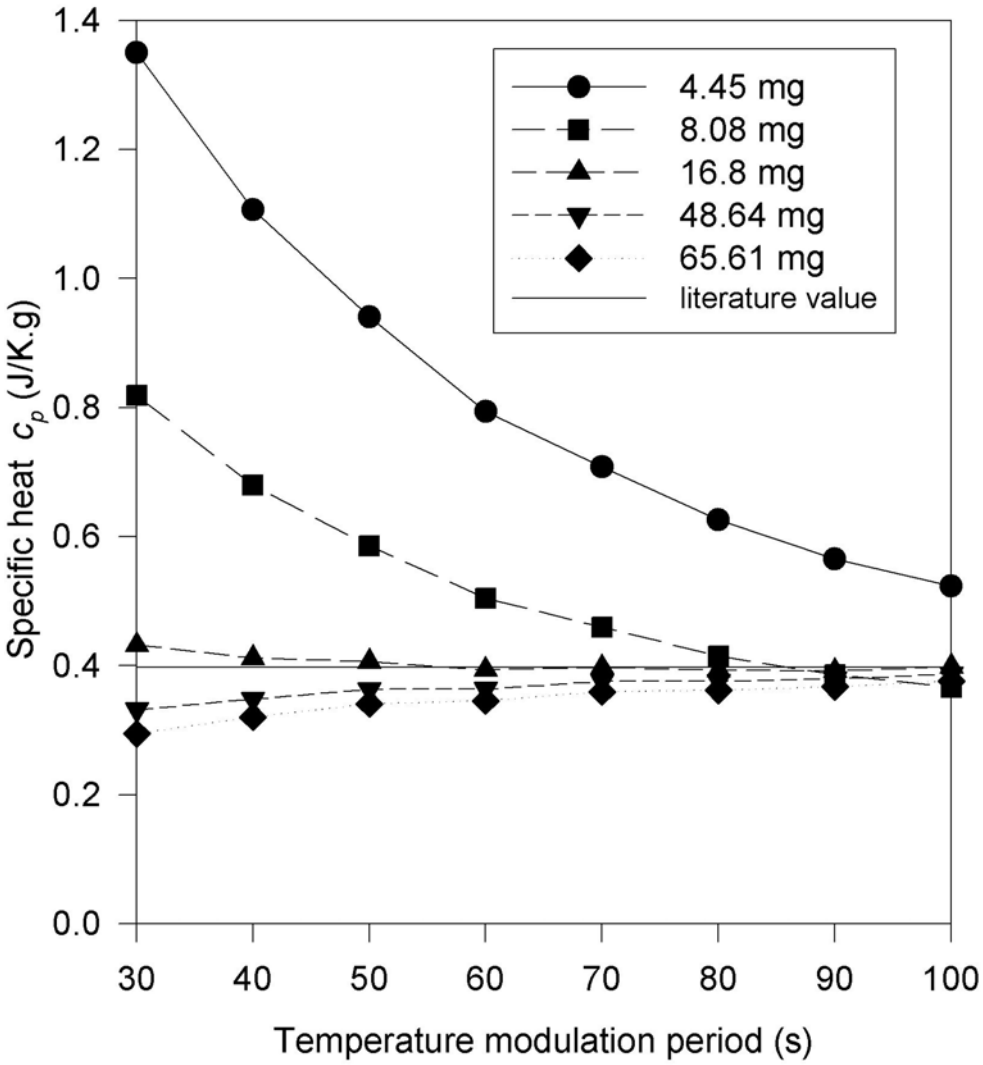

Fig. 2.7 Effect of sample mass and temperature modulation period on the measured specific heat of pure copper (calibration factor Kc_p has been taken into account)

Compared with the simulation results shown in Fig. 2.6, the experimental results are slightly complicated. Fig. 2.7 shows the relationship between the c_p of copper and modulation period obtained by the experiments. The c_p of samples with masses of 4.45 mg and 8.08 mg decreases significantly as the modulation period increases. The c_p of the sample of 16.80 mg drops slightly, while the c_p of the other samples increases when the period increases from 30 to 100 s. The c_p of the sample of 8.08 mg drops below that of the 65.61 mg when the modulation period reaches 100 s. This drop in c_p could be a result of TMDSC cell bias and purge gas convection, which are not taken into consideration in the simulations. Yet, the relationship between the c_p and modulation period is still quite similar to that of the simulations: The specific heat measured by TMDSC is indeed mass-sensitive. The sample mass should not be too small as it results in higher c_p. On the other hand, the sample mass should not be too large either, which produces c_p smaller than that of the literature, even after calibration factors are taken into account.

As shown in Fig. 2.6, between the small samples that yield higher c_p and the large samples, which produce smaller c_p, there seems to be an optimal sample mass, which has a measured c_p that is equal to the literature value. Simulation results (Fig. 2.6) indicate that only when the heat capacity of the sample C_s equals that of the calibration sapphire reference, the measured specific heat will be exactly the same as the actual value regardless of the modulation period. Because the internal thermal gradient of the sample or reference is ignored by the model (see Fig. 2.4), hence the sample and reference can be treated as a single point. The temperature signal from the thermal couple is affected by the heat capacity (C_s) which is a product of the mass and specific heat (c_p) of the sample rather than the specific heat alone. As long as the heat capacity of the sample is the same as that of the sapphire reference, the measured

temperatures for both the sapphire and the sample will be the same under the same experimental conditions. If their heat capacities are different, then the calibration factor, Kc_p, obtained from the sapphire reference cannot completely correct the errors in the measurement of specific heat of another sample. To be more specific, if the heat capacity of the sample is lower than that of the sapphire reference, the measured specific heat, c_p, will be larger than the actual specific heat. However, if the heat capacity of the sample is higher than that of the sapphire reference, the measured specific heat c_p will be lower. This deviation depends largely on the thermal properties of the TMDSC device, such as the thermal resistance and heat capacities of all the heat conducting paths. The heat capacities of the five copper samples with masses of 5, 20, 40, 80, and 160 mg are 0.002, 0.00795, 0.0159, 0.0318, and 0.0636 J/K, respectively. The heat capacity of the sapphire calibration reference with a mass of 18.25 mg, denoted as $C_{s\_calibration}$, is 0.0172 J/K as the specific heat of sapphire is 0.9423 J/g·K at 400 K [9]. 0.0172 J/K is closest to the heat capacity of the copper sample of 40 mg which is 0.0159 J/K. Therefore, the most stable and accurate c_p is obtained from the sample with a mass of 40 mg.

Experimental results show similar trend with that of the simulations. As shown in Fig. 2.7, it can be seen that the optimal copper sample mass should be somewhere between 16.80 mg and 48.34 mg in order to obtain the most stable specific heat, which is least dependent on the modulation period. Fig. 2.8 shows the effect of the modulation period on the measured c_p of pure aluminum obtained from experiments. It is found that the most favorable sample mass falls between 14.16 mg and 19.31 mg. The optimal mass obtained from simulation is $C_{s\_calibration}/c_{p\_Al}$ =18.1 mg, where c_{p_Al} is the specific heat of aluminum, this agrees well with that of experiment.

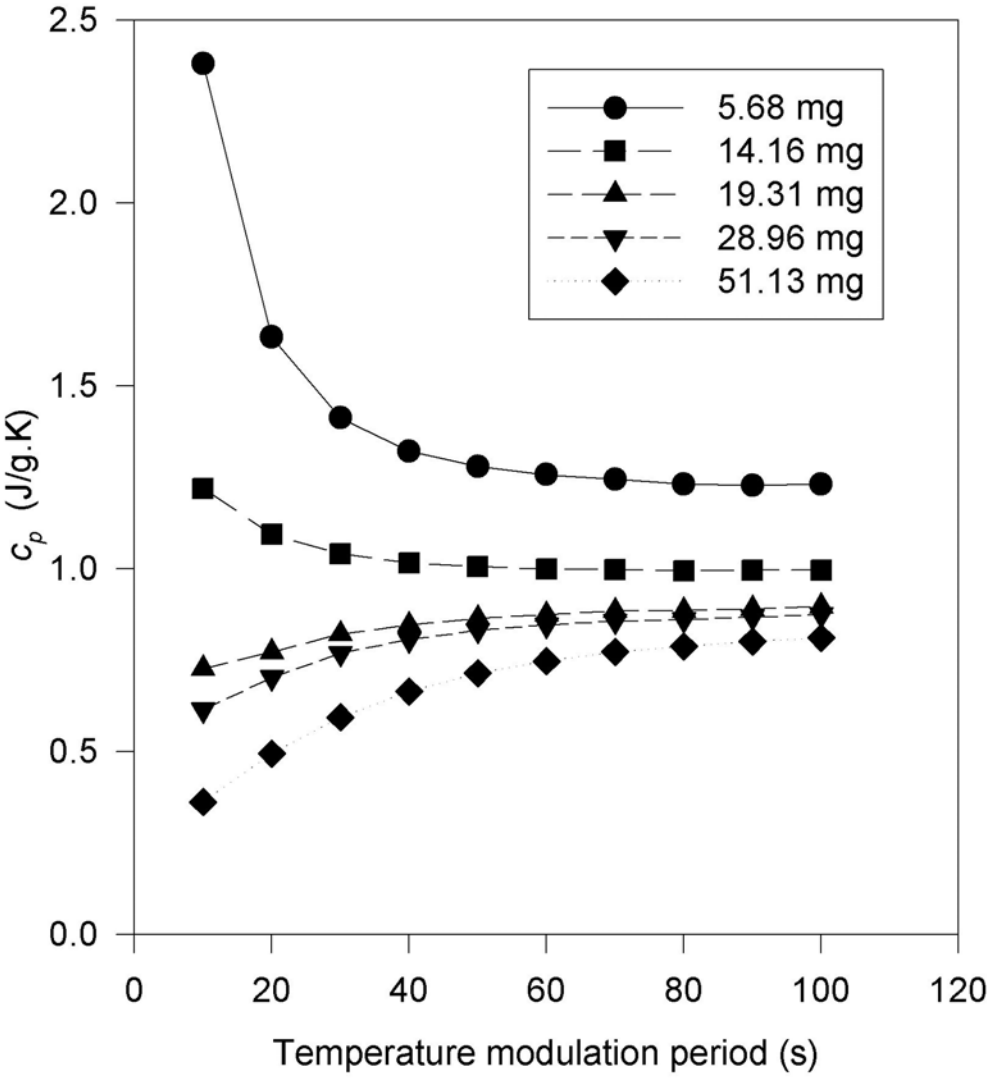

Fig. 2.8 Effect of sample mass and temperature modulation period on the measured specific heat of pure Al (calibration factor Kc_p has been taken into account)

2.3.2 TMDSC system output characteristics

From a systematical point of view, we can treat the TMDSC system as a black box (a commonly used term in system analysis) without considering the details of its internal structure. Treating the temperature modulation frequency as an input, and the ratio between the measured heat capacity and actual heat capacity ($C_{s\_m}'/C_s = 1/Kc_p$) as the output, one can plot the relationship between the input and output in Fig. 2.9.

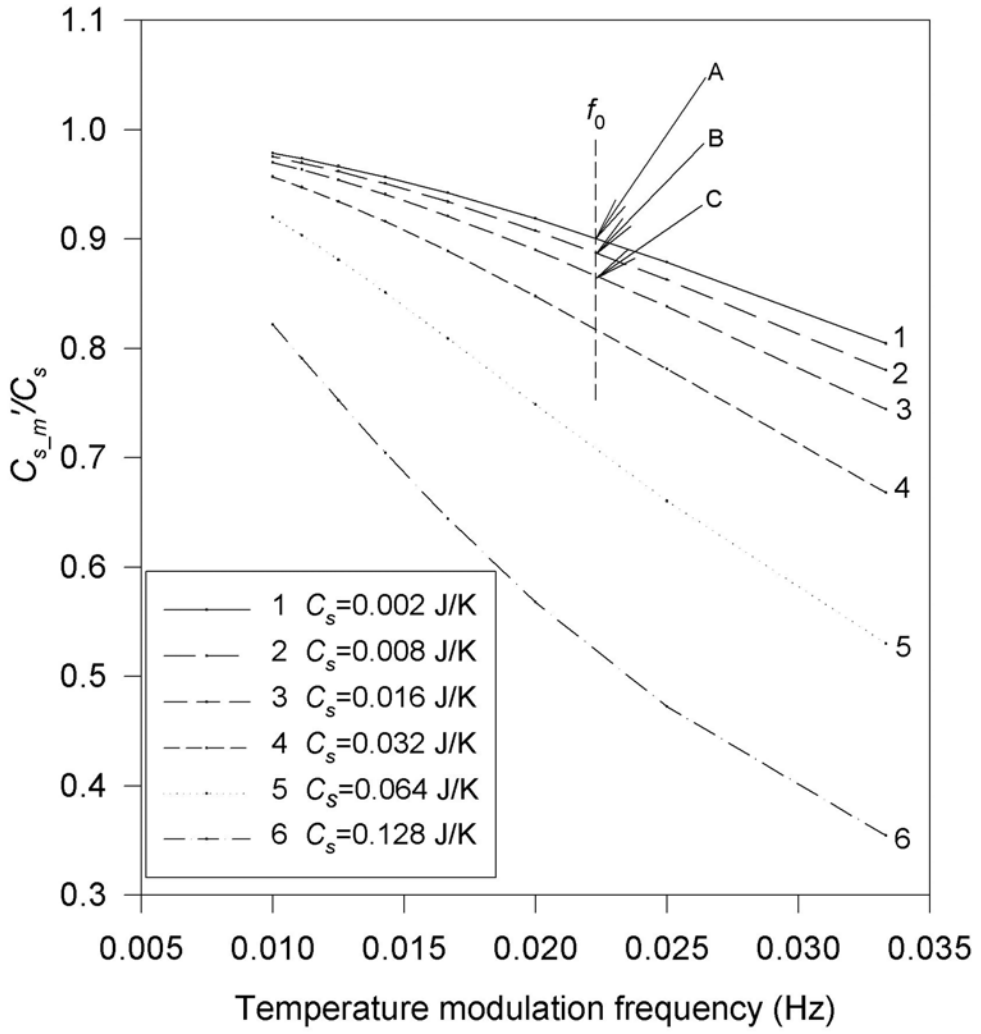

Fig. 2.9 Simulated TMDSC output characteristics as a function of the temperature modulation frequency and the heat capacity of the sample

As can be seen clearly, samples with different heat capacities follow different characteristic curves. The larger the heat capacity of the sample, the lower the characteristic curve we obtain. These curves remind us of a typical low pass filter in a "thermal version". Suppose the sapphire reference used for calibration has a heat capacity of $C_{s\_calibration}$ = 0.008 J/K, its characteristic curve will follow curve 2. At any given modulation frequency, f_0 =0.022 Hz, for example, the C_{s_m}'/C_s value is

determined by point B. This calibration factor is denoted as K_{Cp_B}. Then there are three possible situations for the sample to be measured:

(1) If $C_s < C_{s\_calibration}$, for example, C_s = 0.002 J/K, the characteristic curve follows curve 1 and the calibration factor is K_{Cp_A}. Apparently, $K_{Cp\_B} > K_{Cp\_A}$. If K_{Cp_B} is used to correct the measured specific heat, the result will be larger than the actual value.

(2) If $C_s = C_{s\_calibration}$, for example, C_s = 0.008 J/K, the characteristic curve follows curve 2 and the calibration factor is K_{Cp_B} , which is the same as that of the calibration reference. Then the measured result will be the same as the actual value.

(3) If $C_s > C_{s\_calibration}$, say, C_s = 0.016 J/K, the characteristic curve follows curve 3 and the calibration factor is K_{Cp_C}. In this case, $K_{Cp\_B} < K_{Cp\_C}$. If K_{Cp_B} is used to correct the measured specific heat, the result will be lower than the actual value.

From the above analysis, we can draw a conclusion that the error in the measured heat capacity of the sample can be eliminated if $C_s = C_{s\_calibration}$. However, the heat capacity, C_s, of the to-be-tested sample is not known beforehand, so this condition ($C_s = C_{s\_calibration}$) cannot be met. Before a TMDSC experiment is carried out, if the specific heat of that sample is known to be in a certain range, then it is at least possible to select a mass so that its heat capacity is close to that of the calibration reference. Although still not perfect, this may reduce the error in the measured heat capacity than if the sample mass is just randomly selected. For instance, as a general guide line, at room temperature, many metals have a specific heat close to 3R, where R is the gas constant, thus the optimal sample mass should be around $C_{s\_calibration}$/3R. As a result, for a sapphire calibration reference with a mass of 20 mg, we may use a

sample of ~20 mg for aluminum-based materials or ~45 mg for copper-based ones. Alternatively, samples with different masses can be tested on the TMDSC to obtain the "specific heat-modulation period" curves, and a more accurate result can be interpolated or extrapolated from these curves, since all the curves converge as shown in Fig. 2.6.

The contact resistance between the sample and the support or the reference plays an important role in TMDSC since it makes the measured c_p sensitive to the sample mass. Ozawa and Kanari [10] also used an R-C network model to analyze heat capacity measurement in TMDSC without taking the contact resistance into account. However, their simulation results [10] indicated that the "measured" c_p was much more accurate than those that could be achieved in a real measurement. This simulation cannot effectively explain the mass dependence of the measured c_p in TMDSC.

As has been discussed in Chapter 1, Hatta and Katayama [11] proposed a method to eliminate the error from contact resistance by using the phase angle information. This approach requires no reference on the reference side but uses the support plate itself as the reference. Because the calibration coefficient is a function of the modulation period as well as the specific heat of the sample in the model, this method requires extensive calibration with multiple standard samples for each modulation period of interest. Although theoretically sound, the calibration process could be overwhelming if the long-term stability of the instrument is poor. Osaza and Kanari [12] adopted a similar approach and modified one of their earlier R-C network models [10] on the sample side. The result was similar to that of Hatta and Katayama [11], and thus may be subjected to the same limitations in the calibration of the TMDSC device.

2.3.3 The effect of modulation period

It can be seen from both the results by simulation as shown in Fig. 2.6 and by experiments as shown in Figs. 2.7 and 2.8, shorter modulation periods (e.g. 10—20s) or higher modulation frequencies lead to increased errors. Increasing the modulation period can improve the accuracy of the measured specific heat. Furthermore, simulation results indicate that when the temperature modulation period approaches infinity, the measured specific heat converges to the exact specific heat of the sample regardless of the sample mass. However, in a real experiment, the potential issue is if the modulation period becomes too large (e.g. 500s), slow TMDSC system drift or low frequency noise of the system will interfere with temperature signals due to the overlapping of the frequencies of noise and temperature signals.

2.3.4 The effect of modulation amplitude

Fig. 2.10 shows the measured c_p of sapphire with a sample mass of 18.25 mg under different modulation amplitude. The modulation period was maintained at 100 s and the isothermal temperature was 400 K. The amplitude of the sample temperature was able to follow the programmed values such as 0.2, 0.5, 1, 2 and up to 4 K, as indicated by the first five steps of the amplitude of the sample temperature in Fig. 2.10. When the programmed modulation amplitude was further increased to 6, 7 and 8K, the amplitude of the sample temperature could not reach the programmed values instantly. However, the measured c_p is rather stable: it only varies between 1.0 and 1.1 J/g·K for the different modulation amplitudes. This suggests that the modulation amplitude has little effect on the measured c_p if compared with the effect of the modulation period and sample mass.

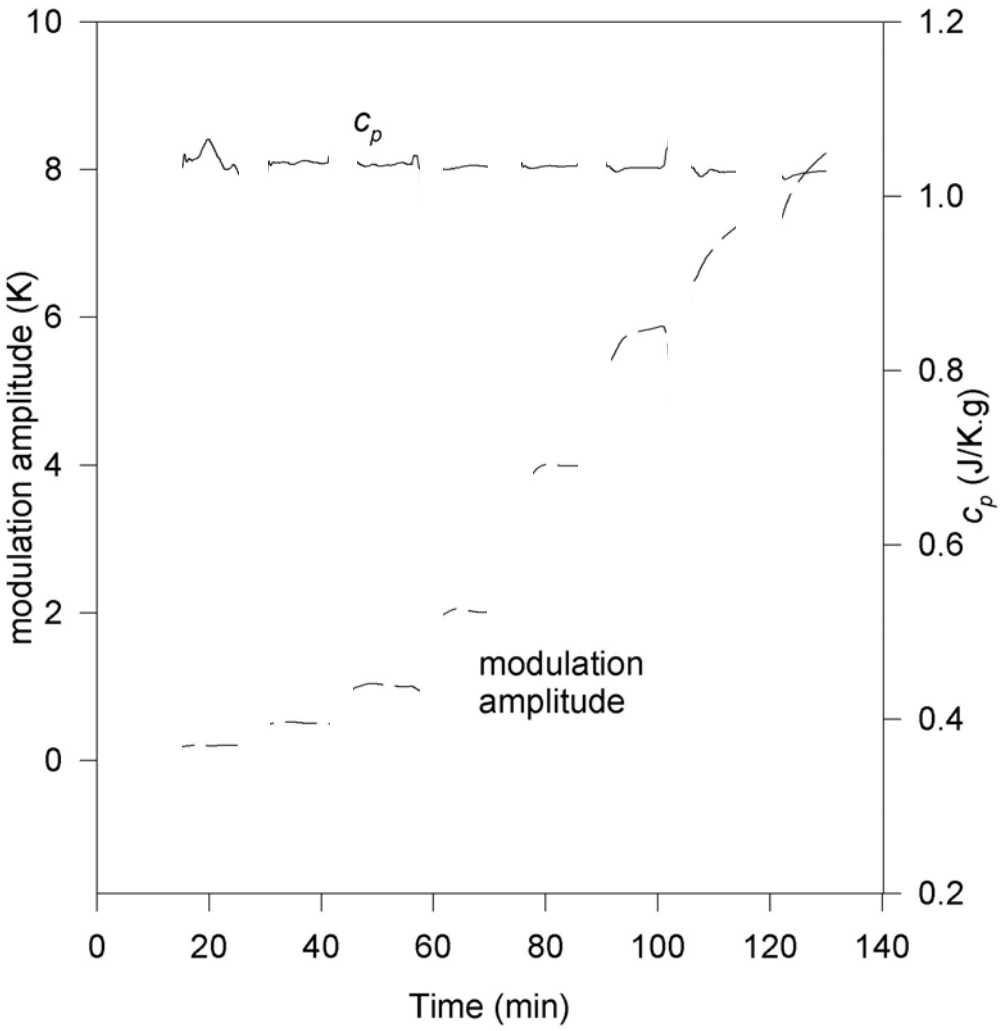

Fig. 2.10 Effect of temperature modulation amplitude on the measured specific heat of a sapphire disk. Sapphire disk mass = 18.25 mg, temperature modulation period = 10 s

2.3.5 Calibration factor of sapphire and mass dependence

Fig. 2.11 shows the calibration factor (Kc_p) as a function of temperature modulation period for two sapphire references. A standard sapphire reference with a mass of 61.2 mg is used to compare the calibration factors with the previous sapphire reference of 18.25 mg. As can be seen in Fig. 2.11, the sapphire reference of 61.2 mg exhibits a lager calibration factor than that of the reference of 18.25 mg over the entire modulation period of 10 to 100 s. For both sapphire references, Kc_p increases with a

decreasing modulation period. When the modulation period is larger than 60 s, the Kc_p curve becomes relatively flat. It seems that the difference in Kc_p between these two sapphire references will be negligible at a much larger modulation period (>100s). Thus we not only have to select the sample and calibration reference with appropriate masses, but also need to select the modulation period carefully when TMDSC is used to measure heat capacities, as modulation period also affects the measurement results.

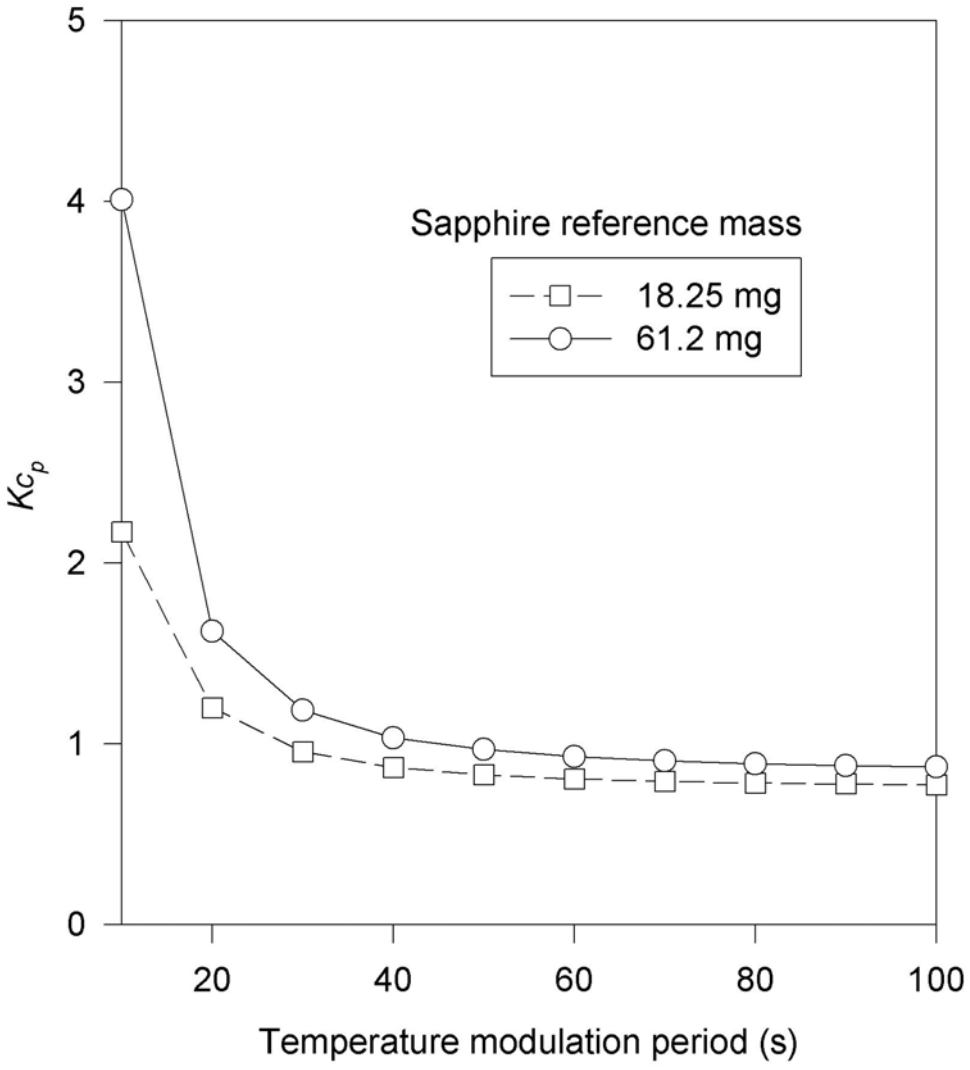

Fig. 2.11 Calibration factor Kc_p of two different sapphire reference samples

2.3.6 Possible effect of the temperature profile in metallic samples

Simulation was also carried out to evaluate the temperature profile in the sample and its possible effect on the TMDSC result. A copper disk with a mass of 200 mg which is much larger than those used in the experiments is assumed to be heated from the bottom surface only. The disk has a diameter of 6 mm and a thickness of 0.8 mm. The relative temperature profile calculated with finite element method is shown in Fig. 2.12.

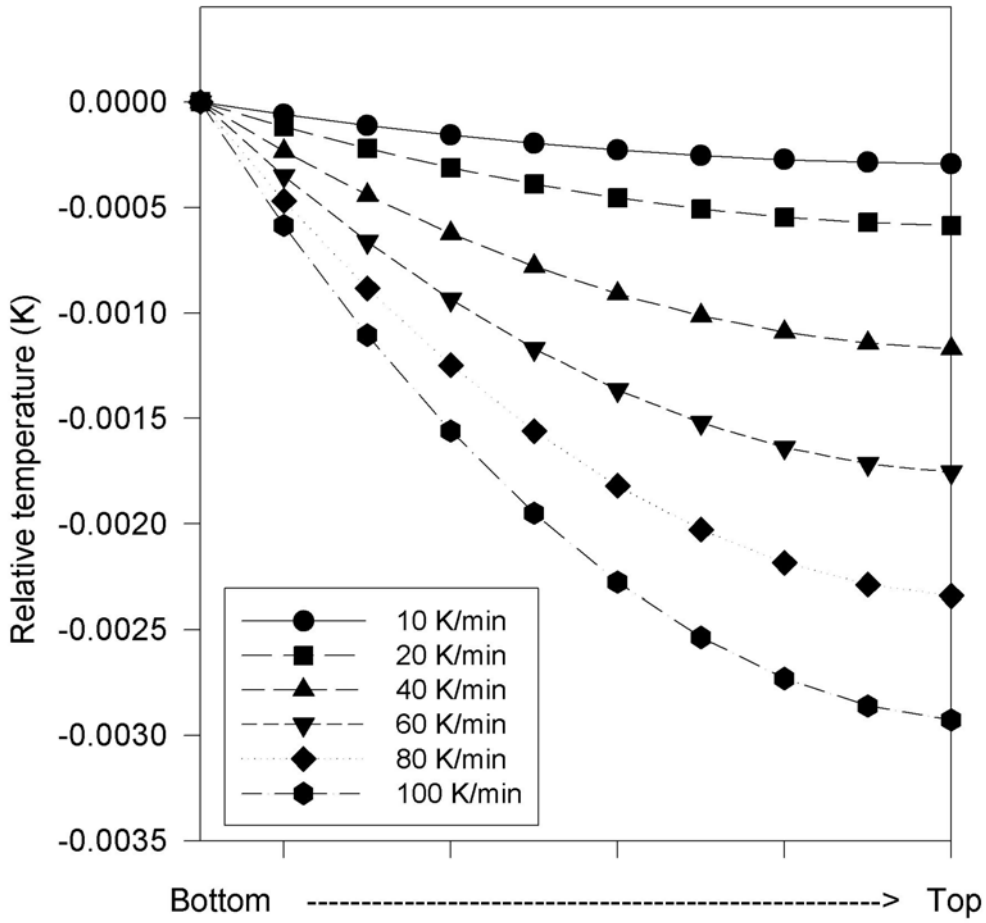

Fig. 2.12 The temperature profile under different linear heating rates in a 200 mg cylindrical copper sample with a diameter of 6 mm. The bottom temperature is used as a reference point and set to zero.

The results show that even under a linear heating rate of 100 K/min, the temperature difference between the bottom and top in the sample is only 0.003 K. This is three orders of magnitude lower than the typical modulation amplitude, 0.2 to 1 K, for example. In the TMDSC experiments as discussed in section 2.3.1, the masses of the copper samples are much smaller than 200 mg and the maximum instantaneous heating rate is only 12.6 K/min at a modulation period of 30 s and modulation amplitude of 1 K. Based on these results, it is believed that for copper and most other metals, the temperature gradient in the sample should be of no major concern in TMDSC.

However, for low heat-conductive materials like polymers, their thermal conductivities are often two to three orders of magnitude lower than that of copper. In such cases, the thermal resistance of the sample itself may significantly affect the R-C network and the measured specific heat, which will be discussed in Chapter 3.

2.4 Comparison of specific heat measurements in the conventional DSC and TMDSC

In this section, the differences in the measurement of specific heat between the conventional DSC and TMDSC are compared. For the R-C network model shown in Fig. 2.4, it can be proven that under a linear heating rate of q, when the steady state is achieved in DSC mode, the sample and the reference temperatures, T_s and T_r, are given by (see Appendix 2 for the detailed derivation)

$$T_r = T_b - 3C \cdot q \cdot R - \frac{4C_s \cdot R^2 + C_r\left(4R^2 + 2R \cdot R_c\right)}{R_c + 4R} \cdot q\,, \qquad (2.9)$$

$$T_s = T_b - 3C \cdot q \cdot R - \frac{4C_r \cdot R^2 + C_{s0}\left(4R^2 + 2R \cdot R_c\right)}{R_c + 4R} \cdot q\,, \qquad (2.10)$$

respectively. Then we have

$$T_r - T_s = \frac{2(C_{s0} - C_r)R \cdot R_c \cdot q}{R_c + 4R}. \tag{2.11}$$

Thus,

$$(T_r - T_s)\frac{R_c + 4R}{2R \cdot R_c} = (C_{s0} - C_r) \cdot q = K(T_r - T_s). \tag{2.12}$$

Equation (2.12) demonstrates a linear relationship between the heat capacity of the sample and the temperature difference $T_r - T_s$. As a result, the measured heat capacity is proportional to the heat flow since the heat flow is proportional to $T_r - T_s$.

To study the linear range of conventional DSC, experiments were conducted with two standard sapphire references and five copper samples. Table 2.2 lists the masses of the copper samples. These masses are larger than those used in TMDSC as we already know DSC has good linearity at smaller masses.

Table 2.2 Copper samples used in DSC

Sample#	Mass (mg)
Sample 1	16.8
Sample 2	65.61
Sample 3	125.55
Sample 4	200.04
Sample 5	423.55

Because the baseline heat flow of the DSC cell, which is the heat flow obtained without a sample and reference depends on the heating rate (see Fig. 2.13), all experiments were carried out under the same heating rate to eliminate this cell bias. The heat flows of the samples were compared to obtain the specific heat:

$$c_p = \frac{HF(t)_i - HF(t)_j}{q \cdot (m_i - m_j)}, \tag{2.13}$$

where m_i and m_j are the masses of two different samples and the calibration factor is

$$K_{Cp} = \frac{c_p(literature)}{c_p}. \tag{2.14}$$

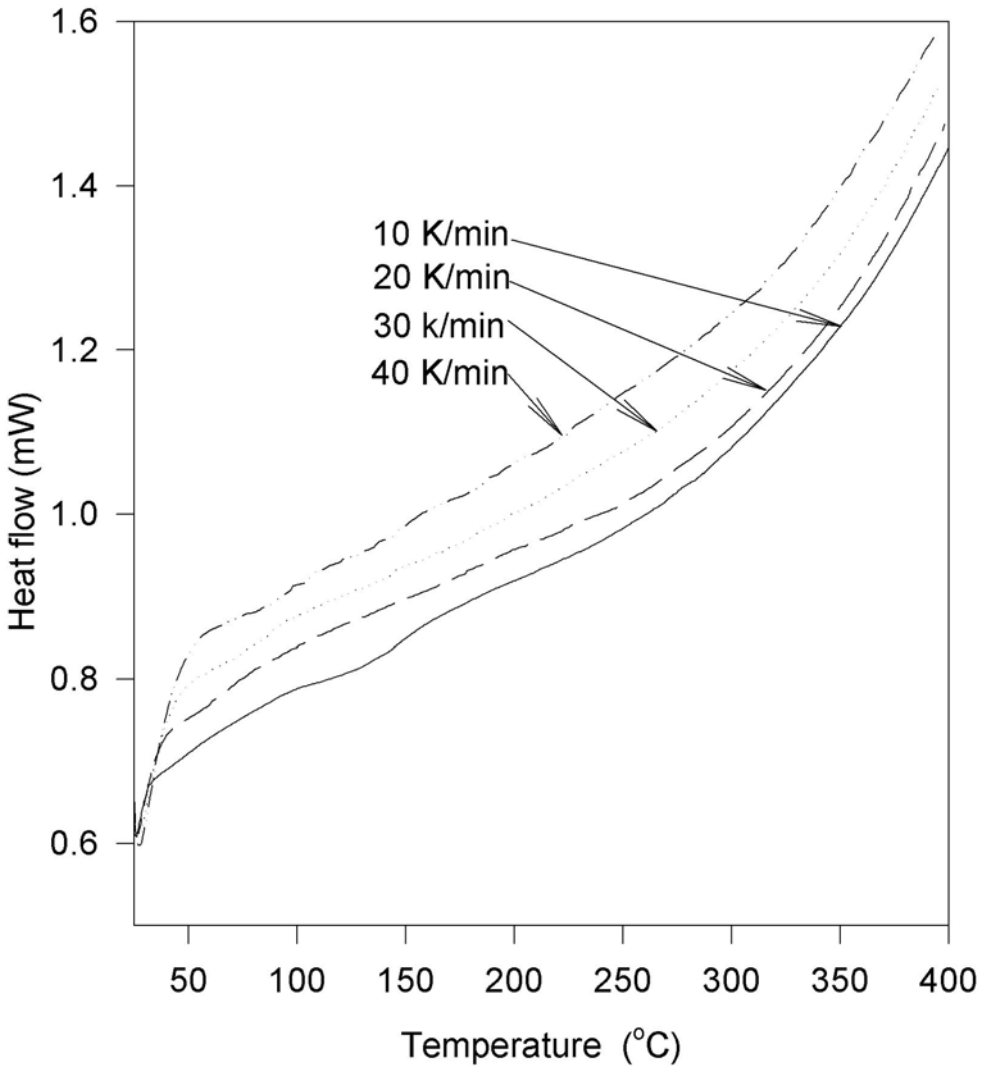

Fig. 2.13 The baseline heat flow curves in DSC2920 under different linear heating rates

The results of specific heat for the copper samples are given in Table 2.3. The corresponding calibration factors are listed in Table 2.4. As shown in Table 2.4, it is noticed that for the wide ranges of sample mass, heating rate, and temperature, the maximum value of the calibration factor, Kc_p, is 0.96 and the minimum is 0.92. The difference between 0.96 and 0.92 is only about 5%, which is much smaller than that in TMDSC as shown in Fig. 2.11, of which can reach as high as 80% (4.0 vs. 2.2). This

is a significant difference considering the fact that the TMDSC data were obtained only for a single temperature point of 400 K with a much smaller sample mass range.

Table 2.3 Measured c_p (in J/g·K) of copper vs. heating rate

Heating rate (K/min)	Temperature				Measured from
	150°C	200°C	250°C	300°C	
20	0.43	0.44	0.44	0.44	Sample2,sample1
20	0.43	0.43	0.44	0.44	Sample3,sample1
20	0.42	0.43	0.44	0.44	Sample4,sample1
20	0.42	0.43	0.43	0.44	Sample5,sample1
40	0.43	0.43	0.44	0.45	Sample2,sample1
40	0.43	0.44	0.44	0.44	Sample3,sample1
40	0.42	0.43	0.43	0.44	Sample4,sample1
40	0.42	0.42	0.43	0.44	Sample5,sample1

Table 2.4 c_p calibration factors of copper vs. heating rate

Heating rate (K/min)	Temperature				Measured from
	150°C	200°C	250°C	300°C	
20	0.92	0.93	0.94	0.94	sample2,sample1
20	0.94	0.93	0.93	0.94	sample3,sample1
20	0.95	0.94	0.94	0.94	sample4,sample1
20	0.96	0.95	0.94	0.95	sample5,sample1
40	0.92	0.93	0.94	0.93	sample2,sample1
40	0.92	0.92	0.94	0.93	sample3,sample1
40	0.94	0.95	0.96	0.95	sample4,sample1
40	0.96	0.95	0.95	0.94	sample5,sample1

The values of specific heat obtained from the two sapphire references with a mass of 18.25 mg and 62.10 mg respectively are listed in Table 2.5. The heating rate was varied from 5 to 40 K/min and the measuring temperature range was between 100 and 200°C. The corresponding calibration factors are given in Table 2.6. As shown in the table, the maximum value of Kc_p is 0.94 and the minimum is 0.91. The difference between 0.94 and 0.91 is less than 4%, which is close to that of the copper samples,

5% as given before. This shows that DSC has good system linearity over wide ranges of measuring temperature, heating rate and sample mass.

Table 2.5 Measured c_p (in J/g·K) of sapphire vs. heating rate

Heating rate (K/min)	Temperature			
	100°C	150°C	175°C	200°C
5	0.96	1.05	1.08	1.12
10	0.97	1.05	1.08	1.11
20	0.97	1.06	1.09	1.11
40	0.96	1.05	1.08	1.11

Table 2.6 c_p calibration factors of sapphire vs. heating rate

Heating rate (K/min)	Temperature			
	100°C	150°C	175°C	200°C
5	0.94	0.92	0.92	0.91
10	0.94	0.92	0.92	0.92
20	0.93	0.92	0.92	0.92
40	0.94	0.93	0.92	0.92

2.5 Conclusions

An R-C network model was used to analyze the effect of experimental parameters and thermal properties of the TMDSC calorimetry device on the specific heat measurement. TMDSC experiments were conducted with sapphire, copper and aluminum. Sapphire was used to obtain calibration factors to correct the specific heat of other samples. Both the simulation and experiments show that the measured specific heat using TMDSC depends on many factors such as the sample mass, the period of temperature modulation, the difference of heat capacity between the calibration reference and the sample to be tested. However, the amplitude of temperature modulation has little influence on the results. The typical behavior of a heat flux TMDSC instrument can be described by a low pass filter in terms of the relationship between the actual specific heat and the measured ones. Results of

simulation and experiments indicate that when the heat capacity of the sample, which is the product of the specific heat and sample mass, exceeds that of the calibration reference, the measured specific heat tends to be smaller than the actual value. Otherwise, the measured specific heat will be larger. When the thermal gradient in the sample can be ignored, as in the cases of metallic materials, more accurate results of measured specific heat can be obtained if the heat capacity of the sample is close to that of the calibration reference.

References

[1] S. R. Sauerbrunn, B. S. Crow, M. Reading, 21st Proc. NATAS Conf, Sept. 13-16, Atlanta GA, USA 1992.

[2] A. Boller, Y. Jin, B. Wunderlich, J. Therm. Anal. **42** (1994) 307.

[3] B. Wunderlich, Y. Jin, A. Boller, Thermochim. Acta **238** (1994) 277.

[4] F. U. Buehler, C. J. Martin, J. C. Seferis, J. Therm. Anal. **54** (1998) 501.

[5] F. U. Buehler, J. C. Seferis, Thermochim. Acta **334** (1999) 49.

[6] B. Schenker, F. Stager, Thermochim. Acta **304/305** (1997) 219.

[7] M. Merzlyakov, C. Schick, Thermochim. Acta **330** (1999) 65.

[8] I. S. Grigoriev, E. Z. Meilikhov, *Handbook of Physical Quantities*, CRC Press, Inc, Boca Raton, 1977, p.258.

[9] *Operator's manual, Rev. B DSC2920 Differential Scanning Calorimetry*, TA Instruments, Nov. 1996, p.C-48.

[10] T. Ozawa, K. Kanari, Thermochim. Acta **288** (1996) 39.

[11] I. Hatta, N. Katayama, J. Therm. Anal. **54** (1998) 577.

[12] T. Ozawa, K. Kanari, J. Therm. Anal. **54** (1998) 521.

Chapter 3 Study of Temperature Profile and Specific Heat in TMDSC with a Low Sample Heat Diffusivity

3.1 Introduction

As discussed earlier, TMDSC uses the linear raising temperature that is used in the conventional DSC, superimposed with a periodic modulation of the temperature in the dynamic calorimetry. Since low frequency random noise that may be related to reactions in samples has been observed in conventional DSC, the temperature modulation technique has been used to obtain a more consistent experimental result in the measurement of heat flows and heat capacities [1]. (The frequency of this noise was too low to be of electrical origin). Among other capabilities, TMDSC can be used to measure thermal properties of materials such as specific heat under quasi-isothermal (which has a zero underlying heating rate) conditions and non-zero underlying heating rate conditions [2—3].

In a heat flux TMDSC, if the thermal resistance of the contact between the sample and the supporting plate is ignored, we have the following heat transfer equation,

$$HF_s = C_{s0}\frac{dT_s}{dt} = K(T_b - T_s)\ , \qquad (3.1)$$

where HF_s is the heat flow to the sample side, T_b is the temperature of the heating block, T_s is the sample temperature, C_{s0} ($=C_s+C_r$) is the total heat capacity of the sample and the reference (normally sealing pan), C_s is the heat capacity of the sample, C_r is the heat capacity of the reference.

The heat flow to the reference, HF_r , is

$$HF_r = C_r \frac{dT_r}{dt} = K(T_b - T_r) \ , \qquad (3.2)$$

where T_r is the reference temperature. The heat capacity of the sample can be obtained by Eq. (2.1) in TMDSC.

Boller et al. [2] had noticed that the measured specific heat of sapphire dropped considerably when the sample mass was over 100 mg if compared to that at 20 mg. This was attributed to insufficient heat diffusion in the sample. Efforts have also been made to analyze the temperature profile within the sample in both the conventional DSC and TMDSC techniques. It was found that low thermal conductivity of the sample could produce a larger phase lag [4—6], and this could lead to controversies in the explanation of certain experimental results. For example, much debate existed in the physical meaning of the complex heat capacity and in the in-phase and out-of-phase parts of the heat flow [7—9]. In general, metallic materials are good heat conductors such that the internal temperature is almost uniform throughout the sample, which has been discussed in Chapter 2. In this case, heat diffusivity has little effect on the measurement of specific heat. However, for materials that have very low heat diffusivities, the excessive thermal resistance introduced by the sample itself may affect the measured specific heat significantly.

In this Chapter, polyethylene terephthalate (PET), which has a thermal conductivity about one-thousandth that of aluminum, is used to demonstrate the effect of the thermal resistance of the sample on the measured specific heat. A TMDSC model is used to show the importance of understanding the effect of the internal thermal resistance of the sample, which is described in section 3.2. An analytical solution of the measured specific heat is derived and the effects of the thermal conductivity, sample thickness and modulation conditions on the measurement of specific heat are discussed. A numerical solution is also given and results of

numerical and analytical methods are compared. The experimental procedures are discussed in section 3.3. PET with indium temperature tracers is selected as the test material. In section 3.4, I will discuss the effect of the thermal gradient within the sample and of the temperature modulation parameters on the measurement of specific heat.

3.2 A TMDSC model with thermal diffusivity

In this section, I discuss a case in which the thermal resistance of the sample is significant. Fig. 3.1 shows the cell structure of a heat flux type TMDSC. Different from the R-C network model shown in Fig 2.4, it takes into account the internal thermal resistance of the sample, but the contact resistance between the sample and supporting plate and the heat capacities of the thermal conducting path are neglected. As shown in Fig. 3.1, C_r is the heat capacity of the supporting plate, which is used as the reference in this model. T_r is the temperature of the reference, and T_s is the temperature of the sample obtained at its bottom surface.

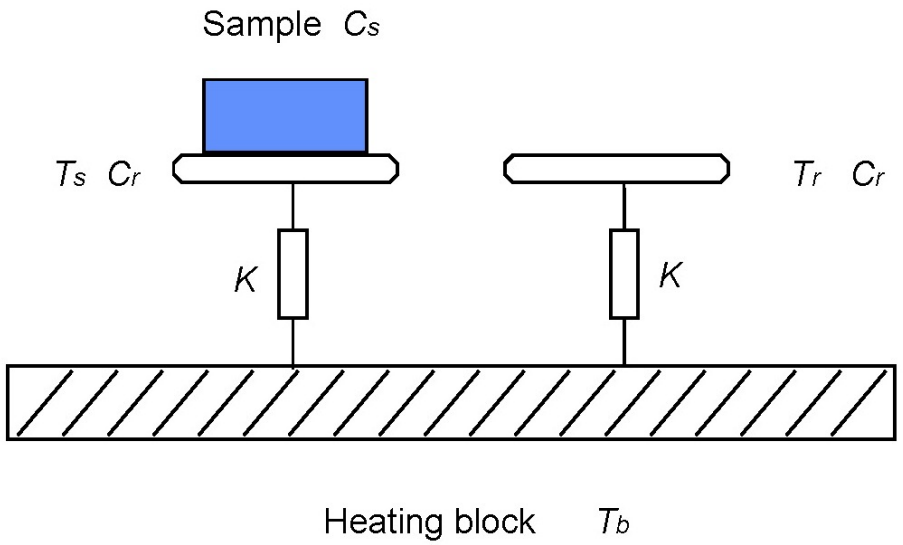

Fig. 3.1 A model of a DSC or TMDSC cell with the temperature gradient in consideration. *Tr* is the reference temperature, *Ts* is the sample temperature at the bottom surface, *Cr* the is heat capacity of the support plate, *K* is the system thermal constant, *Cs* the is heat capacity of the sample.

The actual temperature of the sample cannot be directly measured in DSC or TMDSC since the thermal couple is not in direct thermal contact with the sample. Instead, the temperature measured by the thermal couple is used to evaluate the specific heat of the sample. In the following analysis we assume that the sample is heated only from the bottom surface. There is no heat exchange between the top or side surfaces of the sample and the environment either by convection or by radiation, and there is no heat exchange between the sample and the reference either.

3.2.1 An analytical solution to the heat conduction equation

With the above assumptions, the heat conduction in the sample is treated as an ideal one-dimensional heat transfer problem. The heat flow in the sample is described by the general heat transfer equation,

$$\frac{\partial T(x,t)}{\partial t}\frac{1}{\alpha_T} = \frac{\partial^2 T(x,t)}{\partial x^2}\ , \tag{3.3}$$

where x is the distance measured from the bottom of the sample and the thermal diffusivity of the sample α_T is given by

$$\alpha_T = \frac{\lambda}{\rho c_p}, \tag{3.4}$$

where λ is the thermal conductivity, ρ is the density and c_p is the specific heat of the sample. Imposing a sinusoidal modulation on T_s:

$$T_s = T_s(0,t) + T_0 = T_0 + A\cdot e^{i\omega t}, \tag{3.5}$$

where T_0 is the initial temperature, A is the amplitude, and ω is the angular frequency, the cyclic part of the sample temperature in Eq. (3.3) takes the form

$$T_s(x,t)\,|_{cyclic} = F(x)\cdot e^{i\omega t}, \tag{3.6}$$

where $F(x)$ is a complex function and it can be shown that [10]

$$F(x) = A_1\cdot e^{-x(1+i)\sqrt{\omega/2\alpha_T}} + A_2\cdot e^{x(1+i)\sqrt{\omega/2\alpha_T}}. \tag{3.7}$$

Because there is no heat flow through the top surface of the sample, by utilizing the boundary conditions, $F(0)=A$ and $\partial T(x,t)/\partial x|_{x=d}=0$, where d is the sample thickness, we obtain

$$A_1 = \frac{e^{\beta d}}{e^{\beta d} + e^{-\beta d}}, \tag{3.8}$$

$$A_2 = \frac{e^{-\beta d}}{e^{\beta d} + e^{-\beta d}}, \tag{3.9}$$

where

$$\beta = (1+i)\sqrt{\frac{\omega}{2\alpha_T}}. \tag{3.10}$$

Thus, the cyclic part of the sample temperature is

$$T_s(x,t)\,|_{cyclic} = \frac{1}{e^{\beta d} + e^{-\beta d}}(e^{\beta d}e^{-\beta x} + e^{-\beta d}e^{\beta x}) \cdot A \cdot e^{i\omega t}. \tag{3.11}$$

A comparison of $T_s(x,t)$ given in Eq. (3.11) with the imposed temperature modulation at the sample bottom (x=0) as given in Eq. (3.5) indicates that the internal temperature of the sample is also a periodic function of the angular frequency ω, but has an amplitude which is a much more complicated function of x.

In Eq. (3.1), HF_s is the total heat absorbed by the supporting plate and the sample. Hence, it can be obtained that

$$K \cdot [T_b - T_s(0,t)] = C_r \frac{dT_s(0,t)}{dt} + \int_0^d \left[S \cdot c_p \cdot \rho \cdot \frac{\partial T_s(x,t)}{\partial t} \right] dx, \tag{3.12}$$

where S is the cross sectional area of the sample. Combining Eqs. (3.8) to (3.12)

$$\begin{aligned} T_b &= \frac{1}{K}\left\{ K \cdot T_s(0,t) + C_r \frac{dT_s(0,t)}{dt} + \int_0^d \left[S \cdot c_p \cdot \rho \cdot \frac{\partial T_s(x,t)}{\partial t} \right] dx \right\} \\ \cdots &= \frac{1}{K} \cdot A \cdot e^{i\omega t} \cdot \left(K + i\omega \cdot C_r + i\omega \cdot S \cdot c_p \cdot \rho \cdot \frac{1}{\beta} \cdot \frac{e^{\beta d} - e^{-\beta d}}{e^{\beta d} + e^{-\beta d.}} \right) \end{aligned} \tag{3.13}$$

Substituting Eq. (3.13) into Eq. (3.2) yields the cyclic part of the reference temperature T_r:

$$T_r = A \cdot e^{i\omega t} \cdot \left(K + i\omega \cdot C_r + i\omega \cdot S \cdot c_p \cdot \rho \cdot \frac{1}{\beta} \cdot \frac{e^{\beta d} - e^{-\beta d}}{e^{\beta d} + e^{-\beta d}} \right) \frac{1}{i\omega \cdot C_r + K} . \quad (3.14)$$

Substituting Eqs. (3.14) and (3.5) into Eq. (2.1), we obtain the measured heat capacity of the sample

$$C_s = \left(\frac{K + i\omega \cdot C_r + i\omega \cdot S \cdot c_p \cdot \rho \cdot \frac{1}{\beta} \cdot \frac{e^{\beta d} - e^{-\beta d}}{e^{\beta d} + e^{-\beta d}}}{i\omega \cdot C_r + K} - 1 \right) \sqrt{\left(\frac{K}{\omega} \right)^2 + {C_r}^2}$$

$$= \left(\frac{e^{2\beta d} - 1}{e^{2\beta d} + 1} \cdot \frac{1}{\beta} \cdot \frac{i\omega \cdot S \cdot c_p \cdot \rho}{i\omega \cdot C_r + K} \right) \sqrt{\left(\frac{K}{\omega} \right)^2 + {C_r}^2} . \quad (3.15)$$

Equation (3.15) describes the effects of the various parameters on the measured heat capacity under various modulation situations within the framework of the model as shown in Fig. 3.1.

Table 3.1 Relationship among the theoretical errors in measured heat capacity (C_s), sample thickness and temperature modulation period. Material: PET

Modulation period	**Sample thickness**						
	0.2mm	0.6mm	1.0mm	1.4mm	1.8mm	2.2mm	2.6mm
10s	0.0%	-0.3%	-2.6%	-8.9%	-19.7%	-32.4%	-44.0%
30s	0.0%	0.0%	-0.3%	-1.1%	-3.0%	-6.3%	-11.3%
50s	0.0%	0.0%	-0.1%	-0.4%	-1.1%	-2.4%	-4.6%
70s	0.0%	0.0%	-0.1%	-0.2%	-0.6%	-1.3%	-2.4%
90s	0.0%	0.0%	0.0%	-0.1%	-0.3%	-0.8%	-1.5%

The results showing the relationship among the sample thickness, temperature modulation period and the error in the measured c_p for PET are given in Table 3.1. To better illustrate the relationship among the error in the measured c_p, sample thickness and modulation period, the contents of Table 3.1 are presented in Fig. 3.2.

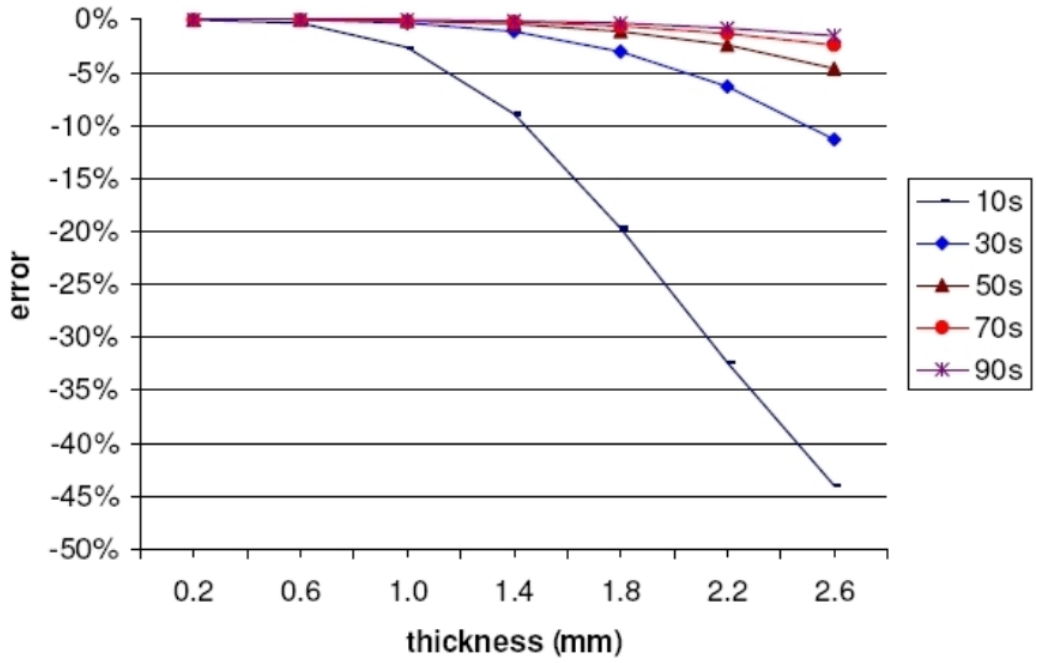

Fig. 3.2 Relationship among the errors in the measured heat capacity, sample thickness and temperature modulation periods (in s). Material: PET

The five different curves represent the errors in the measured c_p under a modulation period of 10, 30, 50, 70 and 90 s, respectively, as a function of the sample thickness. The sample thickness varies from 0.2 to 2.6 mm and the modulation period varies from 10 to 90 s. Apparently the effect of the internal resistance is negligible when the modulation period is larger than 30 s and the sample thickness is smaller than 1.0 mm. For example, the error in the measured specific heat is less than 0.5% when the thickness is less than 0.6 mm. The error is less than 5% if the modulation period is larger than 50 s. It is also noticed that the measured c_p is always smaller than the real c_p. For other poor heat conductors, the appropriate range of parameters depends on their corresponding thermal diffusivity according to Eq. (3.15). Now we look at the effects of some of the parameters on the measured specific heat.

(1) Effect of the thermal conductivity λ of the sample

For samples with high thermal conductivity, our analytical solution shows that the effect of the internal thermal resistance is negligible. For example, the thermal conductivity of copper is 4W/cm.K at room temperature [11], even for a sample thickness of 2 mm, the error due to internal thermal resistance in the measured specific heat c_p ($c_p=C_s/m_s$, where m_s is the sample mass) is less than 0.01%. In the case of the ideal TMDSC model in which the sample has a uniform temperature, as mentioned in the beginning of this chapter, discussions in Chapter 2 are applicable. On the other hand, if the thermal conductivity is low, a small error is introduced in the measured c_p. For example for PET, λ=0.0029W/cm.K [11], the error in the measured c_p is 2.6% when the sample thickness is 1 mm and 25% when the thickness is 2 mm at a modulation frequency of 0.1 Hz.

(2) Effect of sample thickness d

Again take PET as an example and consider a small thickness (d) of 0.2 mm, the error due to the internal thermal resistance in the measured c_p is less than 0.005%. However, for a sample thickness of 1.8 mm, the error can be as large as 20% at a modulation frequency of 0.1 Hz. Obviously, for poor heat conductors, the measured specific heat is more accurate if the sample thickness is small.

(3) Effect of modulation frequency

Consider again a PET sample with a thickness of 1.0 mm. When the modulation frequency is 0.1 Hz, the error in measured c_p is 2.6%. However, at a modulation frequency of 0.02 Hz, the error is about 0.1%, which is a significant improvement over that at 0.1 Hz. This means that theoretically, we shall be able to obtain more accurate specific heat with a lower modulation frequency (such as 0.01 Hz) or a longer modulation period (e.g. 100 s).

Similar calculation was also carried out for copper, for the same ranges of sample thickness and modulation period. It was found that the error in the measured specific heat due to the internal thermal resistance is less than 0.01%. Thus the effect of the internal thermal resistance of the sample itself can be ignored for copper and most metallic materials.

In summary, at least within the framework of the TMDSC model shown in Fig. 3.1, a combination of thin sample with large thermal diffusivity and long modulation period (or low modulation frequency) is beneficial to improving the measurement accuracy of TMDSC.

As Eqs. (3.5), (3.14) and (3.15) are in complex form, it can be derived that the phase angle, φ, between heat flow and T_s is

$$\varphi = \frac{\pi}{4} + \arctan\left[\frac{2e^{y}\sin(y)}{e^{2y}-1}\right] - \arctan\left(\frac{\omega \cdot C_r}{K}\right), \tag{3.16}$$

where

$$y = 2d\sqrt{\frac{\omega}{2\alpha_T}}. \tag{3.17}$$

It can be proven that the second term on the right hand side of Eq. (3.16) is equal to $\pi/4$ and $\varphi=\pi/2-\arctan(\omega C_r/K)=\arctan(K/\omega C_r)$ when the sample is treated as a single point with no internal thermal resistance. In this case, our TMDSC model is essentially the same as that dicussed by Wunderlich et al. [2—3].

From Eq. (3.15), it can be seen that the specific heat, thickness and cross sectional area of the sample all can affect the measured specific heat. There is no simple relationship between the real specific heat and the measured value, but a proper selection of the experimental parameters can still help to reduce the effect of internal thermal resistance to a negligible level (<0.5% in error).

3.2.2 A numerical approach

For the purpose of comparison with the above analysis, we now resort to a numerical approach to study the thermal processes in TMDSC. The cylindrical sample is divided into n (n=10) equally sized small disks along its vertical axis. Based on the model shown in Fig. 3.1, the following heat transfer equations can be obtained.

For the sample supporting plate, we have

$$(T_b - T_s)K - \frac{(T_s - T_1)}{R_{unit}} = C_r \frac{dT_s}{dt} . \tag{3.18}$$

For the first disk at the bottom of the sample (i=1), it can be shown that

$$\frac{(T_s - 2T_1 + T_2)}{R_{unit}} = C_{unit} \frac{dT_1}{dt} . \tag{3.19}$$

For the i-th disk (i=2 to n-1),

$$\frac{(T_{i-1} - 2T_i + T_{i+1})}{R_{unit}} = C_{unit} \frac{dT_i}{dt} . \tag{3.20}$$

For the disk on top of the sample (i=n),

$$\frac{(T_{n-1} - T_n)}{R_{unit}} = C_{unit} \frac{dT_n}{dt} . \tag{3.21}$$

In Eqs. (3.18) to (3.21), R_{unit} and C_{unit} are the thermal resistance and the heat capacity of one disk respectively, and T_i is the temperature of the "i"th disk. The heat flow to the reference HF_r obeys

$$HF_r = (T_b - T_r)K = C_r \frac{dT_r}{dt} . \tag{3.22}$$

Numerical solutions of conventional DSC are carried out to obtain the temperature profile in the sample under different linear heating rates, while simulations of TMDSC are used to find the effect of the internal thermal resistance of the sample on the measured specific heat. The simulation parameters are listed in

Table 3.2. The Finite difference method and discrete Fourier transform are used to calculate the specific heat given in Eq. (2.1).

Table 3.2 Parameters used in numerical simulation

Simulation parameters and description	**Value**
Reference heat capacity C_r (in J/K)	0.02
PET density (in g/cm^3)	1.37 [11]
PET sample diameter (in mm)	5
PET sample mass (in g)	0.02
PET specific heat (in J/g·K)	1.25 [11]
PET thermal conductivity (in W/cm·K)	0.0029 [11]
System thermal constant K (in W/K)	0.01

3.3 Experimental procedures for temperature profile study

To study the actual temperature profile in PET, a method of placing metal indium in the sample as a temperature tracer is adopted, as shown in Fig. 3.3.

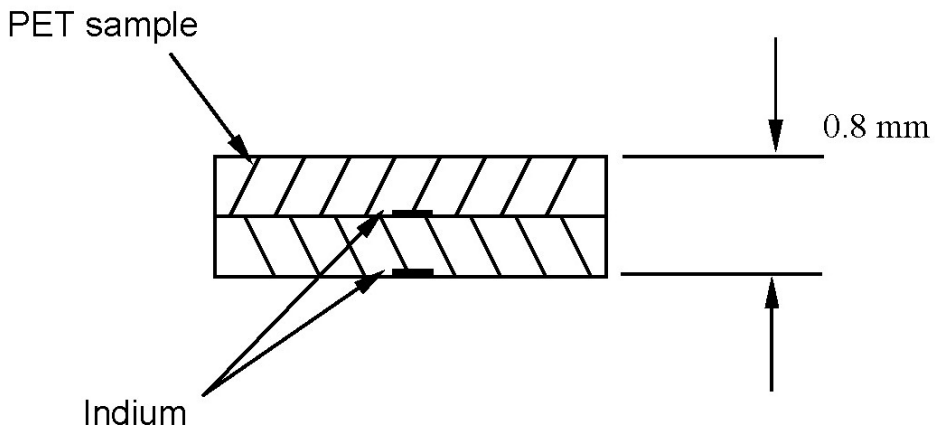

Fig. 3.3 A PET sample used in the conventional DSC experiments. A tiny amount of indium is embedded in the middle and at the bottom positions respectively. The sample is then sealed in an aluminum pan.

The thickness of the PET sheet is 0.4 mm. Small quantities of indium with a mass between 0.06 and 0.69 mg were placed between the two pieces of PET sheet and at the bottom of the lower sheet, respectively. Then the samples are sealed in a standard aluminum pan. Upon linear temperature scan, when the temperature reaches the melting point of indium, the embedded indium melts and the heat signal is picked up by the thermal couple. Since there are two indium temperature tracers at different locations in the PET sample, due to the internal temperature gradient in PET, two heat flow peaks associated with the melting of indium can be detected during the linear temperature scan. From the difference between the temperatures corresponding to the two peaks, we can roughly deduce the temperature profile in the sample. Since the signal from the melting of indium in the middle of the sample takes longer to arrive at the thermal couple than the signal from the bottom, the temperature difference between the two melting peaks has to be corrected by the time difference in heat diffusion. Given a heat diffusivity of 0.093×10^{-6} m^2/s [12] for PET and a sample thickness of 0.4 mm, the time difference is estimated to be $(0.4\times10^{-3})^2/0.093\times10^{-6}$ = 1.7 second. This delay results in a temperature difference of $1.7q$, where q is the heating rate. This temperature difference needs to be deducted from the temperature difference between the two melting peaks. The heating rate used in our DSC experiments varies from 2 to 40 K/min.

In the TMDSC experiments, two indium-free PET samples with a mass of 6.71 mg and 19.6 mg respectively are used. The sample of 6.71 mg has a single layer of the PET sheet while the 19.6 mg sample has two layers of the PET sheet. The temperature modulation amplitude varies from 0.5 to 2 K, and the modulation period varies from 10 to 100 s. The quasi-isothermal temperature is 160^oC (433 K). A standard sapphire sample with a mass of 18.25 mg is used as the calibration reference,

and calibration of K_{Cp} is conducted at the same modulation periods as those used for the two indium-free PET samples.

All DSC and TMDSC experiments are carried out on a TA 2920 DSC&MDSC thermal analysis instrument that is equipped with a rapid cooling system. The purge gas is pure nitrogen with a flow rate of 70 cc/min.

3.4 Results and discussions

The heat flows of the PET samples using indium as temperature tracers in conventional DSC are shown in Fig. 3.4. On each heat flow curve, there are two peaks corresponding to the melting of the embedded indium in the middle and at the bottom, respectively.

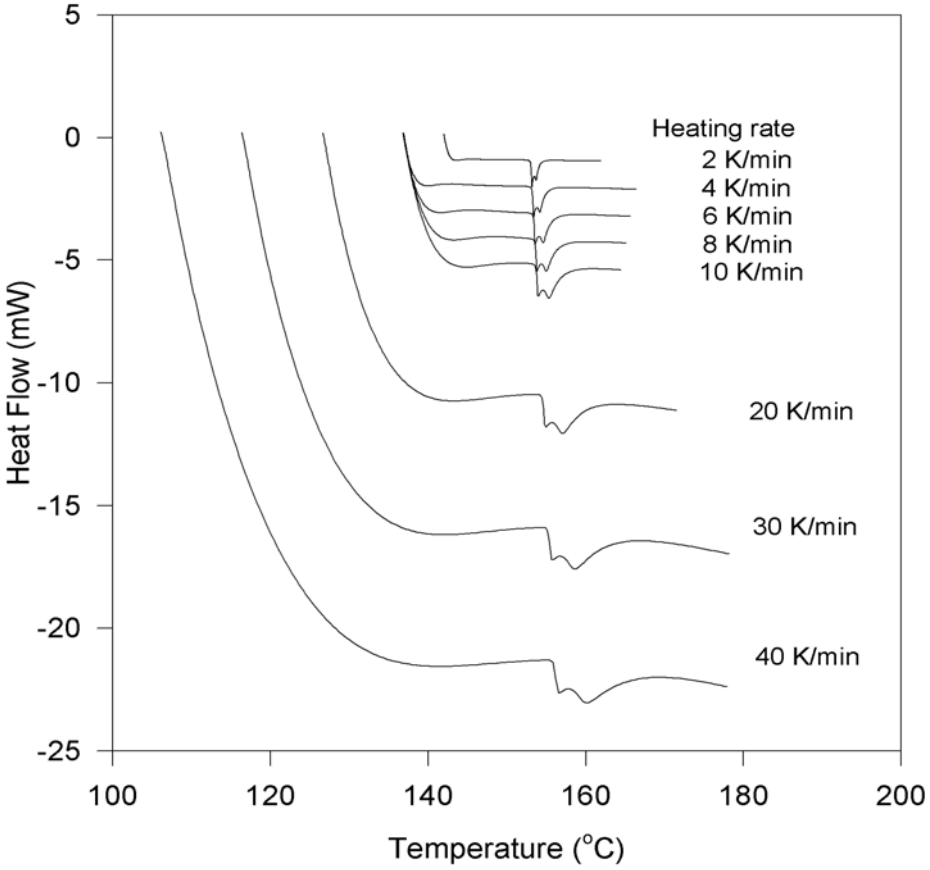

Fig. 3.4 The heat flow curves of a PET sample with indium temperature tracers under different heating rate

Fig. 3.5 shows the difference in the peak temperatures due to the melting of the two indium temperature tracers obtained from experiments and those from the numerical solutions. Curves 1 to 4 of the four PET samples exhibit a near linear relationship between the peak temperature difference and the heating rate. Although the embedded indium mass in the four samples varies from 0.06 to 0.69 mg, there seems to be no obvious correlation between the indium mass and the peak temperature difference.

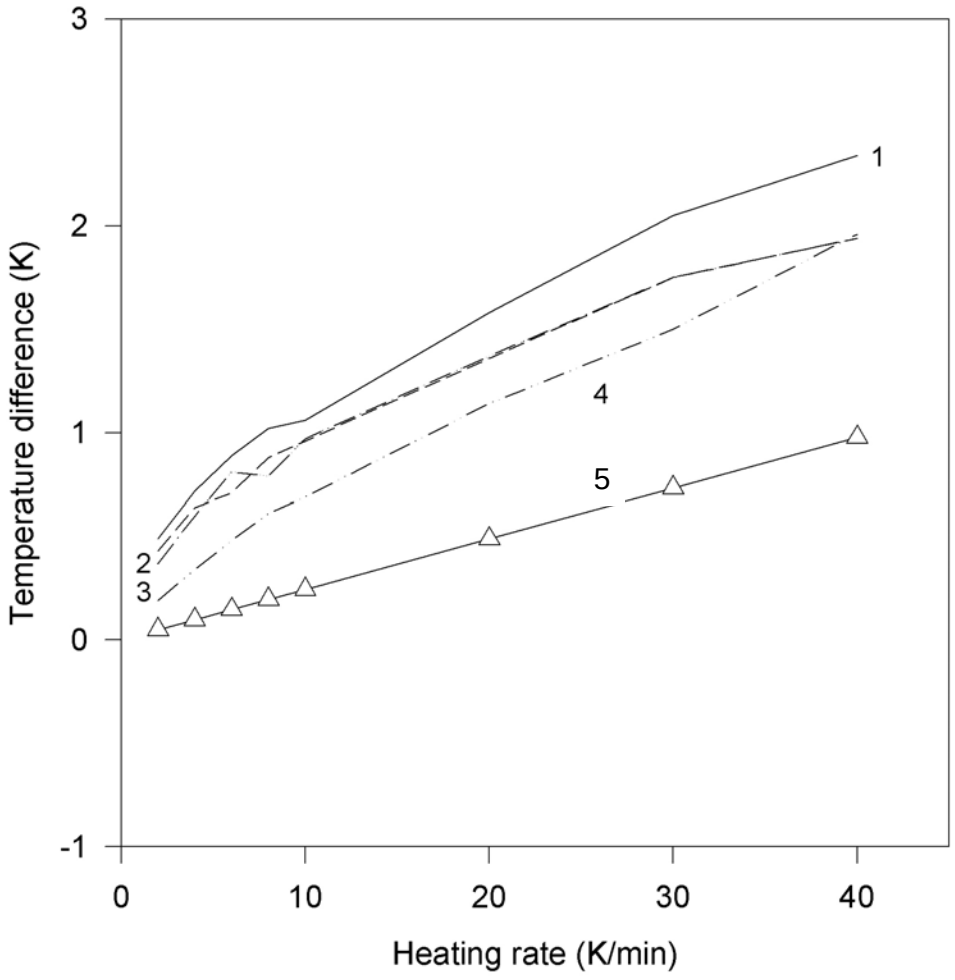

Fig. 3.5 Temperature difference between the two indium tracers as a function of heating rate. Curves 1 to 4 show the measured temperature difference. The straight line (5) is obtained from simulation. Curve 1: PET mass: 14.24 mg, middle/bottom indium mass: 0.43/0.38mg. Curve 2: PET mass: 13.02 mg, middle/bottom indium mass:0.27/0.23mg. Curve 3: PET mass: 12.94 mg, middle/bottom indium mass: 0.17/0.12mg. Curve 4: PET mass: 18.17 mg, middle/bottom indium mass: 0.69/0.07mg. Curve 5: Simulated results. PET mass: 20 mg, 0.74 mm thick.

It is noticed that in the simulation, the mass of the PET sample is 20 mg and it is assumed to have a perfect contact with the supporting plate. Based on the density and diameter given in Table 3.1, the sample has a thickness of 0.74 mm; while in the experiments, the distance between the middle and the bottom of the sample is only 0.4 mm, as indicated in Fig. 3.3. Yet the mid-to-bottom temperature difference is larger than the simulated top-to-bottom temperature difference. This may be caused by the imperfect heat transfer conditions, such as purge gas convection, radiation and partial thermal contact between the PET sample and the aluminum sealing pan.

Fig. 3.6 shows the simulated temperature profile in the PET sample at different heating rates when the temperature reaches a quasi-steady state in DSC. The temperature at the bottom of the sample is taken as the reference and is set to zero. It is noticed that the temperature profile curves are not a straight line. When the heating rate is 100 K/min, a temperature difference of 2.4 K is developed between the top and bottom surfaces.

For TMDSC, the relationship between the amplitude profile of temperature in the sample and modulation period obtained from simulation is shown in Fig. 3.7. Here the PET sample of 20 mg has a thermal resistance of 130 K/W, which is even larger than that of the DSC/TMDSC cell itself (R_s=100 K/W). This additional thermal resistance changes the effective thermal constant and results in a biased or asymmetric DSC/TMDSC cell. Since the reference sample for calibration does not have such a large internal thermal resistance, it is expected that deviations in the specific heat can be produced if the calibration factor obtained from the calibration reference is used to correct the measured specific heat of the PET sample. Obviously, if the PET sample becomes thinner, the internal amplitude profile of temperature will be more uniform, hence the measured specific heat is more accurate. Heat diffusion in the sample is

rather limited at short modulation periods (5 to 20 s, for example). Due to the significant internal thermal resistance, the amplitude of the modulated temperature drops below the programmed amplitude of 2 K as one moves from the bottom to the top surfaces of the sample. When the modulation period increases, the modulation amplitude at each point in the sample becomes closer to the programmed value and the amplitude curve becomes flatter.

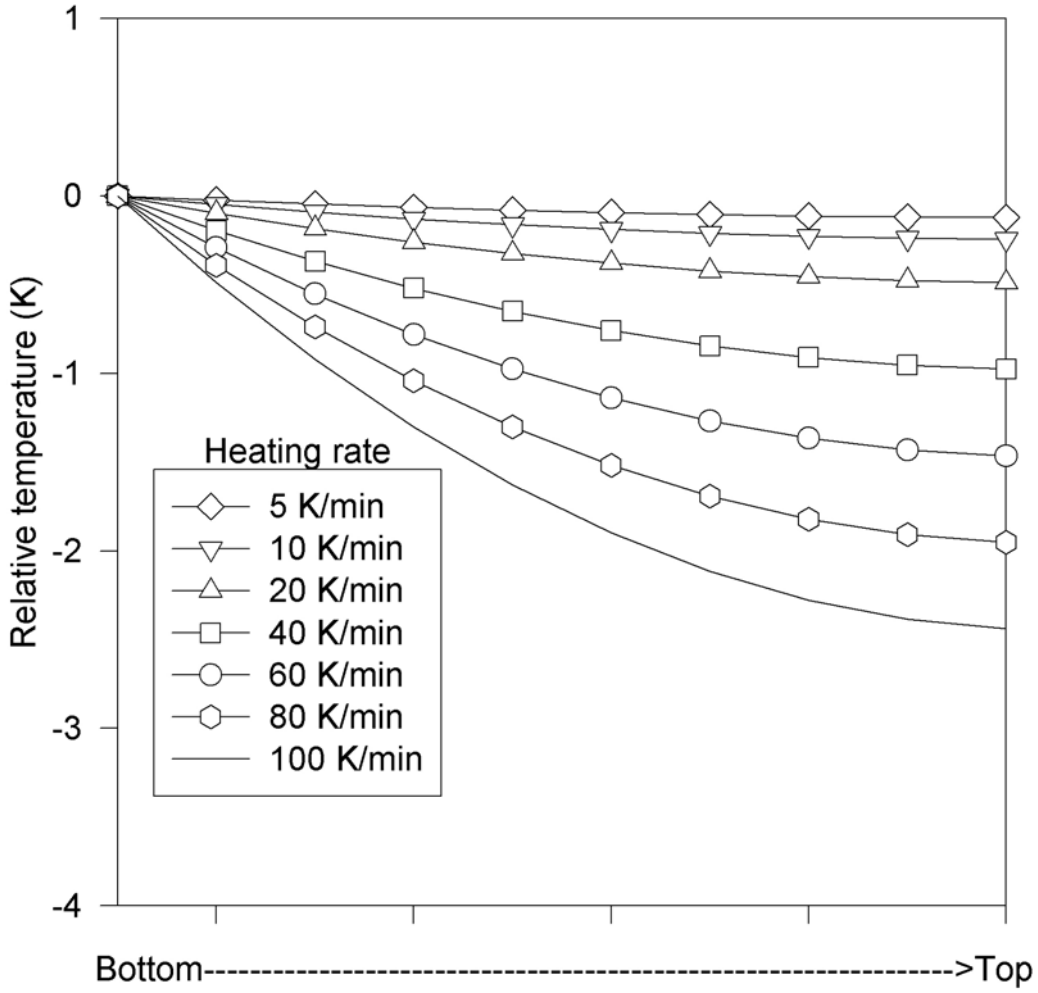

Fig. 3.6 Relative temperature profile in the sample as a function of the heating rate in conventional DSC by simulation. The temperature at the sample bottom is the reference point and is set to zero.

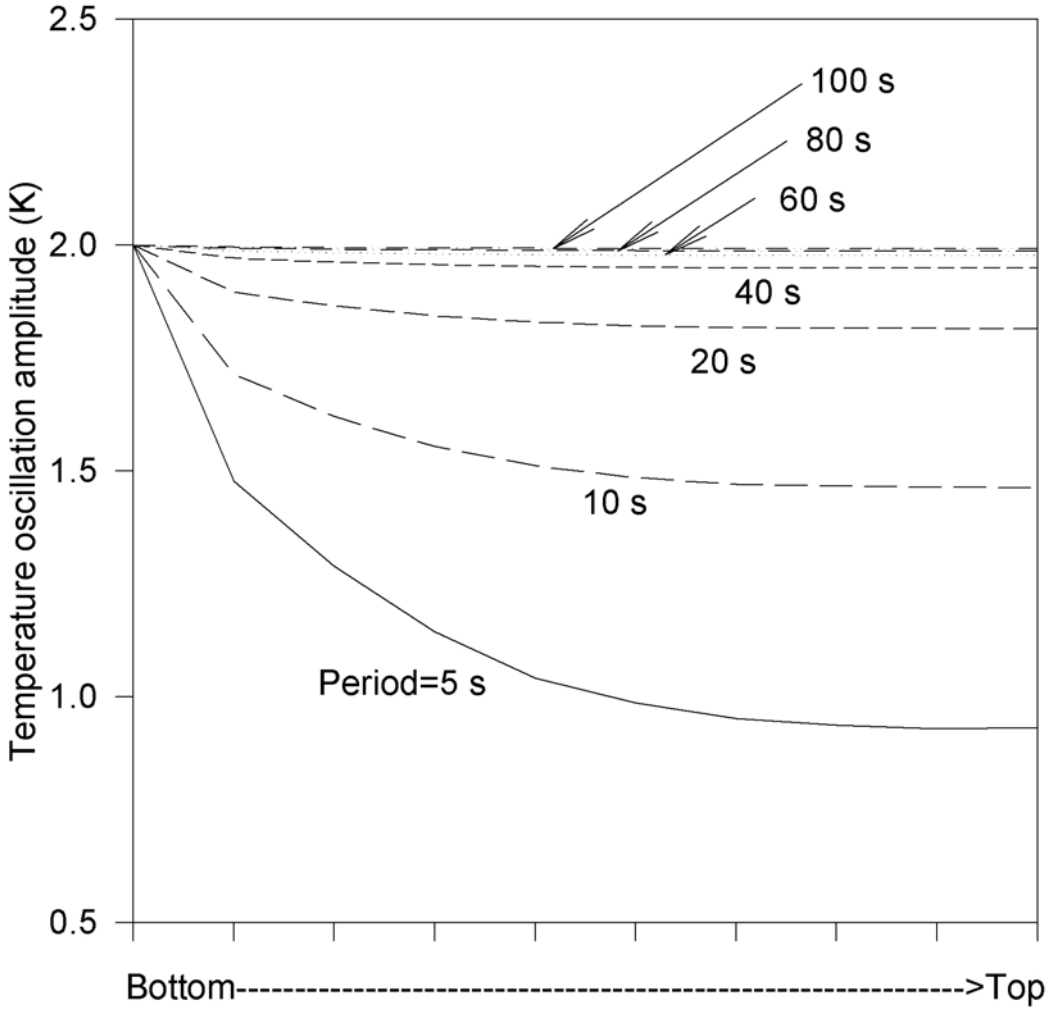

Fig. 3.7 Simulated temperature oscillation amplitude as a function of temperature modulation period in TMDSC. The programmed modulation amplitude (at the sample bottom) is 2 K. The PET sample mass is 20 mg.

Fig. 3.8 shows the relationship between the amplitude of the heat flow and the modulation period obtained from simulations, while Fig. 3.9 shows this relationship obtained from experiments. In Fig. 3.8, the amplitude of the heat flow increases as the modulation period increases before a maximum point is reached at about 10 s, then the amplitude drops with further increase in modulation period. Compared with the experimental results shown in Fig. 3.9, this trend is similar, except that in Fig. 3.9, the heat flow amplitude reaches a maximum at a different modulation period. As can be

seen in Fig. 3.9, when the temperature modulation amplitude is 0.5K, the maximum appears at a modulation period of 30 s, but when the temperature modulation amplitude is 2 K, the maximum shifts to 45 s. The shift in the peak position could be attributed to the much more complicated heat transfer properties of the TMDSC cell compared to the simple model used for the simulations.

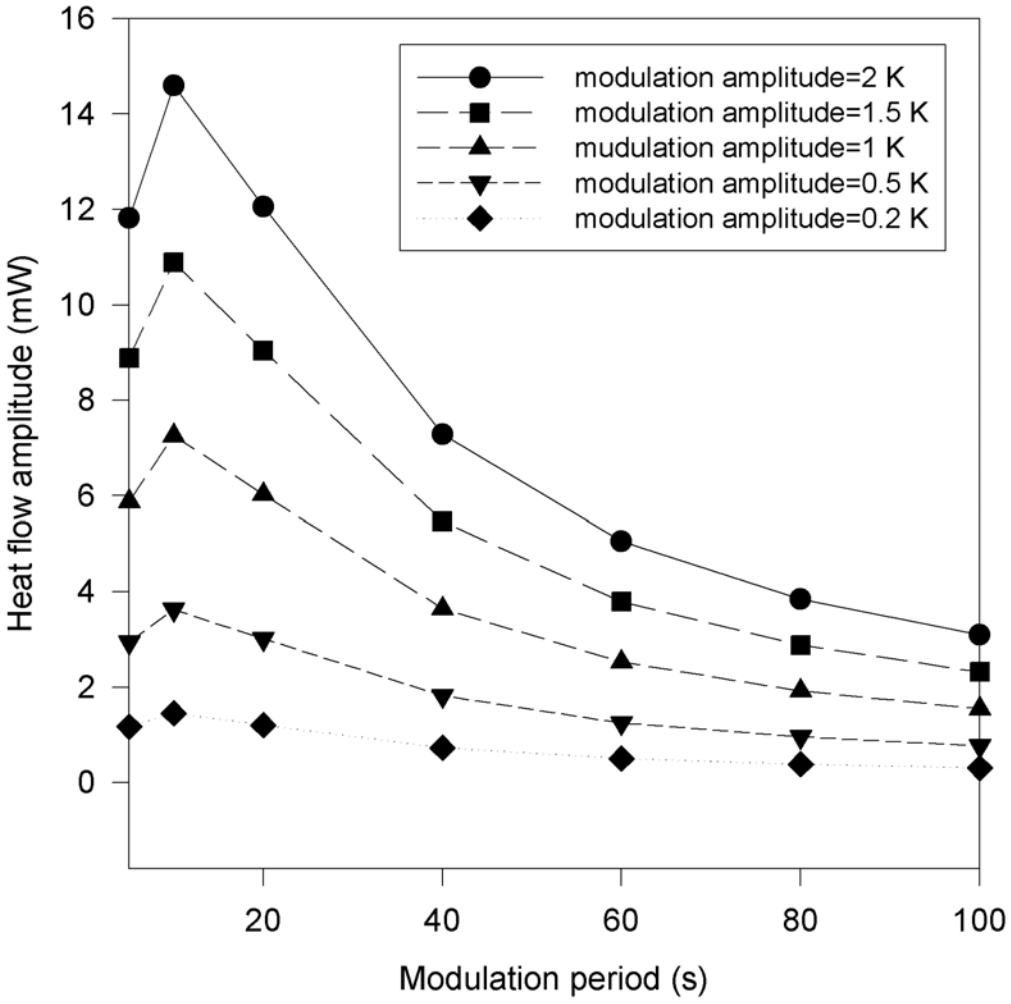

Fig. 3.8 Simulated heat flow amplitude as a function of temperature modulation period and amplitude in TMDSC. The PET sample mass is 20 mg.

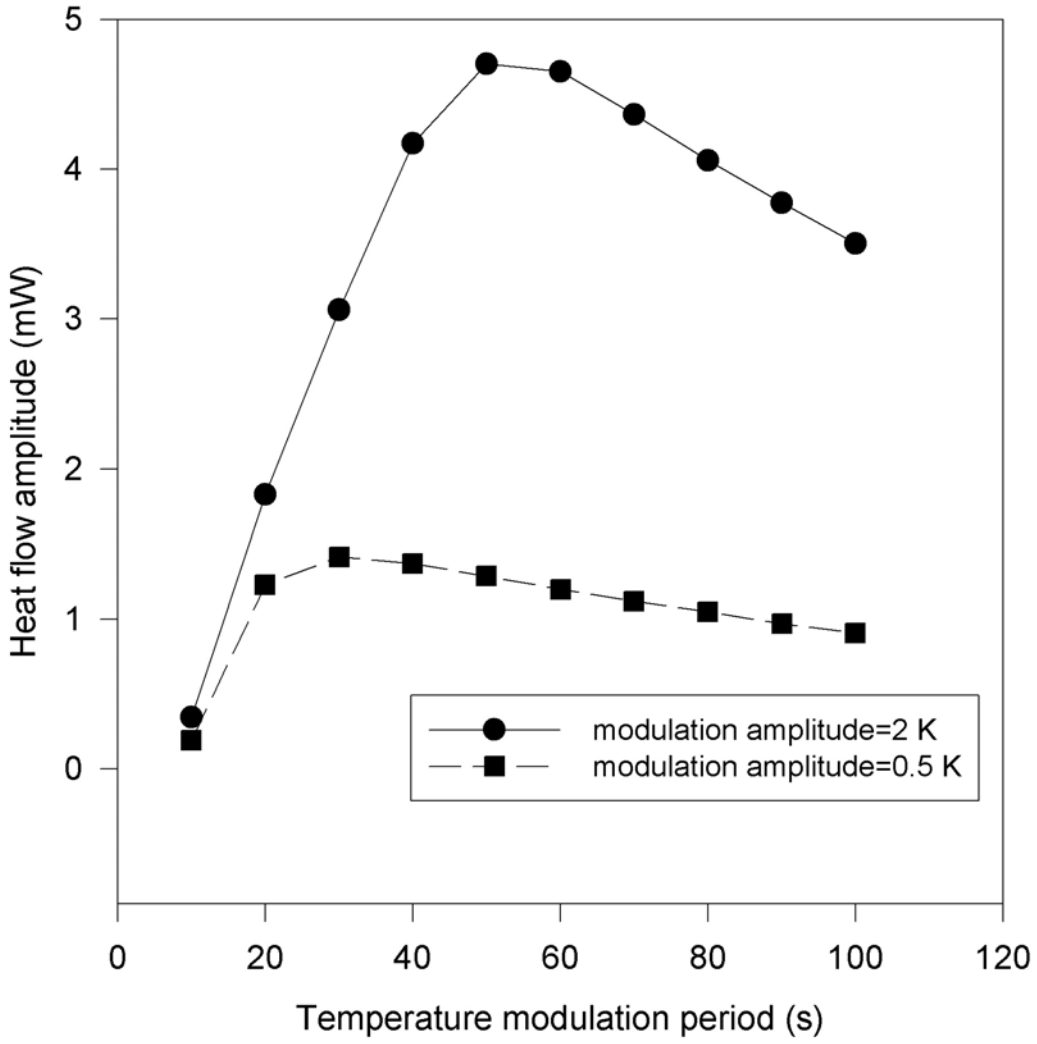

Fig. 3.9 Experimentally obtained heat flow amplitude in TMDSC. The PET sample mass is 19.6 mg.

Fig. 3.10 shows the experimentally determined relationship between the temperature modulation amplitude and the modulation period. It demonstrates the limitations on the cooling and heating capabilities of the TMDSC device. A maximum modulation amplitude of 0.5 K can be reached when the modulation period reaches 20 s and above, while a modulation amplitude of 2 K requires a modulation period of 60 s or more. However, this effect is not considered in the model used in the simulations.

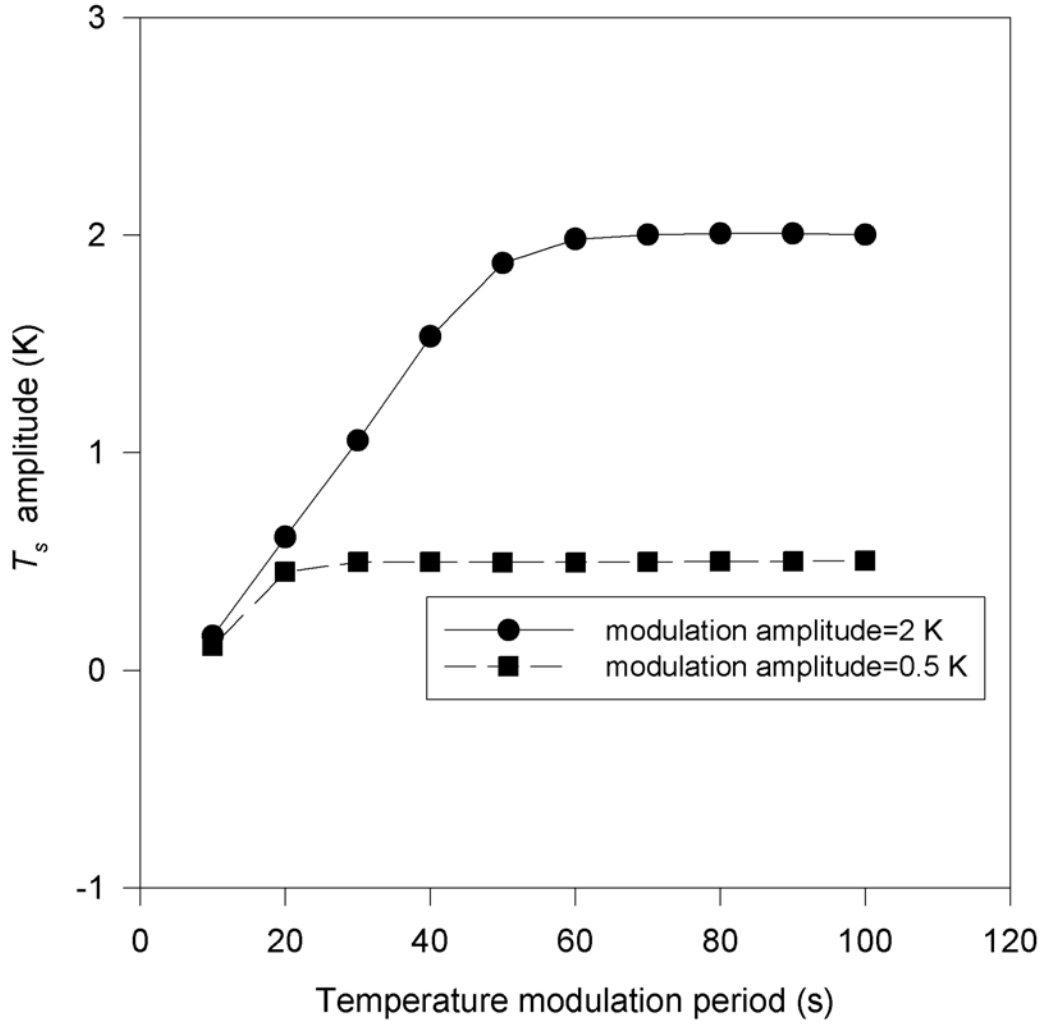

Fig. 3.10 Experimentally obtained amplitude of the sample temperature T_s as a function of the temperature modulation period and amplitude

With a sinusoidal temperature modulation, the maximum heating rate for TMDSC in quasi-isothermal state is $A\omega$, where A is the modulation amplitude and ω is the angular frequency. This produces a maximum heating rate ranging from 7.5 to 75 K/min for an amplitude of 2 K, and a maximum heating rate ranging from 1.9 K/min to 19 K/min for an amplitude of 0.5 K when the modulation period is between 10 s and 100 s. By referring to the measured curves in Fig. 3.5, it is believed that the modulation can produce a temperature difference in the order of 0.1 to 1K in the

sample. Although these values do not seem to be very large, the ratio to the modulated temperature amplitude is not negligible, which can cause significant error in the measured specific heat. Interestingly, simulation results indicate that there is a linear relationship between the modulated temperature amplitude and the heat flow amplitude. This means that for a given sample and modulation period, the accuracy of the measured specific heat is a constant regardless of the modulation amplitude. This can be explained by the characteristics of the linear equations used in the model (see Eqs. (3.18) to (3.22)). The simulated effect of the sample mass or thickness on the observed specific heat is shown in Fig. 3.11.

The measured c_p of the PET sample of 20 mg can deviate more than 20% from the value given in literatures, especially at lower modulation periods (<20s), while the situation is much better for the sample of 5 mg. As a matter of fact, the results of both the analytical method and numerical simulations, agree well with those obtained from other dynamic temperature differential scanning calorimeters such as power-compensated DSC, DDSC, and SSADSC, although the detailed algorithms and implementations are different from one another [13—15].

The relationship among the modulation amplitude, modulation period and c_p obtained from TMDSC experiments is shown in Fig. 3.12. When the programmed modulation amplitude increases from 0.5 to 2 K, the c_p does not change significantly. The relationship between the sample mass and the observed c_p agrees well with the simulation result. For the sample of 6.71 mg, the c_p curve is much more flat than that of 19.6 mg. However, when the modulation period is shorter than 15 s, the c_p increases if the modulation period decreases. This phenomenon can be explained by the contact resistance that is important in the low modulation period or high-frequency region, which was already discussed in Chapter 2. Apparently, in our

TMDSC experiments, a sample mass of 19.6 mg appears to be too large for the specific heat measurement of PET. This is because according to the results shown in Fig. 3.12, a modulation period longer than 100 s which is the upper limit of the TMSDC device is needed for the c_p curve to become relatively flat.

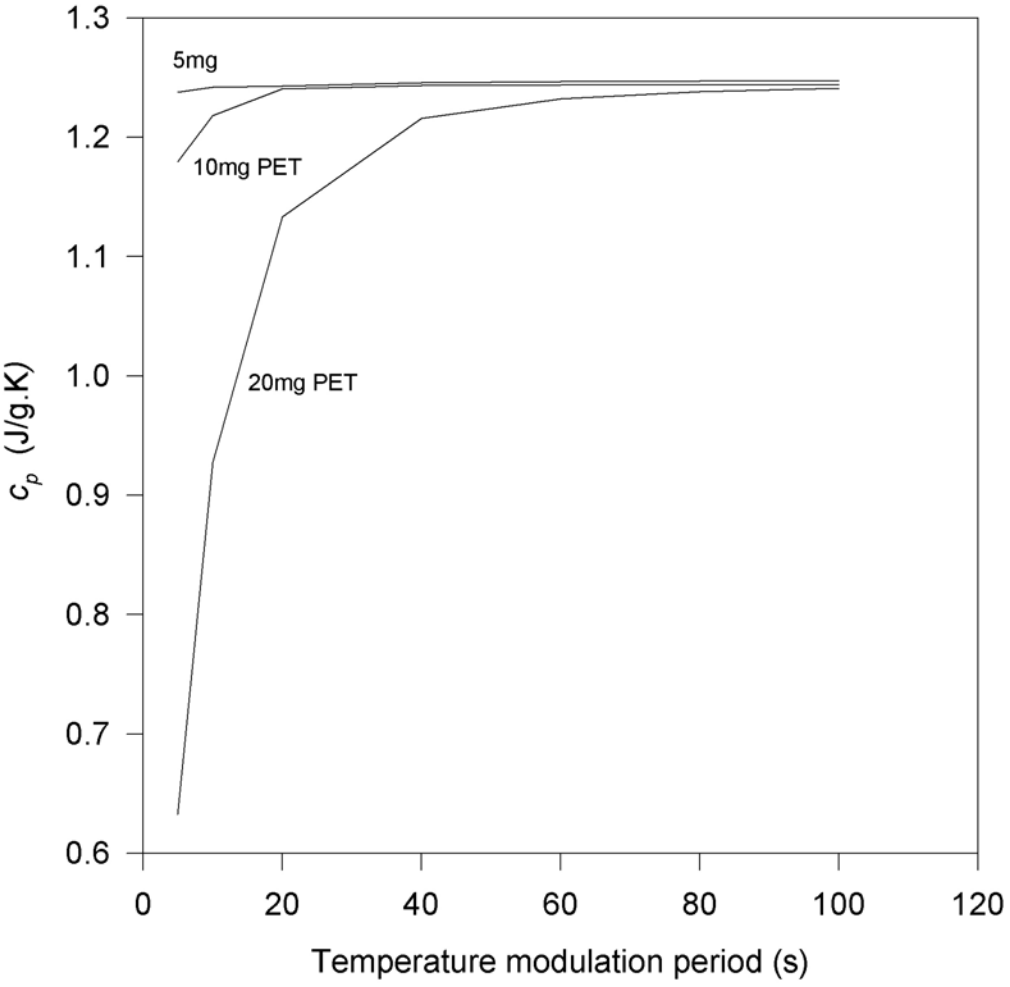

Fig. 3.11 The "measured" specific heat as a function of the temperature modulation period (obtained from simulation). The three PET samples have the same foot print, thus the smaller the mass the thinner the sample.

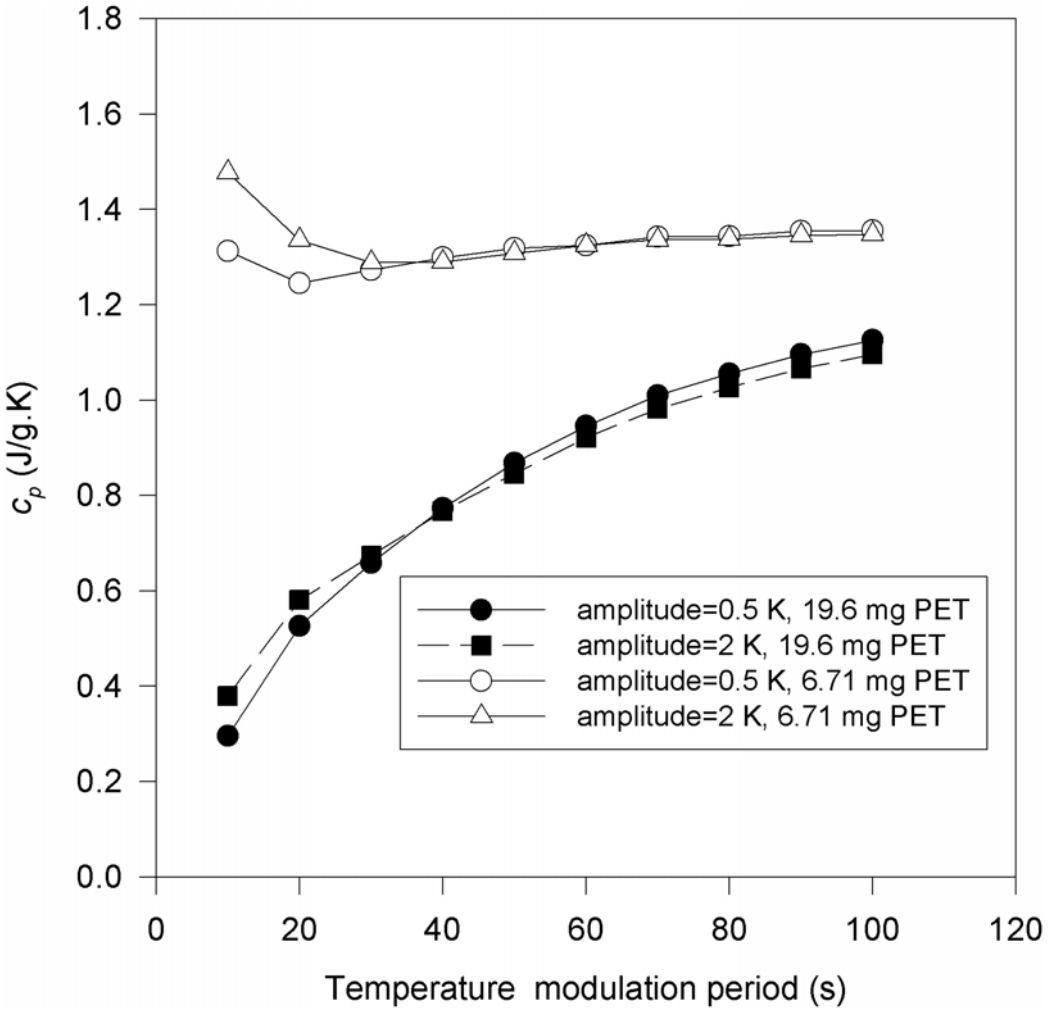

Fig. 3.12 Experimentally obtained specific heat as a function of the temperature modulation period. The thickness of the 6.71 mg sample is 0.4 mm (single layer of PET sheet), while the thickness of the 19.6 mg sample is 0.8 mm (double layer of PET sheet).

3.5 Conclusions

Although the effect of heat diffusivity of the sample on the measured specific heat normally can be ignored for metallic materials in differential scanning calorimetry, this may not always be the case for poor heat conductors. In this chapter, an analytical solution for c_p measurement in TMDSC with a sample of low thermal conductivity is derived. Numerical simulation and experiments of c_p measurement for both DSC and TMDSC using PET samples are carried out. The effects of the

temperature modulation period, thickness and thermal conductivity of the sample on the measured c_p are discussed.

Proper selection of modulation parameters can help to minimize the effect of the internal thermal resistance on the experimental results. To measure the specific heat of poor heat conductors such as polymer, fiber and wood by TMDSC, it is suggested that the sample thickness be as small as possible, e.g., a 0.2 mm thick sample is better than a 0.5 mm thick one. Also, a longer modulation period is preferred, e.g., 70 s is better than 20 s. In the case of PET the preferred sample thickness should be less than 1.0 mm with a modulation period longer than 30 s. This can reduce the error caused by the internal thermal resistance to less than 0.5%, which is valid for materials that have larger heat diffusivities than PET. For other low-heat-conducting materials, the appropriate combination of the parameters depends on their thermal diffusivities. The fact that the temperature modulation amplitude has a very small effect on the measured specific heat is a good indication of the overall system linearity of the TMDSC device, especially at large modulation periods (>50 s) that are well within its cooling and heating capabilities.

References

[1] M. Reading, J. Therm. Anal. **54** (1998) 411.

[2] A. Boller, Y. Jin, B. Wunderlich, J. Therm. Anal. **42** (1994) 307.

[3] B. Wunderlich, Y. Jin, A. Boller, Thermochim. Acta **238** (1994) 277.

[4] Z. Jiang, C. T. Imrie, J. M. Huchinson, Thermochim. Acta **315** (1998) 1.

[5] Z. Jiang, C. T. Imrie, J. M. Huchinson, Thermochim. Acta **336** (1999) 27.

[6] S. Weyer, A. Hensel, C. Schick, Thermochim. Acta **305** (1997) 267.

[7] P. Skoglund, A. Fransson, Thermochim. Acta **276** (1996) 27.

[8] F. U. Buehler, J. C. Seferis, Thermochim. Acta **334** (1999) 49.

[9] F. U. Buehler, C. J. Martin, J. C. Seferis, J. Therm. Anal. **54** (1998) 501.

[10] S. Kakac, Y. Yener, *Heat conduction*, 3rd edition, Hemisphere Pub. Corp., Washington, c1985, p.215.

[11] I. S. Grigoriev, E. Z. Meilikhov, *Handbook of Physical Quantities*, CRC Press, Inc., Boca Raton, 1977, p.253.

[12] J. Brandrup, E. H. Emergut, *Polymer Handbook*, 2nd edition, J. Wiley and Sons, New York, 1975, p.V-71.

[13] M. Merzlyakov, C. Schick, Thermochim. Acta **330** (1999) 65.

[14] B. Schenker, F. Stager, Thermochim. Acta **304/305** (1997) 219.

[15] E.-Y. Ding, R.-S. Cheng, Y.-H. Huang, Thermochim. Acta **336** (1999) 1.

Chapter 4 Numerical Modeling and Analysis of TMDSC: On the Separability of Reversing Heat Flow and Non-reversing heat flow

4.1 Introduction

Besides being able to measure the specific heat in a single run, another important capability of TMDSC is the separation of the reversing heat flow (*RHF*) from the non-reversing (or kinetic) heat flow (*NHF*), such as the *NHF* from a glass transition, a curing process and chemical reactions. This is important in identifying the kinetic processes and better characterizing materials [1—3] as the *RHF* and *NHF* signals often mix together in a conventional DSC experiment. One related issue in the separation of *RHF* and *NHF* is the reproducibility of experimental results, which has been studied by Schawe and co-workers [4, 5].

In TMDSC, depending on the actual implementation, the temperature of the heating block may satisfy the following equation

$$T_b(t) = T_0 + qt + A_{Tb}\sin(\omega t), \tag{4.1}$$

where T_0 is the initial temperature of the experiment, A_{Tb} is the oscillation amplitude of the heating block temperature, ω ($=2\pi/p$) is the angular frequency of temperature modulation, and p is modulation period, q is the underlying heating rate. Correspondingly, the sample and reference temperatures are

$$T_s(t) = T_0 + qt - \frac{qC_s}{K} + A_{Ts}\sin(\omega t - \varphi_1), \tag{4.2}$$

$$T_r(t) = T_0 + qt - \frac{qC_r}{K} + A_{Tr}\sin(\omega t - \varphi_2), \tag{4.3}$$

respectively,

where A_T and A_{Ts} are the oscillation amplitudes of the reference and the sample temperatures, respectively, K is the thermal constant, φ_1 and φ_2 are the phase angles of the sample and reference temperature, respectively.

Detailed mathematical descriptions of TMDSC are available elsewhere [6—9]. If T_0 is constant and the underlying heating rate q=0 or is small, for example, a few degrees per minute, it has been shown [6] that

$$C_{s0} - C_r = \left(\frac{A_{\Delta T}}{A_{Ts}}\right)\sqrt{\left(\frac{K}{\omega}\right)^2 + C_r^{\,2}}\,, \tag{4.4}$$

where C_{s0} is the total heat capacity of the sample and the sealing pan

$$C_{s0}=c_{p\_s}m_s + c_{p\_r}m_r\,, \tag{4.5}$$

where c_{p_s} and c_{p_r} are the specific heats of the sample and sealing pan, respectively, m_s is the sample mass, m_r is the mass of the sealing pan.

In TMDSC, the relationship among the heating rate, the total heat flow (HF), and the kinetic heat flow satisfies the general heat flow equation Eq.(1.21). As has been pointed out by Wunderlich et. al. [6—9], it is possible to measure the specific heat by deconvoluting the temperature signals even in the presence of a non-reversing heat flow. This is based on the assumption that the thermal response in TMDSC is linear or not far from the linear state. Hence the reversing heat flow can be separated from the total heat flow.

In this chapter, two different types (time dependent and temperature dependent) of non-reversing heat flows are employed in the simulations of the heat flows and temperature of the sample in TMDSC. Discrete Fourier transform and finite difference method are used to calculate the specific heat of the sample, total heat flow, reversing and non-reversing heat flows. In section 4.2, I will depict a model where a kinetic or non-reversing heat flow in the sample is taken into consideration. In section

4.3, we describe the procedure of numerical simulation and the two different types of non-reversing heat flows. The effects of the non-reversing heat flow on the specific heat of the sample are demonstrated in section 4.4.

4.2 Model of TMDSC for numerical calculations

Fig. 4.1 shows the schematic diagram of the TMDSC model used in this chapter. For simplicity, the heat exchange between the sample and the reference is neglected, plus the TMDSC cell is assumed symmetric.

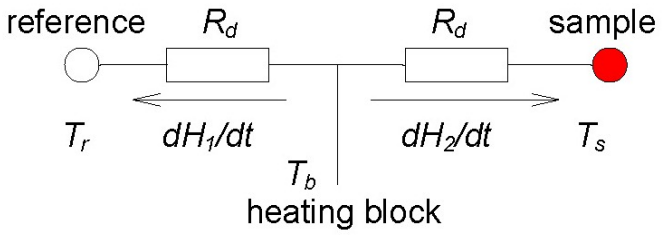

Fig. 4.1 Schematic diagram of a simplified TMDSC model. R_d is the thermal resistance between the heating block and reference or sample. dH_1/dt, and dH_2/dt are the heat flows to the reference and sample respectively

The thermal resistance between the heating block and the sample or reference is R_d and

$$K = \frac{1}{R_d}, \tag{4.6}$$

where K is the thermal constant of the TMDSC device.

The difference between this model and that given in Chapter 3 is that any temperature gradient in the sample is ignored and a non-reversing heat flow is considered in the present model. From the above assumptions, we may consider two different heating conditions of the sample in TMDSC:

(a) There is no non-reversing heat flow involved. According to Newton's law of cooling, we have

$$\frac{dH_1}{dt} = \frac{(T_b - T_r)}{R_d} = C_r \frac{dT_r}{dt} \ , \tag{4.7}$$

where, dH_1/dt is the heat flow to the reference side, T_b and T_r are the temperatures of the heating block and reference, respectively, and C_r is the heat capacity of the reference. The sealing pan is used as the reference, and $C_r = c_{p\_r} m_r$. Similarly, the following equation can also be obtained:

$$\frac{dH_2}{dt} = \frac{(T_b - T_s)}{R_d} = C_{s0} \frac{dT_s}{dt} \ , \tag{4.8}$$

where dH_2/dt is the heat flow to the sample side, T_s is the sample temperature.

Subtracting Eq. (4.7) from Eq. (4.8) yields

$$\frac{dH_2 - dH_1}{dt} = \frac{(T_r - T_s)}{R_d} = K(T_r - T_s) , \tag{4.9}$$

where $(dH_2 - dH_1)/dt$ is equal to the heat flow in or out of the sample.

(b) If there is a non-reversing heat flow, $NHF(T,t)$, during the heating or cooling process, Eq. (4.8) becomes

$$\frac{dH_2}{dt} + NHF(T,t) = \frac{(T_b - T_s)}{R_d} + NHF(T,t) = C_{s0} \frac{dT_s}{dt} . \tag{4.10}$$

With Eqs. (4.7) to (4.10), the following differential equations as the basis for subsequent simulation can be obtained.

If there is no NHF, then

$$dT_r = \frac{dH_1}{C_r} = \frac{(T_b - T_r)}{R_d C_r} dt , \tag{4.11}$$

$$dT_s = \frac{dH_2}{C_{s0}} = \frac{(T_b - T_s)}{R_d C_{s0}} dt . \tag{4.12}$$

If there is a NHF,

$$dT_r = \frac{dH_1}{C_r} = \frac{(T_b - T_r)}{R_d C_r} dt \ , \tag{4.13}$$

$$dT_s = \frac{dH_2 + NFH(T,t)dt}{C_{s0}} = \left[\frac{T_b - T_s}{R_d} + NHF(T,t)\right]\cdot\left(\frac{dt}{C_{s0}}\right). \qquad (4.14)$$

4.3 Simulation procedure and data treatment

The purpose of the simulations is to compare the "measured" and the given values of specific heat, *HF*, *RHF*, and *NHF*, and to study the separability of *RHF* from *NHF*. The simulations consist of the following steps:

(a) Set up temperature for the heating block according to a given modulated heating procedure.

(b) At a certain time in the simulation, a *NHF* which varies according to the assumed *NHF* model is introduced.

(c) Calculate the temperatures of the sample, reference, and heating block, $T_b(t)$, $T_r(t)$, $T_s(t)$, and the heat flows to the sample and reference, $dH_1(t)/dt$ and $dH_2(t)/dt$.

(d) Apply the discrete Fourier transform with a sliding transform window to find the first-order harmonics of $(T_r\text{-}T_s)$ and T_s so as to calculate the specific heat of the sample c_{p_s}, and *HF*.

(e) With c_{p_s} and *HF*, one can obtain *RHF* and *NHF*

$$RHF = c_{p\_s} m_s q, \qquad (4.15)$$

$$NHF = HF - RHF. \qquad (4.16)$$

To simulate the modulated heating, the temperature of the heating block takes the form given in Eq. (4.1). It is assumed that the specific heat of the sample, c_{p_s}, remains constant over the entire temperature range.

In the following simulations, two different *NHF*s are considered: a temperature dependent *NHF* and a time dependent *NHF*. There is an important

difference between the two *NHF*s. For the time dependent *NHF*, once the non-reversing heat flow process begins, it only varies with time but not with temperature. Hence it cannot be modulated by the sinusoidal part of the heating block temperature. The temperature dependent *NHF*, on the other hand, can be modulated by the sinusoidal part.

As a hypothetical case study, I assume that the energy distribution function of the non-reversing reaction follows

$$\int_{x_2}^{x_1} H(x)dx = E. \tag{4.17}$$

In Eq. (4.17), variable x is either time or temperature depending on the *NHF* type. The non-reversing reaction only occurs between x_1 and x_2, which means $H(x)=0$ for the region outside x_1 to x_2. E is the integrated *NHF* energy and is assumed to be a constant. To facilitate the simulation, we choose arbitrarily a periodic function for $H(x)$

$$H(x) = \frac{2Y \cdot E \cdot \sin^2\left[Y\left(x - x_0\right)\right]}{\pi}. \tag{4.18}$$

It is easy to show that $H(x)$ satisfies

$$\int_{x_0}^{(x_0+\pi/Y)} \frac{2Y \cdot E \cdot \sin^2\left[Y\left(x - x_0\right)\right]}{\pi} dx = E, \tag{4.19}$$

where x_0 is the starting time or temperature of *NHF*, $x_0+\pi/Y$ is the ending time or temperature of *NHF*, and Y is an adjustable factor of the time or temperature range of the non-reversing reaction. Here we assume $H(x)=0$ when x is outside $[x_0, x_0+\pi/Y]$.

Because the energy is fixed at E, by adjusting Y, the non-reversing reaction range can be increased to reduce the *NHF* peak value. Similarly the range can be decreased in order to enhance the *NHF* peak value, as shown in Fig. 4.2. The

simulation parameters are listed in Table 4.1. These values are from Ref. [10] or typical of those used in actual TMDSC experiments.

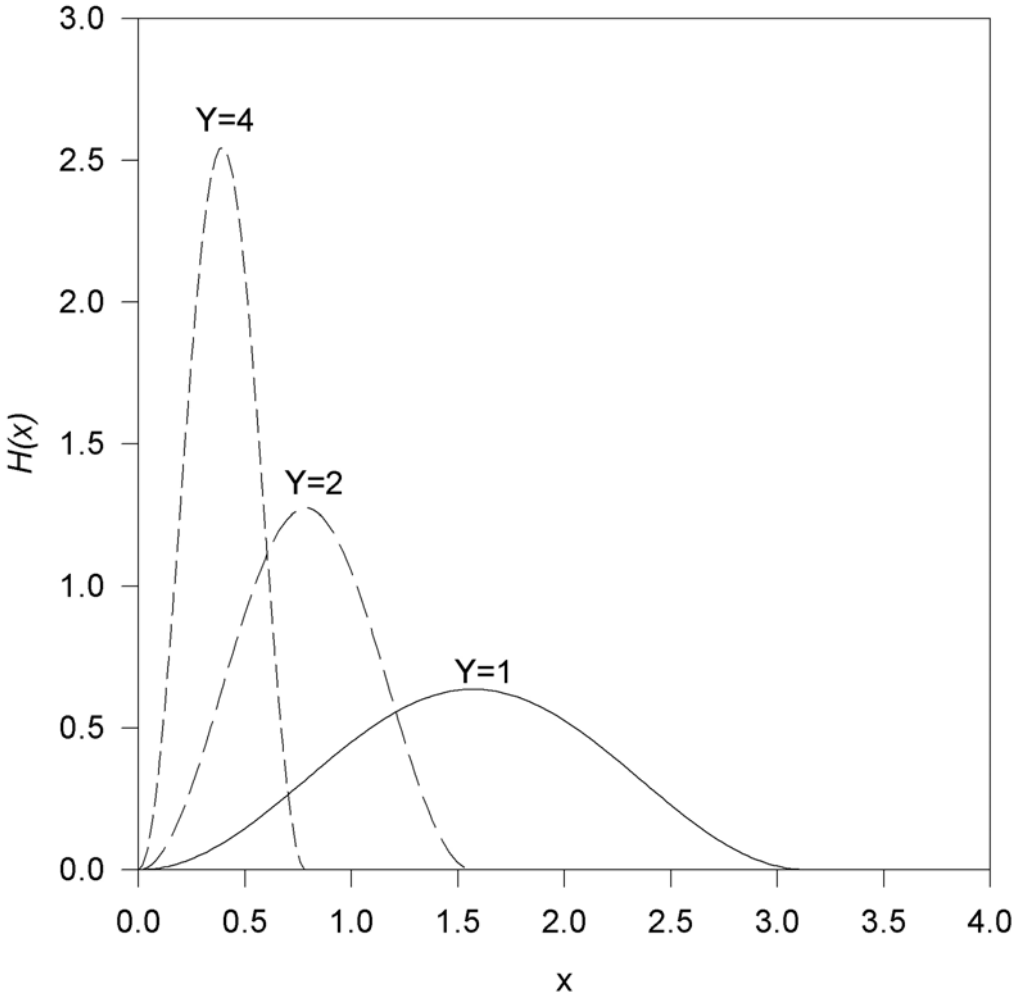

Fig. 4.2 *H(x)* vs. intensity adjusting factor *Y*. *H(x)* increases with *Y*, but the peak width decreases accordingly so that the integrated area keeps constant. *x* is either time or temperature.

The dimension for these two kinds of *H(x)* is different. For the time dependent process, *H(t)* is in J/s and Eq. (4.14) can be used directly. For the temperature dependent process, *H(T)* is in J/K and a slight modification to Eq. (4.14) is necessary

$$\Delta H_2|_{(n-1)} + H\,[T_s(t)]\,\Delta T_s|_{(n-1)} = C_{s0}\Delta T_s|_n\,, \qquad (4.20)$$

where $\Delta T_s|_{(n-1)}$ and $\Delta T_s|_n$ are the temperature increment at time $(n-1)\Delta t$ and $n\Delta t$, respectively, $\Delta H_2|_{(n-1)}$ is the heat input from the heating block at time $(n-1)\Delta t$, and Δt is the time step used in the finite difference simulation. The sample temperature at time $n\Delta t$ is

$$T_s|_n = T_s|_{(n-1)} + \{\Delta H_2|_{(n-1)} + H\,[T_s(t)]\,\Delta T_s|_{(n-1)}\}/C_{s0}\ . \qquad (4.21)$$

Table 4.1 Parameters used in numerical simulation

Parameter	Description	Value
c_{p_r}	Specific heat of aluminum reference pan (in J/g·K)	0.951 [10]
c_{p_s}	Specific heat of sample (in J/g·K)	0.134
m_r	Mass of reference and sample pan (in mg)	24
m_s	Sample mass (in mg)	20
R_d	System thermal resistance (in K/W)	100
Δt	Time step used in Finite difference method (in s)	0.0001
E	*NHF* energy (in J/g)	6
A	Amplitude of modulated temperature (in K)	0.20
p	TMDSC modulation period (in s)	30

4.4 Simulation results and discussions

4.4.1 Temperature dependent *NHF*

Figs. 4.3 and 4.4 show the c_{p_s}, *HF*, *RHF* and *NHF* of a TMDSC simulation for the temperature dependent *NHF* as discussed above. The modulation period is 30 s, the modulation amplitude is 0.2 K, and the underlying heating rate is 3 K/min. The temperature range of the *NHF* is preset between 200 and 250 ^{o}C in Fig. 4.3, while it is preset between 200 and 210 ^{o}C in Fig. 4.4.

As shown in Fig. 4.3, there are more than 10 modulation cycles in the *NHF* temperature range, while there are only 5 in Fig. 4.4. Due to the wider temperature range (50 against 10 ^{o}C), the *NHF* peak value of ~0.2 mW in Fig. 4.3 is lower than the

peak value of ~2 mW in Fig. 4.4. Since the integrated *NHF* energy is 6 J/g in both cases, it takes a longer time (17 against 3.3 min) to complete the non-reversing reaction. Hence Fig. 4.3 represents a slow kinetic process. Compared with that of Fig. 4.3, Fig. 4.4 represents a faster non-reversing reaction.

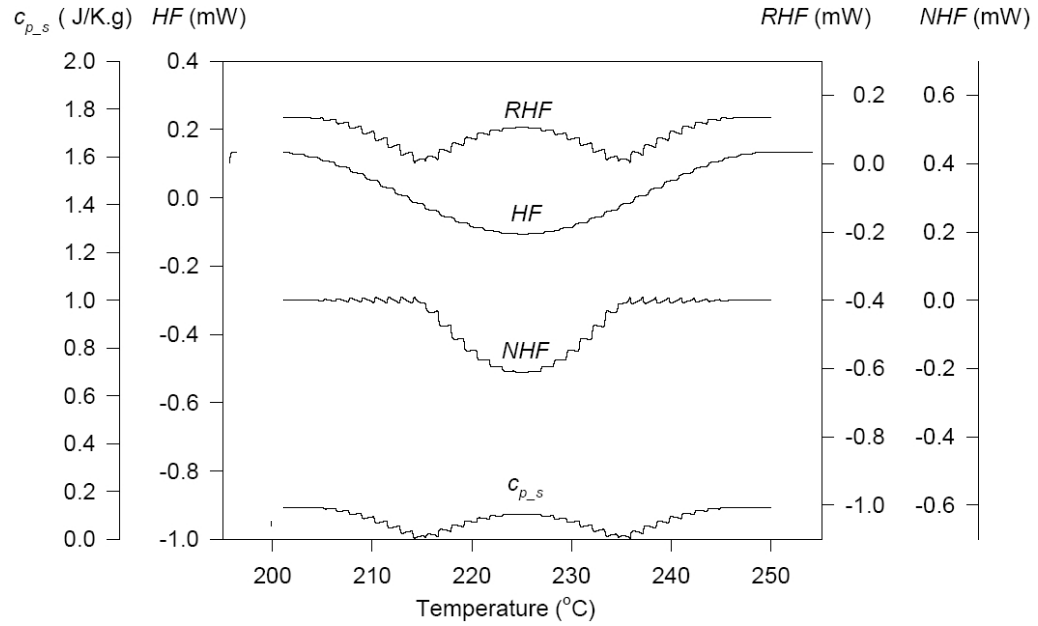

Fig. 4.3 c_{p_s}, *HF*, *RHF*, and *NHF* as a function of temperature for a temperature dependent *NHF*, with more than 10 modulation cycles in the *NHF*.

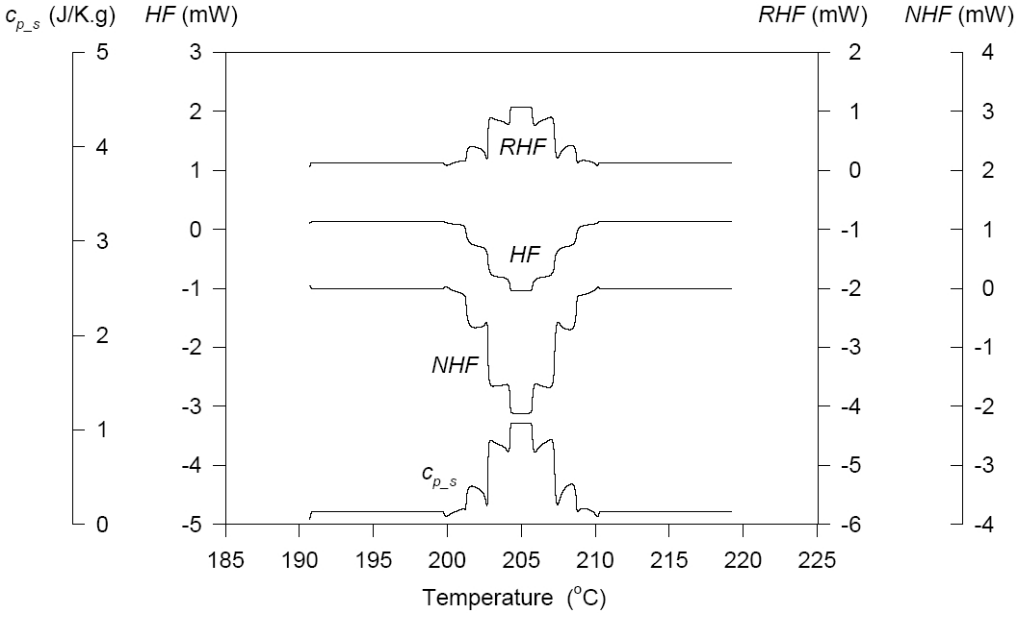

Fig. 4.4 c_{p_s}, *HF*, *RHF*, and *NHF* as a function of temperature for a temperature dependent *NHF*, with only 5 modulation cycles in the *NHF*.

As shown in both Figs. 4.3 and 4.4, the c_{p_s} can be accurately obtained at a steady state where *NHF* is absent. Once the *NHF* is introduced, the exact c_{p_s} can no longer be obtained. The shape of c_{p_s} shown in Fig. 4.3 is different from that in Fig. 4.4: in Fig. 4.3, two "valleys" appear in the c_{p_s} with a "hump" in-between, while in Fig. 4.4, a strong peak appears in the c_{p_s} with a maximum of 1.3 J/g·K. This is much larger than the c_{p_s} under steady state conditions, which is only 0.134 J/g·K.

From the above simulations, it seems that when a temperature dependent *NHF* is mixed with the *RHF*, they cannot be effectively separated from each other by TMDSC. One may draw a conclusion that the TMDSC system is not working in a linear state due to the temperature dependence of the *NHF*. As a result, significant deviations appear in the measured specific heat.

4.4.2 Time dependent *NHF*

Figs. 4.5 and 4.6 show the c_{p_s}, *HF*, *RHF* and *NHF* of the time dependent non-reversing reaction. The modulation period is 30 s, the modulation amplitude is 0.2 K, and the underlying heating rate is still 3 K/min. The time range of the *NHF* is preset between 200 and 800 s for those shown in Fig. 4.5, while it is between 200 and 400 s for those shown in Fig. 4.6. The c_{p_s} at a steady state both before and after the non-reversing reaction remains the same as the value given in Table 4.1 (0.134 J/g·K). This demonstrates that the specific heat of a sample can be effectively measured with a single run in TMDSC if there no *NHF* during the heating or cooling.

As shown in Fig. 4.5, there are over 15 modulation cycles in the *NHF* time range, the "measured" c_{p_s} has a deviation of less than 0.1 J/g·K from the value at steady state. While in Fig. 4.6, there are only 6 modulation cycles, the deviation in the "measured" c_{p_s} is increased to ~0.3 J/g·K. It is obvious that with further data

smoothing, such as averaging c_{p_s} over a sliding window, the "measured" c_{p_s} can be fairly close to the value at steady state, even if there is a *NHF* as illustrated in Fig. 4.5.

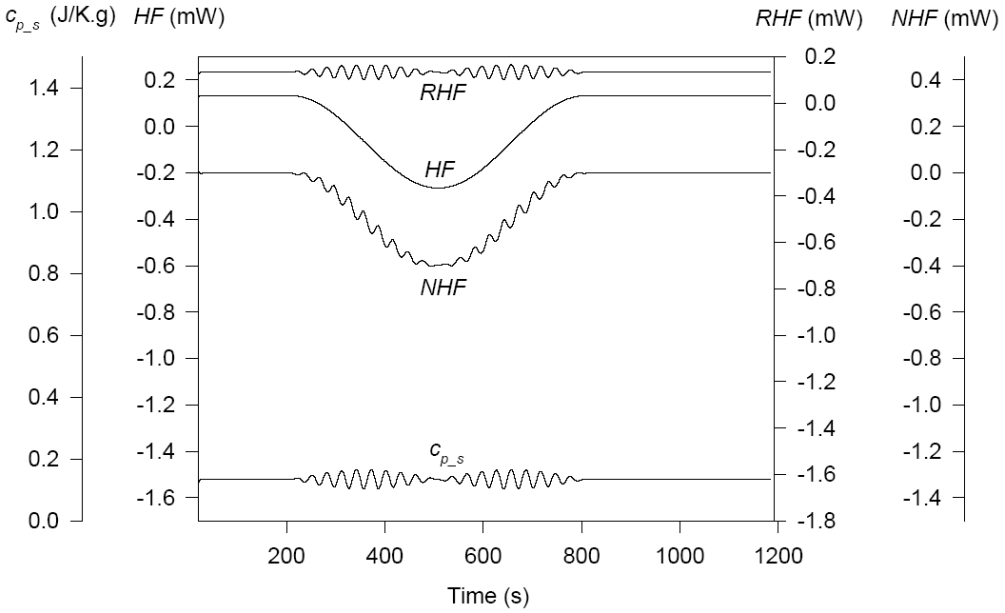

Fig. 4.5 c_{p_s}, *HF*, *RHF*, and *NHF* as a function of temperature for a time dependent *NHF*, with more than 10 modulation cycles in the *NHF*.

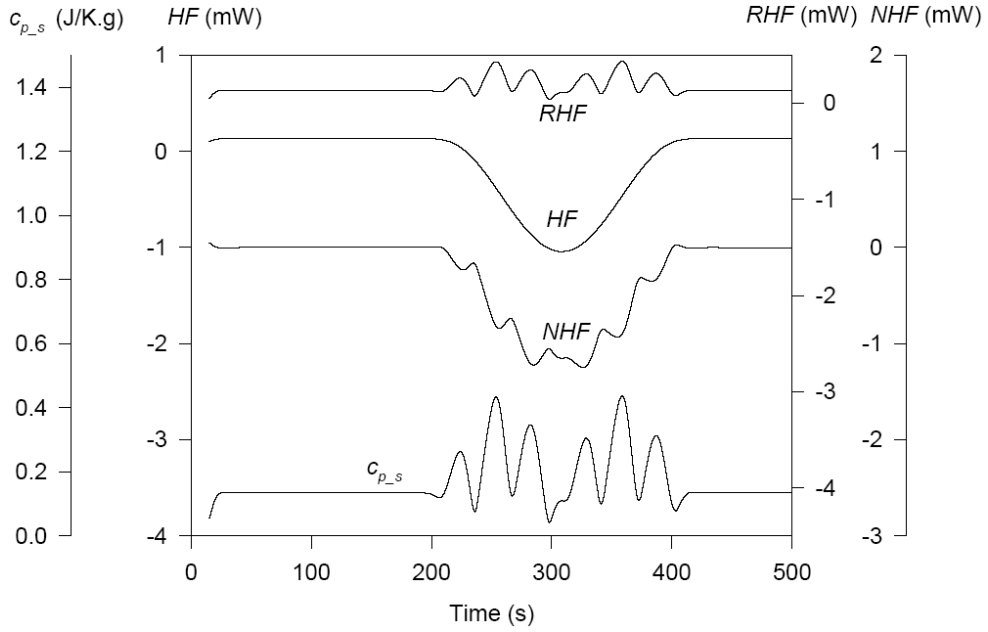

Fig. 4.6 c_{p_s}, *HF*, *RHF*, and *NHF* as a function of temperature for a time dependent *NHF*, with only 6 modulation cycles in the *NHF*.

Lacey et al. [11] obtained analytical solutions of specific heat where the *NHF* is a chemical reaction that is both time and temperature dependent. With a number of mathematical approximations in the analysis, they showed that the "measured" specific heat of the sample had deviations during an endothermic reaction where it was assumed that the specific heat stays constant. It was noticed that the deviations in the specific heat were decreased by increasing the modulation frequency. This agrees well with the results of the simulations as indicated in Fig. 4.5 and 4.6. For reactions that take a long time (relative to the modulation period) to complete, it is feasible to obtain a better measurement of specific heat by increasing the modulation frequency. For other reactions that complete in a much shorter time or in a narrow temperature range, there are some limitations. The thermal inertia of the TMDSC device and temperature resolution already set a lower limit to the modulation period. For example, the suggested minimum modulation period for TA Instruments DSC&TMDSC2920 is 10 s. The temperature gradient in the sample also increases with increasing frequency. These factors could contribute to the errors in the measurement of c_{p_s}. Furthermore, according to the results shown in Figs. 4.3 and 4.4, even if there are no limitations to the modulation frequency, whether the measured specific heat can accurately reflect the actual specific heat still depends on the characteristics of the reaction itself. That is, the time and temperature dependence of the *NHF*.

From the above simulations, it can be seen that even for time dependent kinetic processes, there is still a frequency limit within which reasonably accurate separation can be achieved. For a completely time dependent non-reversing heat flow, we have $\partial f(t,T)/\partial T=0$ and $f(t,T)=f(t)$. In a single Fourier transform window (t_0, t_0+p), which has the same duration as the modulation period, p, if the non-reversing heat flow, $f(t)$, can be linearized, then we can approximate $f(t)$ with the following,

$$f(t) \approx \left[f(t_0 + p) - f(t_0)\right] \cdot \left[\frac{1}{2} - \frac{1}{\pi}\sum_{n=1}^{\infty}\frac{1}{n}\sin(n\omega t)\right]. \qquad (4.22)$$

Equation (4.22) also contains a first harmonic contribution from the non-reversing heat flow, which is determined by the change of $f(t)$ in a modulation cycle. The first harmonic in Eq. (4.22) is mixed with the reversible heat flow from the heat capacity of the sample. To improve the accuracy of the experiment, we may need to reduce this first harmonic contribution. Apparently, reducing the width of the transform window or the modulation period reduces $f(t_0+p)$-$f(t_0)$. However, this has no influence on the measured specific heat. Thus the reversing heat flow can be more effectively separated from the non-reversing heat flow.

4.4.3 Effect of the underlying heating rate

With an underlying heating rate q, comes the underlying heat flow from the heat capacity of the sample, qC_s, which is a first order thermal response. A lower underlying heating rate seems beneficial to improving the separability of *HF* and *NHF* according to Eq. (4.22). Fig. 4.7 shows the results of deconvoluted specific heat with an underlying heating rate of 1, 5, and 10 K/min, respectively. The total time for non-reversing reaction is set to 600 s. For a modulation period of 30 s, this duration can accommodate 20 modulation cycles regardless of the underlying heating rate. Oscillations in the c_{p_s} in the *NHF* region are quite similar among the three conditions. With increased underlying heating rate, ripples begin to appear outside the *NHF* region. Hence, a slower underlying heating rate produces more stable results of c_{p_s}, and the step-wise quasi-isothermal TMDSC technique may be the most favorable since the underlying heating rate is zero on each individual temperature step.

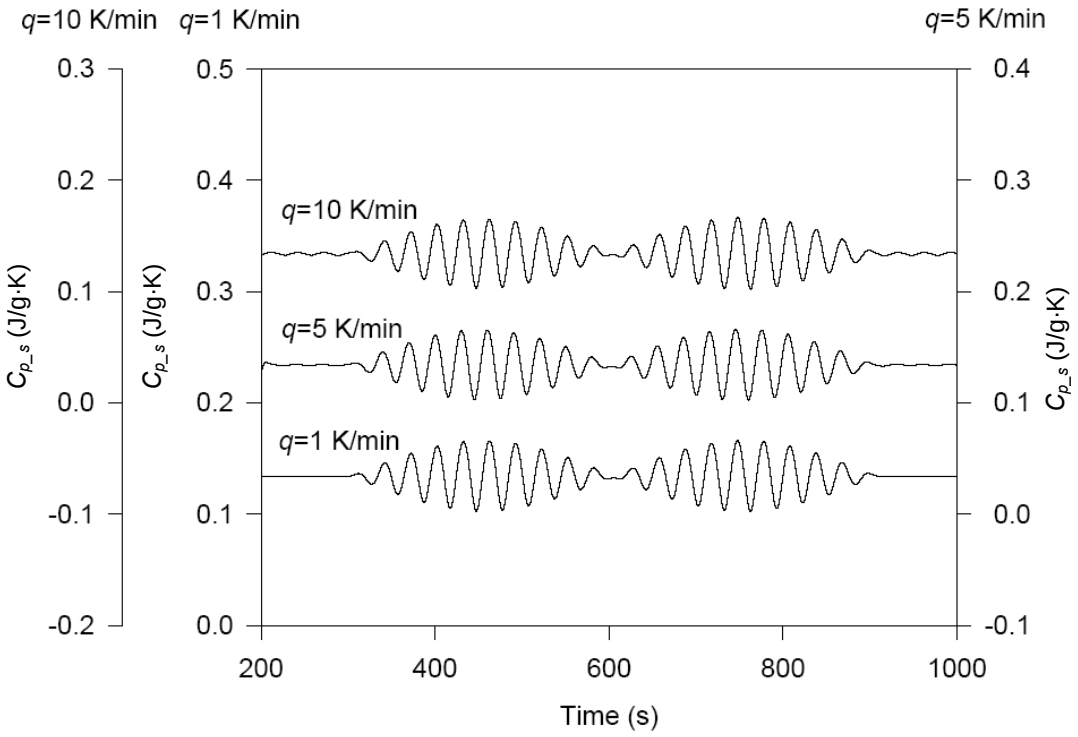

Fig. 4.7 c_{p_s} for the time dependent kinetic event with different underlying heating rates. Vertical axes are the c_{p_s} of different heating rates.

Fourier transform is applicable to linear response systems [12, 13]. For satisfactory results to be obtained the entire system, including the measurement device and the sample to be tested, must meet the linear superimposition principle.

In a real experiment, *NHF* may come from chemical reactions, kinetic reactions such as crystallization from an amorphous state, re-crystallization, or their combinations. The resultant *NHF* could be much more complicated than those described in this chapter. Furthermore, the specific heat of the sample may change in the non-reversing reaction, depending on the characteristics of the *NHF*. Thus, the TMDSC system may not behave in a linear fashion. In this case, although qualitative separation of reversing and non-reversing heat flow is possible, quantitative separation still remains a challenge.

4.5 Conclusions

From the above studies, the "measured" or "observed" specific heat of a sample is dependent on the *NHF* and the parameters of temperature modulation. The measurement of specific heat is applicable for steady state where there is no *NHF*. If *NHF* is time dependent and the modulation frequency is high enough, it still allows determination of the specific heat, *HF*, *RHF*, and *NHF* by Fourier transform. The effect of temperature dependent *NHF* on the heating or cooling process is non-linear and can influence the thermal response of TMDSC to such an extent that the measured specific heat of the sample can no longer accurately reflect its true value.

References

[1] M. Reading, D. Elliott, V. L. Hill, J. Therm. Anal. **40** (1993) 949.

[2] P. S. Gill, S. R. Sauerbrunn, M. Reading, J. Therm. Anal. **40** (1993) 931.

[3] M. Reading, United States Patent Number 5,224,775, Jul. 6, 1993.

[4] J. E. K. Schawe, Thermochimica Acta **271** (1996) 127.

[5] J. E. K. Schawe, G. W. H. HÖhne J. Therm Anal **46** (1996) 893.

[6] B. Wunderlich , Y. Jin, A. Boller, Thermochimica Acta **238** (1994) 277.

[7] A. Boller, Y. Jin, B. Wunderlich, J. Therm Anal. **42** (1994) 307.

[8] M. Varma-Nair , B. Wunderlich, J. Therm Anal. **46** (1996) 879.

[9] B. Wunderlich, J. Therm Anal. **48** (1997) 207.

[10] I. S. Grigoriev, E. Z. Meilikhov, *Handbook of Physical Quantities*, CRC Press, Inc., Boca Raton, 1977.

[11] A. A. Lacey, C. Nikolopoulos, M. Reading, J. Therm. Anal. **50** (1997) 279.

[12] T. Ozawa, K. Kanari, Thermochimica Acta **288** (1996) 39.

[13] B. Wunderlich, A. Boller, I. Okazak, S. Kreitmeier, Thermochimica Acta **282/283** (1996) 143.

Chapter 5 System Linearity and the Effect of Kinetic Events on the Observed Specific Heat

5.1 Introduction

There has been much interest in applications of TMDSC in materials research, such as the measurement of heat capacity and thermal conductivity, studies on crystallization and melting, as indicated by the large number of papers published in the last ten years [1—11]. Analysis of TMDSC data is based on a linear response assumption, a pre-requisite of Fourier transform. This places a stringent requirement on the TMDSC device. The first-order harmonics of heat flow and sample temperature signals are employed using Fourier transform to calculate the specific heat of the sample and phase angles of the heat flows [1, 4, 8, 10]. If the experimental parameters are not chosen properly or the thermal response is non-linear or deviates from the thermal equilibrium due to the reaction kinetics, the measured or observed specific heat can be different from the actual value.

In this chapter, the importance of linearity in TMDSC is demonstrated through analytical as well as numerical analyses. In section 5.2, I will present a general solution to the thermal conduction equation of TMDSC through linearization when a kinetic event is considered. In section 5.3, several common kinetic models and the effects of the kinetic events on the reversing heat flow (*RHF*) as well as non-reversing heat flow (*NHF*) are analyzed. TMDSC experiments on several aluminum-based amorphous alloys are also performed to substantiate the results of the theoretical analyses. The TMDSC results and the effects of the kinetic events on the observed specific heat are discussed in section 5.4.

5.2 Analysis of complex heat capacity and the effect of kinetic events

In this section, we discuss a general situation of TMDSC in which a time and temperature dependent kinetic event is included. We also discuss the physical implications of the complex heat capacity and the importance of the system linearity in the interpretation of the measured heat capacity. We choose a typical heat flux type TMDSC device in our discussion. A similar analysis can be carried out for a power compensation type TMDSC.

If the thermal constant between the heating block and the reference or sample is K, the existence of a temperature gradient in the sample and the heat exchange between the sample and purge gas are ignored, the following general differential equation of heat transfer in TMDSC can be obtained [12, 13]:

$$C_r\left(\frac{d\Delta T}{dt}\right)+K\Delta T=C_s\left(\frac{dT_s}{dt}\right), \tag{5.1}$$

where ΔT is the difference between the sample temperature (T_s) and the reference temperature (T_r). C_s and C_r are the heat capacities of the sample and reference, respectively, and t is time. In the presence of a kinetic event, $f(t,T)$, on the sample side, Equation (5.1) becomes

$$C_r\left(\frac{d\Delta T}{dt}\right)+K\Delta T=C_s\left(\frac{dT_s}{dt}\right)+f(t,T_s)\,. \tag{5.2}$$

The kinetic event can be a chemical reaction or a crystallization process and in general it can depend on both time and temperature. In TMDSC, the temperature of the heating block is often modulated so that the sample temperature consists of a linear part and a sinusoidal variation, which is also valid in the presence of the kinetic event,

$$T_s=T_0+qt+A_{Ts}\sin(\omega t)\,. \tag{5.3}$$

Substituting Eq. (5.3) into Eq. (5.2), we have

$$C_r\left(\frac{d\Delta T}{dt}\right)+K\Delta T=C_s\left[q+A_{Ts}\omega\cos(\omega t)\right]+f\left[t,T_0+qt+A_{Ts}\sin(\omega t)\right]. \quad (5.4)$$

Equation (5.4) suggests that although the kinetic event, $f(t,\ T)$, is a function of both time and temperature, the two variables t and T are now linked together by the modulation condition as defined in Eq. (5.3). Thus, $f(t,T)$ is only a function of a single variable, t. If the temperature modulation amplitude A_{Ts} is small, (e.g., 0.2 K), then $f\,[t,T_0+qt+A_{Ts}\sin(\omega t)]$ may be approximated by

$$f\left[t,T_0+qt+A_{Ts}\sin(\omega t)\right]\approx f(t,T_0+qt)+f_T'(t,T_0+qt)A_{Ts}\sin(\omega t), \quad (5.5)$$

where f_T' is the first-order derivative of temperature.

It is difficult, if not impossible, to derive an analytical solution to Eq. (5.4) and obtain the heat capacity of the sample in the general case. However if the perturbation by the kinetic event is small, we may obtain an approximate solution. If we assume that the kinetic reaction takes a long time to complete so that both $f(t,T_0+qt)$ and f_T' (t,T_0+qt) change little during one or even more modulation cycles, both functions can then be roughly treated as "constants" in Eq. (5.5). Furthermore, we may assume the underlying heating rate is only a few degrees per minute or even slower, which is typical of TMDSC experiments, and the heat capacity of the sample remains constant. As a result, equation (5.4) becomes a simple linear differential equation based on these assumptions. Substituting Eq. (5.5) into Eq. (5.4), one can easily derive the cyclic part of the general solution to Eq. (5.4)

$$\Delta T_{cyclic}=\frac{A_{Ts}}{\sqrt{(K^2+\omega^2{C_r}^2)}}\left[C_s\omega\cos(\omega t+\varphi)+f_T'(t,T_0+qt)\sin(\omega t+\varphi)\right], \quad (5.6)$$

where φ is the phase angle and φ=arctan($-\omega C_r/K$). This phase angle would be the same with or without the kinetic event.

Since f_T' is nearly a constant in each modulation cycle, equation (5.6) can be further simplified

$$\Delta T_{cyclic} = \frac{A_{Ts} C_s}{\sqrt{\left(\frac{K}{\omega}\right)^2 + C_r{}^2}} \left[\cos(\omega t + \varphi) + \frac{f_T'}{C_s \omega} \sin(\omega t + \varphi) \right]$$

$$= \frac{A_{Ts} C_s}{\sqrt{\left(\frac{K}{\omega}\right)^2 + C_r{}^2}} \sqrt{1 + \left(\frac{f_T'}{C_s \omega}\right)^2} \cos(\omega t + \varphi - \delta), \qquad (5.7)$$

where δ is the additional phase angle caused by the kinetic event, and

$$\cos\delta = \frac{1}{\sqrt{1 + \left(\frac{f_T'}{C_s \omega}\right)^2}}, \qquad (5.8)$$

$$\sin\delta = \frac{\frac{f_T'}{C_s \omega}}{\sqrt{1 + \left(\frac{f_T'}{C_s \omega}\right)^2}}. \qquad (5.9)$$

The right-hand side of Eq. (5.6) consists of two terms which represent two different sources of temperature changes. The first term $C_s \omega \cos(\omega t + \varphi)$ is related to the heat capacity of the sample, corresponding to the so-called non-cooperative atomic motion that has a relaxation (or response) time in the order of 10^{-13} s [14]. This atomic motion is much faster compared with the temperature modulation period. Thus the atomic motion follows instantaneously the external temperature modulation. The heat flow related to this motion is commonly known as the *RHF*. The second term [$f_T'(t, T_0 + qt)\sin(\omega t + \varphi)$] is contributed by the temperature sensitivity of the kinetic event, such as a glass transition in a polymer, corresponding to the motions of large

organic molecules. The corresponding relaxation or response time can be comparable to the temperature modulation period.

In the presence of a kinetic event, $f(t,T)$, the measured heat capacity is determined from Eqs. (2.1) and (5.7), which is affected by both the heat capacity of the sample and the kinetic event

$$|C^*| = \frac{A_{\Delta T}}{A_{Ts}}\left(\frac{K}{\omega}\right)\sqrt{1+\left(\frac{C_r\omega}{K}\right)^2}\sqrt{1+\left(\frac{f_T'}{C_s\omega}\right)^2}\ . \tag{5.10}$$

Symbol C^* on the left hand side of Eq. (5.10) is complex and defined as a complex heat capacity. With this complex heat capacity and Eqs. (5.8), (5.9), and (2.1), we can obtain the reversing (also called "in-phase" or real) heat capacity and non-reversing (called "out-of-phase" or imaginary) heat capacity separately:

$$C' = C_s = |C^*|\cos\delta\ , \tag{5.11}$$

$$\frac{f_T'}{\omega} = |C^*|\sin\delta\ . \tag{5.12}$$

Since the complex heat capacity is defined as $C^*=C'-iC''$, the imaginary part, C'', is

$$C'' = -\frac{f_T'}{\omega}\ . \tag{5.13}$$

It should be noted, however, that the concept of complex heat capacity is still controversial [15—17] as has been discussed in Chapter 1 because it can be a result of insufficient heat diffusion in some materials with low thermal conductivity such as polymers, wood, glass and fiber. A significant thermal gradient can be developed in such materials, causing an additional phase lag which influences the measured heat capacity, HF, RHF and NHF by TMDSC.

By definition, heat capacity is the heat energy needed to raise the temperature of a substance by 1 K or 1 ^{o}C. Besides, heat capacity is related to the internal

vibrational and translational motions of the sample, which are thermodynamic in nature. These motions are normally very fast and can immediately follow any external temperature changes. The energy stored in these motions is fully reversible, which means that the energy absorbed when the temperature is increased by 1 K can be completely released by reducing the temperature by 1 K. That is why the heat flow related to the heat capacity is called reversing heat flow and "in phase" with the temperature modulation. Given that the temperature modulation period is in the 10-second magnitude as often seen in a TMDSC device, a kinetically hindered event, even if it is reversible over a certain temperature range, takes a significantly longer time that may be comparable to the modulation periods to respond to the external temperature changes. Due to the fact that the measured heat capacity in Eq. (5.10) is not solely dependent on the heat capacity itself, complex heat capacity may be an appropriate term to describe it. If the phase angle δ is close to zero, then the heat capacity cab be approximated by the complex heat capacity according to Eq. (5.11).

To obtain the real and imaginary part of the complex heat capacity, and hence the *RHF* and *NHF*, we have to find the phase angle introduced by the kinetic event. This requires an approach to filter out the phase lag caused by the thermal transfer from the phase angle information. Reading and Luyt [18] proposed a baseline method that was realized by subtracting an interpolated straight line between the start and end point of the kinetic transition (see Fig. 1.19, as discussed in Chapter 1). Weyer et al. [19] proposed another method that used the c_p to deduce a fitting baseline to find the phase angle due to the kinetic event (Fig. 1.20). Nevertheless, linearity is assumed in the phase angle calculation. Without this basic pre-requisite, Equation (5.6) can result in an unpredictable error to the solution of Eq. (5.4). The heat capacity of the sample, C_s, appears on the right-hand side of Eq. (5.10), which can introduce an error to C^*

because C_s is an item that has to be measured. Although increasing the temperature modulation frequency can reduce the error in the measured heat capacity, the available modulation frequency is typically restricted to only 0.01 to 0.1 Hz due to the thermal inertia of the TMDSC system. This modulation frequency range is much narrower than those available in other dynamic methods such as dynamic mechanical analysis (DMA). However, as long as the relationship between the kinetic event and modulation parameter selection satisfies

$$\left(\frac{f_T'}{C_s\omega}\right)^2_{\max} << 1, \tag{5.14}$$

the heat capacity of the sample can still be measured and the RHF can be separated from the total heat flow (HF) with relatively small uncertainties. This is where TMDSC is advantageous compared to the conventional DSC. If the condition required by Eq. (5.14) is not satisfied, significant deviation from the actual value in the measured heat capacity may occur.

The physical interpretation of the imaginary part of the complex heat capacity, C'', is still controversial and several different explanations have been proposed, as has been discussed in the literatures [20—23]. However, according to Eq. (5.13), it is obvious that C'' is introduced by the kinetic event and depends on the modulation frequency. More precisely, C'' reflects the sensitivity of $f(t,T)$ to the temperature change and should not be directly correlated with the value of $f(t,T)$. In other words, even if $C''=0$, it does not necessarily mean $f(t,T)=0$. In view of this, we may say that the imaginary part or C'' is not really a type of heat capacity in a strict sense.

From the above analysis, it can be seen that the key to a successful measurement of the heat capacity is the system linearity, which includes the linearity of the TMDSC device and the linearity of the thermal response to the kinetic event.

That is, a system function, $F(x)$ should satisfy $F(a+b)=F(a)+F(b)$ and $F(kx)=kF(x)$; the system can then be described by linear differential equations. Any kinetic event added to the right hand side of Eq. (5.4) that meets this condition has its corresponding linear component in the total heat flow, and Fourier transform can be used here in the data analysis. Furthermore, for a complete deconvolution by Fourier transform that takes into account the additional phase angle caused by the kinetic event, the key issues are still "small perturbation" and system linearity. Obviously, if Eq. (5.14) cannot be met due to improper experimental parameter selection, or the kinetic event itself, Eqs. (5.7) to (5.12) are no longer true and Fourier transform will produce mathematical artifacts which may lead to inconsistent conclusions. Below, several models of chemical reactions are used in the simulations to support this point of view.

5.3 Case studies on several kinetic models

In this section, we further illustrate the importance of system linearity in the measurement of specific heat, the separation of *RHF* and *NHF* in TMDSC with several commonly used kinetic models and discuss the conditions for successful applications of TMDSC. First, we discuss the case of TMDSC where there is a first-order decomposition process in the sample, which obeys the classical Arrhenius equation:

$$\frac{d\alpha}{dt} = B \cdot \alpha \cdot \exp\left(-\frac{E_a}{RT}\right), \tag{5.15}$$

where α is the concentration of the reaction agent, B is a constant, E_a is the activation energy, R is the gas constant, and T is the temperature. Therefore, we can obtain α by integrating Eq. (5.15) over time interval [*0*, *t*],

$$\alpha = \alpha_0 \exp\left[\int_0^t B \cdot \exp\left(-\frac{E_a}{RT}\right) dt\right], \tag{5.16}$$

where α_0 is the initial concentration of the decomposing agent. The associated kinetic heat flow, $f(t,T)$, generated by the decomposition is

$$f(t,T) = \Delta H \cdot m_s \cdot B \cdot \alpha_0 \exp\left[\int_0^t B \cdot \exp\left(-\frac{E_a}{RT}\right) dt\right] \cdot \exp\left(-\frac{E_a}{RT}\right). \tag{5.17}$$

In Eq. (5.17), ΔH is the reaction heat per unit mass and m_s is the sample mass. With a linear underlying heating rate, $T=T_0+qt$, it can be derived that

$$\begin{aligned} f_T' &= \Delta H \cdot m_s \cdot \frac{B}{q} \cdot \alpha_0 \exp\left[\int_0^t B \cdot \exp\left(-\frac{E_a}{RT}\right) dt\right] \cdot \exp\left(-\frac{E_a}{RT}\right) \cdot \left[\frac{E_a q}{RT^2} + B \cdot \exp\left(-\frac{E_a}{RT}\right)\right] \\ &= f(t,T)\left[\frac{E_a q}{RT^2} + B \cdot \exp\left(-\frac{E_a}{RT}\right)\right]\left(\frac{1}{q}\right). \end{aligned} \tag{5.18}$$

It is assumed for simplicity that the specific heat of the sample remains constant during the entire decomposition process. Then the following heat transfer equations can be obtained

$$K(T_b - T_s) = (C_s + C_r)\left(\frac{dT_s}{dt}\right) + f(t,T), \tag{5.19}$$

$$K(T_b - T_r) = C_r\left(\frac{dT_r}{dt}\right), \tag{5.20}$$

where T_b, T_r and T_s are the temperatures of the heating block, reference and sample, respectively, K is system thermal constant. Equations (5.19) and (5.20) are the well-known differential equations for TMDSC and the detailed derivation can be found in references [12] and [13]. These two equations will be used in the finite difference numerical simulation. Simulation parameters are given in Table 5.1 [24, 25].

Table 5.1 Parameters used in numerical simulation

Simulation parameters and description	**Value**
Amplitude of heating block temperature (in K)	0.2 *
Underlying heating rate q (in K/min)	3 *
Temperature modulation period (in s)	10* to 1000
Heat capacity of sample C_s (in J/K)	0.004 *
Heat capacity of reference C_r (in J/K)	0.0228 *
TMDSC system thermal constant K (in W/K)	0.01 *
Decomposition reaction constant B (in s^{-1})	$2X10^8$ **
Activation energy E_a (in J/mol)	$8.314X10^4$ **
Reaction heat per unit mass ΔH (in J/g)	75 **
Sample mass m_s (in g)	0.02 *
Initial temperature T_0 (in ^oC)	30 *
Initial concentration of the reaction agent α_0	0.95 **
Gas constant R (in J/mol·K)	8.314

Notes:
* Values typical of TMDSC device or experiments
** Values similar but not identical to those used in Ref. [24, 25]

Discrete Fourier transform is used in the calculation of the *HF*, *RHF* and *NHF*. Detailed description of discrete Fourier transform can be found in Appendix 1. A sliding Fourier transform window with a width which is the same as the corresponding modulation period (10 s, 100 s, and 1000 s respectively) is employed. The *HF*, *RHF*, and *NHF* are sliding averages of the results obtained by Fourier transform over the transform window. Figs. 5.1, 5.3 and 5.5 show the *HF*, *RHF*, and *NHF* of the first-order decomposition described by Eq. (5.15) using TMDSC simulations. Lissajous figures (Figs. 5.2, 5.4 and 5.6) showing the relationship between the heating rate, dT_s/dt, and the heat flow are used to demonstrate the system linearity. The separability of *RHF* and *NHF* can be clearly seen under different modulation parameters in these cases.

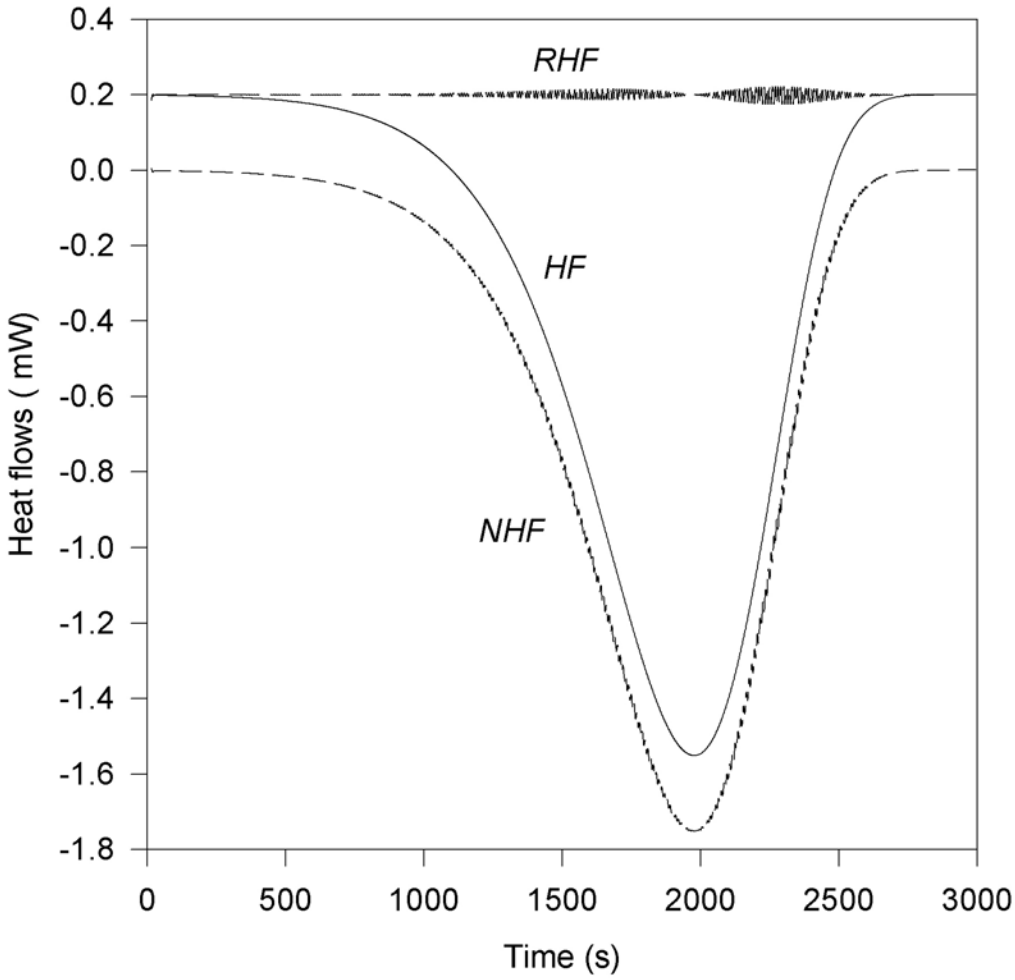

Fig. 5.1 Simulated *HF*, *RHF* and *NHF* as a function of time. Conditions of simulation: Temperature modulation period = 10 s, modulation amplitude = 0.2 K, underlying heating rate=3 K/min.

Fig. 5.1 shows the simulated *HF*, *RHF* and *NHF* for a case where the temperature modulation period is 10 s, or the frequency is 0.1 Hz. The results indicate that the decomposition takes approximately 2000 s to complete when the underlying heating rate is 3 K/min. Hence, this decomposition can be thought of as a rather slow reaction. There are more than 100 modulation cycles during the decomposition. According to Eqs. (5.7) and (5.10), due to the fast modulation frequency of 0.1 Hz, we know that the contribution of the kinetic part to the measured heat capacity is relatively small. In this case, the *RHF* and *NHF* are separated satisfactorily.

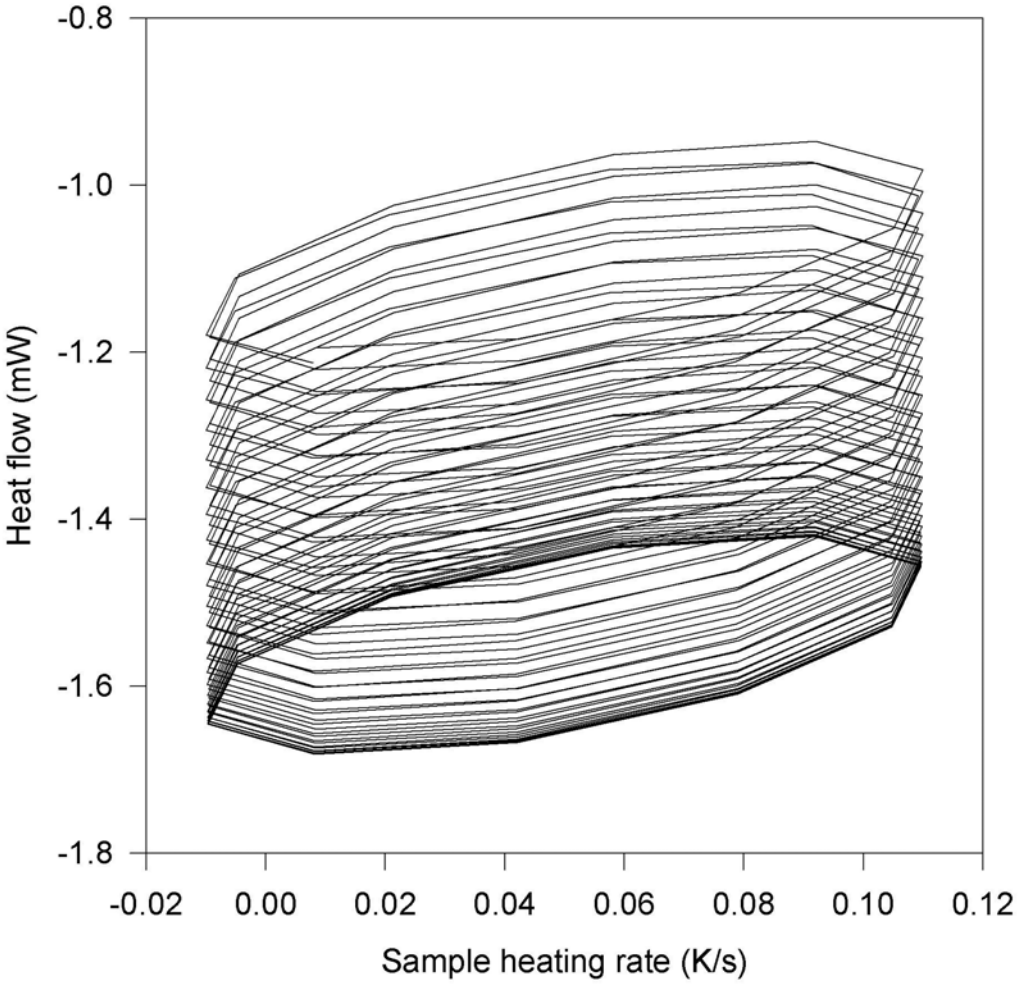

Fig. 5.2 Simulated Lissajous figure showing the relationship between heating rate and heat flow. Temperature modulation period = 10 s, modulation amplitude = 0.2 K, underlying heating rate = 3 K/min.

With Eq. (5.18), it is found via numerical calculation that the maximum value of f_T' during the decomposition is 0.086 mJ/K when the linear heating rate is 3 K/min. Hence, $(f_T'/\omega C_s)^2_{max}$=0.0012, and the condition given by Eq. (5.14) is satisfied. According to the results shown in Fig. 5.1, the error in the measured specific heat (c_p) is almost negligible. Fig. 5.2 shows the corresponding Lissajous figure. The curve shows an elliptical pattern with a small amount of overlap between adjacent modulation cycles, which is an indication of good system linearity in the entire reaction process.

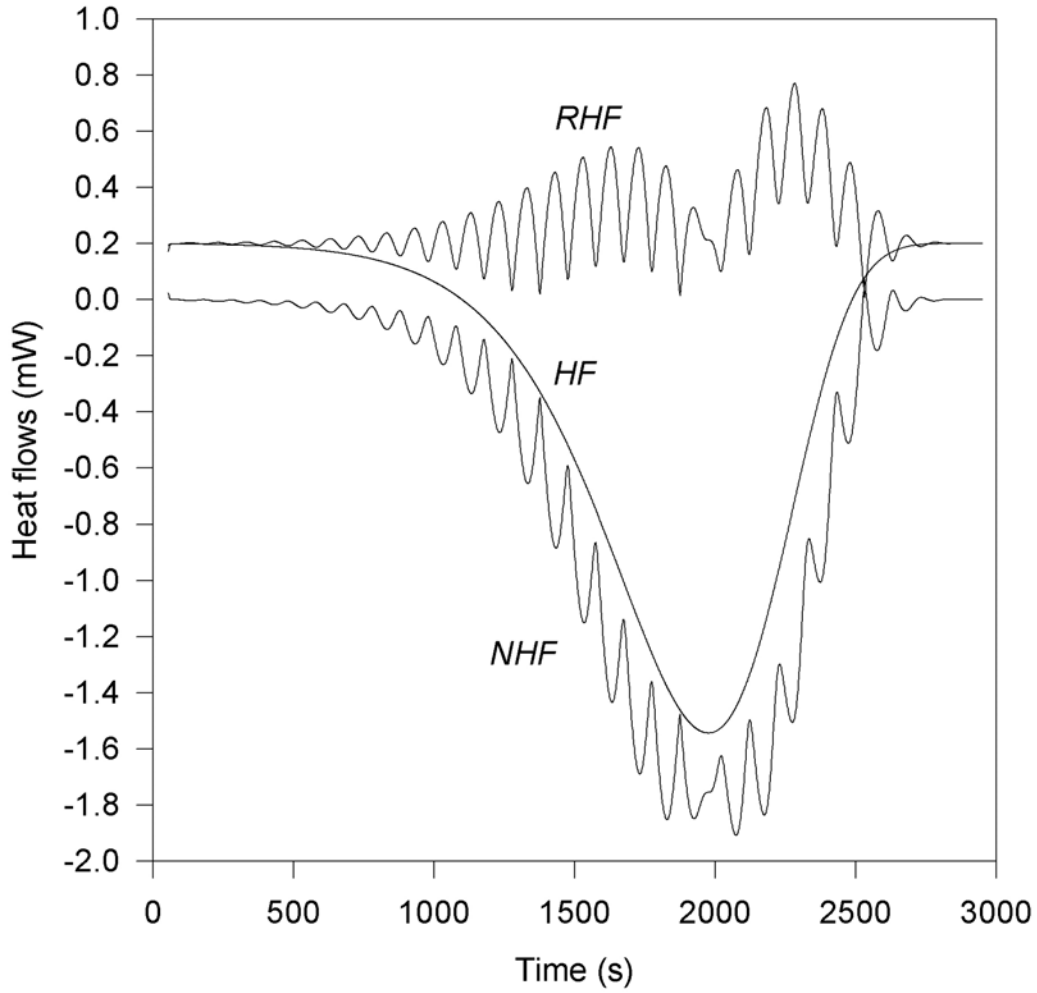

Fig. 5.3 Simulated *HF*, *RHF* and *NHF* as a function of time. Conditions of simulation: Temperature modulation period = 100 s, modulation amplitude = 0.2 K, underlying heating rate = 3 K/min.

Fig. 5.3 shows the simulation results of the case where the temperature modulation period is 100 s. All other simulation parameters are kept the same as those for 10 s. The maximum value of $(f_T'/\omega C_s)^2$=0.12, which is 100 times larger than that for 10 s. Although there are still more than 15 modulation cycles during the decomposition, the system linearity begins to deteriorate and much larger ripples or spikes are observed in the *RHF* and *NHF*.

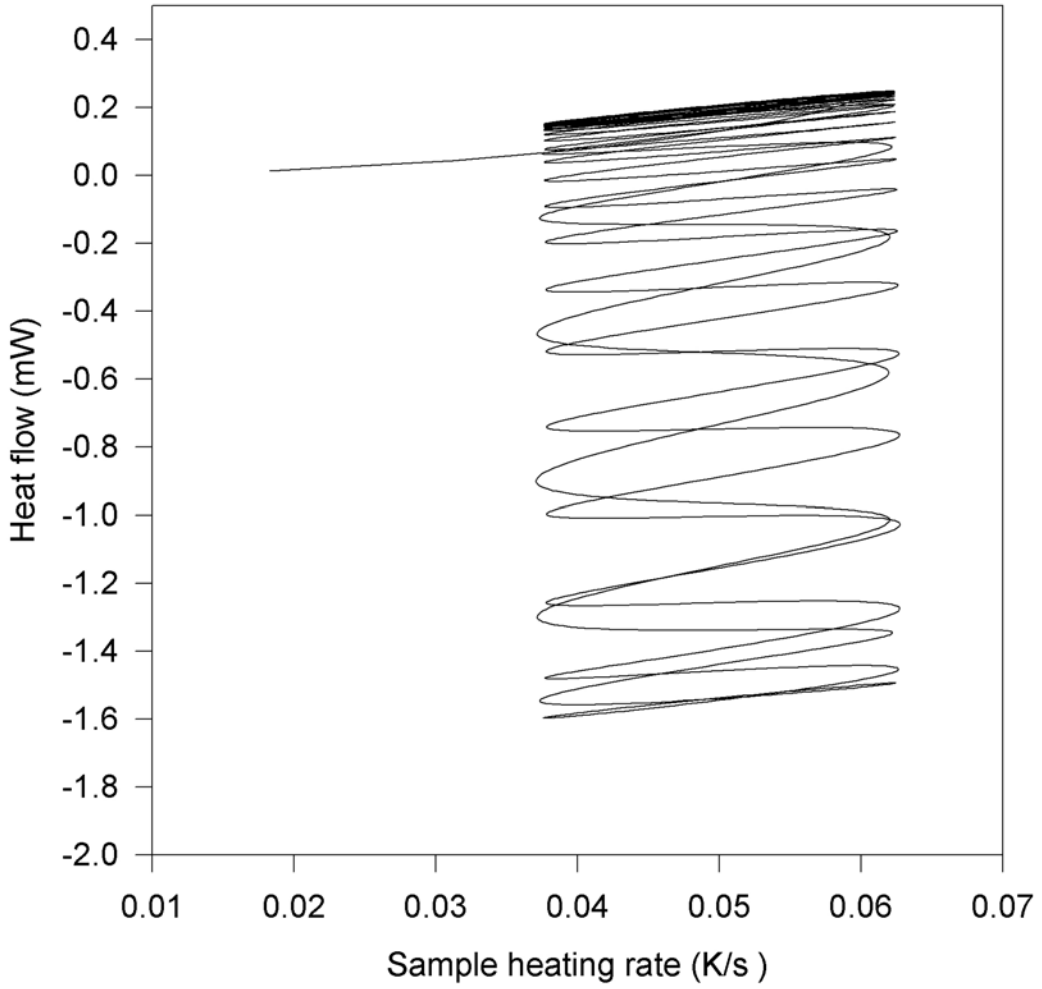

Fig. 5.4 Simulated Lissajous figure showing the relationship between heating rate and heat flow. Temperature modulation period = 100 s, modulation amplitude = 0.2 K, underlying heating rate = 3 K/min.

The corresponding Lissajous figure as shown in Fig. 5.4 deviates from the elliptical pattern, and becomes similar to an overlapped sinusoidal curve. We can infer from this that much of the linearity is lost and the system is entering into an unstable state. In Fig. 5.3, although the total heat flow *HF* still looks similar to that in Fig. 5.1, the *RHF* and *NHF* are different from those in Fig. 5.1. More than 10 maxima are seen in the *RHF* but they are only artifacts, as we know the *RHF* should not change because the specific heat is already assumed to be a constant. This may lead to

incorrect conclusions in terms of the sample properties, for example, the specific heat seems to have changed during the kinetic reaction.

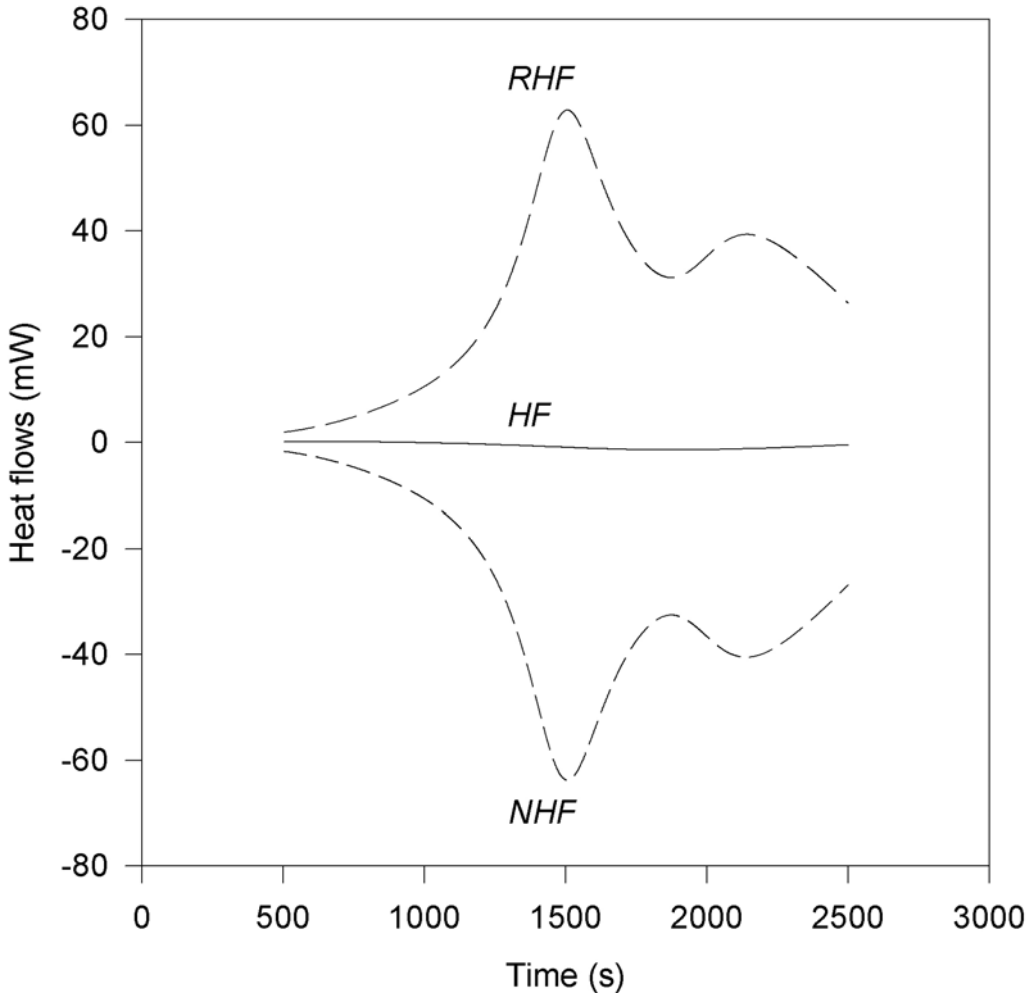

Fig. 5.5 Simulated *HF*, *RHF* and *NHF* as a function of time. Conditions of simulation: Temperature modulation period = 1000 s, modulation amplitude = 0.2 K, underlying heating rate = 3 K/min.

A similar simulation was carried out for the modulation period of 1000s and the results are shown in Fig. 5.5. This modulation period is less than but of the same order of magnitude as the total reaction time. Again, all other parameters are kept the same as those used for Fig. 5.3. In this case $(f_T'/\omega C_s)^2_{max}$=11.8, which is 100 times larger than that for 100 s and 10,000 times larger than that for 10 s. We can no longer assume constant $f(t,T)$ and f_T' in a modulation cycle, which is a pre-requisite for Eq.

(5.4) to be linearized. The kinetic perturbation is too strong to be approximated as a linear one. The corresponding Lissajous figure in Fig. 5.6 shows that the system completely loses linearity and is far from a stable state. The *RHF* and *NHF* are severely deformed. The total heat flow has been drastically changed as well. Apparently, they can no longer provide meaningful information with regard to the sample properties under these circumstances.

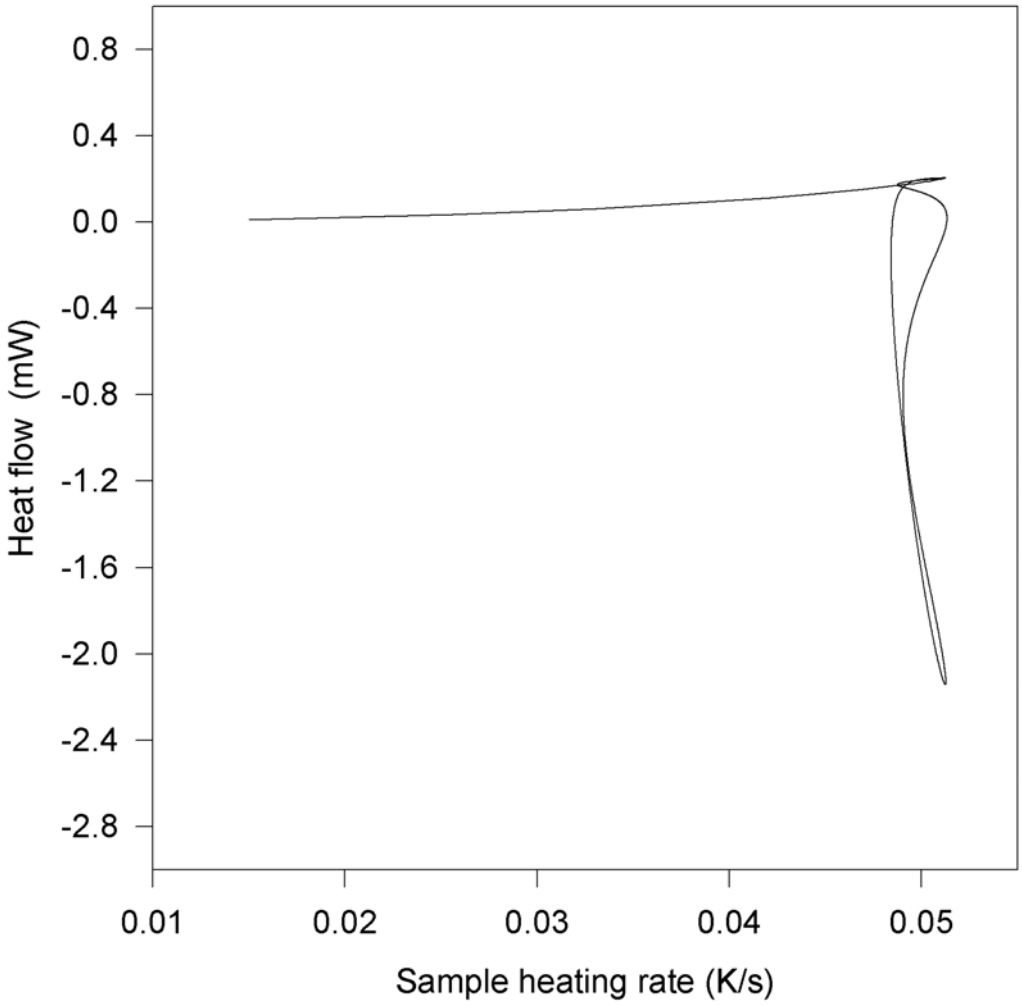

Fig. 5.6 Simulated Lissajous figure showing the relationship between heating rate and heat flow. Temperature modulation period = 1000 s, modulation amplitude = 0.2 K, underlying heating rate = 3 K/min.

Similar results for *RHF* and *NHF* can be found in the analysis by Lacey et al. [26] although their approach is much more complicated. They believe that in many

cases it is possible to separate the reversing heat flow and the non-reversing heat flow provided that the experimental conditions are selected properly. This is consistent with our analysis.

Now we will study several other derivatives of the classical Arrhenius model. This is done by simply replacing the concentration of the reaction agent, α, in Eq. (5.15) with different functions, $f(\alpha)$. The definitions of $f(\alpha)$ for five different kinetic reactions studied are listed in Table 5.2, which include Sestak-Berggren (SB), Johnson-Mehl-Avarami (JMA), two-dimensional diffusion (D2), Jander (D3), and Ginstling-Brounshtein (D4) models [27]. The SB reaction is a more general form of the traditional kinetic one that is related to the Avarami equation. The JMA reaction is often used to describe phase transformation behavior in many systems involving growth and nucleation. D3 is a diffusion-controlled solid-state reaction model using the planar diffusion assumption to correlate the reacted fraction with time, while D4 is a three-dimensional diffusion model proposed by Ginstling and Brounshtein. Variables m and n in function $f(\alpha)$ represent the order of the reactions. For simplicity, m=n=2 in our simulations.

Table 5.2 Definitions of $f(\alpha)$ for several kinetic models [27]

Model	Symbol	$f(\alpha)$
Sestak-Berggren eqn.	SB(m,n)	$\alpha^m(1-\alpha)^n$
Johnson-Mehl-Avarami eqn.	JMA(n)	$n(1-\alpha)[-\ln(1-\alpha)]^{1-1/n}$
Two dimensional diffusion	D2	$1/[-\ln(1-\alpha)]$
Jander eqn.	D3	$3(1-\alpha)^{2/3}/2[1-(1-\alpha)^{2/3}]$
Ginstling-Brounshtein eqn.	**D4**	$3/2[(1-\alpha)^{-1/3}-1]$

Note: m=n=2

The simulation results of both conventional DSC and TMDSC based on these five kinetic models are discussed in the following sections. Fig. 5.7 shows the simulated heat flow in conventional DSC of the five models under a heating rate of

3 K/min. Obviously, even under such a low heating rate, D2, D3, and D4 type reactions have a rather short but sharp heat flow peak, while the heat flow peaks of JMA and SB type reactions are much smaller with much longer durations.

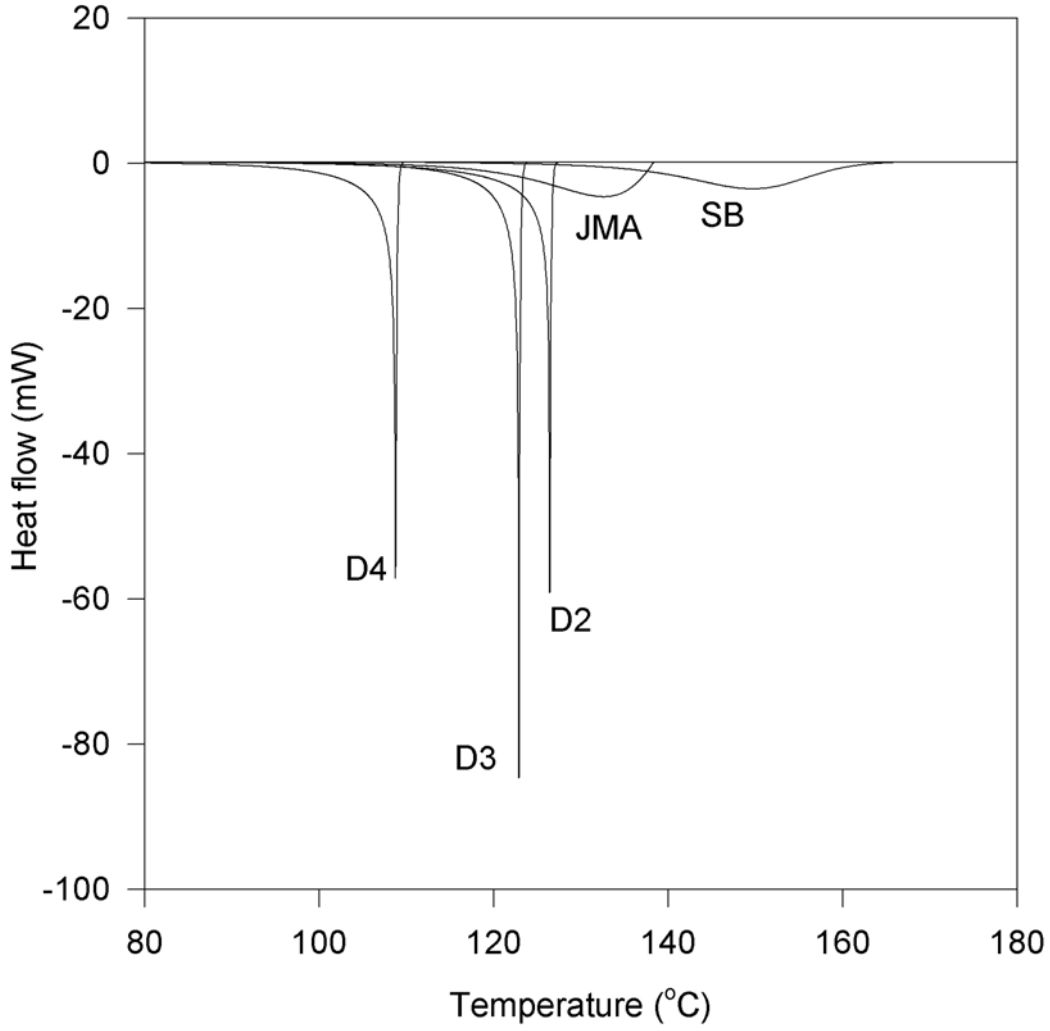

Fig. 5.7 Simulated DSC heat flow curves for kinetics reactions of a two-dimensional diffusion (D2), Jander (D3), Ginstling-Brounhtein (D4), Johnson-Mehl-Avarami (JMA), and Sestak-Berggren (SB) models respectively. Heating rate = 3 K/min

Figs. 5.8, 5.10 and 5.12 show the simulated *HF*, *RHF*, and *NHF* of D2, D3, and D4 type reactions respectively with a modulation period of 10 s. It can be seen that even under this short modulation period, multiple sharp peaks still appear in the *RHF* and *NHF*. Hence, TMDSC analysis is not suitable for these reactions, at least not within the framework of our studies. This can also be seen from the Lissajous

figures shown in Figs. 5.9, 5.11, and 5.13 respectively. It is found that the linearity is quite poor for these three types of reactions in that the curves are not elliptical or circular indicating that the system is not in a thermal equilibrium state.

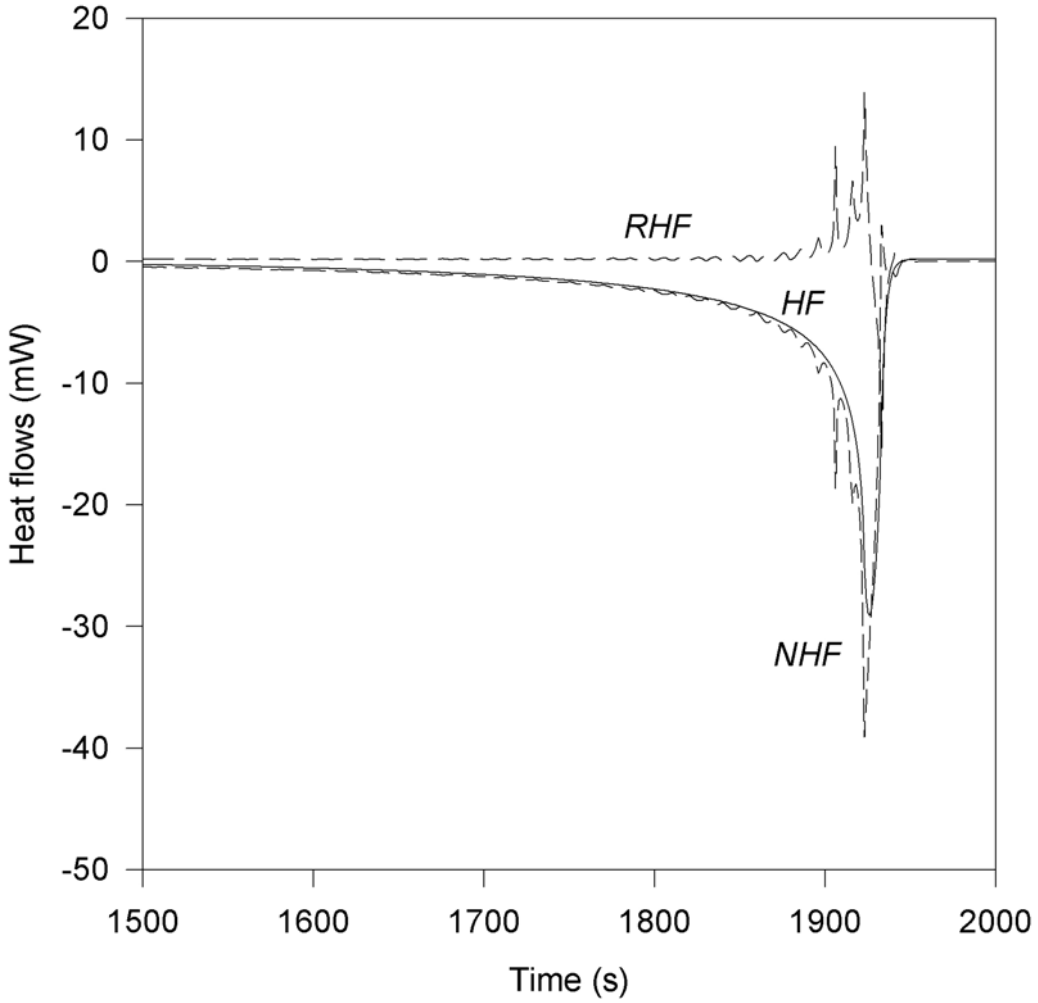

Fig. 5.8 Simulated *HF*, *RHF* and *NHF* as a function of time for D2 model. Conditions of simulation: Temperature modulation period = 10 s, modulation amplitude = 0.2 K, underlying heating rate = 3 K/min.

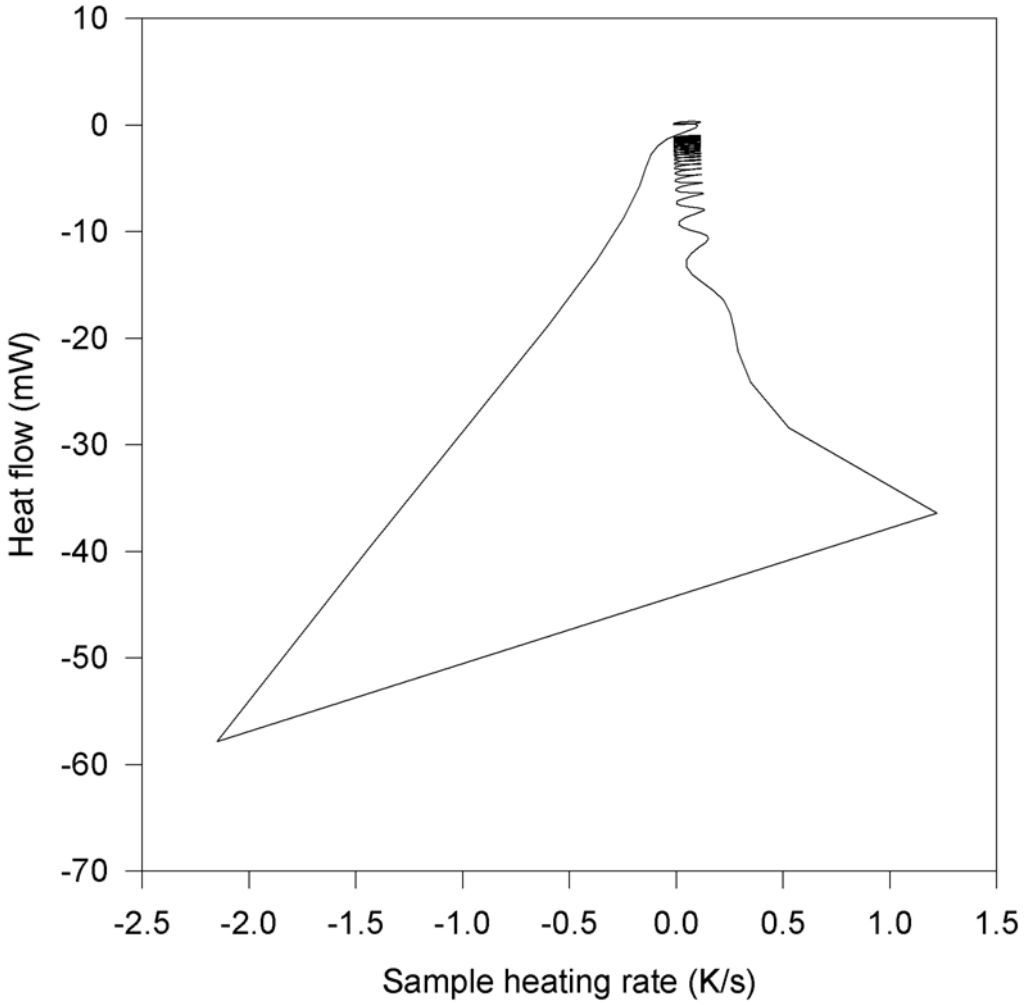

Fig. 5.9 Simulated Lissajous figure for D2 model showing the relationship between heating rate and heat flow. Temperature modulation period = 10 s, modulation amplitude = 0.2 K, underlying heating rate = 3 K/min.

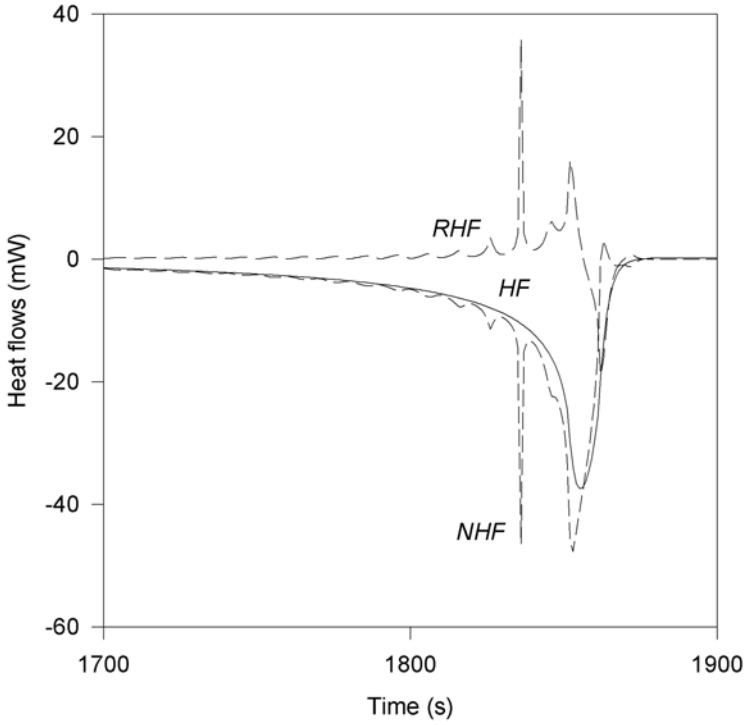

Fig. 5.10 Simulated *HF*, *RHF* and *NHF* as a function of time for D3 model. Conditions of simulation: Temperature modulation period = 10 s, modulation amplitude = 0.2 K, underlying heating rate = 3 K/min.

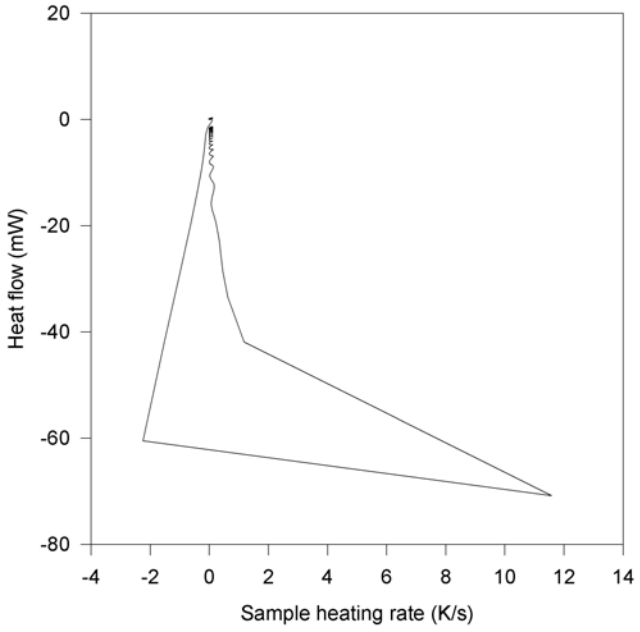

Fig. 5.11 Simulated Lissajous figure for D3 model showing the relationship between heating rate and heat flow. Temperature modulation period = 10 s, modulation amplitude = 0.2 K, underlying heating rate = 3 K/min.

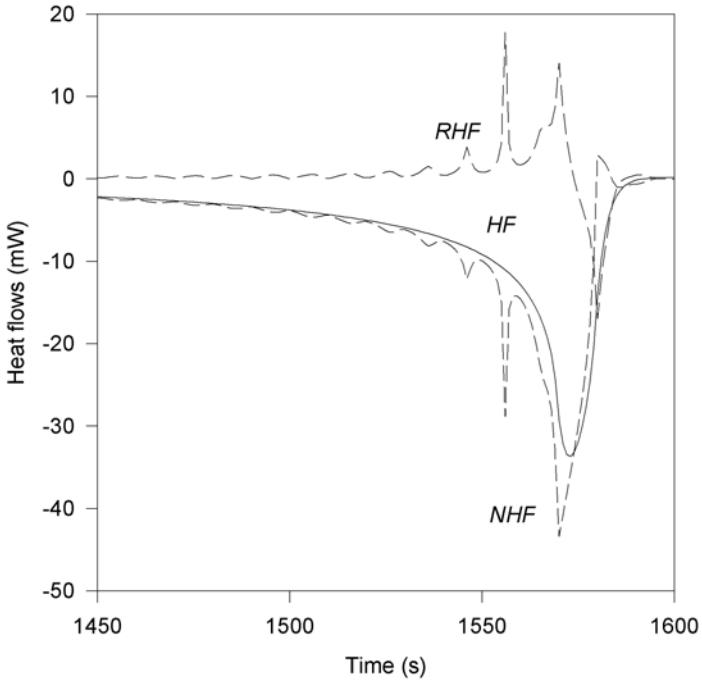

Fig. 5.12 Simulated *HF*, *RHF* and *NHF* as a function of time for D4 model. Conditions of simulation: Temperature modulation period = 10 s, modulation amplitude = 0.2 K, underlying heating rate = 3 K/min.

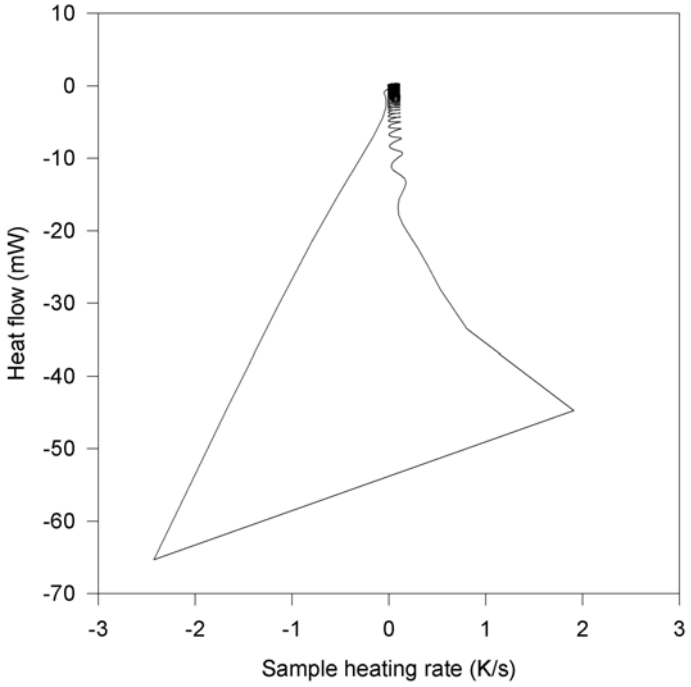

Fig. 5.13 Simulated Lissajous figure for D4 model showing the relationship between heating rate and heat flow. Temperature modulation period = 10 s, modulation amplitude = 0.2 K, underlying heating rate = 3 K/min.

Simulated *HF*, *RHF*, and *NHF* of the JMA type reaction with a modulation period of 10 s and 100 s are shown in Figs. 5.14 and 5.16, respectively, while those of the SB type reaction can be found in Figs. 5.19 and 5.21. It can be seen that for these two types of reactions, the simulated *RHF* and *NHF* are much more accurate at the period of 10 s than at 100 s, and they show a similar trend as that of the analytical solution and the first-order reaction, as discussed in sections 5.2 and 5.3. Their Lissajous figures as shown in Figs. 5.15, 5.17, 5.20 and 5.22 have demonstrated that better linearity and hence better separation of *RHF* and *NHF* can be achieved for shorter modulation periods. Figs. 5.18 and 5.23 show the effect of the underlying heating rate on the measured c_p for JMA and SB type reactions respectively. The effect is quite significant since the intensity of reaction drops significantly with decreasing heating rate. Consequently, the corresponding value of $f_T'(t,T)$ drops too, thus allowing a more accurate deconvolution of heat capacity according to Eqs. (5.10) and (5.14). In both figures, the measured c_p shows the smallest ripples at the slowest heating rate of 1 K/min.

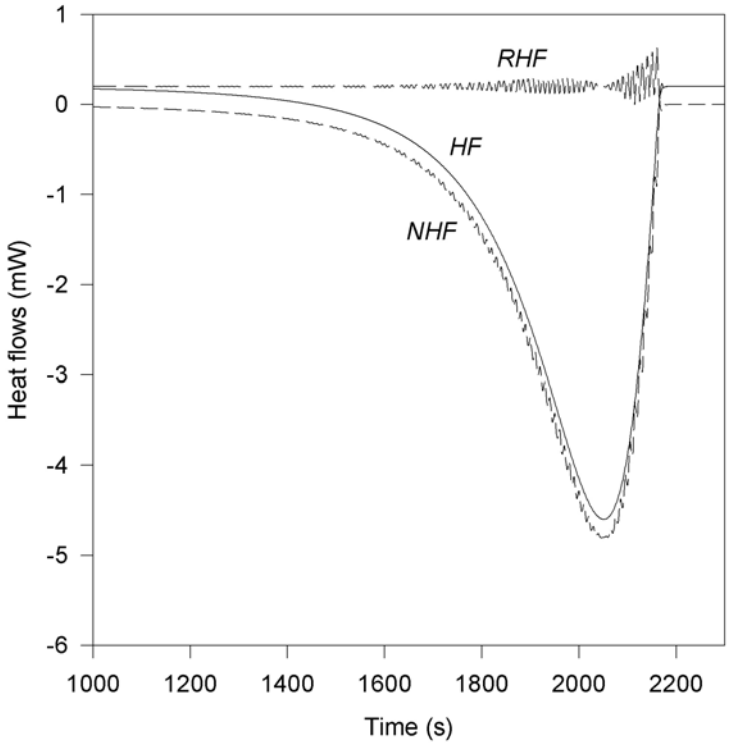

Fig. 5.14 Simulated *HF*, *RHF* and *NHF* as a function of time for JMA model. Conditions of simulation: Temperature modulation period = 10 s, modulation amplitude = 0.2 K, underlying heating rate = 3 K/min.

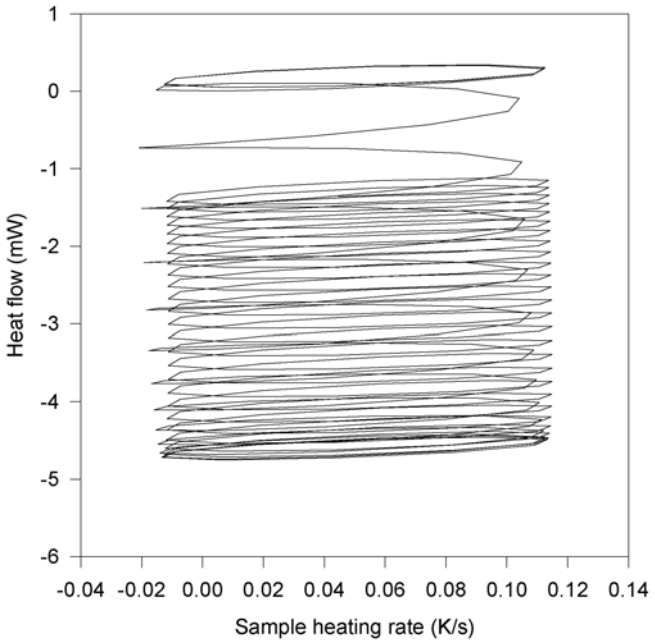

Fig. 5.15 Simulated Lissajous figure for JMA model showing the relationship between heating rate and heat flow. Temperature modulation period = 10 s, modulation amplitude = 0.2 K, underlying heating rate = 3 K/min.

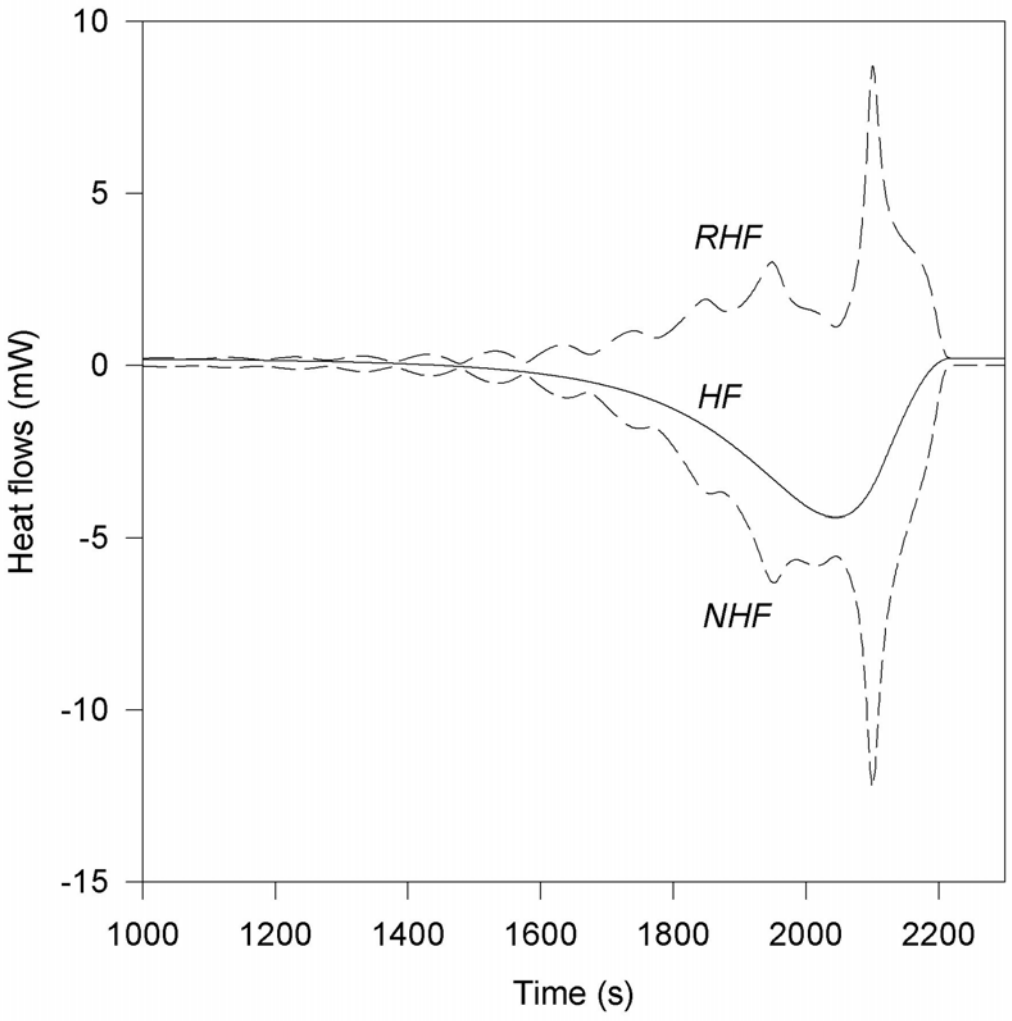

Fig. 5.16 Simulated *HF*, *RHF* and *NHF* as a function of time for JMA model. Conditions of simulation: Temperature modulation period = 100 s, modulation amplitude = 0.2 K, underlying heating rate = 3 K/min.

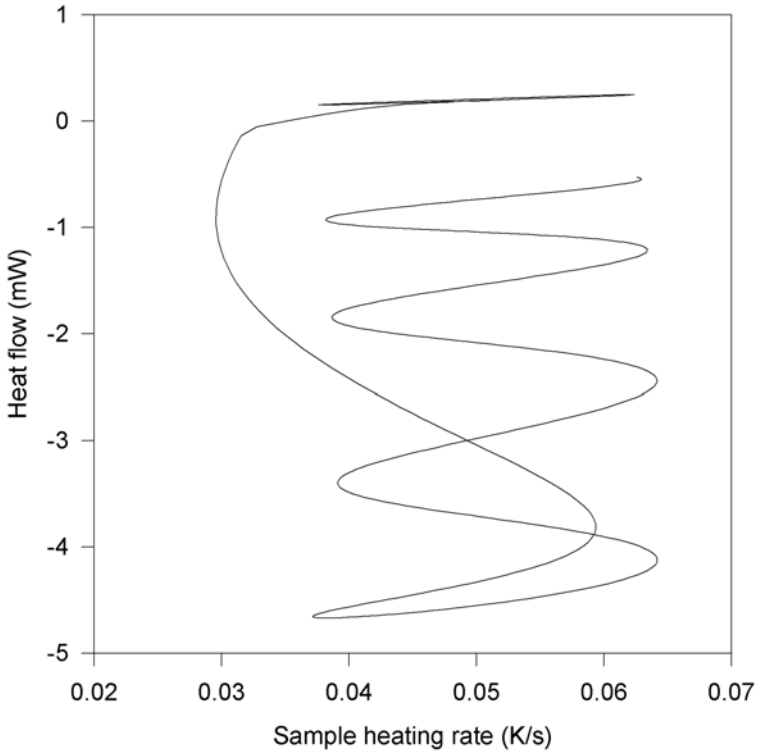

Fig. 5.17 Simulated Lissajous figure for JMA model showing the relationship between heating rate and heat flow. Temperature modulation period = 100 s, modulation amplitude = 0.2 K, underlying heating rate = 3 K/min.

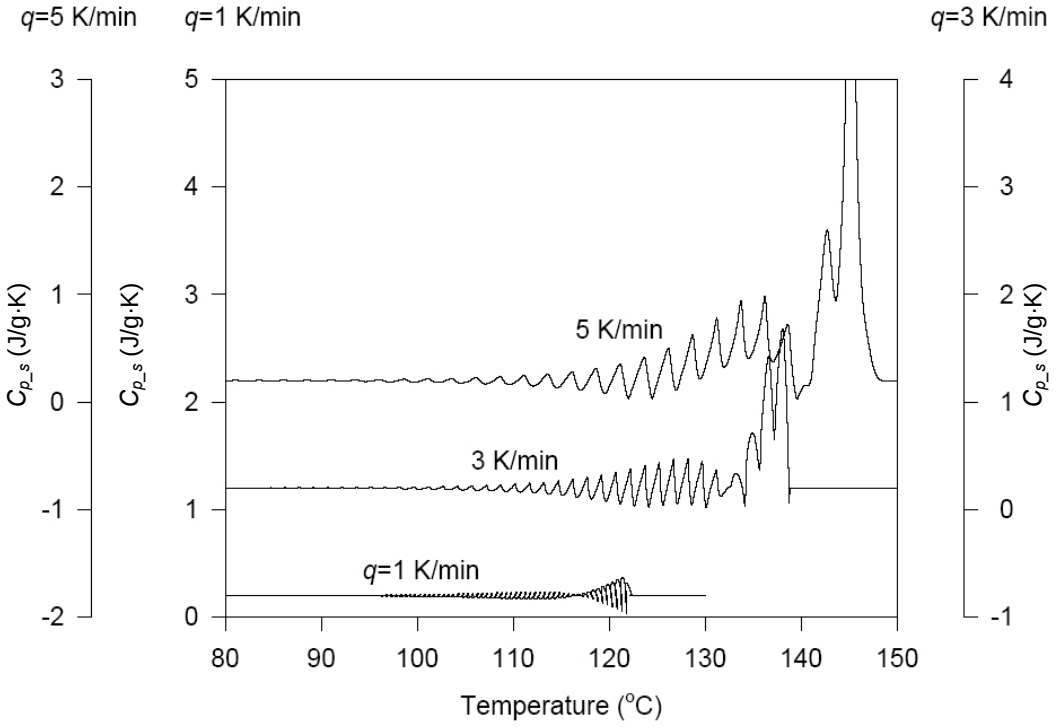

Fig. 5.18 c_p (J/g·K) as a function of temperature under various underlying heating rate (K/min) for JMA model

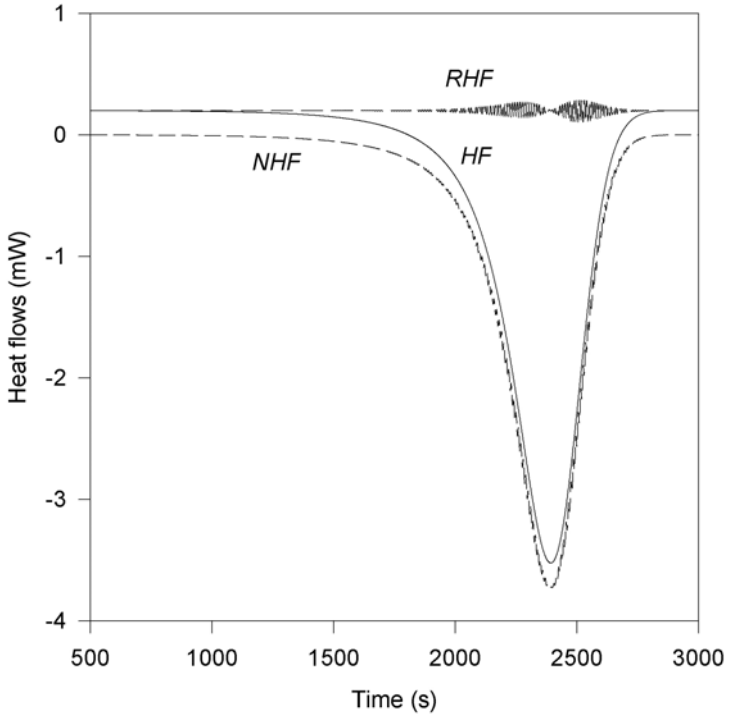

Fig. 5.19 Simulated *HF*, *RHF* and *NHF* as a function of time for SB model. Conditions of simulation: Temperature modulation period = 10 s, modulation amplitude = 0.2 K, underlying heating rate = 3 K/min.

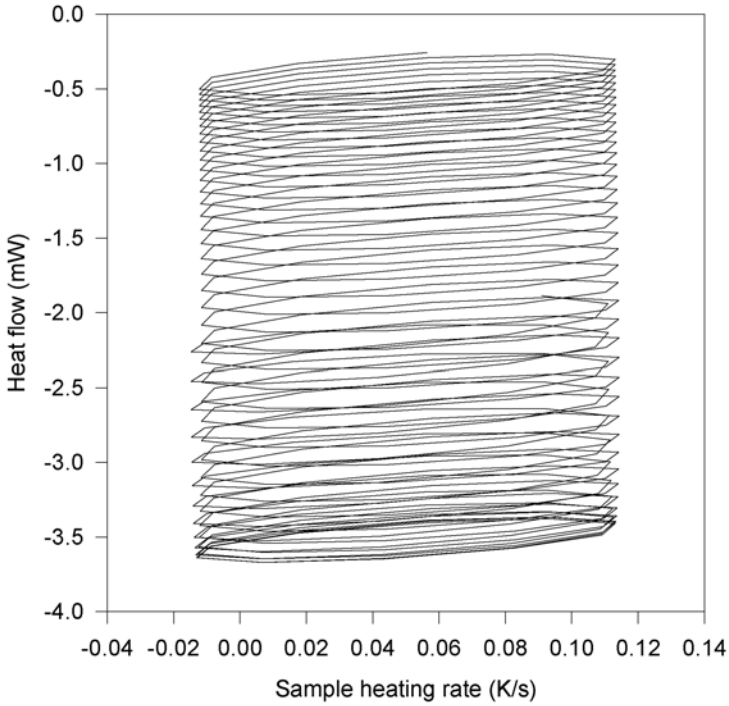

Fig. 5.20 Simulated Lissajous figure for SB model showing the relationship between heating rate and heat flow. Temperature modulation period = 10 s, modulation amplitude = 0.2 K, underlying heating rate = 3 K/min.

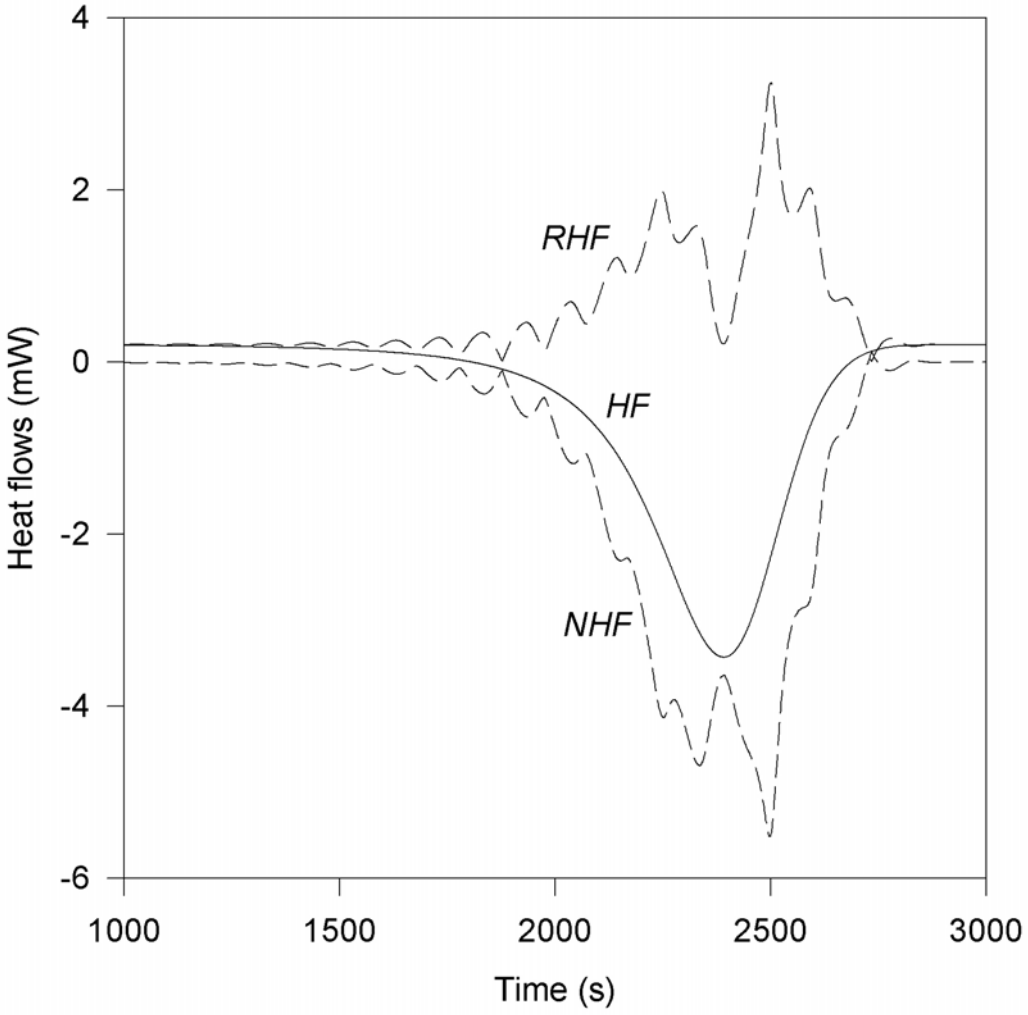

Fig. 5.21 Simulated *HF*, *RHF* and *NHF* as a function of time for SB model. Conditions of simulation: Temperature modulation period = 100 s, modulation amplitude = 0.2 K, underlying heating rate = 3 K/min.

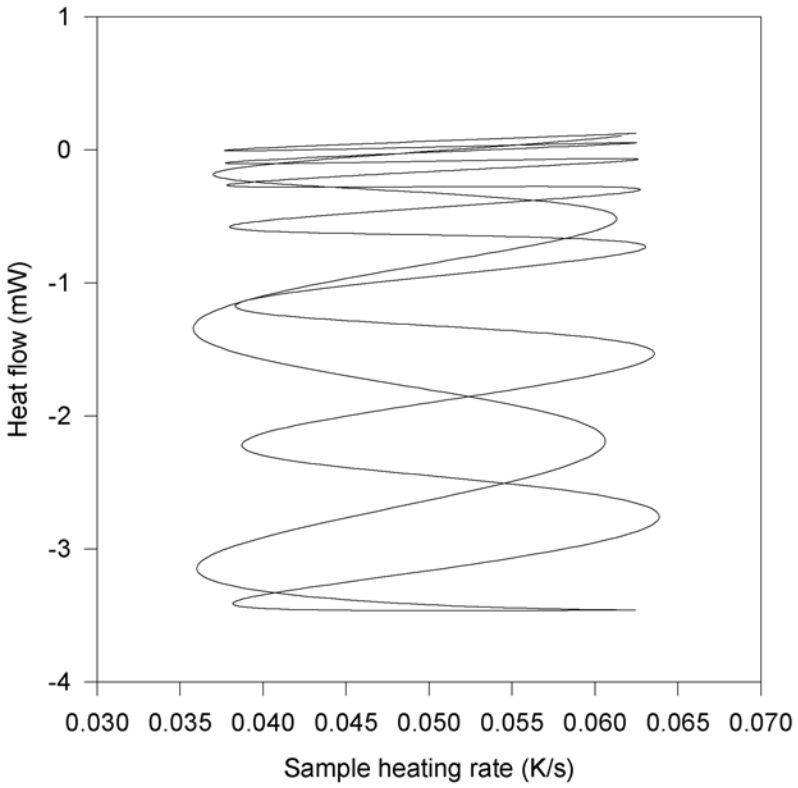

Fig. 5.22 Simulated Lissajous figure for SB model showing the relationship between heating rate and heat flow. Temperature modulation period = 100 s, modulation amplitude = 0.2 K, underlying heating rate = 3 K/min.

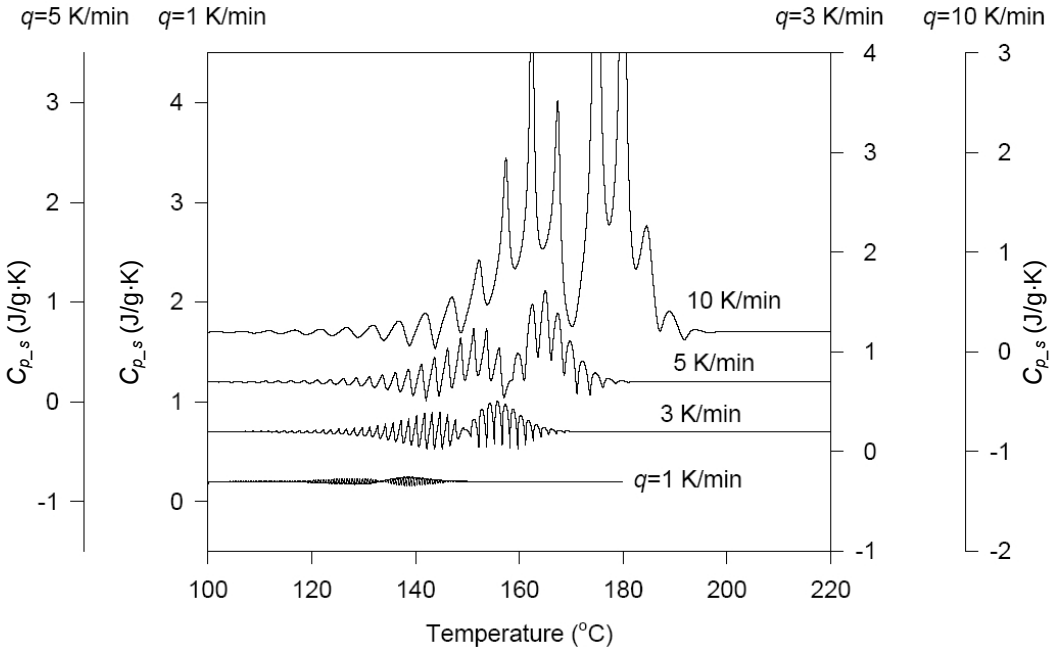

Fig. 5.23 c_p (J/g·K) as a function of temperature under various underlying heating rate (K/min) for SB model

5.4 Experimental analysis on several melt-spun amorphous alloys

In this section, we discuss how experimental parameters can affect the TMDSC results of several melt-spun amorphous alloys and the advantages of TMDSC over conventional DSC. Fully amorphous $Al_{84}Nd_9Ni_7$ ribbons were prepared by the melt-spinning technique. The chilling copper wheel has a diameter of 20 cm with a line speed of 30 m/s. TMDSC experiments were carried out on a TA Instruments MDSC2920 device that was equipped with a liquid nitrogen cooling system. The sample mass is 13.00 mg, the modulation amplitude is 0.8 K, the period is 30 s, and the underlying heating rate is 1 K/min. XRD analysis is used to determine the phase structures of the ribbons.

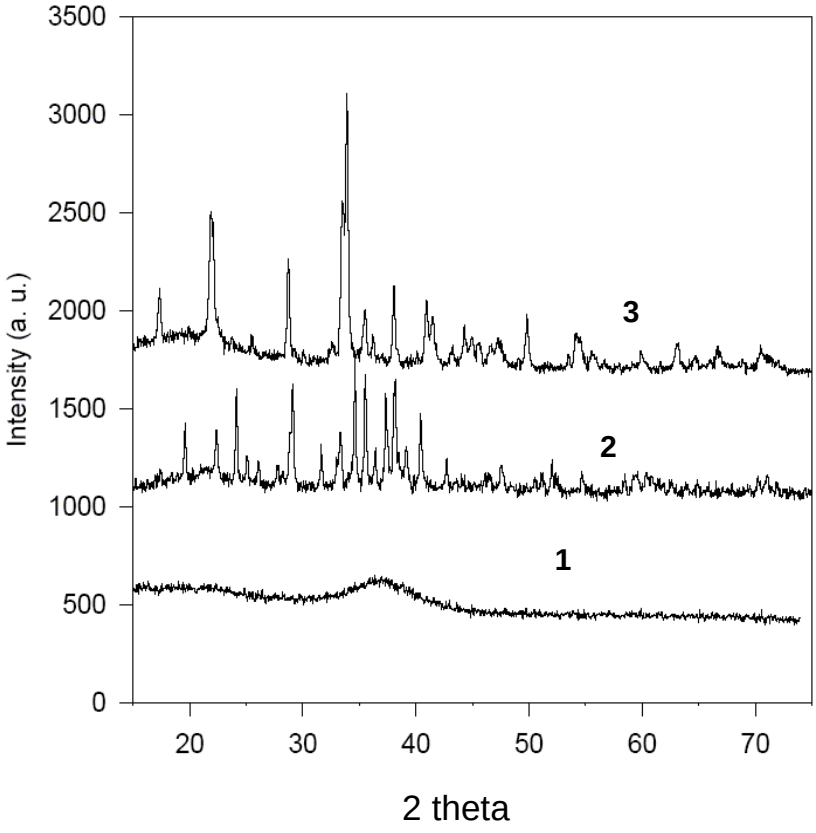

Fig. 5.24 XRD results of melt spun $Al_{84}Nd_9Ni_7$ ribbon. 1: as spun ribbon 2: ribbon heated to 320^{o}C, then quenched down to room temperature 3: ribbon heated to 370^{o}C, then quenched down to room temperature.

Fig. 5.24 shows the XRD results of the ribbon after being heated to different temperatures and then quenched to the ambient temperature. XRD spectrum 1 of the as-spun ribbon represents a fully amorphous structure. XRD spectrum 2 is for the ribbon after it was heated to 320°C then cooled down to room temperature, indicating a partially crystallized amorphous structure. XRD spectrum 3 is for the ribbon after it was heated to 370°C then cooled down to room temperature, confirming that it is now fully crystallized.

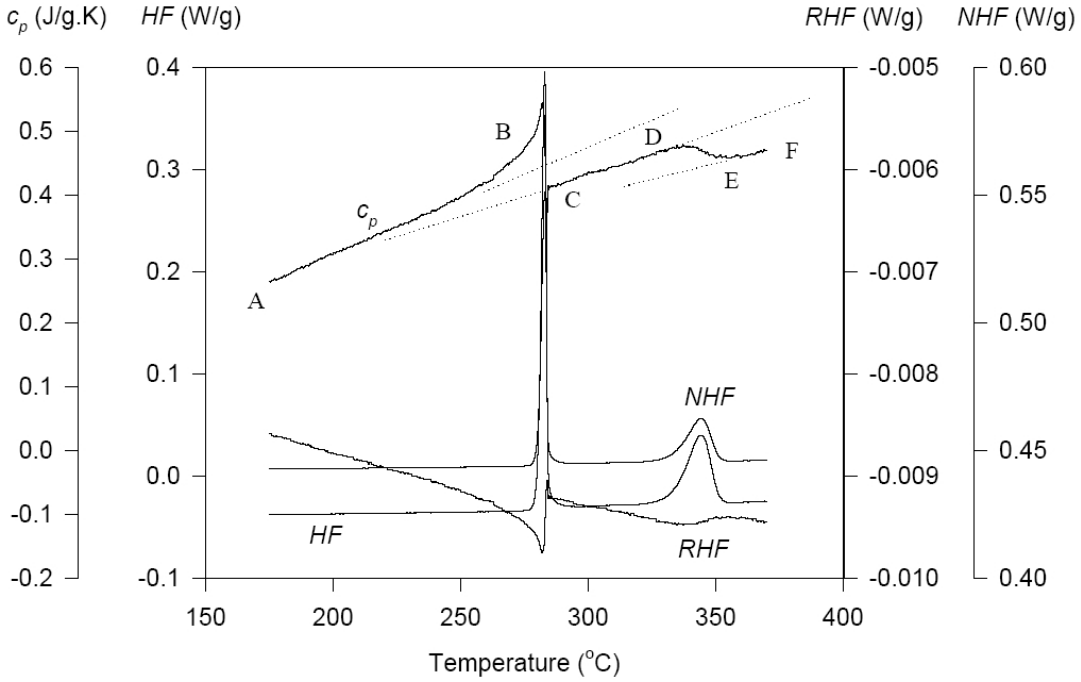

Fig. 5.25 Experimentally obtained specific heat of the sample (c_p), *HF*, *RHF* and *NHF* Sample: melt spun $Al_{84}Nd_9Ni_7$ ribbon. Temperature modulation period =30 s, modulation amplitude =0.8 K, underlying heating rate =1 K/min, sample mass =13.00 mg.

Fig. 5.25 shows the experimentally determined specific heat, *HF*, *NHF*, and *RHF* by TMDSC of the melt-spun $Al_{84}Nd_9Ni_7$ ribbon. On the *HF* curve, there are two exothermic peaks corresponding to the crystallization process of inter-metallic and α-Al, respectively. The first exothermic peak occurs between 260 and 290°C, while the second exothermic peak appears between 330 and 360°C. The specific heat curve can be roughly divided into three distinct segments. The dotted lines are used to help

explain the difference in specific heat among the three segments. The first segment, AB, represents an amorphous state and has the highest c_p if we compare the positions of the three dotted lines. The second segment, CD, represents a partial amorphous status and shows an intermediate c_p among the three segments. Segment EF, where the sample is fully crystallized, has the lowest c_p. Although the difference in specific heat between crystalline and amorphous states is rather small, TMDSC is able to distinguish them in a single run, demonstrating a high sensitivity which cannot be matched by the conventional DSC. This is especially useful for those cases where thermal history can significantly change the thermal properties if the experiment has to be conducted in two separate runs.

Comparison of the two exothermic peaks in *HF* (Fig. 5.25) indicates that the first peak is relatively sharp and narrow, and the corresponding c_p shows different patterns during these two exothermic peaks. Between B and C, c_p exhibits considerable positive deviation from the dotted line (representing the linear relationship between c_p and temperature), reaching a maximum during the crystallization and then dropping sharply as the temperature increases, while in segment DE, the c_p changes smoothly to segment EF without any apparent peak in specific heat.

Lissajous figures corresponding to the two exothermic peaks are shown in Figs. 5.26 and 5.27, respectively. The curve shown in Fig. 5.26 shifts considerably in the vertical direction during the crystallization. Apparently, the linearity shown in Fig. 5.26 is poor compared to that in Fig. 5.27 in which the Lissajous figure consists of ellipses that are slightly offset, similar to that obtained by the computer simulation as shown in Fig. 5.2. Furthermore, from the shape of the two peaks in the total heat flow, it is believed that the temperature sensitivity, f_T', of the first exothermic peak is much

larger than that of the second one. Thus the kinetic heat flow, $f(t,T)$, cannot be constant in each of the modulation cycles for the first crystallization. The difference in linearity together with Eq. (5.14) explain the difference between the c_p curves of the two exothermic peaks.

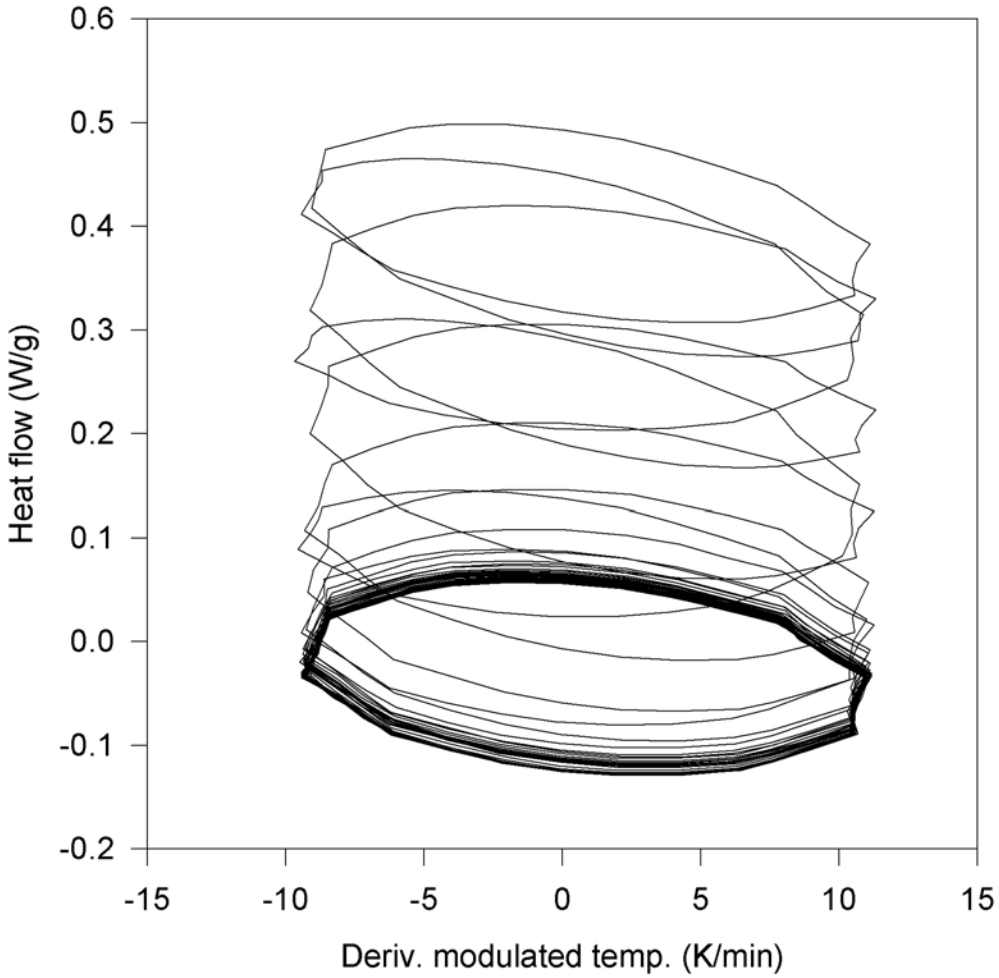

Fig. 5.26 Lissajous figure for the first crystallization peak in Fig. 5.25. Temperature range: 260 to 290°C. Temperature modulation period = 30 s, modulation amplitude = 0.8 K, underlying heating rate = 1 K/min, sample mass = 13.00 mg.

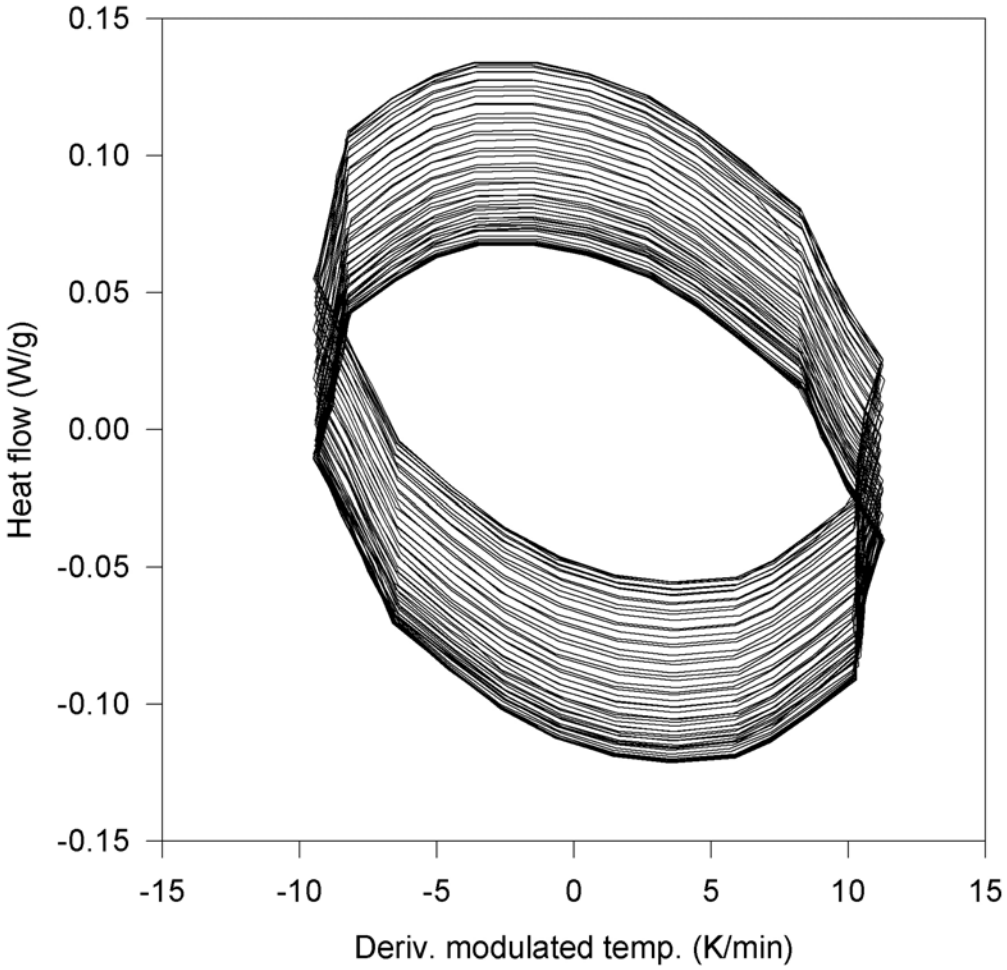

Fig. 5.27 Lissajous figure for the second crystallization peak in Fig. 5.25. Temperature range: 330 to 360°C. Temperature modulation period = 30 s, modulation amplitude = 0.8 K, underlying heating rate = 1 K/min, sample mass = 13.00 mg.

The specific heat, *HF*, *RHF*, and *NHF* obtained from a second as-spun sample with a mass of 13.20 mg are given in Fig. 5.28. Compared with the earlier case shown in Fig. 5.25, an underlying heating rate of 0.5 K/min is used here in order to reduce the intensity of the crystallization peak and accommodate more modulation cycles. The end effect is similar to an increase in the modulation frequency but without affecting the calibration factor as severely as frequency does. The modulation period and the amplitude were kept unchanged. The c_p shows a much smaller deviation from the dotted line (which represents the linear relationship between c_p and temperature) at the temperature of the first crystallization peak and changes smoothly at the second

transition. The Lissajous figures in the same temperature ranges as the first sample (260 to 290°C and 330 to 360°C), are plotted in Figs. 5.29 and 5.30, respectively. Both of them show improved linearity over that obtained from the first sample.

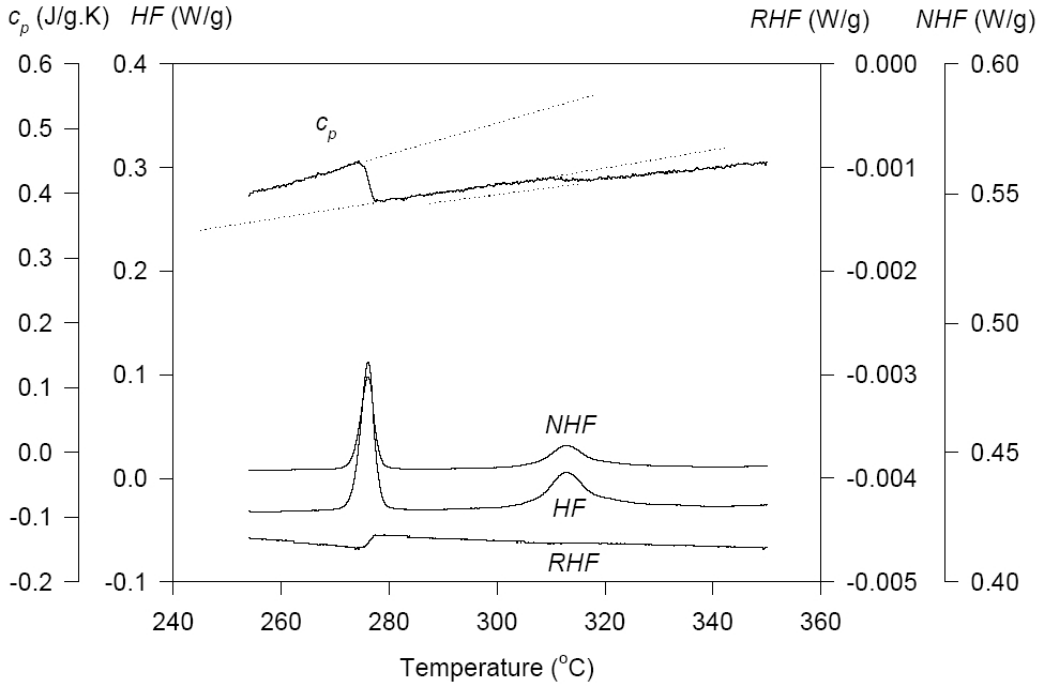

Fig. 5.28 Experimentally obtained c_p, *HF*, *RHF* and *NHF*. Sample: melt spun $Al_{84}Nd_9Ni_7$ ribbon. Temperature modulation period = 30 s, modulation amplitude = 0.8 K, underlying heating rate = 0.5 K/min, sample mass = 13.20 mg.

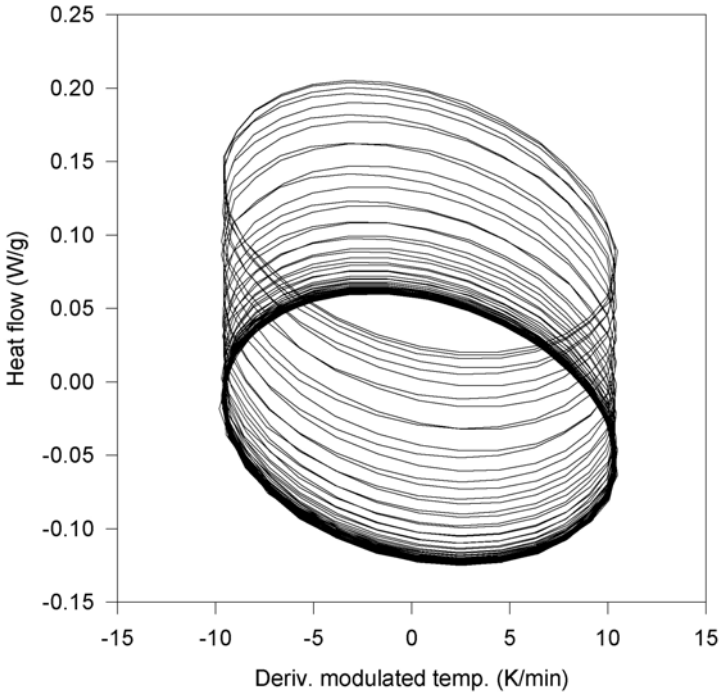

Fig. 5.29 Lissajous figure for the first crystallization in Fig. 5.28. Temperature range: 260 to 290°C. Temperature modulation period = 30 s, modulation amplitude = 0.8 K, underlying heating rate = 0.5 K/min, sample mass = 13.20 mg.

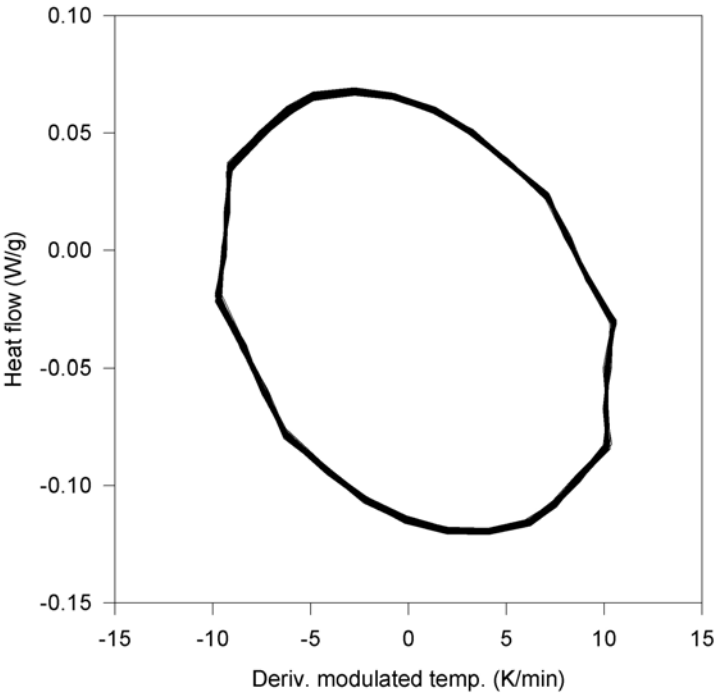

Fig. 5.30 Lissajous figure for the second crystallization in Fig. 5.28. Temperature range: 330 to 360°C. Temperature modulation period = 30 s, modulation amplitude = 0.8 K, underlying heating rate = 0.5 K/min, sample mass = 13.20 mg.

TMDSC experiments were also carried out on melt-spun $Al_{92}Sm_8$, $Al_{88}Ni_{10}La_2$, and $Al_{88}Ni_{10}Y_2$ ribbons. All these alloys are Al-based and have a similar feature in their heat flows——a primary Al precipitation hump followed by a major crystallization peak, as shown in Figs. 5.31 to 5.33. The temperature modulation conditions are identical for these three figures. The temperature modulation period is 30 s, the modulation amplitude is 0.8 K, and the underlying heating rate is1 K/min.

Fig. 5.31 shows the TMDSC result of an $Al_{92}Sm_8$ ribbon. It is noticed that a concave dip appeared at about 150^{o}C in the *RHF* curve. This is similar to that obtained by Wu et al. [28] for the same alloy. It is believed that this is probably a hidden glass transition point which could not be observed previously by conventional DSC. Because the heat flow signal from the glass transition is fairly weak compared with the much stronger signal from the Al precipitation, it could be easily covered by the latter. It can be seen that the *RHF* given in Fig. 5.32 has a similar pattern as that in 5.33, as indicated by the arrows. This is interesting since the glass transition may be used in annealing that allows the development of certain microstructures in order to obtain the optimized mechanical properties.

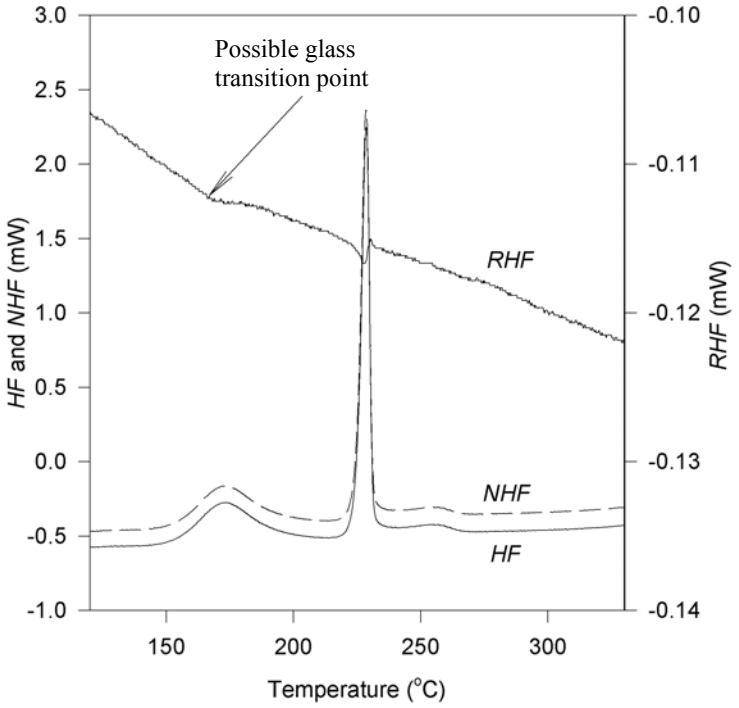

Fig. 5.31 TMDSC results of $Al_{92}Sm_8$. Sample mass = 12.1 mg, temperature modulation period = 30 s, modulation amplitude = 0.8 K, underlying heating rate = 1 K/min.

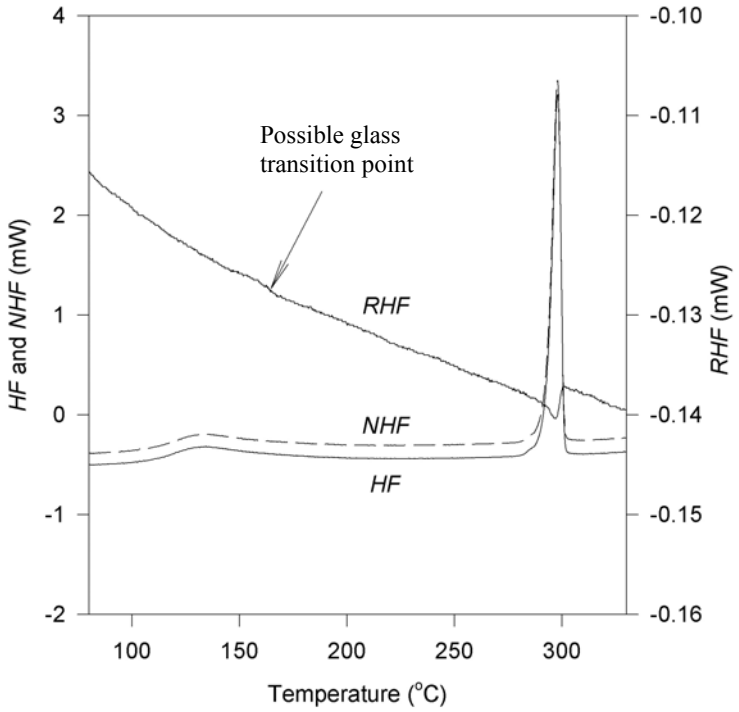

Fig. 5.32 TMDSC results of $Al_{88}Ni_{10}La_2$. Sample mass = 11.4 mg, temperature modulation period = 30 s, modulation amplitude = 0.8 K, underlying heating rate = 1 K/min

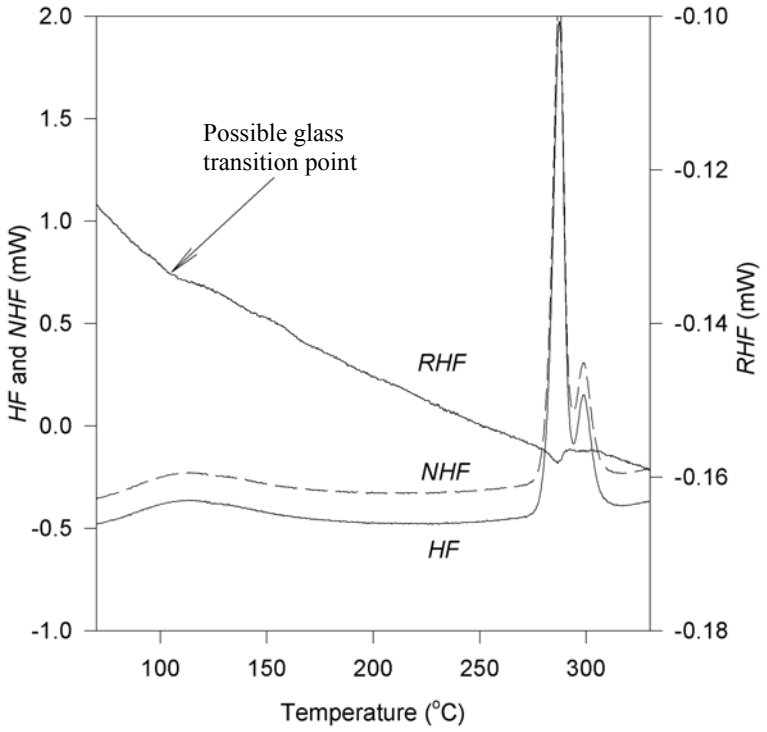

Fig. 5.33 TMDSC results of $Al_{88}Ni_{10}Y_2$. Sample mass = 13.8 mg, temperature modulation period = 30 s, modulation amplitude = 0.8 K, underlying heating rate = 1 K/min.

5.5 Considerations in the selection of experiment parameters

It has been shown that kinetic events can affect the heat flows as well as the measured specific heat in TMDSC. Based on the above analytical, numerical and experimental results, it can be seen that in order to really exploit the power of TMDSC, the key factor is to carry out the experiments under a linear or close to a linear condition. Some measures can be taken to make this more likely to occur:

(a) Wherever possible, a low underlying heating rate, such as 0.5K/min should be used. Hence, a time and temperature dependent kinetic reaction takes a longer time to complete, this can effectively reduce f_T'.

(b) A small modulation amplitude, e.g. 0.2 to 0.5K, is preferred in order to lower the thermal perturbations. As a result the linearity can be improved.

(c) A high modulation frequency (0.05 to 0.1 Hz, corresponding to a temperature modulation period of 10 to 20s), together with (a) can accommodate more modulation cycles during the kinetic event. However, increasing the temperature modulation frequency is subjected to some physical limitations. Firstly, due to the thermal latency of the instrument itself, commercially available TMDSC device has a relatively narrow range of modulation frequency, e.g., 0.1 to 0.01 Hz. This is much smaller than some other dynamic evaluation methods. The limitations to modulation frequency could be overcome by the later development in light modulated TMDSC [29, 30]. Furthermore, high modulation frequency can introduce an extra temperature gradient and phase lag for poor thermal conducting materials, which can increase the difficulty in quantitative analysis of the experimental results, unless a much smaller sample mass, e.g. in the magnitude of micro-grams, is used. It has been found that the specific heat obtained from TMDSC at a high frequency spectrum deviates considerably even after calibration factors have been taken into account [31]. Finally, a sharp, intense kinetic event can have a major effect on the observed specific heat and produce spurious artifacts, while a broad and gentle kinetic reaction is more favorable to the quantitative separation of reversing and non-reversing heat flows with TMDSC [32]. All these can make the situation complicated. Thus selection of experimental parameters is important in order to make more accurate measurement of specific heat, *HF*, *RHF*, and *NHF* using TMDSC.

5.6 Conclusions

In this chapter, the general case of TMDSC with a kinetic event that was both time and temperature dependent in the sample was studied. A concise analytical solution to the heat transfer equation in TMDSC is obtained and the conditions for linear thermal response are discussed. It has been demonstrated that TMDSC has

several advantages over conventional DSC, such as the separation of reversing and non-reversing heat flow, detailed information on the change in specific heat before, during and after glass transition from amorphous state. In order to obtain meaningful results, care must be taken in the selection of experimental parameters so that TMDSC works in or close to the range of linear response.

Through simulation and experiments, several factors such as a low underlying heat rate, e.g. 0.5K/min and small temperature modulation amplitude, e.g. 0.2 to 0.5K have been identified that can improve the overall system linearity as well as the accuracy of the measured specific heat.

References

[1] P. S. Gill, S. R. Saurbrunn, M. Reading, J. Therm. Anal. **40** (1993) 931.

[2] M. Reading, Trends Poly. Sci. **8(1)** (1993) 248.

[3] M. Reading, D. Elliot, V. L. Hill, J. Therm. Anal. **40** (1993) 949.

[4] B. Wunderlich, Y. Jin, A. Boller, Thermochim. Acta,**238** (1994) 277.

[5] M. Reading, A. Luget, R. Wilson, Thermochim. Acta **238** (1994) 295.

[6] M. Song, A. Hammiche, H. M. Pollock, D. J. Hourston, M. Reading, Polymer **36** (1995) 3313.

[7] M. Wuff, M. Alden, Thermochim. Acta **256** (1995) 151.

[8] J. E. K. Schawe, G. W. Hohne, J. Therm. Anal. **46** (1996) 893.

[9] N. J. Coleman, D. Q. M. Craig, Int. J. Pharmaceut. **135** (1996) 13.

[10] F. Roussel, J. M. Buisine, J. Therm. Anal. **47** (1996) 715.

[11] I. Okazaki, B. Wunderlich, Macromolecules **30** (1997) 1758.

[12] A. Toda, M. Hikosaka, Y. Saruyama, Thermochim. Acta **293** (1997) 47.

[13] B. Wunderlich, *Thermal Analysis*, Academic Press, Boston, 1990, Chapter 4.

[14] R. Sherrenberg, V. Mathot, P. Steeman, J. Therm. Anal. **54** (1998) 477.

[15] I. Hatta, N. Katayama, J. Therm. Anal. **54** (1998) 577.

[16] F. U. Buehler, C. J. Martin, J. C. Seferis, J. Therm. Anal. **54** (1998) 501.

[17] H. Baur, B. Wunderlich, J. Therm. Anal. Calorim. **54(2)** (1998) 437.

[18] M. Reading, R. Luyt, J. Therm. Anal. **54** (1998) 535.

[19] S. Weyer, A. Hensel, C. Schick, Thermochim. Acta **304/305** (1997) 267.

[20] C. J. Martin, J. C. Seferis, J. Therm. Anal. **54** (1998) 501.

[21] F. U. Buehler, J. C. Seferis, Thermochim. Acta **334** (1999) 49.

[22] H. Baur, B. Wunderlich, J. Therm. Anal. **54** (1998) 437.

[23] S. Weyer, A. Hensel, C. Schick, Thermochim. Acta **304/305** (1997) 267.

[24] S. D. Kaloshkin, I. A. Tomilin, Thermochim. Acta **280/281**(1996) 303

[25] C. T. Moynihan, S. N. Crichton, S. M. Opalka, J. Non-cryst. Solids **131-133**(1991) 420

[26] A. A. Lacey, C. Nikolopoulos, M. Reading, J. Therm. Anal. **50** (1997) 279.

[27] J. Malek, J. M. Criado, Thermochim. Acta. **175** (1991) 305.

[28] R. I. Wu, G. Wilde, J. H. Perepezko, Mater. Sci. & Eng. A **301(1)** (2001) 12.

[29] T. Ozawa, K. Kanari, J. Therm. Anal. **54** (1998) 521.

[30] T. Ozawa, K. Kanari, J. Therm. Anal. Calori. **56** (1999) 691.

[31] B. Schenker, F. Stager, Thermochim. Acta **304/305** (1997) 219.

[32] M. L. D. Lorenzo, B. Wunderlich, J. Therm. Anal. **57** (1999) 459.

Chapter 6 Overall Conclusions and possible future work

In this thesis, different aspects of TMDSC are studied and the main results are given below.

(1) Effects of the contact thermal resistance on the observed specific heat

- Simulations of a TMDSC device with contact resistance between the sample and the support plate were carried out. The relationship among the measured heat capacity, the actual heat capacity and temperature modulation frequency of heat flux type TMDSC is similar to that of a low-pass filter.
- In TMDSC, because of the contact thermal resistance, the measured specific heat is affected by the sample mass. Careful sample preparation is important because too large or too small a sample mass (relative to the mass of the calibration reference) will lead to increased errors in the measured specific heat. An optimal sample mass is reached when the heat capacity of the sample which is a product of the mass and specific heat equals that of the reference used for calibration. In this case, theoretically, the measured specific heat of the sample will be the same as the actual value. Experimental results obtained with copper and aluminum are in good agreement with this conclusion.
- When TMDSC device works in the conventional DSC mode, the measured specific heat of the sample is not affected by the contact resistance. This is demonstrated by the DSC results of pure copper, even when the sample mass is as large as 400 mg.

(2) Effects of the internal thermal resistance of the sample with a low heat diffusivity

- A model that takes into account the thermal diffusivity of the sample was used and an analytical solution is derived. The effect of heat diffusivity and the geometry of the sample, as well as the modulation conditions on the observed specific heat and phase angle of the heat flow can be explained using the analytical solution.
- To improve the accuracy of measured specific heat, we may use a longer temperature modulation period, or reduce the sample thickness and mass. In the mean time, to satisfy the condition of optimal sample mass, the mass of the calibration reference must also be reduced.

(3) Effects of the non-reversing heat flow on the separability of the reversing heat flow and non-reversing heat flow

If there is a kinetic event in the sample, the separability of *NHF* and *RHF* by TMDSC depends on the *NHF* and temperature modulation conditions. Two different types of *NHF* are considered: time dependent *NHF* and temperature dependent *NHF*.

- Time dependent *NHF*: The measurement of specific heat (c_p), is applicable for the steady state where there is no *NHF*. While inside the *NHF* temperature range, if the modulation frequency is high enough, it still allows deconvolution of c_p, *HF*, *RHF*, and *NHF* by Fourier transform.
- Temperature dependent *NHF*: The *NHF* will be modulated by the temperature modulation and the *NHF* will contribute to the modulated part of the total heat flow (*HF*). This in turn can affect the linearity of the entire TMDSC system. When the *NHF* is strongly temperature dependent, it can influence the thermal

response to such an extent that the measured specific heat can no longer accurately reflect the actual specific heat.

(4) Study of the general situation and comparison with experimental results

- A general case that takes into account a kinetic reaction that is both time and temperature dependent was studied. An analytical solution based on small kinetic perturbation was derived.
- Several models of kinetic reactions are used to demonstrate the importance of the selection of the experimental parameters as well as the effects of the reactions on the system linearity. These include a first order chemical decomposition, a two-dimensional diffusion (D2), Jander (D3), Ginstling-Brounhtein (D4), Johnson-Mehl-Avarami (JMA), and Sestak-Berggren (SB) models.
- TMDSC experiments with several melt-spun Al-based amorphous alloys were carried out to demonstrate the unique capabilities of TMDSC. These include the ability to measure the differences between the specific heats of a sample in a fully amorphous, partially crystallized, or fully crystallized state; the separation of glass transition from other exothermal processes, for example, Al precipitation. Several factors have been identified that can improve the linearity of the TMDSC system (including the calorimetry device, the sample, reference and the reactions in the sample if any), e.g. low underlying heating rate, small modulation amplitude, or a high modulation frequency.
- The imaginary part of the complex heat capacity can be defined as $C'' \cong -f_T'/\omega$, where f_T' is the temperature derivative of the kinetic heat flow and ω is the angular frequency of temperature modulation. Obviously, C'' is the contribution from the kinetic event, but it is not a constant and varies with the temperature modulation conditions. It should be pointed out that this definition only holds true

when the linearity of the TMDSC system satisfies ($f_T'/C_s\omega$)<<1. This is different from many of the explanations given earlier by other researchers in terms of the physical meaning of the imaginary part of the complex heat capacity, as have been discussed in the first chapter of the thesis.

Possible future research work

a. Study of more kinetic models and their effects on the separability of *HF* and *NHF*. This may help us understand how TMDSC can be (or cannot be) used to better characterize kinetic reactions.

b. Application of temperature modulation techniques to other thermal analysis areas such as differential photo-calorimetry (DPA), differential thermo-gravimetry (DTG).

Appendix 1. Fourier Transform & Phase Angle Calculation

A1.1 Fourier transform

A periodic function *f(t)* may be expressed as a series of triangular functions,

$$f(t) = a_0 + \sum_{n=1}^{\infty} \left[a_n \cos(n\omega t) + b_n \sin(n\omega t) \right]. \quad \text{(A1.1)}$$

In the above equation,

$$a_0 = \frac{1}{\tau} \int_{t_1}^{t_1+\tau} f(t)dt, \quad \text{(A1.2)}$$

$$a_n = \frac{2}{\tau} \int_{t_1}^{t_1+\tau} f(t)\cos(n\omega t)dt, \quad \text{(A1.3)}$$

$$b_n = \frac{2}{\tau} \int_{t_1}^{t_1+\tau} f(t)\sin(n\omega t)dt, \quad \text{(A1.4)}$$

for n >=1, and τ is the period of *f(t)*.

In a real experiment, a computer-controlled instrument normally does not record the analog signals in a continuous fashion, but sample them periodically, and the data is stored in digital storage equipment such as random access memory, magnetic disk or tape. Discrete Fourier transform is used to analyze the data afterwards.

Discrete Fourier Transform [1, 2]:

$$F(K) = \sum_{n=0}^{N-1} f(x_n) e^{-j\frac{2n\pi K}{N}}. \quad \text{(A1.5)}$$

Inverse discrete Fourier transform:

$$f(x_n) = \frac{1}{N} \sum_{k=0}^{N-1} F(K) e^{j\frac{2n\pi K}{N}}. \quad \text{(A1.6)}$$

where N is the sample quantity in a single period (preferably, an even number), $f(x_n)$ is the corresponding sample value.

Because in TMDSC, the first order harmonic is used to derive the heat capacity and other required signals, it can be obtained that, the first order presentation of $f(x_n)$ is,

$$f_1(x_n) = \frac{1}{N}(a_1 + j \cdot b_1) e^{j\frac{2n\pi}{N}} \quad . \tag{A1.7}$$

According to Eq. (A1.5), we have,

$$F(1) = \sum_{n=0}^{N-1} f(x_n) e^{-j\frac{2n\pi}{N}} = a_1 + j \cdot b_1 \, . \tag{A1.8}$$

Thus the amplitude of the first order harmonic is,

$$amplitude = \sqrt{a_1^{\,2} + b_1^{\,2}} \, . \tag{A1.9}$$

A1.2 Phase angle calculation

While in Eq. (A1.7), the amplitude is decided by both the real and imaginary part, only the real part carries physical meaning and can thus be obtained as,

$$\mathrm{Re}[f_1(t)] = \frac{1}{N}\left[a_1 \cos\left(\frac{2n\pi}{N}\right) - b_1 \sin\left(\frac{2n\pi}{N}\right)\right] = \frac{\sqrt{a_1^{\,2} + b_1^{\,2}}}{N} \sin\left(\frac{2n\pi}{N} - \varepsilon\right), \tag{A1.10}$$

where the phase angle ε satisfies,

$$\sin(\varepsilon) = -\frac{a_1}{\sqrt{a_1^{\,2} + b_1^{\,2}}}, \tag{A1.11}$$

$$\cos(\varepsilon) = -\frac{b_1}{\sqrt{a_1^{\,2} + b_1^{\,2}}} \, . \tag{A1.12}$$

Hence if there are two periodical functions $f(t)$ and $g(t)$ with corresponding phase angle ε_f and ε_g, the difference between them is $(\varepsilon_f - \varepsilon_g)$.

References

[1] D. C. Champeney, *Fourier Transforms and their Physical Applications,* Academic Press, Inc. copyright 1973. London

[2] K. Morita, *Applied Fourier Transform*, IOS Press, copyright 1995. Tokyo

Appendix 2. Steady State Solution of the R-C Network Model (see chapter 2) under Linear Heating Conditions in conventional DSC

For the R-C network model given in chapter 2, if the heating block is heated in a linear pattern, $T_b=T_0+qt$, (T_0 is the initial temperature, q the heating rate, t is time), then, after the system reaches a steady state, transient terms become negligible, every point i in the RC-net work model will bear a similar temperature profile which can be presented by $T_i=T_{i0}+qt$, $dT_i/dt=q$, where is T_{i0} is a constant for that specific point. Thus the original heat conducting differential equations will be turned into linear ones, because $C_1=C_2=C_3=C_4=C$ and $R_1=R_2=R_3=R_4=R$, we have,

$$(T_b - T_1)/R = (T_1 - T_r)/R + C \cdot q, \tag{A2.1}$$

$$(T_1 - T_r)/R = (T_r - T_s)/R_c + (T_r - T_{r1})/R_r + C \cdot q, \tag{A2.2}$$

$$(T_r - T_{r1})/R_r = C_r \cdot q, \tag{A2.3}$$

$$(T_b - T_2)/R = (T_2 - T_s)/R + C \cdot q, \tag{A2.4}$$

$$(T_2 - T_s)/R = (T_s - T_r)/R_c + (T_s - T_{s1})/R_s + C \cdot q, \tag{A2.5}$$

$$(T_s - T_{s1})/R_s = C_{s0} \cdot q. \tag{A2.6}$$

Inserting Eq. (A2.3) into Eq. (A2.2) and Eq. (A2.6) into Eq. (A2.5), we obtain,

$$(T_1 - T_r)/R = (T_r - T_s)/R_c + q(C_r + C), \tag{A2.7}$$

$$(T_2 - T_s)/R = (T_s - T_r)/R_c + q(C_{s0} + C). \tag{A2.8}$$

Adding Eq. (A2.7) to Eq. (A2.8), we can obtain,

$$[(T_1 - T_r) + (T_2 - T_s)]/R = q(2C + C_r + C_{s0}). \tag{A2.9}$$

Re-arranging Eqs. (A2.1), (A2.4), (A2.8) and (A2.9), we have

$$-2T_1 + T_r = C \cdot q \cdot R - T_b = A, \tag{A2.10}$$

$$-2T_2 + T_s = C \cdot q \cdot R - T_b = A, \tag{A2.11}$$

$$T_1 - T_r + T_2 - T_s = q(2C + C_r + C_{s0})R = B\,, \tag{A2.12}$$

$$R \cdot T_r + R_c \cdot T_2 - (R_c + R)T_s = q(C_{s0} + C)R_c R = D\,. \tag{A2.13}$$

On the right hand side of Eqs. (A2.10) to (A2.13), A, B and D are introduced to simplify the derivation process. Hence Eqs. (A2.10) to (A2.13) can be represented with the following matrix,

$$\begin{Bmatrix} -2 & 1 & 0 & 0 \\ 0 & 0 & -2 & 1 \\ 1 & -1 & 1 & -1 \\ 0 & R & R_c & -(R_c + R) \end{Bmatrix} \begin{Bmatrix} T_1 \\ T_r \\ T_2 \\ T_s \end{Bmatrix} = \begin{Bmatrix} A \\ A \\ B \\ D \end{Bmatrix} \quad . \tag{A2.14}$$

Through further transform we can obtain,

$$\begin{Bmatrix} -2 & 1 & 0 & 0 \\ 0 & R & R_c & -(R_c + R) \\ 0 & 0 & (R_c + 2R) & -(R_c + 3R) \\ 0 & 0 & 0 & -(R_c + 4R)/2 \end{Bmatrix} \begin{Bmatrix} T_1 \\ T_r \\ T_2 \\ T_s \end{Bmatrix} = \begin{Bmatrix} A \\ D \\ (2B + A)R + D \\ A(2R + R_c)/2 + (2B + A)R + D \end{Bmatrix}. \tag{A2.15}$$

Solving for Eq. (A2.15), we have

$$\begin{aligned} T_s &= \frac{A(2R + R_C) + 2(2B + A)R + 2D}{-(R_c + 4R)} \\ &= T_b - 3C \cdot q \cdot R - \frac{4C_r \cdot R^2 + C_{s0}\left(4R^2 + 2R \cdot R_C\right)}{R_C + 4R} \cdot q \end{aligned}\,, \tag{A2.16}$$

$$T_r = T_b - 3C \cdot q \cdot R - \frac{4C_{s0} \cdot R^2 + C_r\left(4R^2 + 2R \cdot R_C\right)}{R_C + 4R} \cdot q\,. \tag{A2.17}$$

Because T_r and T_s are the measured temperatures of the thermal couples, the difference between T_r and T_s is

$$T_r - T_s = \frac{2(C_{s0} - C_r)R \cdot R_C \cdot q}{R_c + 4R}. \tag{A2.18}$$

According to the definition in conventional DSC,

$$K \cdot (T_r - T_{s0}) = m_s \cdot c_{p\_s} \cdot q\,, \tag{A2.19}$$

where $m_s c_{p\_s} = C_{s0} - C_r$, m_s is sample mass, the system thermal constant K is found to be

$$K = \frac{R_C + 4R}{2R \cdot R_C} . \qquad \text{(A2.20)}$$

Also we can obtain the temperatures for other points of interest as below,

$$T_{r1} = T_r - C_r \cdot q \cdot R_r , \qquad \text{(A2.21)}$$

$$T_{s1} = T_s - C_r \cdot q \cdot R_s , \qquad \text{(A2.22)}$$

$$T_1 = (T_r + T_b - C \cdot q \cdot R)/2 , \qquad \text{(A2.23)}$$

$$T_1 = (T_r + T_b - C \cdot q \cdot R)/2 , \qquad \text{(A2.24)}$$

From Eq. (A2.18) and Eq. (A2.20), it is noticed that, for the ideal symmetric DSC model, the relationship between the heat flow (which equals $K(T_r - T_s)$) and the measured heat capacity ($C_{s0} - C_r$) is linear. ($C_{s0} - C_r$) is not affected by the thermal resistance between the thermal couple and the sample or reference (R_r or R_s), nor is the constant K affected by R_r or R_s. Obviously this can be an advantage of conventional DSC over TMDSC.

Appendix 3. Finite Difference Method for One-dimensional Steady State Heat Transfer Problems

While analytical methods can give a precise solution to some simple heat transfer problems, they are not always suitable for practical situations. With the rapid development in computer technology, computing power is becoming much cheaper than it used to be, and numerical methods can be used to solve almost any heat conducting problems. Among them, the most widely used is Finite difference method.

The governing differential equation for one-dimensional heat transfer problem is given as below,

$$\frac{\partial^2 T}{\partial x^2} = \frac{1}{\alpha}\frac{\partial T}{\partial t} \quad , \tag{A3.1}$$

where T is temperature, t is time, X is distance. The above equation can be presented in an approximated form. If the space increment is Δx, the time increment is Δt, then

$$\frac{\partial^2 T}{\partial x^2} \approx \frac{T_{n+1}{}^p - 2T_n{}^p + T_{n-1}{}^p}{(\Delta x)^2}, \tag{A3.2}$$

and

$$\frac{\partial T}{\partial t} \approx \frac{T_n{}^{p+1} - T_n{}^p}{\Delta t}. \tag{A3.3}$$

Inserting Eqs. (A3.2) and (A3.3) into Eq. (A3.1) yields

$$\frac{T_{n+1}{}^p - 2T_n{}^p + T_{n-1}{}^p}{(\Delta x)^2} = \frac{1}{\alpha}\cdot\frac{T_n{}^{p+1} - T_n{}^p}{\Delta t}. \tag{A3.4}$$

In Eqs. (A3.2) to (A3.4), $T_n{}^p$ is the temperature at point $x=n\Delta x$ at time $t=p\Delta t$, then Eq. (A3.1) becomes

$$T_{n+1}{}^p = \left[1 - \frac{2\alpha\cdot\Delta t}{(\Delta x)^2}\right]T_n{}^p + \frac{\alpha\cdot\Delta t}{(\Delta x)^2}\left(T_{n+1}{}^p - T_{n-1}{}^p\right). \tag{A3.5}$$

To obtain a stable and convergent solution, it is required that [1]

$$\frac{2\alpha \cdot \Delta t}{(\Delta x)^2} \le 1. \qquad \text{(A3.6)}$$

More accurate solution can be obtained with a smaller Δx and Δt. In our computer programs, double precision data type is used to reduce the round off errors.

Reference

[1] S. Kakac, Y. Yener, *Heat conduction*, 3rd edition, Copyright 1993, Taylor & Francis. Washington, DC